

Measurement of protein  
transport and confinement  
in heterogeneous membranes  
by k-space Image Correlation Spectroscopy

Elvis Pandžić

Doctor of Philosophy

Department of Physics

McGill University

Montreal, Quebec

2013-02-15

A Thesis submitted to McGill University in partial fulfilment of the requirements  
for the degree of Doctor of Philosophy

©Elvis Pandžić, 2013

## DEDICATION

This thesis is dedicated to my dear and loving grandmother Arifa

## ACKNOWLEDGEMENTS

There are a number of people without whom this thesis might not have been written and to whom I am greatly indebted.

First, I would like to thank my supervisor, Dr. Paul Wiseman. Paul offered all the available resources, for the successful completion of this work. He promoted the creativity in research and encouraged a respectful and a collaborative working environment. His confidence in my capacities and open mindedness toward the new scientific ideas allowed me to explore (in  $k$ -space!) confidently different avenues in this endeavour. Moreover, his great sense of humour and innumerable stories made his presence throughout my graduate studies everything but boring!

Working in a research lab makes you discover people who exchange ideas, help you solve problems, do experiments with you or simply have pint of beer with you from time to time. Whatever the interaction, these people participated in my intellectual fulfilment throughout the years of my graduate studies. First, I would like to thank Dr. Asmahan Abu Arish, who helped me in many aspects of my project and for being a great colleague and a friend. I would like to thank Hussein Sangji for working with me over a course of last summer and helpful discussions related to the theoretical development of this thesis. Another special mention goes to Hugo Brandao and Jean-Francois Desjardins for numerous scientific discussions in the office or around a cup of coffee. As well, I would like to thank the other Wiseman lab members: Tim Toplak, Angelica Gopal, Nageswara Rao Ghattamaneni and Dr. Sherdeep Singh. I would like to thank the former

group members, Dr. Antoine Godin and Laurent Potvin, for useful discussions on simulator development. These and all previous lab members I had pleasure to share the moments at group meetings, conferences, summer and Christmas BBQ parties or hockey games, is what made this lab a great place to work at.

Outside of Wiseman lab, many people have shared their knowledge and resources, which helped me progress in my scientific development. I would like to thank my former supervisor Dr. Maria Kilfoil for helping and guiding me in my early scientific development. Also, I would like to thank Dr. Jay Louise Nadeau, of Biomedical Engineering at McGill, who offered her lab resources and knowledge for my training in molecular and cell biology. Dr. Jackie Vogel merits acknowledgement for her help in training on the spin-disk confocal microscope and Dr. Ian Bates for training on TIRF microscope and FCS. I would not like to forget enormous help we get, as graduate students, from staff members of our department. I would like to give special mention to Juan Gallego, Paul Mercure, Robert Gagnon, John Smeros and Saverio Biunno for offering their help whenever it was needed. Also, all of our precious administrative staff with special mentions to Diane Koziol and Sonia Viera.

I would like to thank all of my fellow graduate student, who shared great moments on soccer pitch and in the hockey arena over the period of my studies. I can not forget my very close friends, Haris, Igor, Sasa and Vedran: thank you for being friends I could rely on anytime. I also thank, a colleague former graduate student Dr. Mathieu Gaudreault for being a great friend since the undergraduate years.

I would like to thank my dear Stephanie Denizard for her patience, support and all the wonderful memories from the past year and a half.

Finally, I am grateful to my mother Mehira, my father Husein, my grandmother Arifa and my sister Arnela for their love and support throughout my career as a professional student over the past several years.

Thank you all!

## ABSTRACT

This thesis presents the application of k-space Image Correlation Spectroscopy (kICS) to the analysis of fluorescence microscopy image time series for the measurement of particle diffusion in heterogeneous membranes, composed of micro-domains. The extension, testing and application of kICS for such measurements is developed both in silico with simulation and with in vivo cellular experiments.

Connections between kICS analysis and other existing fluorescent microscopy techniques used in the study of heterogeneous membranes, such as single particle tracking (SPT) and spot vary Fluorescence Correlation Spectroscopy (FCS) are introduced. This is followed by the development of kICS theory of fluorescent particle diffusion within a heterogeneous two dimensional (2D) environment. Two possible membrane heterogeneities, isolated lipid micro-domains and actin proximal meshwork, are considered separately. The emergent models suggest that the kICS correlation function (CF) can be fit by a sum of two Gaussians in the case of particle diffusion in the presence of isolated micro-domains. These two fit components, called 'fast' and 'slow', with the fast associated with the rapid decay of the kICS CF at small spatial frequencies due to particle motion on large spatial scales outside domains while the slow component refers to the confined particle motion on large spatial frequencies or small spatial scales in domains. On the other hand, the meshwork confinement is well fit with a single Gaussian model for the analysis of kICS CF. These models suggest that the exponents and amplitudes of the fits embed the characteristic system parameters such as diffusion coefficients

outside and inside domains, the partitioning rates, micro-domains radii and mesh pore size.

Furthermore, systematic simulations to study different confinement scenarios were conducted and the calculated kICS correlation functions were fit and the output interpreted for recovery of self system parameters. The characterization of the simulated data suggests that kICS CFs exhibit various confinement dependent features, such as decays due to effective slow and fast dynamics populations and effective domain sizes. The *in silico* characterization of different confinement scenarios, suggests a connection between the apparent measured confinement properties, and the set system defining parameters. We explore the range and limits where confinement effects can be detected and accurately measured by kICS analysis. Possible systematic errors in the values of the fit extracted parameters due to background noise is discussed with possible alternative solutions.

Finally, we apply this extension of kICS to the heterogeneous membrane environment to explore the confinement dynamics of GPI-GFP anchored proteins in the basal plasma membrane of COS-7 cells. We employ a novel labelling approach of GPI-GFP using anti-GFP-Alexa594 and image the protein in COS-7 cell membranes with TIRF microscopy. Cells were exposed to enzymatic treatments, using the Cholesterol Oxidase (COase) and Sphingomyelinase (SMase), in order to disrupt membrane domains and change GPI-GFP confinement dynamics. We observe that GPI-GFP mobility and the effective domain size measured correlates with the enzymatic exposure time. We attribute it to the conversion of the membrane domain constituents, cholesterol and sphingomyelin, upon the enzymatic reactions,

leading to membrane domain that are effectively larger and leakier. Finally, we conclude with possible improvements and future directions.

## ABRÉGÉ

La thèse qui suit est a propos de l'adaptation de la technique de la spectroscopie par la corrélation des images dans l'espace de Fourier, appelle kICS. La nouveauté consiste en utilisation de kICS pour analyser les séries temporelles d'images fluorescentes afin de caractériser la diffusion des particules en présence des membranes hétérogènes, composées de micro-domaines.

Tout d'abord, une parallèle est exposée entre l'analyse fondée sur kICS proposé ci-dessus et d'autres techniques de microscopie à fluorescence existantes et utilisées dans l'étude des membranes hétérogènes. Ensuite, on expose le développement de la théorie de kICS dans les cas de la diffusion des particules fluorescentes dans un espace hétérogène bidimensionnel (2D). Les deux hétérogénéités membranaires possibles, micro-domaines lipidiques isolés et le réseau de l'actine proximale, sont considérés séparément. Les modèles émergents suggèrent que la fonction de corrélation de kICS doit être caractérisé par une somme de deux Gaussiennes dans le cas de la dynamique des particules en présence de micro-domaines isolés. Ces deux éléments, appelés 'rapide' et 'lent', représentent les composantes dynamiques a deux échelles d'espace différentes. La rapide est associé à la décroissance rapide de la fonction de corrélation de kICS à petites fréquences spatiales dues au mouvement des particules sur de grandes échelles spatiales. La composante lente réfère au mouvement des particules confinées à des petites échelles spatiales, observées sur de grandes fréquences spatiales de kICS. D'autre

part, la fonction de corrélation de kICS due au confinement par le réseau du cytoskeleton peut être caractérisée par une unique décroissance Gaussienne. Ces modèles suggèrent que les exposants et les amplitudes obtenus par la caractérisation de la fonction kICS dépendent des paramètres caractéristiques du système tels que les coefficients de diffusion à l'extérieur et à l'intérieur de domaines, les taux de migration de particules vers l'intérieur ou l'extérieur de micro-domaines ou des tailles de porosités du réseau du cytoskeleton.

Les études systématiques par les simulations des scénarios différents de confinement et leurs effets sur la fonction de corrélation de kICS ont été explorées. La caractérisation des données simulées suggère que les fonctions de corrélation ont des caractéristiques qui dépendent du confinement et des propriétés spécifiques, tels que la dynamique des populations lentes et rapides et la taille effective de micro-domaines. La caractérisation des scénarios de confinement différents, représente les liens entre les propriétés apparentes mesurées de confinement, et un ensemble de paramètres définissant l'hétérogénéité. Nous explorons les limites pour lesquelles des effets de confinement ne sont pas observés dans la fonction de corrélation kICS. Les éventuelles erreurs systématiques dans les valeurs des paramètres extraits à cause du bruit de fond est discuté avec des possibles solutions.

Finalement, nous utilisons l'analyse afin d'explorer la dynamique de confinement de la protéine ancrée à GPI-GFP dans la membrane plasmique basale des cellules COS-7. Nous explorons une approche nouvelle de la conjugaison entre le GPI-GFP et les anti-GFP-Alexa594 et imagé par la microscopie TIRF. Les cellules

ont été exposées à des traitements enzymatiques, par Coase et SMase, afin de perturber domaines membranaires et changer la dynamique de confinement de GPI-GFP. Les réactions enzymatiques augmentent la mobilité et la taille effective des domaines de GPI-GFP. Nous attribuons cela à la conversion des constituants des domaines, le cholestérol et la sphingomyéline, par les réactions enzymatiques, ce qui conduit aux plus grandes et moins étanches domaines membranaires.

## STATEMENT OF ORIGINALITY

The author claims that the following aspects of the thesis constitute original scholarship and an advancement of knowledge:

- **chapter 2** The theoretical link connecting the dynamic light scattering related metrics and image correlation spectroscopy correlation functions was made. For the first time, clear equivalence between the spatio-temporal image correlation spectroscopy (STICS) and k-space image correlation spectroscopy (kICS) CF was made. The theory for kICS in presence of two phase media, characterized by isolated microscopic domains, is linked with the chemical reaction-diffusion system of equations. The model is the first instance in which STICS or kICS are applied for the measurement of the confined particles dynamics and system parameters from an image time series. The kICS theory for analyzing a meshwork type confinement is suggested based on a phenomenological observation of data and from theoretical models published in the SPT and FCS literature.
- **chapter 3** The development of an image time series simulator with realistic convolutions taking into account possible sub-pixel displacements of the particles. Implementation of a continuous value for membrane domain sizes, in contrast to the old methodology employing the use of raftMask images. A novel approach to the interpretation of kICS correlation functions, using a fit with a sum of two Gaussian functions in order to characterize the effective dynamic populations emerging in the presence of membrane

heterogeneities. A single Gaussian fit vs time lag, at given spatial frequency  $k^2$ , in order to extract the so called ICS diffusion law. An original approach to the GPI-GFP labelling by the anti-GFP-Alexa594 in order to increase the signal-to-background level in the experimental images.

- **chapter 4** The simulations were performed for the isolated membrane domains and meshwork modelling a heterogeneous membrane environment. The parameters governing the particles confined diffusion were varied systematically. kICS was used for first time to characterize all of the confinement scenarios simulated and the fitted correlation function data were interpreted. The parameters extracted, such as diffusion coefficients at small and large spatial scales, their amplitudes, the plateau of the saturation of the slow component are the hallmark of kICS correlation function in presence of a heterogeneous two-phase environment. They were demonstrated to correlate with the variation of the set simulation parameters such as diffusion coefficients inside and outside domains, probabilities of partitioning inside and outside domains, domain size and domain density. The meshwork-like confinement was shown to yield a single Gaussian decay for the calculated kICS CF. The microscopic and macroscopic diffusion coefficients and mesh pore radius in a meshwork system can be determined from the  $4D\tau$  vs  $\tau$  relation extracted from the fit. The confinement statistics, such as average particle domain partitioning  $\beta$ , correlate with kICS extracted properties such as saturation of the slow component plateau and amplitudes saturation for different components.

- **chapter 5** The first measurement and characterization of GPI-GFP dynamics in COS-7 cells using the new extension of kICS analysis. Enzymatic treatments were made to perturb GPI-GFP domains, using coase and smase, and kICS analyzed image time series were characterized for the characteristic confinement parameters.

Because of the interdisciplinary nature of biophysics, some of the work presented here was completed in collaboration with others. The procedures included in this thesis that were completed in collaboration with other people include:

- **Experimental GPI-GFP characterization** The experimental work included in chapter 5 was done together with Dr. Asmahan Abu Arish. The shared tasks involved cell culture, cellular transfection and TIRF microscopy, while the image time series kICS analysis was done solely by the author of this thesis.
- **Theory development** The part of the theory dealing with the inter-conversion of two dynamic species was developed partially by Hussain Sangji during his summer research fellowship in 2012.

## TABLE OF CONTENTS

|                          |  |     |
|--------------------------|--|-----|
| DEDICATION               | . . . . .  | ii  |
| ACKNOWLEDGEMENTS         | . . . . .  | iii |
| ABSTRACT                 | . . . . .  | vi  |
| ABRÉGÉ                   | . . . . .  | ix  |
| STATEMENT OF ORIGINALITY | . . . . .  | xii |
| LIST OF TABLES           | . . . . .  | xix |
| LIST OF FIGURES          | . . . . .  | xx  |
| 1                        | Introduction . . . . .   | 1   |
|                          | 1.1 Heterogeneity in cellular membrane environments . . . . .                | 1   |
|                          | 1.2 Fluorescence . . . . .   | 8   |
|                          | 1.2.1 Definition of fluorescence . . . . .                                   | 8   |
|                          | 1.2.2 Tracers used to probe heterogeneous environment . . . . .              | 11  |
|                          | 1.2.3 Fluorescence microscopy . . . . .                                      | 17  |
|                          | 1.3 Fluorescence techniques for probing membrane heterogeneities . . . . .   | 21  |
|                          | 1.3.1 Single particle tracking . . . . .                                     | 22  |
|                          | 1.3.2 Fluorescence correlation spectroscopy . . . . .                        | 28  |
|                          | 1.4 ICS analysis of heterogeneous membrane . . . . .                         | 37  |
|                          | 1.4.1 Overview of ICS superfamily of techniques . . . . .                    | 37  |
|                          | 1.4.2 Spatio-temporal image correlation spectroscopy . . . . .               | 38  |
|                          | 1.4.3 k-space image correlation spectroscopy . . . . .                       | 41  |
|                          | 1.4.4 Emergent features of kICS in the presence of heterogeneities . . . . . | 43  |
|                          | REFERENCES . . . . .   | 50  |
| 2                        | Theory of kICS for heterogeneous membrane environments . . . . .             | 58  |
|                          | 2.1 kICS analogy to the dynamic light scattering . . . . .                   | 58  |

|       |  |     |
|-------|--|-----|
| 2.2   | kICS theory for a homogeneous environment . . . . .  | 62  |
| 2.2.1 | STICS from kICS . . . . .  | 65  |
| 2.2.2 | Normalization by the zero temporal lag . . . . .   | 66  |
| 2.2.3 | Two freely diffusing populations . . . . .   | 67  |
| 2.3   | Theory for a two phase medium with static domains . . . . .  | 67  |
| 2.4   | kICS theory for a system of chemically inter-converting species . .  | 73  |
| 2.5   | kICS theory for a meshwork confinement . . . . .   | 78  |
|       | REFERENCES . . . . .   | 83  |
| 3     | Materials and Methods . . . . .  | 85  |
| 3.1   | Computer simulations . . . . .   | 85  |
| 3.1.1 | General considerations . . . . .   | 85  |
| 3.1.2 | Isolated domains simulations . . . . .   | 88  |
| 3.1.3 | Meshwork simulations . . . . .   | 93  |
| 3.1.4 | Background noise implementation . . . . .  | 94  |
| 3.2   | Data analysis . . . . .  | 96  |
| 3.2.1 | Data windowing . . . . .   | 96  |
| 3.2.2 | kICS function computation, normalization and averaging .   | 98  |
| 3.2.3 | Nonlinear fitting of the correlation functions . . . . .   | 99  |
| 3.2.4 | Extraction of domain size and particle mobilities . . . . .  | 104 |
| 3.3   | Cell culture, protein labelling and enzyme treatments . . . . .  | 106 |
| 3.4   | TIRF microscopy . . . . .  | 109 |
|       | REFERENCES . . . . .   | 112 |
| 4     | Computer simulations for characterization of kICS applied to heteroge-<br>neous 2D environments . . . . .                | 113 |
| 4.1   | Computer simulated data for isolated domains . . . . .   | 113 |
| 4.2   | kICS analysis for different confinement simulations . . . . .  | 115 |
| 4.2.1 | kICS analysis for simulations with a varying $D_{in}$ . . . . .  | 115 |
| 4.2.2 | kICS analysis for simulations with a varying domain radius   | 116 |
| 4.2.3 | kICS analysis for simulations with a varying domain area<br>occupancy . . . . .  | 116 |
| 4.2.4 | kICS analysis for simulations with varying $\frac{P_{in}}{P_{out}}$ . . . . .  | 119 |
| 4.3   | kICS analysis for simulations of two freely diffusing populations .  | 123 |
| 4.4   | Two Gaussian fit of the kICS correlation functions for the simu-<br>lations of different confinement scenarios . . . . . | 124 |

|                              |   |     |
|------------------------------|---|-----|
| 4.4.1                        | Two Gaussian fit of the kICS correlation functions for simulations with variable $D_{in}$ . . . . .                 | 125 |
| 4.4.2                        | Two Gaussian fit of the kICS correlation functions for simulations with variable domain radius . . . . .            | 128 |
| 4.4.3                        | Two Gaussian fit of the kICS correlation functions for simulations with variable domain area fraction . . . . .     | 130 |
| 4.4.4                        | Two Gaussian fit of the kICS correlation functions for simulations with variable $\frac{P_{in}}{P_{out}}$ . . . . . | 132 |
| 4.5                          | Discussion . . . . .  | 137 |
| 4.5.1                        | Characteristic times for free and trapped particles . . . . .   | 137 |
| 4.6                          | Domain size: aliasing or large effective clusters? . . . . .  | 139 |
| 4.7                          | Systematic characterization of confinement statistics . . . . .   | 142 |
| 4.8                          | Effects of background noise on kICS correlation functions . . . . .   | 149 |
| 4.9                          | Results for kICS analysis of simulations of meshwork confinement domains . . . . .                                  | 153 |
| 4.9.1                        | Results for kICS analysis of meshwork simulations to establish the ICS diffusion law . . . . .                      | 156 |
| 4.10                         | ICS diffusion law for Isolated domains . . . . .  | 159 |
| Appendix Chapter 5 . . . . . |   | 164 |
| REFERENCES . . . . .         |   | 167 |
| 5                            | Experimental characterization of GPI-GFP dynamics in live COS-7 cells   | 168 |
| 5.1                          | Alexa dye labelled GPI-GFP on COS-7 plasma membranes . . . . .  | 168 |
| 5.2                          | Correlation functions for GPI-GFP under different enzyme treatments . . . . .                                       | 171 |
| 5.2.1                        | Characterization of the average trends from multiple cells . . . . .  | 179 |
| 5.2.2                        | Characterization of the individual cell trends . . . . .  | 182 |
| 5.3                          | Discussion of experimental results . . . . .  | 187 |
| REFERENCES . . . . .         |   | 193 |
| 6                            | Conclusions and future perspectives . . . . .   | 195 |
| 6.1                          | Conclusions . . . . .   | 195 |
| 6.1.1                        | Adaptation of kICS to confinement analysis . . . . .  | 195 |
| 6.1.2                        | Perspectives and possible future directions . . . . .   | 205 |
| REFERENCES . . . . .         |   | 211 |

Biohazardous Materials Certificate . . . . . 214  
Copyright Permission Form . . . . . 215  
KEY TO ABBREVIATIONS . . . . . 216

LIST OF TABLES

| <u>Table</u> |   | <u>page</u> |
|--------------|---|-------------|
| 3-1          | Adjustable parameters for isolated domains simulations . . . . .  | 92          |
| 3-2          | Adjustable parameters for meshwork simulations . . . . .  | 95          |
| 4-1          | Summary of results for trends in kICS measured parameters for the<br>isolated domains simulations . . . . . | 136         |

## LIST OF FIGURES

| <u>Figure</u>  | <u>page</u> |
|--|-------------|
| 1-1 Fluid Mosaic membrane model . . . . .  | 3           |
| 1-2 Modern view of cell membrane . . . . .   | 7           |
| 1-3 Jablonski diagram . . . . .  | 9           |
| 1-4 Fluorescent dyes spectra . . . . .   | 10          |
| 1-5 Fluorescent dyes . . . . .   | 12          |
| 1-6 IgG Antibody Crystal Structure . . . . .   | 15          |
| 1-7 Antibody labelling of GPI-GFP . . . . .  | 16          |
| 1-8 The principle of Epi-Fluorescence . . . . .  | 18          |
| 1-9 Total Internal Reflection Microscopy Principles . . . . .                                  | 19          |
| 1-10 SPT trajectories and MSD for a freely and confined diffusing simulated particle . . . . . | 26          |
| 1-11 Principle of Fluorescence Correlation Spectroscopy . . . . .                              | 29          |
| 1-12 FCS free diffusion example intensity trace and temporal ACF . . . . .                     | 30          |
| 1-13 Simulations of beam varying FCS for three simulated diffusion mechanisms . . . . .        | 32          |
| 1-14 Beam varying FCS for free and isolated domains limited diffusion . . . . .                | 34          |
| 1-15 Beam varying FCS for meshwork limited diffusion . . . . .                                 | 36          |
| 1-16 STICS basic concept with three scenarios . . . . .  | 39          |
| 1-17 kICS in case of a purely diffusing single species . . . . .                               | 42          |

|   |     |
|---|-----|
| 1–18 Steps for calculation of a normalized averaged kICS correlation function . . . . .   | 43  |
| 1–19 kICS data analysis example . . . . .   | 44  |
| 1–20 Examples of kICS CFs for three different simulated populations . . . . .   | 46  |
| 1–21 kICS diffusion laws for free and confined dynamics . . . . .   | 48  |
| 2–1 Emergence of two dynamic populations in the kICS correlation functions calculated from simulations with particles diffusing inside and outside domains on a 2D surface. . . . . | 79  |
| 3–1 Change in Image Convolution . . . . .   | 87  |
| 3–2 Change in raft creation in simulations . . . . .  | 89  |
| 3–3 Examples of simulated meshworks. . . . .  | 94  |
| 3–4 Hann Windowing prior to Fourier transform . . . . .   | 97  |
| 3–5 Example of k-space correlation function for an isolated domain case . . . . .   | 101 |
| 3–6 Example of data processing to extract domain size and particle mobilities . . . . .   | 105 |
| 3–7 Schematic overview of the correlation function analysis, fitting and confinement parameter output calculated from image time series inputs. . . . .                             | 107 |
| 4–1 Examples of computer simulated domains images . . . . .   | 115 |
| 4–2 Average correlation functions for case of $D_{in}$ variation . . . . .  | 117 |
| 4–3 Average simulated correlation functions for case of domain radius variation . . . . .   | 118 |
| 4–4 Average correlation functions for case of domain density variation . . . . .  | 120 |
| 4–5 Average correlation functions for case of $P_{in}$ variation . . . . .  | 122 |
| 4–6 kICS analysis of simulations of two freely diffusing populations. . . . .   | 124 |
| 4–7 Fast and slow mobilities for variation of $D_{in}$ . . . . .  | 126 |

|      |   |     |
|------|---|-----|
| 4-8  | Effective system properties for varying $D_{in}$ . . . . .  | 127 |
| 4-9  | Fast and Slow mobilities for variation of raft size . . . . .   | 129 |
| 4-10 | Effective system properties for variation of domain radius . . . . .  | 131 |
| 4-11 | Fast and Slow mobilities for variation of domain area fraction . . . . .  | 132 |
| 4-12 | Effective system properties for variation of domain area occupancy . . . . .  | 133 |
| 4-13 | Fast and Slow mobilities for variation of $\frac{P_{in}}{P_{out}}$ . . . . .  | 134 |
| 4-14 | Effective system properties for variation of $\frac{P_{in}}{P_{out}}$ . . . . .                                       | 135 |
| 4-15 | Plots of fractional confinement statistics calculated from particle positions from the computer simulations . . . . . | 138 |
| 4-16 | Average (DC) image from time series for different domain radii. . . . .   | 141 |
| 4-17 | Example of retrieval of the confinement statistics from the known particle positions. . . . .                         | 145 |
| 4-18 | Confinement statistics calculated for simulations with $P_{out} = 0.01$ . . . . .                                     | 146 |
| 4-19 | kICS analysis fitted parameters for single image series simulations with $P_{out}=0.01$ . . . . .                     | 150 |
| 4-20 | Background noise variation effect on images . . . . .   | 151 |
| 4-21 | Background noise variation effect on correlation functions . . . . .  | 154 |
| 4-22 | Example of kICS correlation function for meshwork . . . . .   | 156 |
| 4-23 | kICS analysis of simulations with varied P or mesh pore size of a meshwork. . . . .                                   | 158 |
| 4-24 | ICS diffusion law from single temporal Gaussian fit to the correlation functions . . . . .                            | 160 |
| 4-25 | Data extracted from ICS diffusion law of isolated domains simulations with the variation of domain radius. . . . .    | 162 |
| 4-26 | Confinement statistics calculated for simulations with $P_{out}=0.1$ . . . . .  | 165 |

|      |  |     |
|------|--|-----|
| 4-27 | $R^2$ and $\sigma(R^2)$ for two Gaussians fit of kICS data of a single image<br>series simulation for two $P_{out}$ scenarios considered . . . . . | 166 |
| 5-1  | Comparison of old and new labelling approaches for GPI-GFP . . . . .   | 170 |
| 5-2  | Example of GPI-GFP-IgG-Alexa-594 images . . . . .  | 172 |
| 5-3  | Examples of an average and a typical correlation function for GPI-<br>GFP-Alexa-594 . . . . .  | 174 |
| 5-4  | Correlation functions for GPI-GFP-Alexa-594 after DC removal . . . . .   | 176 |
| 5-5  | The characteristic decays for fast and slow components for GPI-GFP<br>data . . . . .   | 178 |
| 5-6  | Parameters extracted for GPI-GFP data . . . . .  | 183 |
| 5-7  | Boxplot for the parameters extracted for GPI-GFP data . . . . .  | 185 |

## CHAPTER 1

### Introduction

#### 1.1 Heterogeneity in cellular membrane environments

Our view of matter in terms of structure and function is constantly evolving due to new experimental findings obtained with newly developed techniques. For instance, the modern view of the atom has evolved ever since John Dalton proposed the atomic hypothesis [1]. The development of quantum theory in the early 20<sup>th</sup> century suggested several experiments, which were carried out and established radical new views about the structure of atoms. It also led to the emergence of a more detailed view of molecules and stimulated afresh the interest for defining the physical basis of biological molecules, cells and their constituents, as was exemplified in Schrödinger's "What is Life?" [2].

In a similar way, molecular biology has been driven by advances in techniques. The investigation of the structure of cellular membranes started with a series of pioneering experiments in 1925. Measurement of the capacitance of erythrocyte (red blood cell) membranes provided an initial estimate of 3.3 nm for the cell barrier thickness [3]. The misinterpretation of these results led to the belief that this was the thickness of a mono-layer. Later that year, quantification of erythrocyte lipid content led to the conclusion that the cellular membrane

is a bilayer [4]. Lipids are molecular building blocks of cellular membranes, usually composed of two generally two hydrocarbon tails and a polar head group. Therefore, within a bilayer the polar head of each mono-layer would face the aqueous exterior and interior of cell while the hydrophobic hydrocarbon chains would be forming the ‘oily’ core of the bilayer. This model of the membrane was still a static one, where lipids simply form a passive barrier between the cell’s interior and exterior. The subsequent extension of the cellular membrane model suggested that the lipid bilayer is coated with globular proteins on both surfaces, by simple absorption from the surrounding solution [5]. Furthermore, the advent of the painted “black lipid membrane” technique allowed researchers to determine that lipid bilayers exhibit a high lateral fluidity [6]. As a consequence, lipids were no longer considered as static components of a cellular barrier. The revolutionary experiment by Frye and Edidin [7], in 1970, demonstrated that membrane proteins actually diffuse in the cell membrane. These experiments set the stage for the development of the fluid mosaic model of biological membranes by Singer and Nicholson in 1972 [8]. In this model, the cell membrane acts as a two-dimensional lipid bilayer in which proteins play a functional role and are embedded in the outer or inner mono-layer or span the bilayer. The key feature of the model is that proteins diffuse freely within the two dimensional fluid lipid matrix and the lipids are free to diffuse laterally and rotationally as well. Although Singer and Nicholson did not explicitly postulate the existence of other forms of heterogeneity, they specified that "the absence of long-range order should not be taken to imply an absence of short-range order in the membrane" [8].

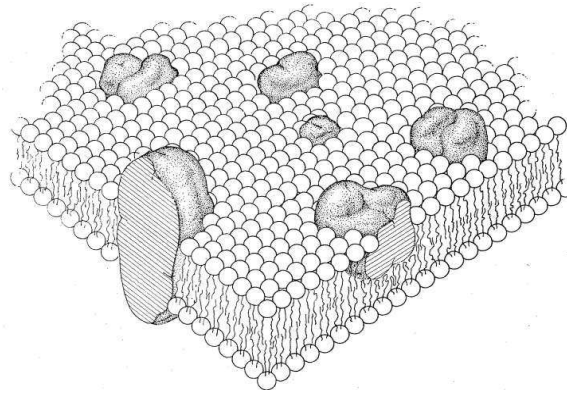


Figure 1–1: Singer and Nicholson Fluid Mosaic model of cell membrane with larger proteins embedded in a fluid lipid bilayer. Adapted from [8] with a permission.

In reality, cells can generate over 1000 different types of lipids [9] that can partition asymmetrically in the two leaflets, creating a composition heterogeneity perpendicular to the membrane plane.

Moreover, membrane proteins represent approximately 30 % of proteins present within a cell. Various published experiments show that the surface coverage by membrane proteins is in the range of 30-70 % [10, 11, 12]. Given this crowded molecular environment of the cell membrane, there is only a small reservoir of lipids that one can accommodate around a given protein. In turn, this would suggest that the immediate lipid environment of the embedded membrane protein will play a crucial role in the regulation of its function. In addition, one may infer, based on the richness of lipid species, that the heterogeneity will not only exist perpendicular to the membrane plane, but also in the lateral plane. One such heterogeneity occurs in Golgi apparatus membranes, that serve as a protein sorting centres. Indeed, in late 80's, Simons and van Meer [13, 14] discovered

that glycosphingolipids form clusters in the Golgi apparatus that serve as sorting regions for the selective transport of proteins to the apical surface of polarized epithelial cells. Subsequent studies of these clusters by the non-ionic detergent solubilization of membranes at low temperatures, suggested that they are contained within the detergent resistant membrane (DRM) fractions [15]. DRM's were shown to be rich in cholesterol and glycosylphosphatidyl inositol (GPI)-anchored proteins. Biophysical experiments using an optical tweezer, determined the domain radius to be 50 nm [16] in radius. The term “rafts” was coined to describe these assemblies of sphingolipids, cholesterol and proteins, that were believed to play a role in membrane trafficking and signalling [13]. Since then, many biochemical studies suggested the presence of various proteins inside these rafts, based solely on the appearance of these proteins in the DRM fraction. Nevertheless, later studies have questioned the validity of the biochemical fractionation approach due to the potential membrane altering properties of detergents [17]. Furthermore, a number of attempts at microscopy imaging to visualize these membrane domains were tried without success. As well, the standard biophysical fluorescence microscopy based techniques, fluorescence recovery after photobleaching (FRAP) and förster resonance energy transfer (FRET), did not yield the same spatial scale when applied to these objects [18], which added to the scepticism about the raft concept. The difficulty in characterizing these objects in the cellular membrane by biophysical means, was due to the fact that these objects are smaller than the diffraction limited resolution of the light microscopy and they have short lifetimes (i.e. they are transient) [19]. Widely accepted criteria for defining rafts were lacking 10

years ago, when the raft constituents were defined as an insoluble residue or DRM remaining after non-ionic detergent solubilization at a low temperature. Other treatments, such as addition of the cyclodextrin, which extracts the cholesterol from membranes, were attempted in order to reinforce the presence of membrane domains in live cells. Nevertheless, the detergent solubilization of membranes was criticized for being an inherently artificial method leading to many possible outcomes, depending of the concentration and type of detergent, duration of extraction and temperature [20]. Also, a cyclodextrin treatment leads to serious side effects that change the protein mobility [21] and many cellular functions can be perturbed [22].

This impasse in the raft field encouraged and inspired new efforts to find biophysical methods to study the behaviour of these small and transient membrane structures. This included techniques such as single molecule spectroscopy and microscopy which were already developed and applied to other problems in cell biology. New adaptations of these techniques such as FRET and single particle tracking (SPT) at a higher spatial and temporal resolutions, were able to answer some central questions. For instance, the homo- and hetero- FRET revealed that GPI-anchored proteins exist in cholesterol dependent nano-clusters [23]. On the other hand, SPT of GPI revealed the existence of mobile smaller rafts, while bigger stationary domains were found to be composed of several raft proteins [24].

A new adaptation of a fluorescence fluctuation technique named fluorescence correlation spectroscopy (FCS) revealed partitioning of membrane proteins at

timescales of a few  $\mu\text{s}$  to ms [25]. Their FCS adaptation involved varying the beam radius of the excitation focus (see section 1.3.2). Indeed, by applying a milder treatment using cholesterol oxidase or sphingomyelinase, enzymes which convert some of the cholesterol and sphingomyelin, respectively within rafts, into different chemical components, the authors were able to change dynamics of postulated raft embedded proteins. They also used the method to measure yet another type of membrane heterogeneity, the meshwork. Such membrane heterogeneity can be caused by several sources and it is commonly thought that it is due to the actin cytoskeleton mesh that is in close proximity of the inner leaflet of cellular plasma membrane as shown in the diagram of the figure 1–2. If a trans-membrane protein extends its cytoplasmic domain into the cell, this could potentially be confined by or interact with the actin meshwork, much like getting caught in a net. Consequently, a protein that would otherwise freely diffuse unrestricted in the membrane, remains confined within the given mesh pore until the cytoskeleton relaxes allowing the particle to “hop” from one compartment into an adjacent one. Another possible source of meshwork that can confine a membrane protein comes from the collagen extra-cellular matrix as shown in the figure 1–2. This type of membrane associated heterogeneity was the subject of SPT experiments over past 15 years [27, 28, 29] which led to the solution of an old observation that puzzled the scientific community: why do membrane proteins appeared to move an order of magnitude slower in real cell membranes as compared to the model membranes? A high speed image acquisition with SPT showed that the molecular motion within the meshwork defined compartment, was on same order

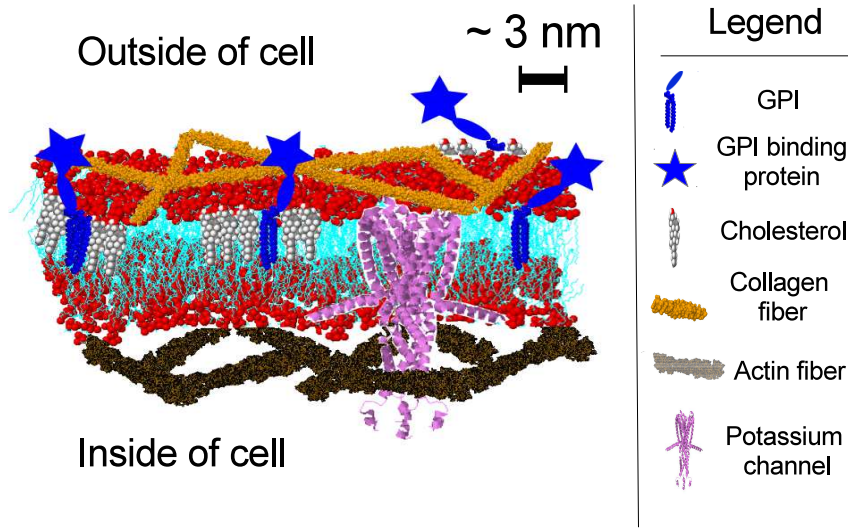


Figure 1–2: Membrane in the presence of Lipid Rafts, Extracellular and Intracellular Meshwork. Red spheres represent the major lipid (DPPC) head group and cyan its hydrocarbon tails. GPI-anchored protein inserts preferentially into cholesterol rich domains. A trans-membrane protein, a potassium channel in this case, can be confined by the actin cytoskeleton. PDB entries: 1N83 (cholesterol), 1BKV (collagen), 3B63 (actin), 1F6G (potassium channel). Lipid structures (DPPC) were found at [26])

of magnitude as the motion of proteins in a reconstituted artificial model lipid bilayer system. The slower hopping from one compartment to another is what was typically observed before when particle motion was acquired at lower imaging rates and lower spatial resolution. These findings suggested the compartmentalization of plasma membrane by the underlying actin cytoskeleton. In summary, over the past two decades our knowledge of the cell membrane structure have evolved dramatically to the extent that the membrane is now considered “more mosaic than fluid” [30].

In this thesis, we develop and explore a new approach for studying membrane heterogeneity, using another biophysics technique. It is an extension of the existing Image Correlation Spectroscopy (ICS) techniques that we will exploit in order to elucidate dynamics of particles exploring heterogeneous membrane and its characteristic length scales. The remainder of this chapter will consist of a summary introduction to the principles of fluorescence, fluorescent dyes and fluorescence microscopy, including Total Internal Reflection (TIRF) microscopy. We will compare the results of two biophysical techniques introduced previously, SPT and FCS, as they have played a major role in most recent studies of the membrane heterogeneity and share similarities with the new ICS approach. We conclude the chapter with preview of the material that will be the subject of this thesis.

## **1.2 Fluorescence**

Methods developed in this thesis are all based on the fluorescence microscopy. Therefore, we will provide an introduction to the key concepts of fluorescence in following sections.

### **1.2.1 Definition of fluorescence**

The photoluminescence is a process by which a matter absorbs light (electromagnetic radiation) and re-radiates new light after a period of time. Although there exists the resonant (the absorbed and emitted photons have same energy) type of photoluminescence, we will describe the two most widely used variants in biological sciences: fluorescence and phosphorescence. The fluorescence consists

of the absorption of the light by a molecule (a fluorophore), and the excitation of an electron, on a time scale of  $10^{-15}$  s, from the ground singlet (spin) state to an excited singlet state. The electron relaxes vibrationally within the excited state, without emitting light, and then emits light at higher wavelengths photon (the energy smaller than that of excitation). In order to visualize the electronic states of a molecule, one can refer to the Jablonski energy diagram [31] as depicted in figure 1–3.

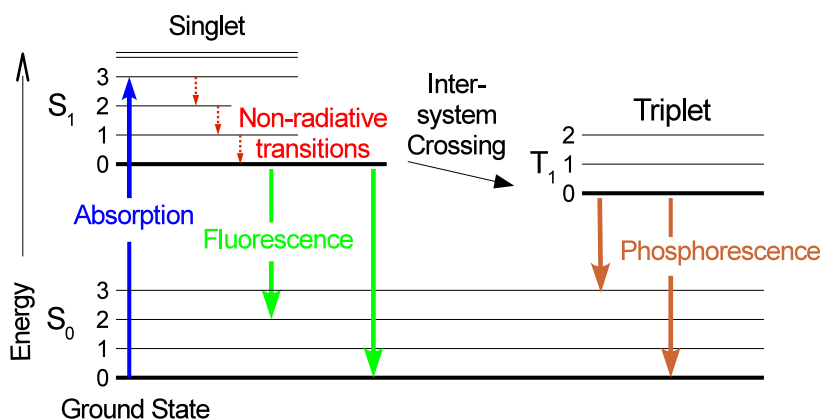


Figure 1–3: Jablonski diagram for Fluorescence and Phosphorescence

This transition to the ground electronic state is on the ns timescale. On the other hand, during phosphorescence the molecule undergoes a transition from the excited singlet to excited triplet state, and the return to ground states is spin-prohibited. As a consequence, the phosphorescence occurs on a much longer time scale (ms to seconds) in comparison to the fluorescence. This is the basic principle of “glow in the dark” substances. The difference between the lower emission energy light and excitation radiation is called the Stokes shift, after

G.G. Stokes who described it in 1852 [32]. Fluorescence usually occurs due to a transition from the ground vibrational level of the excited singlet state  $S_1$  to the ground vibrational level of the ground singlet state ( $S_0$ ) giving rise to the major peak in the fluorescence emission spectra 1–4. The transitions from other excited vibrational  $S_1$  levels to other vibrational levels of  $S_0$  are less likely, but are still possible and result in the spread of the emission spectrum about its peak wavelength.

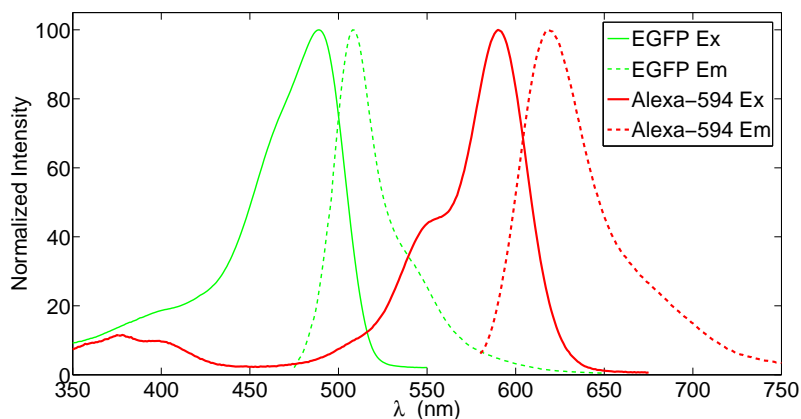


Figure 1–4: GFP and Alexa 594 fluorescence excitation and emission spectra.

Fluorophores can undergo non-radiative transitions from the excited state to the ground state (termed internal conversion) as well. The ratio of the number of emitted to absorbed photons on average per molecule is called the quantum yield which defines the efficiency of this process (it is always smaller than one). Several effects can influence the quantum yield, including the inter-system crossing (like phosphorescence), non-radiative transitions from excited to ground state and

non-radiative transfer of energy to nearby fluorophores (the resonance transfer or quenching).

Perhaps the greatest advantage of fluorescence is the ability to observe specifically labelled molecules inside a cell, with high sensitivity because we detect the fluorescence at a longer wavelength than the excitation light. Our measurement exploit this sensitivity in order to study the motion and distribution of membrane proteins in live cells.

### **1.2.2 Tracers used to probe heterogeneous environment**

In order to observe a particular protein of interest in a live cell, one needs a non-invasive and specific labelling of the target molecule. Currently, the fusion of genes of the protein of interest with that of green fluorescent protein (GFP) variants, is a common practise in molecular biology laboratories. The GFP is a small protein that is found in the jellyfish *Aequoria victoria* [33] that produces a green light after being excited by the aequorin blue light, giving the animal an overall green color. The excitation of wild-type GFP occurs primarily in the UV to blue range, which is not a desirable characteristic for a marker of proteins in live cells, since several naturally occurring proteins in the cell can absorb UV and blue light, and UV light is known to damage cells. Several research groups developed mutations of GFP, that not only shifted the excitation spectrum to higher wavelengths, but also improved its quantum yield, pH sensitivity, photo-stability and maturation folding time [34]. Elucidation of its crystal structure (figure 1–5 b) by

the X-ray diffraction further opened research into improving the photophysical properties of this molecule and its variants [35].

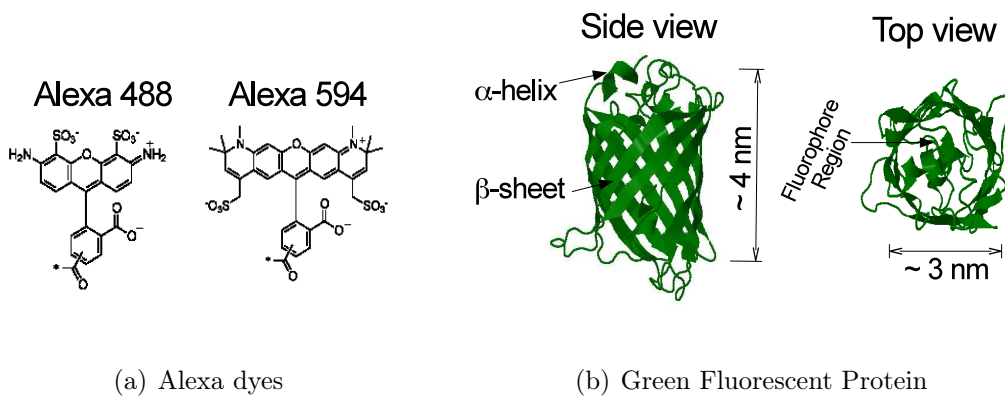


Figure 1–5: a) Organic Fluorescent Alexa dyes. Adapted from [36]. b) Side and top views of the crystallographic structure of Green Fluorescent Protein. PDB entry 1EMA. Source : [37]

Once researchers knew which amino acids formed the external surface of its barrel-like structure, targeted mutations could be employed to create a monomeric version of this protein. In turn, a desirable property of a marker is to be as small as possible in order to minimize the perturbations to the function of the target molecule. In addition, exact knowledge of the fluorophore structure and position of its light absorbing “antenna” (residue 66) was crucial in development of new color variants. In general, there are several aspects to consider when one chooses a fluorescent protein to use for cellular studies including: its excitation and emission spectra, folding rate, monomeric vs multimeric state, its brightness (encompasses the quantum yield of the fluorophore) and wavelength detection window of the imaging system [38]. In the present work, we chose the enhanced green fluorescent protein (EGFP) as it has a single excitation peak at 488 nm and an emission

peak at 510 nm (Fig. 1–4). Moreover, it has an improved fluorescence and photo-stability compared to wild-type GFP as well as shorter maturation time.

There are two major drawbacks of using EGFP (or other fluorescent proteins). One is that it can photo-bleach, which is a photochemical reaction causing a fluorophore to lose fluorescence due to photo-chemical conversion into a “dark state”. When the fluorophore is photo-bleached, we are no longer capturing light from it on the detector, which can influence the outcome of the data analysis from SPT, FCS or other quantitative biophysical techniques. The other is that, despite of the existence of tight controllers of protein expression (production) in cells, one cannot achieve a very precise control on the concentration of GFP (or other proteins) in any given cell. As a consequence, very high densities of proteins may be expressed in a cell membrane resulting in a spatially overlapping fluorescence signals from very closely packed proteins. This will affect the results of biophysical techniques as it introduces density variations from cell to cell.

As a potential replacement of organic fluorophores are the semiconductor nanoparticles, also known as quantum dots (QD), which have reduced photo-bleaching and high quantum yield [39]. They consist of 5-10 nm crystals that can be coated and bioconjugated to selectively bind to a protein of interest on the surface of a cellular membrane. Nevertheless, they exhibit intermittent light emission (a.k.a. blinking) at all time scales, which complicates data interpretation. Moreover, surface conjugation that renders QD specific to a given protein, may create several binding sites that can attach to more than one protein of interest, on a cellular surface. Labelling of GPI or other raft associated marker, with QD,

could induce an artificial clustering, being an undesirable feature for this type of studies. As well, after bioconjugation, they are larger than fluorescent proteins (15-20 nm).

Another alternative to natural fluorescent proteins are organic fluorescent dyes such as the Alexa Fluorophores (Fig. 1–5a). These are sulfated forms of different basic fluorescent chemical dyes like fluorescein, coumarin, cyanine or rhodamine [40]. The advantage of these dyes is their small size (few Angstroms compared to few nm for GFP) without compromising the photo-stability and brightness. It is that characteristic that makes them appealing when labelling proteins on the cell surface. Indeed, from 4-8 Alexa dyes can attach on the surface of a single antibody which in turn binds to the specific protein on the cell surface. This labelling strategy is employed in the present work to mark the GPI-anchored proteins on the surface of live cells, as detailed in the following sections.

### **Fluorescent dye conjugated antibody labelling of proteins of interest**

Immunostaining or immunofluorescence labelling refers to techniques by which a protein of interest is labelled with fluorophore-tagged antibody for microscopy visualization. It was developed in 1940s [41] by Albert Coons and is still widely used. Figure 1–6 shows immunoglobulin G (IgG) , which is a type of antibody composed of four peptide chains: two identical heavy and two light chains. IgG are produced by plasma B lymphocyte cells during an immune response. Its crystal structure reveals a “Y” shape typical of IgG antibody monomers. Each IgG has two antigen binding pockets. These pockets are produced by lymphocytes in

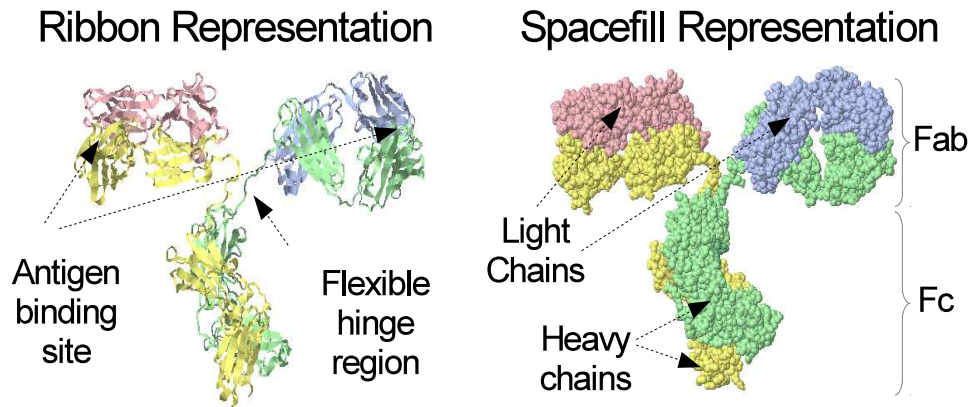


Figure 1-6: IgG Antibody X-ray diffraction resolved crystallographic structure (PDB entry: 1IGT)

response to the invading reagent (antigen) present in the host organism during infection. Therefore, antigen binding pockets have very high specificity, which is a desirable feature for the labelling of a particular protein in cells. Often, proteins are labelled with a primary antibody, followed by a secondary antibody labelling of the primary antibody. As result, multiple fluorophore tagged secondary antibodies can sometimes bind to the primary and amplify the signal from a single target protein. Due to the large antibody size, the labelling often requires cell fixation and permeabilization, consisting of opening large pores in cell membranes, in order to allow antibodies access to the inside of the cell. Luckily, GPI-anchored proteins are inserted in the outer leaflet of the cell plasma membrane which makes them a good candidate for labelling live cells with antibodies without permeabilization. As shown in figure 1-7, anti-GFP IgG can bind a single GPI-GFP complex while being labelled by 4-8 Alexa dyes. [42]. This procedure increases the signal to noise

ratio per GPI molecule which is advantageous for the protein detection in the fluorescence microscopy.

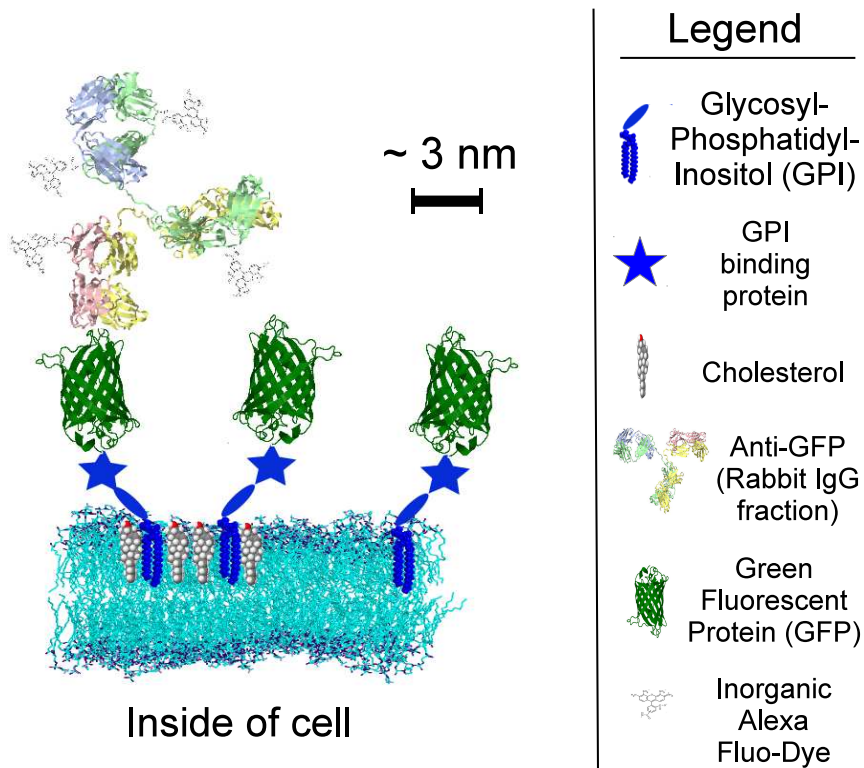


Figure 1–7: GPI-GFP labelled by an Anti-GFP tagged with Alexa-594 dyes. Each Anti-GFP contains 4 to 8 Alexa dyes, giving higher fluorescence signal for a single GPI molecule, than would GFP alone provide.

Moreover, the amount of anti-GFP IgG conjugated to Alexa dye can be controlled in both concentration and exposure time, allowing for low dilution (sparse) labelling of GPI-GFP molecules on the cell surface. Alexa dyes come in a variety of colors and are commercially available as the anti-GFP IgG conjugated to Alexa dyes (Molecular Probes). In this thesis, the choice of Alexa 594 was

obvious, since its excitation spectra was red shifted compared to EGFP. By using a 560 nm laser and appropriate filter sets, we could observe the Alexa 594 signal alone. A possible drawback of this labelling strategy is that there could be possible forced aggregation of GPI-GFP molecules if a single anti-GFP binds two different GFP's. This is likely a very low probability event, as an IgG free binding site is unlikely to have access to another GFP, due to steric effects in the membrane and a limited range of the hinge region of the protein. Nevertheless, such event, if it did occur, would at worst dimerize a fraction of the GPI population. Another possible undesirable outcome of this labelling procedure is the possibility that a single IgG binds two GPI-GFP from closely spaced nano-domains, inducing clustering of domains. Luckily, this was not observed, as macroscopic rafts were not seen to appear in the image time series. Care must be taken to expose the cells to low concentrations of IgG and for minimal periods of time.

### **1.2.3 Fluorescence microscopy**

**Epi-fluorescence microscopy.** Once the cells have been labelled with fluorophores for the target molecule of interest, they are ready for fluorescence microscopy. Modern fluorescence microscopes operate in epi-fluorescence mode, meaning that the excitation and emission light pass through the same optics as shown schematically in Fig 1–8. In its basic form, the light source is a broad-band lamp (such as mercury or tungsten). The light first passes through an excitation filter that narrows the light wavelengths to match the excitation range of the target fluorophore and then is reflected by a dichroic mirror into an objective lens back aperture to be focused on the sample. The fluorophores in the sample

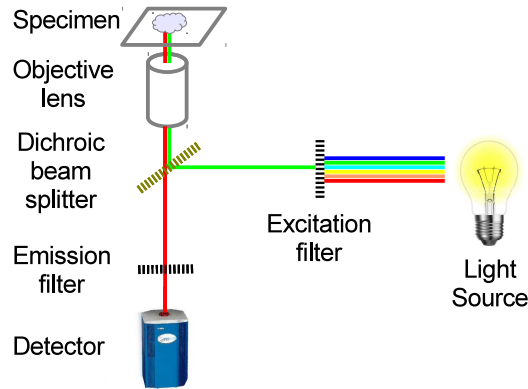


Figure 1–8: In Epi-Fluorescence microscopy, excitation and emission light passes through the same objective lens.

are excited and emit fluorescent light which is collected by the same objective and passes through the dichroic mirror and is directed toward a detector. Before reaching the detector, the emission signal passes through another filter that matches the emission spectrum of the desired fluorophore. This way the detected signal is limited to the desired fluorophore emission, without excitation light or other possible spurious light.

**Total internal reflection fluorescence microscopy.** Despite the advantage conferred by the fluorescence specificity, the simple wide-field epi-fluorescence microscope has a major drawback in that a thick region of sample is being excited simultaneously, both in and out of the focus. Consequently, the background fluorescence from outside the focal plane can decrease the signal-to-noise ratio and reduce the spatial resolution of the features one wants to probe in the specimens. TIRF microscope takes advantage of a unique property of an induced evanescent

wave (or field) within a thin sheet ( 100 nm) at the interface between two media having different refractive indices. The basic principle of the creation of this evanescent field relies on the total internal reflection of light when it crosses the interface from a high to low refractive index medium. The incidence angle at which this happens is called the critical angle. It can be derived from Snell's law with the knowledge of the two media indices of refraction. Although the entire incident light ray may seem to be back reflected into the incident medium, by geometric optics, Maxwell's equations require that an evanescent wave propagates along the boundary of the two media. The expression for the evanescent field can be derived from the transmitted light wave vector and the transmitted plane wave expressions, using the consequence of total internal reflection as predicted by Snell's law [43].

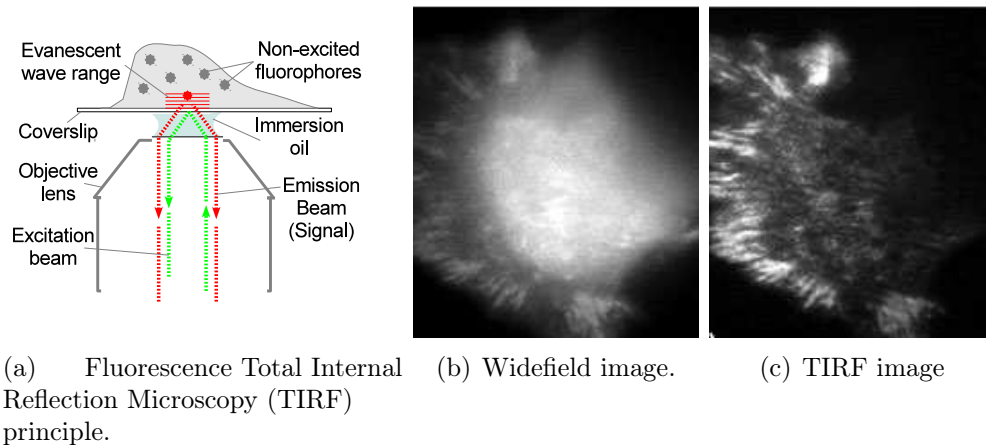


Figure 1–9: a) The evanescent wave produced by a total internal reflection extends over 100 nm from coverslip-sample interface, exciting only cellular components within that range. b) Epi-fluorescence and c) TIRF images of GFP-vinculin, respectively, in PtK1 kangaroo kidney epithelial cells. Source: [43]

For cellular imaging, the interface for TIRF is the contact area between a specimen and a glass coverslip, at which cell grow. As a result, tagged proteins, in an adherent live cell with its basal membrane at the interface in question, will be only excited if they lie within this thin layer (100 nm) of the evanescent field (Figure 1–9). The intensity of the excitation profile decays exponential with distance from the coverslip-specimen interface, which reduces the excitation of out of focus fluorophores. More specifically for this thesis, GPI-GFP expressed in epithelial adherent cells, will be mainly visible if they are present in adherent basal membrane of the cell. Proteins in organelles, such as Golgi apparatus, will be less or completely invisible in TIRF mode as they lie outside of the evanescent field.

**Point spread function and spatial resolution.** The point spread function and spatial resolution of the microscope need to be defined to provide the context for concepts introduced in the rest of this manuscript. Point spread function (PSF) , is a measure of the spatial resolving power of an optical imaging system. The narrower the PSF, the better the spatial resolution will be. As the name implies, PSF defines the spread of light imaged from a point source. That is, if we observe a radiating point source, its image will appear to have expanded to a finite size. This spread is a direct consequence of diffraction by a spatial filter, which in this case is the lens aperture (or lenses) within the microscope. The PSF can be seen as a degree of blurring and represents a good measure of the quality of an imaging system. It can be shown that a point source at the focal point of a lens with circular aperture will produce an Airy disc PSF in the image plane. The Airy disc is often approximated by a 2 dimensional Gaussian, as it captures most of the

features of a PSF. The width of the lateral distribution (full width half maximum) of the PSF is usually defined as:

$$\Delta x = 0.6098 \frac{M\lambda}{NA} \quad (1.1)$$

where  $M$ ,  $\lambda$  and  $NA$  represent the magnification of system, wavelength of light and numerical aperture of the lens, respectively. This is also known as the *Airy disk radius*. This number defines the uncertainty of the position of the image of a point source. If the distance between the centres of two image plane Airy disks of two point sources is equal or smaller than the Airy disk radius, then these objects will not be optically resolved. This is known as the Rayleigh criterion for the optical resolution. It is important to realize that membrane domains (rafts) were estimated (by SPT) to be on the order of a few tens to hundreds of nanometres. For light in the visible range (400-600 nm) and using a lens with numerical aperture of 1.4, yields  $\Delta x$  (in lateral direction, i.e. xy plane) of about 170-300 nm. This implies that membrane heterogeneities are on the same order of size or smaller (most likely) than the PSF of a standard light microscopy system. We will see shortly how techniques, such as SPT and spot-varying FCS, tackle the problem by overcoming the diffraction limited spatial resolution of the optics, and how we extend the image correlation methods to accomplish similar results.

### **1.3 Fluorescence techniques for probing membrane heterogeneities**

Over the last 15 years, several fluorescence based techniques were used to study different aspects of heterogeneous membranes. Several excellent reviews exist that give an overview on techniques used to study these structures [44, 45, 16, 46,

47, 48]. We will outline two techniques, SPT and FCS, as their concepts and basic principles inspired and captured the essential features of the image correlation based approach which is the focus of this thesis.

### 1.3.1 Single particle tracking

The detection and tracking of microscopic particles in order to answer certain physical questions go back to the work of Jean Perrin on the experimental confirmation of Einstein's theory of Brownian motion and the determination of Avogadro's constant [49], which ended a century long debate on the existence of atoms as postulated by Dalton's theory. Since then, our tools have evolved greatly, allowing for the detection and tracking of single molecules in cells. The basic idea behind SPT, is that a molecule's position can be determined with a typical spatial resolution of tens of nm, by fitting the particle's emission light profile (PSF) with a 2D Gaussian function to establish the peak centroid position. The PSF profile depends inversely on the square root of the number of photons collected. The peak position defines the diffraction sub-resolution position of the particle and the standard deviation of the fit defines the position uncertainty. The particles' peak position fitting is repeated for each frame and trajectories are mapped by connecting the peak position series using a tracking code. The strength of this technique is that it produces a high spatial position resolution (and in case of fast imaging, high temporal) data for the particle motion in a given environment. Its chief advantage as a single molecule method is that the particles behaviours are not averaged as an ensemble and each trajectory can be deciphered in order to

define the different modes of motion. Whether the particle moves in Brownian, confined, active transport or anomalous diffusion modes, the trajectory will reflect it if the temporal resolution is high enough. The drawback of the technique is that several hundreds of trajectories of sufficient duration are required in order to be able to deduce significant statistical properties about the sample. The first SPT experiments on the cell membranes involved tracking of a highly scattering colloidal gold labels attached to the membrane proteins and imaged using the bright-field microscopy [50]. With the discovery of new fluorescent organic and inorganic dyes, as well as semi-conductor nano-crystals quantum dots (QDs), more SPT experiments have been conducted using the fluorescence microscopy. Indeed, bright field microscopy is not specific as the images contain background features other than the particle of interest, making it more difficult for particle detection and localization. A good signal-to-noise ratio (SNR) is an essential element in SPT, as a particle with a signal near noise level will not be detectable. Although fluorescence microscopy also has background and counting noise that can potentially reduce the SNR, it has the sensitivity to reach single molecule detection limits. Moreover, a simultaneous labelling of several proteins is achievable with different dyes, allowing detection of protein specific signals within the same sample.

**SPT in presence of heterogeneous membrane.** With the innovation of new fluorescent probes, fast acquisition and high sensitivity detectors, a new experimental era for the study of heterogeneous membrane dawned about 10 years ago. The development of fast and sensitive charge coupled device (CCD) cameras,

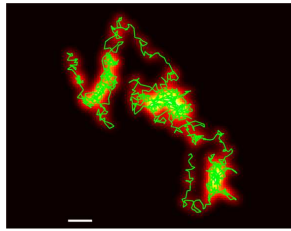
allowed SPT to solve the 20 year dilemma of reduced protein mobility in cellular membranes [27, 28, 29]. In addition to improvement of temporal resolution, new tracking algorithms allowed for the detection and tracking of particles on the surface of cells at very high particle densities [51, 52]. Indeed, these cleverly designed algorithms detect the highest intensity profiles particles first, then subtract detected features, revealing hidden features characterized by the lower intensity peaks. In this manner, more features become detectable, down to the noise level, in a given frame. Following detection, the connection into trajectories is done with optimization algorithms, that are robust for particles disappearing for certain numbers of frames (possibly due to a drift motion or blinking of the fluorophore), trajectories merging (due to a particle interaction) or trajectories splitting. Moreover, new mutations of fluorescent proteins led to the so called photo-activable proteins, which opened a whole new field of “super-resolution” microscopy. The main idea of one of these techniques, called photo-activation light microscopy (PALM), is similar to that of the standard SPT, but advantage of these probes comes from the fact that only a subset of fluorophores could be activated, excited and observed at given time. Indeed, a protein becomes excitable only when it is in its “active” state, achievable by the absorption of ultra-violet light by that molecule. One can think of the photo-activation process as a shift in the excitation spectrum of the fluorophore. Initially, the fluorophore is excitable at 405 nm (case of photo-activable GFP). Following absorption of 405 nm light, the fluorophore structure re-organizes such that it becomes excitable at longer wavelengths. If the exposure time of the 405 nm laser

is carefully controlled, one can achieve the activation of only a subset of molecules present in a membrane. Therefore, only that subset will be excitable at longer wavelengths and its fluorescence emission visible under a fluorescence microscope. In earlier versions of super-resolution microscopy, samples were chemically fixed, such that transport dynamics of molecules were not assessed but only positions recorded [53, 54]. In later versions, the activation-excitation-detection-tracking cycle was repeated and short single molecule trajectories were recorded in live cells [55, 56]. Another approach, called point-accumulation-for-imaging-in-nanoscale-topography (PAINT) takes advantage of the labelling of cell surface molecules by fluorescent probes that diffuse in the solution and become fluorescent upon binding to the target of interest (a membrane receptor for instance) [57, 58]. The advantage of this technique is that it yields many single molecule long-time trajectories for high labelling densities of the receptors on cell surface. Bath application of the fluorescent ligands, at a given concentration allows labelling of a subset of surface receptors allowing for long-time trajectory tracking. Interestingly, this approach of labelling surface receptors is similar to the approach taken for the labelling of GPI-GFP on cellular surfaces described in this thesis.

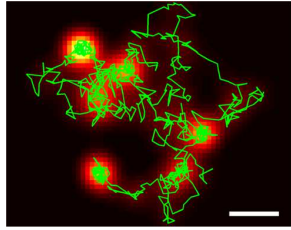
Other techniques improved spatial resolution by the engineering of the effective sub-diffraction PSF [59, 60]. Whether it is through an algorithm implementation, hardware modification or probe engineering, all of these techniques have the goal of achieving sub-diffraction detection and tracking of proteins throughout the cell, at native high densities of proteins. Ultimately one would want to be able to

resolve the complete transport and location history of any labelled molecule. Data interpretation is another challenge.

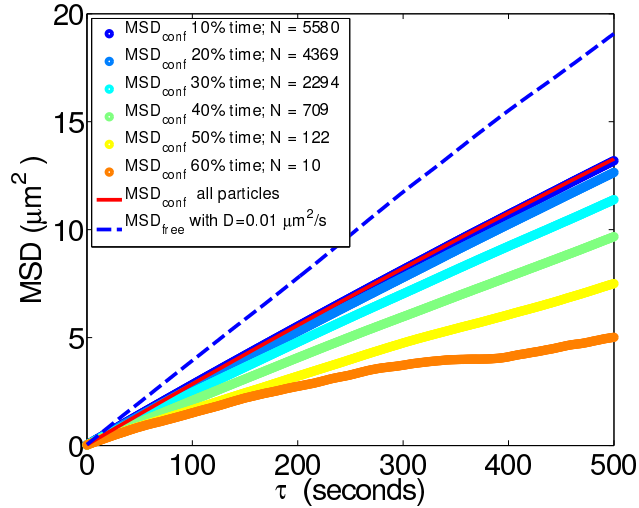
Once trajectories are acquired, it is not an easy task to divide particles into different transport categories by eye. The human visual system has evolved to detect patterns which can sometimes lead us to false conclusions. For example, visual inspection of the free diffusion trajectory shown in figure 1–10 a) might lead to the conclusion that there are confinement zones present in this sample, however the simulated particle is undergoing pure Brownian motion.



(a) Free diffusion trajectory



(b) Confined diffusion trajectory



(c) MSD for free and confined particles diffusion.

Figure 1–10: SPT trajectory for a freely (a) and confined (b) diffusing simulated particles. Trajectories (green) are superimposed on the average image of particle positions convolved with a 2D Gaussian function which models the PSF c) MSD for free and confined particles. N indicates number of particles that were confined X % of total time. Scalebar: 1 μm

The mean squared displacement (MSD) is a quantity that characterizes well the trajectory of a given particle. It is computed as:

$$MSD(\tau) = \langle [r(t) - r(t + \tau)]^2 \rangle \quad (1.2)$$

where  $r(t)$  denotes the position of the particle at time  $t$ . The average is taken over all pairs of positions separated by time lag  $\tau$ . For pure Brownian motion, the MSD will be linear in time and proportionality constant describes the diffusion coefficient of tracer particles. Nevertheless, when a single particle trajectory MSD is considered, only few first temporal lag are significant, while higher temporal lags are computed from fewest pairs of particle position [61]. Indeed, for a trajectory of  $N$  time points,  $N-1$  pairs of positions will contribute to  $M(0)$ , while only one pair of positions contributes to  $MSD(N - 1)$ , according to the equation 1.2. Often multiple particle MSDs are averaged together to achieve suitable statistics of ensemble of particles as expected for Brownian motion. In presence of 2 phase, heterogeneous environment, particles explore outside (of domains) and inside phases, depending on the domain's barriers and diffusion coefficients of particles in each phase (Figure 1–10 b). The size and spatial density of the confining domains phase will also regulate the time a particle spends in either phase. For a given time window, different particles can spend different amounts of time inside and outside of domains. As a result, averaging particles' MSD will not yield the same result if particles that are confined 10% of time are averaged or if those confined 20, 30, 40, 50 or 60 % of time are used (see MSD plot in Figure 1–10 c). Therefore, care

needs to be taken when deciphering the SPT results for cases of particles moving in more complex ways than simple free Brownian motion as suggested in [62].

### 1.3.2 Fluorescence correlation spectroscopy

**Principles of FCS.** FCS was introduced over 40 years ago by Magde and colleagues [63, 64], but first applied to cellular measurements using confocal optics [65, 66]. Later, it was extended as a practical tool for the measurement of diffusive and active transport dynamics and protein subunit counting in living cells [67]. The expansion of applications of FCS was achieved due to the improvement of laser sources, more sensitive detectors and efficient data processing. The basic idea behind FCS is the recording of temporal fluctuations in fluorescence emission within a laser focal spot as fluorescent molecules enter and exit the tiny excitation volume. The small ( $\sim fL$ ) and open excitation and observation volume is produced by focusing a laser beam through a high NA objective lens. Figure 1–11 shows a schematic of a typical FCS apparatus.

Fluorescence photons are collected through same objective lens and detected with an avalanche photo-diode (APD) or photo-multiplier tube (PMT) . The photon counts are correlated in time by a hardware auto-correlator and a temporal auto-correlation (ACF) is outputted to a computer. The temporal ACF is fitted with an appropriate function that depends on the underlying particle transport or chemical kinetics. In the case of free 2D Brownian motion, a simulated time series is shown in figure 1–12 a) and the temporal ACF in figure 1–12 b) can be fitted to extract the characteristic decay time of the ACF. The ACF, which compares

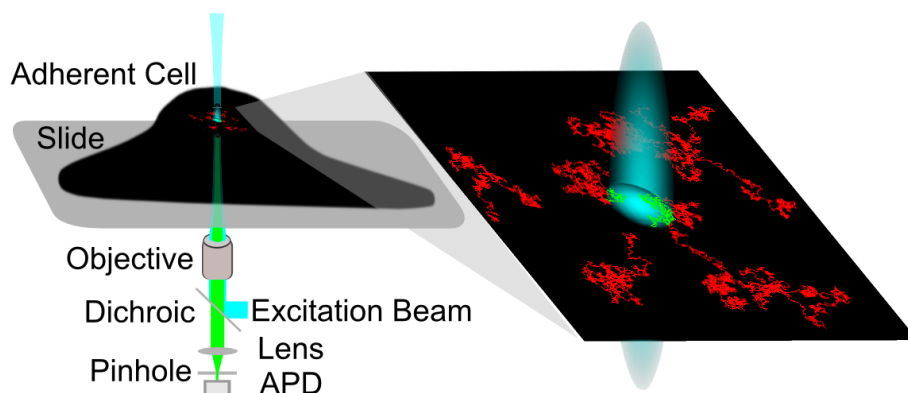


Figure 1–11: FCS setup: fluorescence photons are detected (green line on right zoom in), by an avalanche photo-diode (APD) and fluctuations are recorded and autocorrelated in time as fluorescent particles move in and out of a stationary laser focal beam volume. Red traces show particle trajectories as they diffuse outside the focal volume and green when they enter the focus and emit.

the signal with itself time shifted by lag  $\tau$ , can be thought of as a measure of self-similarity of the signal. The characteristic decay time of the ACF (figure 1–12 b) relates to the mean residence time of a fluorophore in the focal volume. The zero time lag value of the normalized ACF varies inversely with the average number of fluctuation events, and is equal to the average number of particles within the beam focus (assuming noise has been corrected). The temporal resolution of this approach is generally superior to SPT, allowing the measurement of transport coefficients occurring on time scales ranging from a few microseconds to milliseconds. When the system is at thermal equilibrium, fluorescence fluctuations originate from fluorophore transport or from an inter-system conversion (single to triplet). The diffusion, and other modes of transport usually occur on time scales

at least an order of magnitude greater than inter-system crossing, which allows for separation of these two effects during correlation analysis. The excitation within the focus can be achieved by either one- or two-photon absorption and the focus is less than fL in volume for standard high numerical aperture objectives. The relevant advantages of FCS are its sensitivity to low concentrations of fluorophores, it is a minimally invasive approach, it requires a low intensity of laser light, and is accurate when the correct models for data analysis are known. More complete reviews of FCS have been published [68, 69].

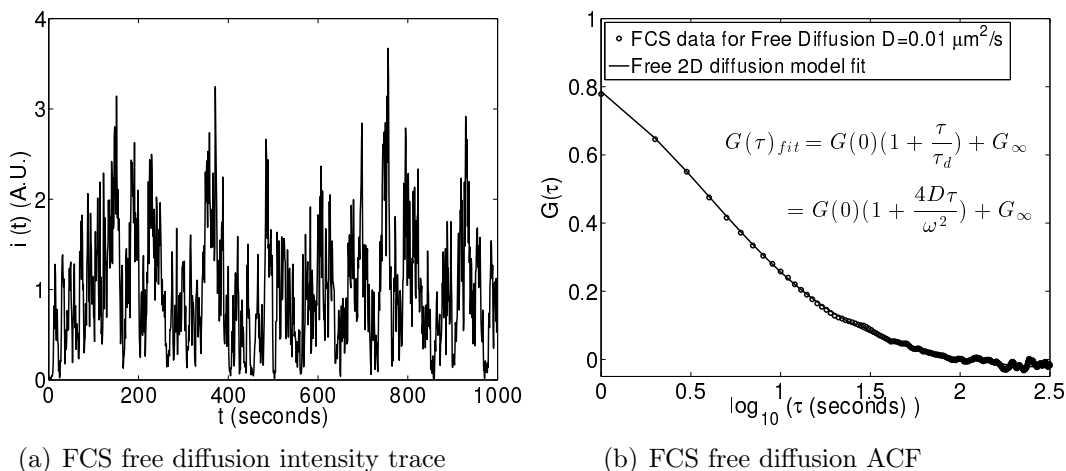


Figure 1-12: a) A simulated FCS intensity trace for free diffusion case with  $D=0.01\mu m^2/s$  and a Gaussian radius  $\omega=0.4\mu m$ . b) Calculated temporal auto-correlation function.

**FCS with varying beam size and the FCS diffusion law.** In 1987, FRAP experiments [70] with a varying bleaching spot size ( $0.35-5\mu m$ ) provided

evidence that micro-domains existed in fibroblast plasma membranes and that the mobile fraction of fluorescently labelled lipid phosphatidylcholine decreased with the increasing size of the bleaching spot. This study likely inspired two different groups ([71] and [72]) to develop an FCS version with varying beam spot size. In the case of simple 2D Brownian diffusion (figure 1–13 top row), there is no barrier to the motion of particles in space. Therefore, the characteristic decay time for the ACF should be proportional to the square of the  $e^{-2}$  radius ( $\omega$ ) of the variable beam spot:

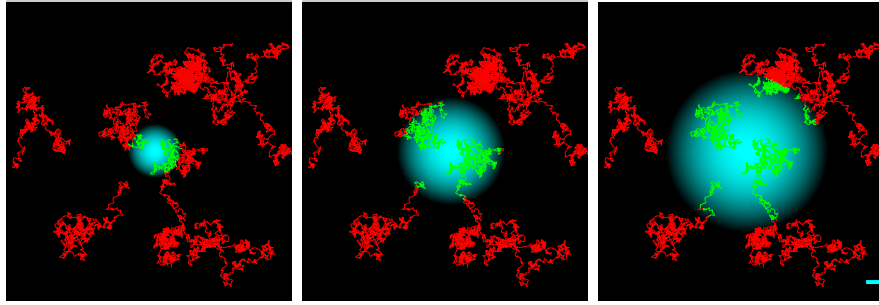
$$t_d = \frac{\omega^2}{4D} \quad (1.3)$$

The plot of  $\omega^2$  vs  $t_d$  is called the “FCS Diffusion Law” and its slope in the case of free diffusion in 2D is equal to  $\frac{1}{4D}$  [71]. On the other hand, the presence of isolated domains can cause particles to be trapped for certain periods of time, increasing the overall residence time for particles within the focal spot (figure 1–13 middle row). For this case the relation becomes:

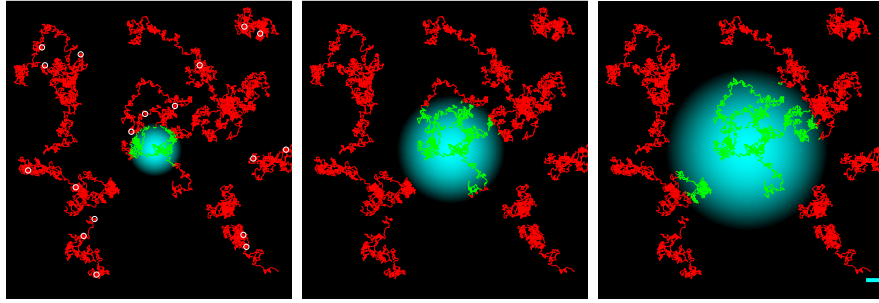
$$t_d = t_0 + \frac{\omega^2}{4D_{eff}} \quad (1.4)$$

where the additive constant is greater than zero in the case of isolated domains and becomes negative in the case of a meshwork confinement (figure 1–13 bottom row). An effective measured diffusion coefficient,  $D_{eff}$ , is less than it would be in the absence of confinement regions.

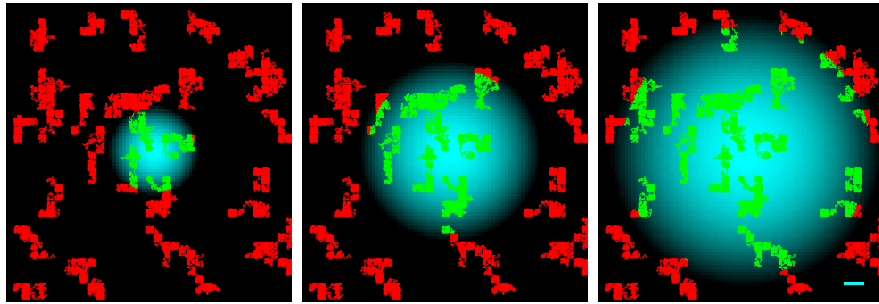
The central idea of spot-varying FCS can be demonstrated by considering computer simulated examples of Brownian diffusion ( $D = 0.01 \frac{\mu m^2}{s}$ , figure 1–13 top row) compared to the motion in the presence of circular isolated domains



(a) Free Diffusion with Beam Radius  $\omega=0.1 \mu\text{m}$  (b) Free Diffusion with Beam Radius  $\omega=0.2 \mu\text{m}$  (c) Free Diffusion with Beam Radius  $\omega=0.3 \mu\text{m}$



(d) Isolated Domains Confined Diffusion with Beam Radius  $\omega=0.1 \mu\text{m}$  (e) Isolated Domains Confined Diffusion with Beam Radius  $\omega=0.2 \mu\text{m}$  (f) Isolated Domains Confined Diffusion with Beam Radius  $\omega=0.3 \mu\text{m}$



(g) Meshwork Confined Diffusion with Beam Radius  $\omega=0.05 \mu\text{m}$  (h) Meshwork Confined Diffusion with Beam Radius  $\omega=0.1 \mu\text{m}$  (i) Meshwork Confined Diffusion with Beam Radius  $\omega=0.15 \mu\text{m}$

Figure 1–13: Simulations of beam varying FCS with particle trajectories superimposed. Three simulated dynamic scenarios are shown, free diffusion (top row), isolated domains confinement with a 200 nm domain radius (middle) and meshwork with a 250 nm mesh pore diameter (bottom row). In each case, few particle trajectories are shown when outside (red) or inside the beam radius (green). Gaussian spots were plotted logged to emphasize their spatial coverage.

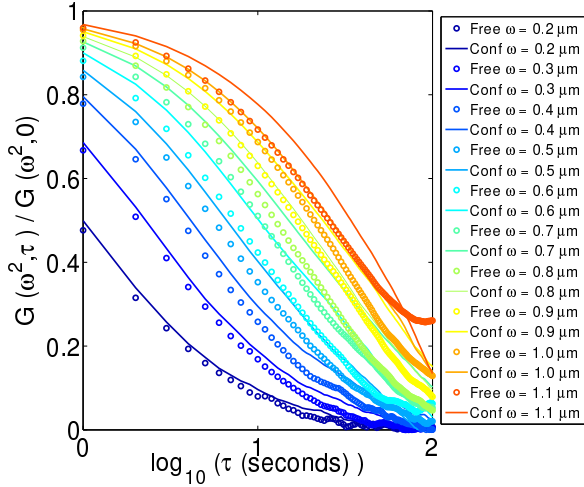
of 0.2  $\mu\text{m}$  radius, with  $D= 0.005$  and  $0.01 \frac{\mu\text{m}^2}{\text{s}}$  inside and outside the domains respectively (figure 1–13 middle row). Confinement boundaries were assigned probabilities of 0.5 and 0.1 for particles to partition in or out of domains, respectively. Figure 1–14 (a) shows that the ACFs are all shifted to higher temporal lags, for all beam sizes, in the case of the simulation in presence of isolated domains. Therefore, the FCS diffusion law will exhibit higher  $t_d$  values for a given  $\omega^2$  in the case of the simulation in presence of isolated domains, compared to the free Brownian motion (Figure 1–14). Moreover, as the slope of FCS diffusion law is greater in the confined case, this entails a smaller effective diffusion coefficient ( $D_{eff} \sim \frac{\omega^2}{4t_d}$ ) than for the free diffusion case. The y-axis intercept,  $t_0$ , is related to the partition factor,  $\beta$ , that defines the ratio of confined particles to the total number of particles in the system by the relation [71]:

$$t_0 \approx 2 \cdot \beta \cdot \tau_{conf} \quad (1.5)$$

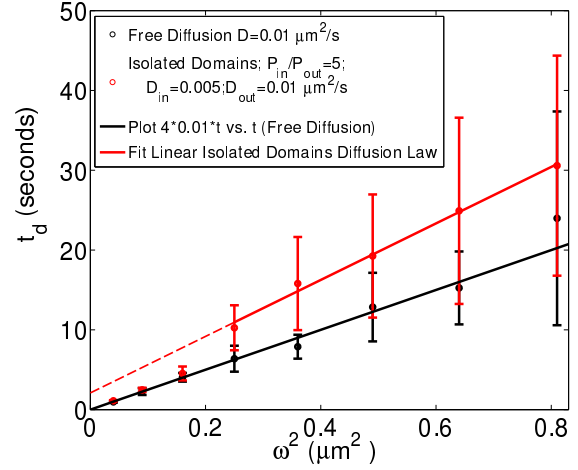
where  $\tau_{conf}$  denotes the average time particles spend within domains. Finally, the FCS diffusion law relates the apparent and actual diffusion coefficients outside of domains through the relation [71]:

$$D_{eff} \approx (1 - \beta) \cdot D_{free} \quad (1.6)$$

The analysis of the simulated FCS data with different beam radii (Figure 1–14 b), gave an effective diffusion coefficient of  $0.007 \pm 0.006 \frac{\mu\text{m}^2}{\text{s}}$  while the intercept was found to be  $2.1 \pm 1.7$  s, which verifies Eq. 1.6 considering that  $\beta$  was approximately 0.3.



(a) Spot Varying FCS temporal ACFs for free and isolated domains simulated scenarios



(b) FCS diffusion law for free and isolated domains simulated scenarios

Figure 1–14: The FCS Diffusion Law for simulated particle diffusion in homogeneous (free) and isolated domains 2D systems. a) Normalized ACFs for various beam radii sizes. Circles show all the simulated free diffusion ACFs, while lines are for isolated domains scenario. b) FCS Diffusion Law for free diffusion and isolated domain confined cases. Black circles are the extracted characteristic diffusion times ( $t_d$ ) for different beam radii in case of free diffusion. The black line is a suggestive plot for 2D free diffusion FCS Diffusion law with a set diffusion coefficient. Red circles display the FCS diffusion law for a simulated isolated domains case. The red line is a linear fit through the data at larger beam radii. Error bars are standard deviations from 100 different beam positions within the field of view.

In the case of meshwork confinement, it was shown [71] that the FCS diffusion law will exhibit two regimes, for spatial scales smaller and larger than the mesh size. For spatial scales smaller than the mesh size, the diffusion law will exhibit a slope that matches the microscopic diffusion coefficient of the particles. For scales larger than the mesh size, the diffusion law deviates from the free diffusion case, since particles start encountering the restrictive boundaries of the mesh. The confinement strength ( $S_{conf}$ ) is defined as the ratio of average confined time to the free diffusion time within the domain (i.e. the mean time a particle requires to explore a domain freely before encountering a wall). It was shown [71] that confinement strength has the following relation to the system parameters:

$$S_{conf} = \frac{\tau_{conf}}{\tau_d^{domain}} = A + B \frac{\sigma}{r} \frac{1 - P}{P} \quad (1.7)$$

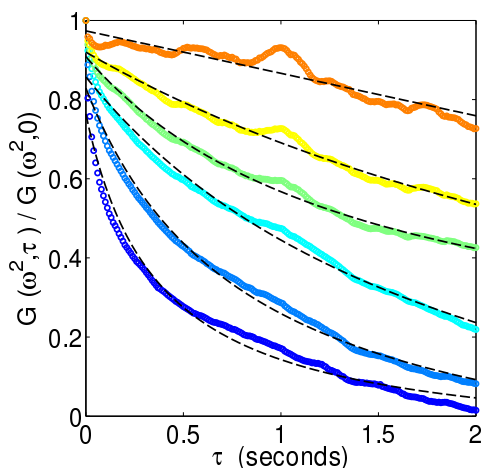
where  $\sigma$ ,  $r$ , and  $P$  represent elementary diffusion jump length, mesh radius and probability of crossing the confinement barrier respectively.  $A$  and  $B$  are phenomenological constants and were shown to equal 1 and 1.34 respectively.  $S_{conf}$  is equal to 1 when no confinement is present (since  $\tau_{conf} = \tau_d^{domain}$ ) and increases as the probability of crossing the boundary decreases. Another relation that links the confinement strength to the diffusion coefficients observed on micro ( $D_\mu$ ) and macro ( $D_M$ ) scales [71]:

$$D_\mu \approx S_{conf} \cdot D_M \quad (1.8)$$

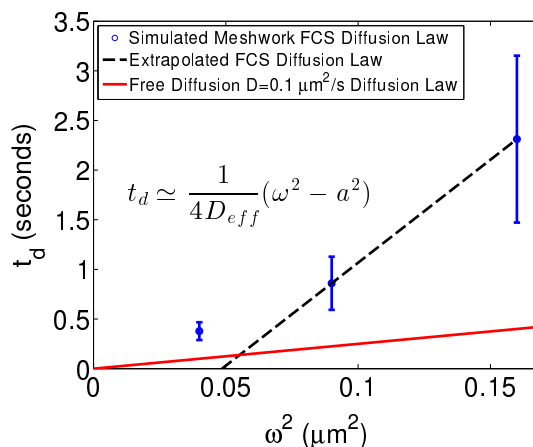
The diffusion law of meshwork shown in figure 1–15 gave  $D_M \sim 0.012 \pm 0.005 \frac{\mu m^2}{s}$ . Since the mesh diameter was set to  $0.25 \mu m$  and the probability to cross a barrier was set to  $P \sim 0.05$  the confinement strength is calculated to be  $\sim$

11.9. Then the microscopic diffusion coefficient should be around  $0.14 \frac{\mu m^2}{s}$ .

That is indeed the case as  $D_\mu$  was set to  $0.1 \frac{\mu m^2}{s}$ . These examples illustrate the



(a) Spot Varying FCS temporal ACFs for meshwork simulated scenario



(b) FCS diffusion law for meshwork simulated scenarios

Figure 1–15: The FCS Diffusion Law for simulated particle diffusion in a meshwork. a) Normalized ACFs for various beam radii sizes. Circles show all ACFs, while lines are the corresponding fits to a 2D diffusion model. b) FCS Diffusion Law for a meshwork. Blue circles are the extracted characteristic diffusion times ( $t_d$ ) for different beam radii in the presence of a meshwork. The red line is a suggestive plot for the 2D free diffusion FCS diffusion law with set diffusion coefficient. The black dashed line is a linear fit through data at larger beam radii.

usefulness of spot-varying FCS for measuring particle dynamics in heterogeneous membrane environments. The complete theory for both isolated domains [73] and meshwork [74] confinements have been derived after the first reports of this technique.

## 1.4 ICS analysis of heterogeneous membrane

### 1.4.1 Overview of ICS superfamily of techniques

Image correlation spectroscopy (ICS) is an extension of FCS to the analysis of fluorescence fluctuations recorded in the spatial domain by imaging. In its original adaptation, ICS was used to count the number density and cluster size of membrane receptors [75, 76]. The basic idea of the technique was to spatially correlate fluorescence fluctuations from pixel to pixel in an image. Assuming ergodicity of the sample, acquiring information from uniform sampling at a fixed point in time, as in FCS, is equivalent to the information acquired at a single time snapshot for a spatial ensemble of points (the image). The amplitude of the spatial intensity fluctuation auto-correlation function of an image provides information on the average number of entities per focal spot (labelled receptors in this case). The ICS spatial correlation function is well modelled and fit with a 2D Gaussian. The origin of the 2D Gaussian shape comes from the shape of the PSF which acts as a correlator, and sub-resolution particles convolved with the PSF give rise to image features of that shape. Later, ICS was extended to study the diffusion properties of membrane receptor clusters [77, 78]. In that adaptation, a pixel within an image time series is correlated with itself at later times, in order to extract the equivalent of the temporal ACF in FCS. The technique, named temporal image correlation spectroscopy (TICS), assumed a homogeneous sample, and provided better statistics by an ensemble averaging of the temporal ACFs of all pixels. Application of TICS relies on membrane proteins diffusing slowly enough so they

remain with a given PSF defined spot in the image in sequential frames and hence are correlated in time. Ever since the introduction of pure image spatial auto-correlation (ICS) several adaptations were made in order to tackle different biophysical problems. Indeed, image cross-correlation spectroscopy (ICCS) was introduced to measure the spatial co-localization of proteins in cells [79, 80], image moment analysis [81] and spatial intensity distribution analysis (spIDA) [82] were developed to measure the oligomerization states and stoichiometry of protein complexes. Spatio-temporal image correlation spectroscopy (STICS) extends the capabilities to measure flow of proteins in cells [83], and the k-space image correlation spectroscopy (kICS) allows the measurement of protein transport independent of fluorophore photophysics [84]. Other adaptations of imaging based correlation analysis methods have emerged in the last 15 years which have been reviewed [85]. STICS and kICS, can be considered to be opposite faces of the same coin, and serve as a basis for the development of the analysis presented in this thesis. Therefore, we will introduce the key concepts of these techniques below.

#### **1.4.2 Spatio-temporal image correlation spectroscopy**

STICS was originally developed to measure the flow of proteins in live cells [83]. The analysis was based on spatially cross-correlating two images of the same cellular area, taken at two different times. That implies that each pixel of an image is correlated with other pixels at later times. This is a full two-pixels-two-times correlation function, or four-point correlation function. If proteins undergo active transport (flow), the correlation function peak will translate in time at the

same rate as the dynamic species do. The peak shape is governed by the PSF and features in the image, and is usually fit with a 2D Gaussian, which is free to translate and spread. The tracking of the correlation peak position with temporal lag allows for the measurement of an average particle flow velocity vector for the region of interest, as shown in figure 1–16 b).

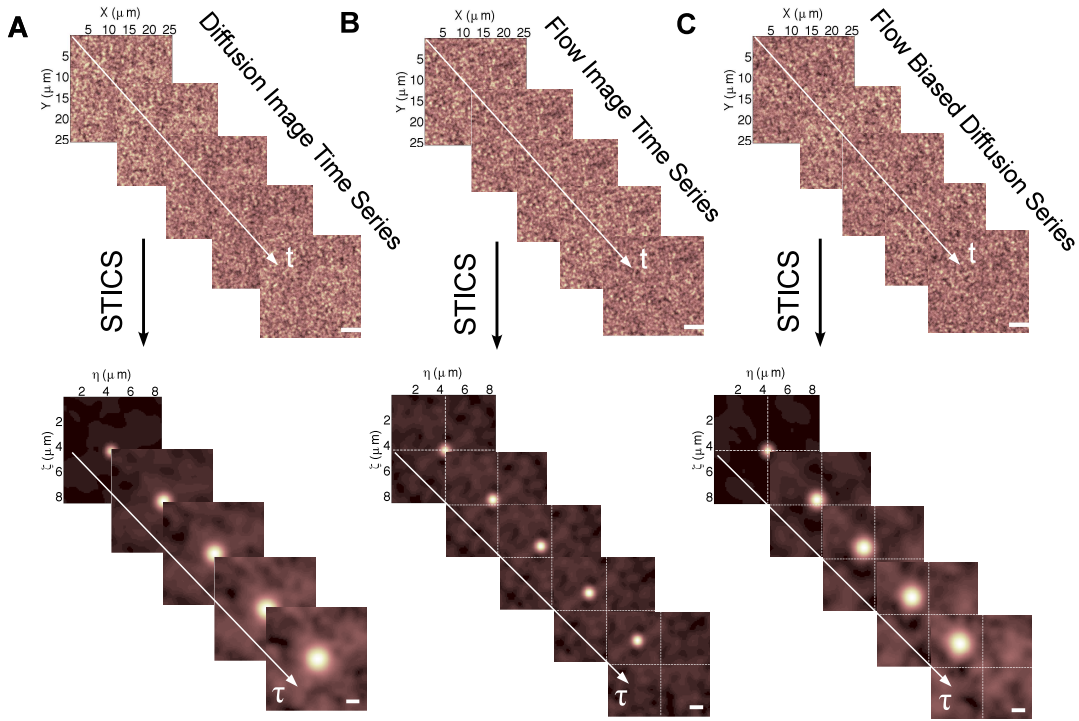


Figure 1–16: STICS of three different scenarios. Top row depicts image series, while bottom row shows correlation functions for each scenario. a) STICS of purely diffusive particles. b) STICS of purely flowing particles. c) STICS of simultaneously flowing and diffusing particles. Scalebar:  $5 \mu\text{m}$  top and  $1 \mu\text{m}$  bottom.

If motion of the particles is predominantly diffusive, then the correlation peak will spread and its peak amplitude will decrease with lag time as shown in

figure 1–16 a). Of course, any combination of dynamics, such as simultaneous diffusing and flowing particles, will give rise to a correlation peak exhibiting a combination of the two basic modes of motion (as in Figure 1–16 c). The original application of STICS studied diffusion, flow, and combined transport in silico, but only protein flow was measured experimentally in cells as the diffusion time scales were shorter than the imaging frame time [83]. The time dependent width of the correlation function was not considered as the main criterion for diffusion measurements, but rather its zero spatial lags decay in amplitude over time was used to measure the diffusion characteristics, which is the same as TICS. This modality of image correlation is also known as Dynamic Image Correlation Spectroscopy (DICS) [86]. The problem with fitting zero spatial lags of the CF to measure the diffusion coefficient, is its sensitivity to the time dependent probe photo-physics. If a fluorophore blinks (emission switches from on to off for a period of time) or photo-bleaches (permanent loss of emission) then its temporal ACF will be biased to a more rapid decay if the photophysics time scale is comparable to or shorter than the characteristic time for diffusion or flow. The width of STICS function peak will not be affected by blinking or photo-bleaching, as a pixel-to-pixel spatial correlation will only occur if a fluorophore is in the “on” state at both pixels at two time points. If it is in the “off” state, it will simply not produce a correlation for that set of spatio-temporal lags. Therefore, the width of the STICS correlation function is not affected by probe photo physics but there is a loss of precision relative to the zero spatial lags time CF. For the two dimensional

Brownian motion with a diffusion coefficient  $D$ , the square of the time dependent  $e^{-2}$  radius of the spatio-temporal CF will follow:

$$\omega_{STICS}^2(\tau) = \omega_0^2 + 4D\tau \quad (1.9)$$

where  $\omega_0$  is the  $e^{-2}$  radius of PSF of a microscopy system. The implementation of the pixels spatio-temporal correlation in the study of diffusive protein motion, was first demonstrated by k-space (Fourier) equivalent of STICS, also known kICS [84].

### 1.4.3 k-space image correlation spectroscopy

STICS and kICS are simply connected by a spatial Fourier transform but there are some advantages of kICS due to the treatment of data in k-space instead of r-space. With kICS, the correlation functions can be normalized by the zero-temporal lag correlation, which removes all static contributions, such as spatially dependent PSF. Also, flow and diffusion components are decoupled as real and imaginary parts of the correlation function. Photo-physics contribution, which is presumably only time dependent, can be also separated out from the dynamics terms. kICS development for the treatment of homogeneous diffusion and flow cases was the subject of an ulterior manuscript [87], and a further characterization was subject of yet another [88]. In the case of pure Brownian motion, kICS correlation function will have a collapsing width as shown in figure 1–17:

Since the correlation function is normalized with the zero temporal lag, the PSF contribution to the width of the correlation as a function of time lag will be eliminated, and will be in case of 2D freely diffusing particles:

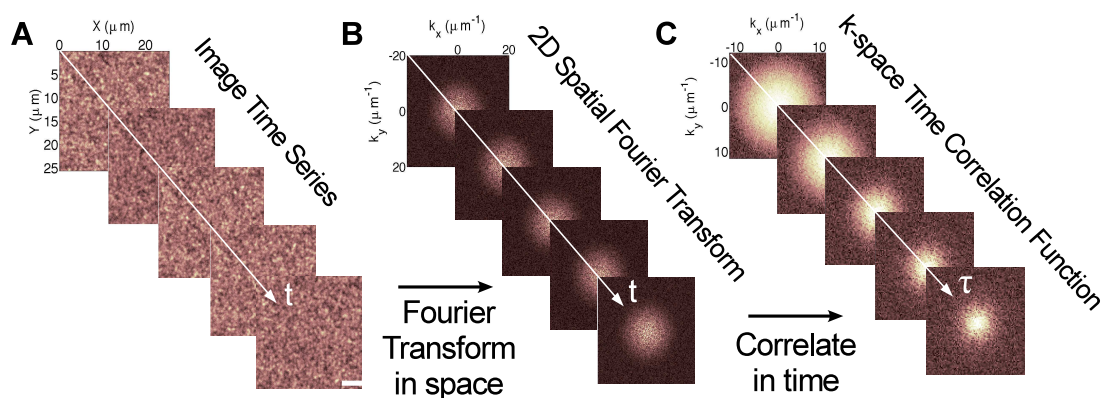


Figure 1–17: kICS in case of a purely diffusing single species. a) A simulated image series in time. b) Image series Fourier transformed into k-space. c) Temporal correlation function in k-space. Scalebar: 5  $\mu\text{m}$ .

$$\omega_{kICS}^2(\tau) = (D\tau)^{-1} \quad (1.10)$$

In practice, each temporal lag of the kICS time correlation function with the zero temporal lag, followed by a circular k-space averaging of the function at different temporal lags (assuming an isotropic system) to enhance statistics and to reduce the binning noise (Figure 1–18).

Therefore, measurement of the radius of the kICS correlation function, at each temporal lag, can be used to extract the average diffusion coefficient of a system of diffusive particles as shown in figure 1–19. Both STICS and kICS, originally were developed and tested through simulations, for one component homogeneous systems with constant transport dynamics. However, biological samples are usually more complex. Multiple dynamic species that can change modes of motions,

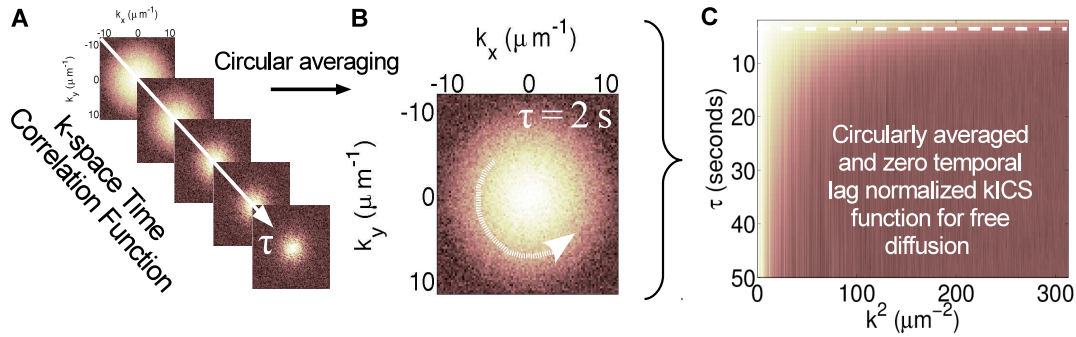
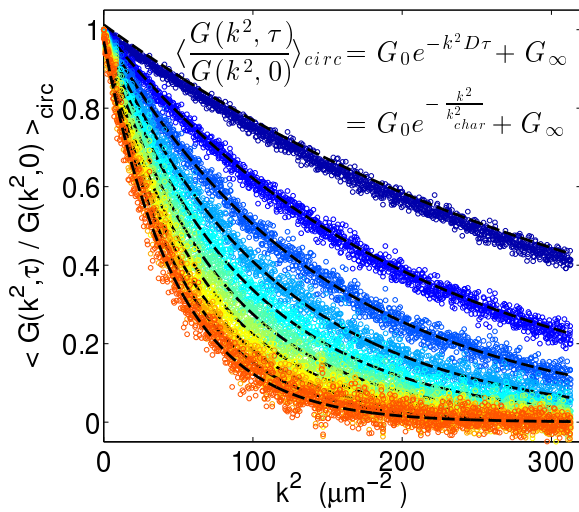


Figure 1–18: Steps for calculation of a normalized averaged kICS correlation function. a) The correlation function is calculated in Fourier space, ensemble averaged for each temporal lag, and normalized to the zero temporal lag. b) At each temporal lag ( $\tau=2$  s here), the correlation function is circularly averaged. c) Plot of the final correlation function, as a function of temporal lag and spatial frequency squared, for the case of free diffusion ( $D=0.002 \mu m^2/s$ ) simulated data. White dashed line delimits the  $\tau=2$  s (from b) contribution to the correlation function.

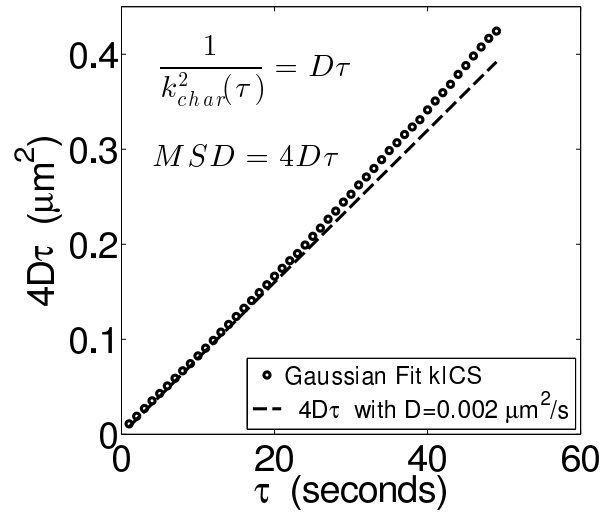
interact with each other or partition into multi-phase heterogeneous environments in the membranes, are more likely. The subject of this thesis is to extend the kICS method to measure these more complex systems.

#### 1.4.4 Emergent features of kICS in the presence of heterogeneities

ICS methods have only recently been used to study transport in heterogeneous membranes. One of the first systems to be explored by ICS and related techniques was the cystic fibrosis trans-membrane receptor (CFTR) [89]. This paper presents an extensive comparison of CFTR mobilities acquired by SPT, FRAP and ICS, and explores by simulations the effect transient confinement zones in the membrane on the overall mobility measured by TICS. The properties explored



(a) kICS function for free diffusion



(b)  $4D\tau$  vs  $\tau$  for free diffusion

Figure 1–19: kICS data analysis example using free diffusion case with  $D=0.002\mu\text{m}^2/\text{s}$ . Circularly averaged and normalized correlation functions are fit with an appropriate model at a given temporal lag. a) Correlation functions are fit with a single Gaussian that models 2D free diffusion. Blue to red data points represent an increasing time lag. Dashed lines are Gaussian fits at each time lag. Extracted parameter is  $\frac{1}{k_{char}^2}=D\tau$  at each value of  $\tau$ . b)  $4D\tau$  is plotted as a function of  $\tau$  in order to extract characteristic mobility (diffusion coefficient).

in the simulations and experimental data were limited to mobile fractions and an effective diffusion coefficient. Another DICS based study explored the mobilities of epidermal growth factor receptor (EGFR) clusters [86]. These studies produced some useful results but were limited by the fact that they only rely on a single pixel stack temporal fluctuations. In other words, these techniques do not explore more than one spatial scale, beyond that of a single pixel. In contrast, STICS and kICS take advantage of all spatial and temporal scales present and accessible from an image series, but involve an average over the dynamic populations present. If a particle population explores a homogeneous medium, through 2D Brownian motion as explained above, its kICS correlation function will decay completely to a noise floor at a given  $k^2$  value for each time lag as shown in figure 1–20 a).

This correlation function depends not only on time, as is the case of TICS or DICS, but also on spatial frequency ( $k^2$ ). A fit with a 2D Gaussian at each temporal lag will give a characteristic  $D\tau$  and a plot of  $4D\tau$  vs  $\tau$  can be seen as an equivalent of the  $MSD(\tau)$  vs  $\tau$  measured in SPT experiments. On the other hand, in the presence of isolated domains (Figure 1–20 b), the kICS CFs will not decay completely at later temporal lags. Instead of a single Gaussian decay, there will be effectively two or more emergent dynamic species present that contribute the CF. The characteristic feature of the kICS CF for dynamics in a heterogeneous 2D system is the presence of late temporal lag “shoulders”, which are due to the dynamics of confined (domain trapped) particles. The kICS CFs for simulated data of diffusive particles in the presence of isolated domains and a meshwork are shown in figure 1–20. b) and c), respectively.

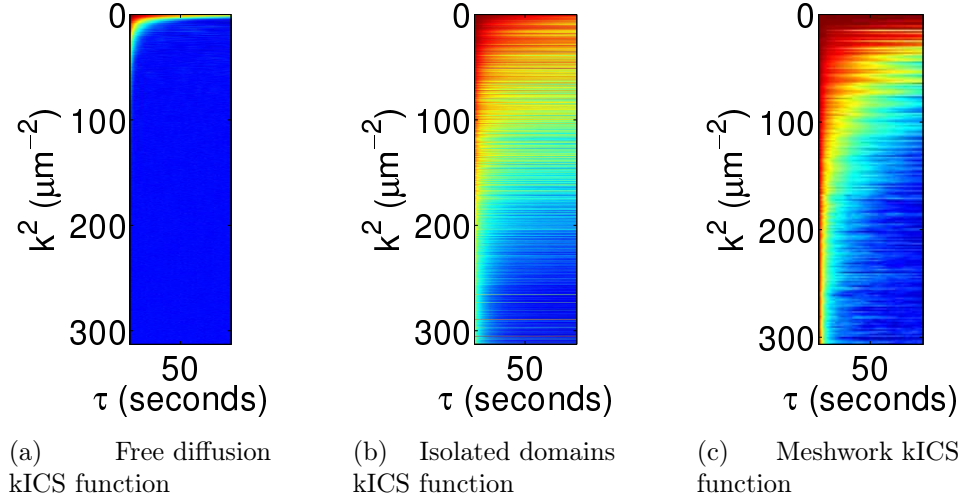


Figure 1–20: Examples of kICS CFs for three different simulated populations. a) kICS CF for free diffusion of particles with a diffusion coefficient of  $0.01 \mu\text{m}^2/\text{s}$ . b) kICS CF for particles diffusing in a system with isolated circular domains of  $0.25 \mu\text{m}$  radius. Diffusion in and out of domain of  $0.001$  and  $0.01 \mu\text{m}^2/\text{s}$  respectively. c) kICS CF for particles diffusing in a system with meshwork type of confinement with a mesh size of  $0.25 \mu\text{m}$ , a diffusion coefficient of  $0.1 \mu\text{m}^2/\text{s}$  within compartments and an escaping probability of  $P=0.05$ . All correlation functions were normalized by the zero-temporal lag correlation such that highest (red) and lowest (blue) values equal 1 and 0, respectively.

One may speculate that there should be an ICS analog in  $r$  or  $k$ -space to the spot-vary FCS method. Indeed, measurement of the spread of the correlation function in these techniques at a given temporal lag should give analogous information to the measurement of the characteristic decay time in spot-vary FCS at a given beam radius. kICS has advantages for the reasons explained above. In order to process the correlation functions, and extract the relevant parameters we need to properly fit the CF vs time or vs spatial frequency. Traditionally, the kICS CF are fitted at a given temporal lag, vs spatial frequency, in order to extract  $D\tau$ . For

measurement of dynamics in a heterogeneous environment a single 2D Gaussian fit vs spatial frequency is not sufficient. On the other hand, a single Gaussian fit can be forced as a fit vs time, at a given spatial frequency, in order to extract a characteristic decay constant. This idea is similar to the forced fit for 2D free diffusion through data in the FCS diffusion law, in order to characterize the decay at a given beam spot radius. If one plots the characteristic decay constant,  $k_{char}^2 D$  vs spatial frequency,  $k^2$ , one obtains an equivalent relation to the FCS diffusion law. We shall call this plot, for the sake of history, the “inverse kICS diffusion law”. The “inverse” part comes from the fact that x-axis has units of  $\mu m^{-2}$  and y-axis has units of  $s^{-1}$ , while in actual FCS diffusion law the units are seconds and  $\mu m^2$ , respectively. For free diffusion, the inverse kICS diffusion law has a slope equal to the  $D$  of the particles, and passes through the origin (Figure 1–21).

For particle’s transport in the presence of isolated domains, the diffusion law has a positive intercept, depending on the confinement strength, and an early slope reflecting the effective diffusion coefficient outside the domains. The fast diffusion implies greater slope which happens at smaller spatial frequencies corresponding to bigger spatial scales. The later slope reflects motions at higher spatial frequencies (smaller spatial scales) which corresponds to motions within the domains. Interestingly, the kICS diffusion law saturates at a spatial frequency that is  $\sim \frac{\pi^2}{2(domain\ radius)^2}$  as shown by the vertical magenta line in figure 1–21 a). It is likely that particles exhibit slower mobility as we increase spatial frequency (going to smaller spatial scales) until we reach the domain size scale, where particles appear immobile (peak position in red symbols of figure 1–21 a). At smaller

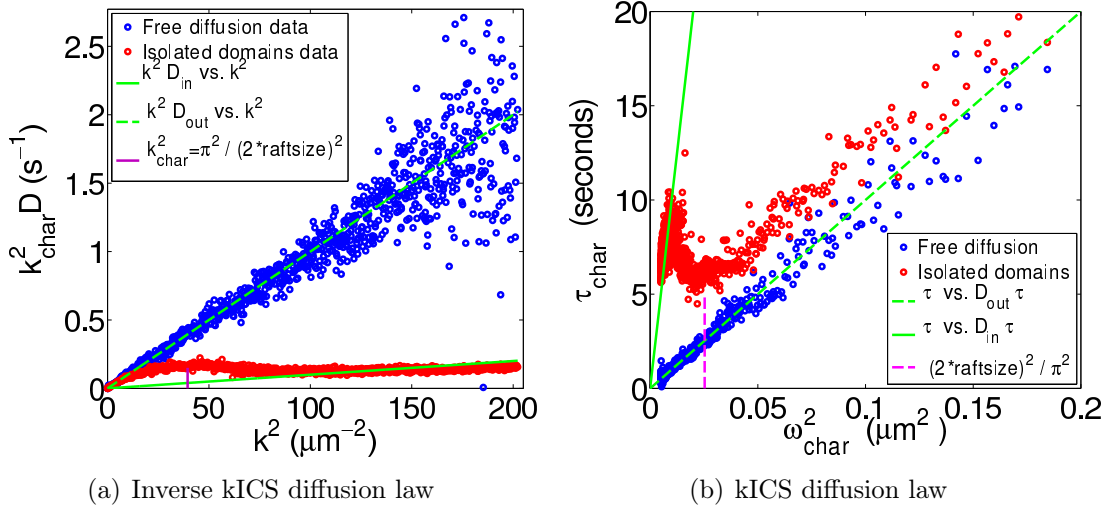


Figure 1–21: kICS diffusion law for free diffusion (blue symbols) and isolated domains cases (red symbols). a) Plot of the characteristic decay constant ( $k_{char}^2 D$ ) of Gaussian fit over temporal lag variable ( $\tau$ ), at a given spatial frequency ( $k^2$ ). Green full and dashed lines represent trends for cases of pure diffusion with diffusion coefficients used for isolated diffusion simulation. Magenta vertical line represents the value of the characteristic spatial frequency one would expect for diameter of raft. b) kICS diffusion law plotted in a format closer to the FCS diffusion law.

scales (even higher spatial frequency) motion inside rafts is detected. A similar observation of reduced mobility with decreasing the size of a bleaching spot was seen in FRAP experiments [70].

Another way to present these data is by the inversion of both  $k_{char}^2 D$  to give  $\tau_{char}$  and  $k^2$  to give  $\omega_{char}^2$  as shown in the kICS diffusion law plot (figure 1–21 b). This is one way to present kICS data, for measurements on heterogeneous environments. The rest of this thesis will present the details of simulations and characterization of kICS applied to measure transport in various types of 2D heterogeneous environment. Chapter 2 presents the theory behind kICS and how it extends beyond the simple homogeneous Brownian diffusion case. In chapter 3, we will present the computer simulations and methods data analysis approaches, as well as experimental methods for cell culture and TIRF microscopy. Chapter 4 will follow with a simulation results and analysis, while chapter 5 will present an experimental application of this method for the study of dynamics of GPI-anchored proteins in live cells.

## REFERENCES

- [1] *A new system of chemical philosophy*. ISBN. 1-153-05671-2, 1808.
- [2] Schrodinger E. *What is Life?* Macmillan, 1946.
- [3] Fricke H. The electrical capacity of suspensions with special reference to blood. *J. of Gen. Phys.*, pages 137–152, 1925.
- [4] Gorter E. Grendel F. On biomolecular layers of lipids on the chromocytes of the blood. *J.Exp.Med.*, 41:439–443, 1925.
- [5] Danielli J.F. Davson H. A contribution to the theory of permeability of thin films. *J. of Cell. and Compar. Phys.*, 5:495–508, 1935.
- [6] Mueller P. Rudin D.O. Tien H.I. Wescott W.C. Reconstitution of cell membrane structure in vitro and its transformation into an excitable system. *Nature*, 194:979–980, 1962.
- [7] Frye L.D. Edidin M. The rapid intermixing of cell surface antigens after formation of mouse-human heterokaryons. *J.Cell Sci.*, 7:319–35, 1970.
- [8] Singer S.J. Nicholson G.L. The fluid mosaic model of the structure of the cell membrane. *Science*, 175:720–730, 1972.
- [9] van Meer G. Cellular lipidomics. *EMBO J.*, 24:3159–3165, 2005.
- [10] Sowers A.E. Hackenbrock C.R. Rate of lateral diffusion of intramembrane particles: measurement by electrophoretic displacement and rerandomization. *Proc Natl Acad Sci*, 78:6246–50, 1981.
- [11] Ryan T.A. Myers J. Holowka D. Baird B. Webb W.W. Molecular crowding on the cell surface. *Science*, 239:61–64, 1988.
- [12] Scheuring S. Sturgis J.N. Chromatic adaptation of photosynthetic membranes. *Science*, 309:484–487, 2005.

- [13] Simons K. Ikonen E. Functional rafts in cell membranes. *Nature*, 387:569–572, 1997.
- [14] Simons K. van Meer G. Lipid sorting in epithelial cells. *Biochemistry*, 27:6197–6202, 1988.
- [15] Brown D. Gpi-anchored proteins and detergent-resistant membrane domains. *Braz.J.Med.Biol.Res.*, 148:997–1007, 1994.
- [16] Pralle A. Florin E.L. Simons K. Horber J.K.H. Sphingolipid-cholesterol rafts diffuse as small entities in the plasma membrane of mammalian cells. *J. Cell Biol.*, 148:997–1007, 2000.
- [17] Brown D.A. Lipid rafts, detergent-resistant membranes, and rafts targeting signals. *Physiology*, 21:430–39, 2006.
- [18] Marguet D. Lenne P.F. Rigneault H. He H.T. Dynamics in the plasma membrane: how to combine fluidity and order. *EMBO J.*, 25:446–57, 2006.
- [19] Pike L.J. Rafts defined: a report on the keystone symposium on lipid rafts and cell function. *J. Lipid Res.*, 47:1597–98, 2006.
- [20] Lingwood D. Simons K. Detergent resistance as a tool in membrane research. *Nature Protoc.*, 2:2159–2165, 2007.
- [21] Kenworthy A.K. Have we become overly reliant on lipid rafts? talking point on the involvement of lipid rafts in t-cell activation. *EMBO Rep.*, 9:531–535, 2008.
- [22] Zidovetcki R. Levitan I. Use of cyclodextrins to manipulate plasma membrane cholesterol content: evidence, misconception and control strategies. *Biochim. Biophys. Acta*, 1768:1311–1324, 2007.
- [23] Sharma P. Nanoscale organization of multiple gpi-anchored proteins in living cell membranes. *Cell*, 116:577–589, 2004.
- [24] Kusumi A. Koyama-Honda I. Suzuki K. Molecular dynamics and interactions for creation of stimulation induced stabilized rafts from small unstable steady-state rafts. *Traffic*, 5:213–230, 2004.
- [25] Wawrezynieck L. Conchonaud F. Wurtz O. Boned A. Guo X.-J. Rigneault H. He H-T. Marguet D. Lenne P.-F. Dynamic molecular confinement in the

- plasma membrane by microdomains and the cytoskeleton meshwork. *EMBO J.*, 25(3245-3256), 2006.
- [26] Dppc pdb file: [www.koders.com](http://www.koders.com).
- [27] Kusumi A. Sako Y. Cell surface organization by the membrane skeleton. *Curr. Opin. Cell Biol.*, 8(566-574), 1996.
- [28] Ritchie K. Lino R. Fujiwara T. Murase K. Kusumi A. The fence and picket structure of the plasma membrane of live cells as revealed by single molecule techniques. *Mol. Membr. Biol.*, 20:13–18, 2003.
- [29] Suzuki K. Ritchie K. Kajikawa E. Fujiwara T. Kusumi A. Rapid hop diffusion of a g-protein-coupled receptor in the plasma membrane as revealed by single-molecule techniques. *Biophys. J.*, 88:3659–3680, 2005.
- [30] Engelman D.M. Membrane are more mosaic than fluid. *Nature*, 438:351–354, 2005.
- [31] Jablonski A. Efficiency of anti-stokes fluorescence in dyes. *Nature*, 131:839–840, 1933.
- [32] Stokes G. On the change of refrangibility of light. *Phil. Trans. Royal Society of London*, 142:463–562, 1852.
- [33] Shimomura F. Johnson H. Saiga Y. Extraction, purification and properties of aequorin, a bioluminescent protein from the luminous hydromedusan. *Aequorea. J. Cell Comp. Physiol.*, 59:223–239, 1962.
- [34] Ormo M. Cubitt A. Kallio K. Gross L. Tsien R. Remington S. Crystal structure of the aequorea victoria green fluorescent protein. *Science*, 273:1392–1395, 1996.
- [35] Yang F. Moss L. Phillips G. The molecular structure of green fluorescent protein. *Nat Biotechnol*, 14:1246–1251, 1996.
- [36] Alexa dyes: [www.atdbio.com/content/34/alexadyes](http://www.atdbio.com/content/34/alexadyes).
- [37] Protein data bank : [www.pdb.org](http://www.pdb.org).
- [38] Shaner N. Steinbach P. Tsien R. A guide to choosing fluorescent proteins. *Nat Methods*, 2:905–909, 2005.

- [39] Bruchez M. Moronne M. Gin P. Weiss S. Alivisatos A.P. Semiconductor nanocrystals as fluorescent biological labels. *Science*, 281:2013–2016, 1998.
- [40] Molecular probes (life technologies) : [www.invitrogen.com](http://www.invitrogen.com).
- [41] Coons A.H. Creech H.J. Jones R.N. Berliner E. The demonstration of pneumococcal antigen in tissues by the use of fluorescent antibody. *Immunol.*, 45:159–170, 1942.
- [42] Anti-gfp igg conjugated with alexa dyes:  
<http://products.invitrogen.com/ivgn/product/a21311>.
- [43] Nikon microscopy tutorial :  
<http://www.microscopyu.com/articles/fluorescence/tirf/tirfintro.html>.
- [44] Stockl M.T. Hermann A. Detection of lipid domains in model and cell membrane by fluorescence lifetime imaging microscopy. *Biochim. Biophys. Acta*, 1798:1444–1456, 2010.
- [45] Owen D.M. Neil M.A.A. French P.M.W. Magee A.I. Optical techniques for imaging membrane lipid microdomains in living cells. *Seminars in Cell and Develop. Biol.*, 18:591–598, 2007.
- [46] Jacobson K. Mourtsen O.G. Anderson R.G.W. Lipid rafts: at a crossroads between cell biology and physics. *Nature Cell Biol.*, 9:7–14, 2007.
- [47] Simons K. Gerl M.J. Revitalizing membrane rafts: new tools and insights. *Nature Mol. Cell Biol.*, 11:693–699, 2010.
- [48] He H.-T. Marguet D. Detecting nanodomains in living cell membrane by fluorescence correlation spectroscopy. *Annu. Rev. Phys. Chem.*, 62:417–436, 2011.
- [49] Perrin M.J. Brownian movement and molecular reality. *Annales de Chimie et de Physique*, 8, 1909.
- [50] De Brabander M. Geuens G. Nuydens R. Moeremans M. De Mey J. Probing microtubule-dependent intracellular motility with nanometre particle video ultramicroscopy (nanovid ultramicroscopy). *Cytobios*, 43:273–83, 1985.

- [51] Jaqaman K. Loerke D. Mettlen M. Kuwata H. Grinstein S. Schmid S.L. Danuser G. Robust single-particle tracking in live-cell time-lapse sequences. *Nature Methods*, 5:695–702, 2008.
- [52] Serge A. Bertaux N. Rigneault H. Marguet D. Dynamic multiple-target tracing to probe spatiotemporal cartography of cell membranes. *Nature Methods*, 5:687–694, 2008.
- [53] Betzig E. Patterson G.H. Sourgat R. Lindwasser O.W. Olenych S. Bonifacino J.S. Davidson M.W. Lippincott-Schwartz J. Hess H.F. Imaging intracellular fluorescent proteins at nanometer resolution. *Science*, 313:1642–1645, 2006.
- [54] Sengupta P. Jovanovic-Talisman T. Skoko D. Renz M. Veath S.L. Lippincott-Schwartz J. Probing protein heterogeneity in the plasma membrane using palm and pair correlation analysis. *Nature Methods*, 8:969–975, 2011.
- [55] Manley S. Gillette J.M. Patterson G.H. Shroff H. Hess H.F. Betzig E. Lippincott-Schwartz J. High-density mapping of single-molecule trajectories with photoactivated localization microscopy. *Nature Methods*, 2008.
- [56] Subach F.V. Patterson G.H. Renz M. Lippincott-Schwartz J. Verkhusa V.V. Bright monomeric photoactivable red fluorescent protein for two-color super-resolution sptpalm of live cells. *J. Am. Chem. Soc.*, (132), 6481-6491 2010.
- [57] Sharonov A. Hochstrasser R.M. Wide-field subdiffraction imaging by accumulated binding of diffusing probes. *Proc. Natl. Acad. Sci.*, 103:18911–18916, 2006.
- [58] Giannone G. Hosy E. Levet F. Constals A. Schulze K. Sobolevsky A.I. Rosconi M.P. Gouaux E. Tampe R. Choquet D. Cognet L. Dynamic super-resolution imaging of endogenous proteins on living cells at ultra-high density. *Biophys. J.*, 99:1303–1310, 2010.
- [59] Gustafsson M. Nonlinear structured-illumination microscopy: Wide-field fluorescence imaging with theoretically unlimited resolution. *Prot. Nat. Acad. Sci.*, 102:13081–13086, 2005.
- [60] Westphal V. Hell S.W. Nanoscale resolution in the focal plane of an optical microscope. *Phys Rev Lett*, 94, 2005.

- [61] Qian H. Sheetz M.P. Elson E.L. Single particle tracking. *Biophys. J.*, 60:910–921, 1991.
- [62] Saxton M.J. Jacobson K. Single-particle tracking: Application to membrane dynamics. *Annu. Rev. Biophys. Biomol. Struct.*, 26:373–399, 1997.
- [63] Elson E.L. Magde D. Fluorescence correlation spectroscopy: I. conceptual basis and theory. *Biopolymers*, 13:1–27, 1974.
- [64] Magde D. Elson E.L. Webb W.W. Fluorescence correlation spectroscopy: II. an experimental realization. *Biopolymers*, 12:29–61, 1974.
- [65] Rigler R. Widengren J. *Ultrasensitive detection of single molecules by fluorescence correlation spectroscopy*. BioScience, 1990.
- [66] Rigler R. Mets U. Widengren J. Kask P. Fluorescence correlation spectroscopy with high count rate and low background: analysis of translational diffusion. *Eur. Biophys. J.*, 22(3):159, 1993.
- [67] Schwille P. Haupts U. Maiti S. Webb W.W. Molecular dynamics in living cells observed by fluorescence correlation spectroscopy with one- and two-photon excitation. *Biophys. J.*, 77:2251–65, 1999.
- [68] Elson E.L. Rigler R. *Fluorescence correlation spectroscopy: Theory and Applications*. Berlin:Springer, 2001.
- [69] Schwille P. Bacia K. A dynamic view of cellular processes by in vivo fluorescence auto- and cross- correlation spectroscopy. *Methods*, 29:74–85, 2003.
- [70] Yechiel E. Edidin M. Micrometer-scale domains in fibroblasts plasma membranes. *J. Cell Biol.*, 105:755–760, 1987.
- [71] Wawrezynieck L. Rigneault H. Marguet D. Lenne P.F. Fluorescence correlation spectroscopy diffusion laws to probe the submicron cell membrane organization. *Biophys. J.*, 89:4029–4042, 2005.
- [72] Masuda A. Ushida K. Okamoto T. New fluorescence correlation spectroscopy enabling direct observation of spatio-temporal dependence of diffusion constants as an evidence of anomalous transport in extracellular matrices. *Biophys. J.*, 88:3584–3591, 2005.

- [73] Ruprecht V. Weiser S. Marguet D. Schutz G.J. Spot variation fluorescence spectroscopy allows for superresolution chronoscopy of confinements times in mebranes. *Biophys. J.*, 100:2839–2845, 2011.
- [74] Destainville N. Theory of fluorecence correlation spectroscopy at variable observation area for two-dimensional diffision on a meshgrid. *Soft Matter*, 4:1288–1301, 2008.
- [75] Petersen N.O. Hoddelius P.L. Wiseman P.W. Seger O. Magnusson K.E. Quantitation of membrane receptor distributions by image correlation spectroscopy: concept and application. *Biophys. J.*, 65:1135–1146, 1993.
- [76] Wiseman P.W. Petersen N.O. Image correlation spectroscopy. ii optimization for ultrasensitive detection of preexisting platelet-derived growth factor- $\beta$  receptor oligomers on intact cells. *Biophys. J.*, 76:963–977, 1999.
- [77] Srivastava M. Petersen N.O. Image cross-correlation spectroscopy: a new experimental biophysical approach to measurment of slow diffusion of fluorescent moleculaes. *Meth. Cell Sci.*, 18:47–54, 1996.
- [78] Srivastava M. Petersen N.O. Diffusion of transferrin receptor clusters. *Biophys. Chem.*, 75:201–211, 1998.
- [79] Costantino S. Comeau J.W.D. Kolin D.L. Wiseman P.W. Accuracy and dynamic range of spatial image correlation and cross-correlation spectroscopy. *Biophys. J.*, 89:1251–1260, 2005.
- [80] Comeau J.W.D. Costantino S. Wiseman P.W. A guide to accurate fluorescence microscopy colocalization measurements. *Biophys. J.*, 91:4611–4622, 2006.
- [81] Sergeev M. Costantino S. Wiseman P.W. Measurement of monomer-oligomer distributions via fluorescence moment image analysis. *Biophys. J.*, 91:3884–3896, 2006.
- [82] Godin A.G. Costantino S. Lorenzo L.E. Swift J.L. Sergeev M. Ribeiro da Silva A. De Koninck Y. Wiseman P.W. Revealing protein oligomerization and densities in situ using spatial intensity distribution analysis. *Proc. Natl. Acad. Sci.*, 108:7010–7015, 2011.

- [83] Hebert B. Costantino S. Wiseman P.W. Spatiotemporal image correlation spectroscopy (stics) theory, verification, and application to protein velocity mapping in living cho cells. *Biophys. J.*, 88:3601–3614, 2005.
- [84] Kolin D.L. Ronis D. Wiseman P.W. k-space image correlation spectroscopy: a method for accurate transport measurements independent of fluorophore photophysics. *Biophys. J.*, 91:3061–3075, 2006.
- [85] Kolin D.L. Wiseman P.W. Advances in image correlation spectroscopy: measuring number densities, aggregation states, and dynamics of fluorescently-labeled macromolecules in cells. *Cell Biochem. Biophys.*, 49:141–164, 2007.
- [86] Keating E. Nohe A. Petersen N.O. Studies of distribution, location and dynamic properties of egfr on the cell surface measured by image correlation spectroscopy. *Eur. Biophys. J.*, 37:469–481, 2008.
- [87] Kolin D.L. *k-space Image Correlation Spectroscopy: theory, verification, and applications*. PhD thesis, McGill University, 2008.
- [88] Schwartzentruber J.A. k-space image correlation spectroscopy: accuracy and precision, capabilities and limitations. Master’s thesis, McGill University, 2010.
- [89] Bates I.R. Hebert B. Luo Y. Liao J. Bachir A.I. Kolin D.L. Wiseman P.W. Hanrahan J.W. Membrane lateral diffusion and capture of cfr within transient confinement zones. *Biophys. J.*, 91:1046–1058, 2006.

## CHAPTER 2

### Theory of kICS for heterogeneous membrane environments

#### 2.1 kICS analogy to the dynamic light scattering

We shall start the theory development by introducing the connection between the measured quantities in the dynamic light scattering (DLS) experiments, such as the intermediate scattering function or spectra, and the space-time correlation functions. The development presented in this section is based on the complete treatment in [1].

We define the particle number density,  $\rho(\vec{r}, t)$ , for a system of  $N$  Brownian particles in a microscopic volume  $V$ :

$$\rho(\vec{r}, t) = \sum_{i=1}^N \delta(\vec{r} - \vec{r}_i(t)) \quad (2.1)$$

where the sum is over all  $N$  particles and  $\delta$  denotes the Dirac  $\delta$ -function. The fluctuation in the number density due to particle diffusion will be:

$$\delta\rho(\vec{r}, t) = \rho(\vec{r}, t) - \bar{\rho} \quad (2.2)$$

where  $\bar{\rho}$  is a mean number density.

In DLS experiments one measures a quantity which is proportional to the Fourier component of the number density fluctuation. Taking the spatial Fourier transform of  $\delta\rho(\vec{r}, t)$  :

$$\tilde{\delta\rho}(\vec{k}, t) = \int_{-\infty}^{\infty} d^3r e^{i\vec{k}\cdot\vec{r}} \delta\rho(\vec{r}, t) \quad (2.3)$$

The temporal autocorrelation function of the number density in Fourier space (k-space) leads to the intermediate scattering function (ISF) :

$$S(\vec{k}, \tau) = \frac{1}{N} \sum_{i=1}^N \sum_{j=1}^N \langle \exp\{i\vec{k} \cdot [\vec{r}_i(t) - \vec{r}_j(t + \tau)]\} \rangle \quad (2.4)$$

Where the ISF quantifies the degree of correlation between the Fourier component of the number density fluctuation at time  $t$  and that at time  $t + \tau$ . The ISF is the spatial Fourier transform of the van Hove space-time correlation function (a.k.a. the pair correlation function),  $G(\vec{r}, \tau)$ :

$$S(\vec{k}, \tau) = (2\pi)^3 \bar{\rho} \int_{-\infty}^{\infty} G(\vec{r}, \tau) e^{-i\vec{k}\cdot\vec{r}} d\vec{r} \quad (2.5)$$

where

$$G(\vec{r}, \tau) = \frac{1}{N} \langle \sum_{i=1}^N \sum_{j=1}^N \delta[\vec{r} + \vec{r}_i(t) - \vec{r}_j(t + \tau)] \rangle \quad (2.6)$$

where the van Hove function is the probability that we will find a particle  $j$  at time  $t + \tau$  at a position  $\vec{r}_j(t + \tau)$  if particle  $i$  is at the position  $\vec{r}_i$  at time  $t$ . For an ergodic system, the time origin is arbitrary. Also, if the system is Brownian, different particle positions will not correlate at later times. This metric effectively measures the step size distributions of the particles.

The van Hove function can be calculated from single particle tracking trajectories or video microscopy data, where the positions of all particles are known at every time point. In most cases we can not track particles or obtain their positions at every time point. Fortunately, we can apply the results derived above to the ISF or to the spectra from scattering, or more particularly to the fluorescence spatio-temporal fluctuation data.

When considering a particle position correlation with its position at a later time, we relate to the *self part* of van Hove correlation function. On the other hand, correlating particle i position at time t with another particle j at time  $t + \tau$ , is called the *distinct part* of the van Hove correlation function. The total van Hove correlation function, from equation 2.6, is the sum of the self and distinct parts. For a dilute and Brownian system of particles, the distinct part does not contribute significantly to the sum in equation 2.6, and consequently the cross terms (when  $i \neq j$ ) in equation 2.4 are negligible. Consequently, the ISF reduces to the *self-intermediate scattering function* (SISF) :

$$F_s(\vec{k}, \tau) = \langle \exp\{i\vec{k} \cdot [\vec{r}(t) - \vec{r}(t + \tau)]\} \rangle \quad (2.7)$$

For freely diffusing particles with a diffusion coefficient D, the above expression will reduce to [1]:

$$F_s(|\vec{k}|, \tau) = \exp\{-k^2 D \tau\} = \exp\left\{-\frac{t}{\tau_k}\right\} \quad (2.8)$$

where  $\tau_k = \frac{1}{k^2 D}$  is the characteristic lifetime of the particles inside the measurement volume.  $|\vec{k}|$  denotes the magnitude of the wave vector  $\vec{k}$ , implying that the system is isotropic so the only absolute value of the k vector counts. The diffusion

coefficient  $D$  can be obtained from the slope of the  $\tau_k^{-1}$  versus  $k^2$  plot, known as the 'slope of the slopes' plot in kICS [2, 3]

Now we show that SISF is the solution to the diffusion equation. The definition of the self-van Hove correlation function at the initial time suggest that  $\Delta r_j(0) = 0$  and therefore:

$$G_s(\vec{r}, 0) = \langle \delta(\vec{r}) \rangle = \delta(\vec{r}) \quad (2.9)$$

and its Fourier transform

$$F_s(\vec{k}, 0) = \langle \exp\{i\vec{k} \cdot [\vec{r}_j(0) - \vec{r}_j(0)]\} \rangle = 1 \quad (2.10)$$

Using the definition of the self-van Hove correlation function it follows that it will be a solution to the diffusion equation subject to the initial value given by equation 2.9:

$$\frac{\partial}{\partial \tau} G_s(\vec{r}, \tau) = D \nabla^2 G_s(\vec{r}, \tau) \quad (2.11)$$

or its Fourier transform equivalent:

$$\frac{\partial}{\partial \tau} F_s(\vec{k}, \tau) = -k^2 D F_s(\vec{k}, \tau) \quad (2.12)$$

subject to the initial value given by equation 2.10 with solution given by:

$$F_s(\vec{k}, \tau) = \exp(-k^2 D \tau) \quad (2.13)$$

which is equivalent to the equation 2.7 for the SISF. The corresponding full spatio-temporal spectrum is obtained by taking the temporal Fourier transform of the

SISF:

$$F_s(\vec{k}, \omega) = \frac{1}{\pi} \left[ \frac{k^2 D}{\omega^2 + [k^2 D]^2} \right] \quad (2.14)$$

In the above derivation we assumed that particles are always detected and hence emitting (i.e. no photo-bleaching or blinking involved) and did not consider other spectral characteristics such as quantum yield or brightness. Moreover, when dealing with detection via fluorescence microscope, one needs to include the effect of the finite spatial resolution of the optical system. These are incorporated and explored in next section.

## 2.2 kICS theory for a homogeneous environment

The following section is a recap of the kICS Theory development as presented in [2, 3]. Originally, kICS was developed assuming a homogeneous and ergodic system. In the fluorescence intensity fluctuation based ICS techniques, one considers the intensity of a given pixel in an image,  $i(\vec{r}, t)$ , to be a convolution of the optical point spread function (PSF),  $I(\vec{r})$ , and the particle concentration,  $\rho(\vec{r}, t)$ :

$$i(\vec{r}, t) = qI(\vec{r}) * \rho(\vec{r}, t) \quad (2.15)$$

where  $q$  is a the constant that takes into account the quantum yield of the fluorophore, the collection efficiency and the detector gain. The number density

now can be written as:

$$\rho(\vec{r}, t) = \sum_{i=1}^N \Theta_i(t) \delta(\vec{r} - \vec{r}_i(t)) \quad (2.16)$$

where the sum is over all N particles and  $\delta$  is again the Dirac  $\delta$ -function. The photo-physics effects (bleaching, blinking, etc) are modelled by the time dependent function:

$$\Theta_i(t) = \begin{cases} 1 & \text{if particle } i \text{ is fluorescent at time } t; \\ 0 & \text{otherwise.} \end{cases} \quad (2.17)$$

The PSF of a confocal microscope can usually be approximated by a 2D Gaussian for cell membrane systems:

$$I(\vec{r}) = I_0 \exp\left[-2\left(\frac{x^2 + y^2}{\omega_0^2}\right)\right], \quad (2.18)$$

where  $I_0$  denotes the laser intensity at the center of the focus, and  $\omega_0$  is the  $e^{-2}$  the beam radius of the laser beam in the lateral direction. We explicitly ignore the third spatial dimension, as we assume measurements on flat quasi 2D membranes.

Since the convolution becomes a product in Fourier space, it is most convenient to take the spatial Fourier transform of the concentration and the PSF functions. Thus equation 2.15 in k-space is:

$$\tilde{i}(\vec{k}, t) = q \tilde{I}(\vec{k}, t) \tilde{\rho}(\vec{k}, t) \quad (2.19)$$

where  $\tilde{X}$  labels the spatial Fourier transform of a quantity X.

Calculating the spatial Fourier transforms of equations 2.16 and 2.18, we can rewrite equation 2.19 as:

$$\tilde{i}(\vec{k}, t) = \frac{qI_0\omega_0^2\pi}{2} \sum_{i=1}^N \Theta_i \exp[i\vec{k} \cdot \vec{r}_i(t) - \frac{\omega_0^2|\vec{k}|^2}{8}]. \quad (2.20)$$

Using Eq. 2.20 to define the intensity fluctuation correlation function in the k-space:

$$\Phi(\vec{k}; \tau, t) = \langle \tilde{i}(\vec{k}, t) \tilde{i}^*(\vec{k}, t + \tau) \rangle \quad (2.21)$$

By combining the equations 2.20 and 2.21 we get:

$$\Phi(\vec{k}; \tau, t) = \frac{q^2 I_0^2 \omega_0^4 \pi^2}{4} \times \left\langle \sum_{i=1}^N \Theta_i(t) e^{i\vec{k} \cdot \vec{r}_i(t) - \frac{\omega_0^2 |\vec{k}|^2}{8}} \sum_{j=1}^N \Theta_j(t + \tau) e^{i\vec{k} \cdot \vec{r}_j(t + \tau) - \frac{\omega_0^2 |\vec{k}|^2}{8}} \right\rangle \quad (2.22)$$

Assuming that the system is sufficiently dilute, the cross-product terms will be negligible and since the  $\Theta(t)$  is only a function of time, we factor it out of the spatial integral so the above expression reduces to:

$$\Phi(\vec{k}; \tau, t) = N \frac{q^2 I_0^2 \omega_0^4 \pi^2}{4} \times \langle \Theta(t) \Theta(t + \tau) \rangle \times \langle \exp[i\vec{k} \cdot (\vec{r}(t) - \vec{r}(t + \tau)) - \frac{\omega_0^2 |\vec{k}|^2}{4}] \rangle \quad (2.23)$$

For a population undergoing diffusion with a coefficient  $D$  and/or flow with a velocity  $\vec{v}$  this reduces to:

$$\Phi(\vec{k}; \tau, t) = N \frac{q^2 I_0^2 \omega_0^4 \pi^2}{4} \times \langle \Theta(t) \Theta(t + \tau) \rangle \times \exp[i\vec{k} \cdot \vec{v}\tau - |\vec{k}|^2 (D\tau + \frac{\omega_0^2}{4})] \quad (2.24)$$

We will simplify the expression, without any loss of generality, to the case where only one population is diffusing and no flow is present (i.e.  $\vec{v} = 0$ ). Then the real

part of the equation 2.24 contains the diffusion part of the correlation function:

$$\Phi(\vec{k}; \tau, t) = N \frac{q^2 I_0^2 \omega_0^4 \pi^2}{4} \times \langle \Theta(t) \Theta(t + \tau) \rangle \times \exp[-|\vec{k}|^2 (D\tau + \frac{\omega_0^2}{4})] \quad (2.25)$$

Careful comparison between this equation and equation 2.13, suggests that the fitting function obtained for kICS, in the case of a single diffusing population, is proportional to the self-intermediate scattering function. In fact, we can define the heterodyne correlation function, used in DLS, in terms of SISF, as follows:

$$F_1(\vec{k}, \tau) = \langle N \rangle F_s(\vec{k}, \tau) \quad (2.26)$$

where  $\langle N \rangle$ , the average number of particles, effectively contains all of the photo-physics effects given in the amplitude,  $N \frac{q^2 I_0^2 \omega_0^4 \pi^2}{4} \times \langle \Theta(t) \Theta(t + \tau) \rangle$ , of equation 2.25.

### 2.2.1 STICS from kICS

We now apply the inverse Fourier transform to equation 2.25:

$$\Phi(\vec{r}; \tau, t) = N \frac{q^2 I_0^2 \omega_0^4 \pi^2}{4} \times \langle \Theta(t) \Theta(t + \tau) \rangle \int_{-\infty}^{+\infty} d\vec{k} e^{i\vec{k} \cdot \vec{r}} e^{-|\vec{k}|^2 (D\tau + \frac{\omega_0^2}{4})} \quad (2.27)$$

and then by making the substitution  $\frac{1}{4\alpha} = D\tau + \frac{\omega_0^2}{4}$  and using the following:

$$\sqrt{\frac{\pi}{\alpha}} \int_{-\infty}^{+\infty} d\vec{k} e^{i\vec{k} \cdot \vec{r}} e^{-\frac{|\vec{k}|^2}{4\alpha}} = e^{-\alpha|\vec{r}|^2} \quad (2.28)$$

we obtain:

$$\Phi(\vec{r}; \tau, t) = N \frac{q^2 I_0^2 \omega_0^4 \pi^{\frac{3}{2}}}{4\sqrt{4D\tau + \omega_0^2}} \times \langle \Theta(t) \Theta(t + \tau) \rangle e^{-\frac{|\vec{r}|^2}{4D\tau + \omega_0^2}} \quad (2.29)$$

This represents the fitting function for STICS in the case of a single freely diffusing population. In this case it is equivalent to the self-van Hove spatio-temporal correlation function,  $G_s(\vec{r}, \tau)$ . The difference between  $F_s(\vec{k}, \tau)$  and  $\Phi(\vec{k}; \tau)$  (in k-space) or between  $G_s(\vec{r}, \tau)$  and  $\Phi(\vec{r}; \tau)$ , is that the fluorescence intensity fluctuation correlation functions take into account the particles photo-physics, intrinsic light emission properties and the finite resolution of the optical instrument employed for the measurement. Even though light scattering and fluorescence are based on two different forms of light and matter interactions, the theory explaining Brownian motion, as measured by the ensemble average spatio-temporal fluctuations of particles density is analogous in the two cases.

### 2.2.2 Normalization by the zero temporal lag

Expression 2.29 has one undesirable characteristic for the study of diffusion properties. The finite width,  $\omega_0$ , of the correlation function at the zero temporal lag can potentially mask the effects of the motion at spatial scales smaller than  $\omega_0$ . In kICS, the contribution of  $\omega_0$  is removed from the correlation function by zero temporal lag normalization [2, 3], as follows:

$$\frac{\Phi(\vec{k}; \tau, t)}{\Phi(\vec{k}; 0, t)} = \frac{\langle \Theta(t)\Theta(t + \tau) \rangle}{\langle \Theta(t)^2 \rangle} \times \exp(-|\vec{k}|^2 D\tau) \quad (2.30)$$

This normalization removes the PSF contribution and other constants embedded in the amplitude of correlation function. This expression is then usually averaged angularly (circularly) to obtain an effective two dimensional, spatial frequency (k) and temporal lag ( $\tau$ ), dependent correlation function:  $r(k^2, \tau)$ .

### 2.2.3 Two freely diffusing populations

In the case of two or more freely diffusing species in the sample, the total correlation function will be the weighted sum of all contributions. Then equation 2.25 becomes:

$$\Phi(\vec{k}; \tau, t) = \frac{I_0^2 \omega_0^4 \pi^2}{4} e^{-\frac{k^2 \omega_0^2}{4}} \sum_p N_p q_p^2 \times \langle \Theta_p(t) \Theta_p(t + \tau) \rangle \times \exp(-|\vec{k}|^2 D_p \tau) \quad (2.31)$$

for each diffusing particle population,  $p$ , the correlation amplitude reflects the fractional contribution of that population as weighted by number and squared yield. In the case of two freely diffusing species, the normalized correlation function becomes:

$$\frac{\Phi(\vec{k}; \tau, t)}{\Phi(\vec{k}; 0, t)} = \frac{N_1 e^{-|\vec{k}|^2 D_1 \tau} + N_2 e^{-|\vec{k}|^2 D_2 \tau}}{N_1 + N_2} \quad (2.32)$$

where the normalized number densities,  $N_i$ , are constants in space and time.

In what follows, we will see that two inter-converting or interacting species will produce a correlation function that can be effectively fit as a sum of two Gaussians. Nevertheless, the amplitudes and exponents of this correlation function will depend on spatial frequency ( $k$ ) and time lag ( $\tau$ ) in a non-trivial way as well on the kinetics parameters defining the inter-conversion rates.

### 2.3 Theory for a two phase medium with static domains

Here we revisit the solution to the coupled differential equations describing the motion of tracer particles inside a heterogeneous two-phase medium. The problem is to find an expression for particle number densities as a function of diffusion

coefficients inside and outside the domains. Phase 1 is assumed to be composed of circular micro domains embedded inside a larger 2D phase 2. The system is defined in terms of a partition coefficient between the two phases, the volume fraction of domains and the absorption rate constant. The problem of diffusion in two-phase media has attracted a lot of attention at the end of the last century and several solutions were proposed [4, 5, 6, 7]. We will base our development on the solution proposed by [8] starting by the definition of two partial differential equations that need to be solved in order to find the number densities for bound and unbound particles,  $N_b(\vec{r}, \tau)$  and  $N_f(\vec{r}, \tau)$  respectively:

$$\frac{\partial N_f(\vec{r}, \tau)}{\partial \tau} = D^+ \nabla^2 N_f(\vec{r}, \tau) - k_a [\eta_s N_f(\vec{r}, \tau) - K N_b(\vec{r}, \tau)] \quad (2.33)$$

and

$$\frac{\partial N_b(\vec{r}, \tau)}{\partial \tau} = k_a [\eta_s N_f(\vec{r}, \tau) - K N_b(\vec{r}, \tau)] \quad (2.34)$$

where  $k_a$  is the absorption rate constant,  $K$  is the partition coefficient,  $\eta_s$  is the microdomain volume fraction, and  $D^+$  is the diffusion coefficient of particles outside microdomains.  $K$  is defined in terms of the chemical potential of the diffusing species  $K \equiv \frac{[\frac{\partial \mu^+}{\partial c}]}{[\frac{\partial \mu^-}{\partial c}]}$ , where +/- denote outside/inside microdomains respectively.

The above problem assumes that particles do not diffuse inside domains, but are rather immobilized. It will become clear in the next section, that assuming a nonzero diffusion inside domains,  $D^-$ , gives a similar solution to equations 2.33 and 2.34. These equations are subject to initial conditions  $N_f(\vec{r}, 0) = (1 - \eta_s)\delta(\vec{r})$

and  $N_b(\vec{r}, 0) = \eta_s \delta(\vec{r})$ , together with the boundary conditions at the interface of microdomains  $D^- \frac{\partial N_b(\vec{r}^-, \tau)}{\partial n} = D^+ \frac{\partial N_f(\vec{r}^+, \tau)}{\partial n}$  and  $N_f(\vec{r}^+, \tau) = K N_b(\vec{r}^-, \tau)$ .

When  $K \rightarrow 0$  the microdomains become traps, while  $K \rightarrow \infty$  produces scatterers. In other words, by the definition of  $K$  in terms of chemical potentials, as  $K \rightarrow 0$ , the affinity for the large (+) phase will approach zero. This makes the microdomains perfect attractors or traps. Similarly, the  $K \rightarrow \infty$  limit implies that particles affinity for the microdomains phase (-) approaches zero, hence they become perfect scatterers.

Another way of seeing this is by computing the Fourier transform of the boundary conditions  $i\vec{k}\hat{n}D^- \tilde{N}_b^- = i\vec{k}\hat{n}D^+ \tilde{N}_f^+$  combined with  $\tilde{N}_f^+ = K \tilde{N}_b^-$  gives  $D^- \equiv K D^+$ . This means that in the case of a perfect trap ( $K \rightarrow 0$ ) we will have  $D^- \rightarrow 0$  which implies that particles diffuse very slowly within the domains and hence almost never encounter the domain boundary and never escape.

On the other hand, in the limit  $K \rightarrow \infty$ , we get  $D^- \rightarrow \infty$  which means that particles diffuse very fast within domains, hence increasing the collisions with the walls and hence the probability that the particles will escape from the domains. This translates into a zero residence time within the domains making them perfect scatterers.

Another interesting case is when the partition coefficient equals 1, hence equal affinity for both phases. In this case the phases are indistinguishable to the particles, hence  $D^- = D^+$  and the rate constants are equal by the definition of the partition coefficient.

In order to solve the above system of equations, we take the Fourier-Laplace transform, taking advantage of the transformation  $\nabla \rightarrow i\vec{k}$ ,  $\nabla^2 \rightarrow -k^2$ , and  $\frac{\partial}{\partial \tau} \rightarrow sY(s) - y(0)$  while considering the initial values for the number densities,  $N_f(\vec{r}, 0) = (1 - \eta_s)\delta(\vec{r})$  and  $N_b(\vec{r}, 0) = \eta_s\delta(\vec{r})$  :

$$s\tilde{N}_f + D^+k^2\tilde{N}_f + k_a(\eta_s\tilde{N}_f - K\tilde{N}_b) - (1 - \eta_s)\delta(\vec{r}) = 0 \quad (2.35)$$

and

$$s\tilde{N}_b - k_a(\eta_s\tilde{N}_f - K\tilde{N}_b) - \eta_s\delta(\vec{r}) = 0 \quad (2.36)$$

After some algebra we obtain:

$$\tilde{N}_f = \frac{(1 - \eta_s)\delta(\vec{r})s + k_aK\delta(\vec{r})}{s^2 + (D^+k^2 + k_a\eta_s + k_aK)s + k_aKD + k^2} \quad (2.37)$$

and a further simplification leads to following:

$$\tilde{N}_f + \tilde{N}_b = \frac{1}{s + \frac{D^+(s(1-\eta_s))k^2 + k_aKD + k^2}{s + k_a(\eta_s + K) + \eta_s D^+k^2}} \quad (2.38)$$

which is expressed as follows in [8]:

$$N_{tot} \equiv N_f(k, s) + N_b(k, s) = \frac{1}{s + D_{eff}(k, s)k^2} \quad (2.39)$$

where s and k denote Laplace and Fourier transforms variables. In the above expression, the effective diffusion coefficient  $D_{eff}(k, s)$  is written as a function of all the parameters established in the present case:

$$D_{eff}(k, s) \equiv \frac{D^+[s(1 - \eta_s) + k_aK]}{s + k_a(\eta_s + K) + \eta_s D^+k^2} \quad (2.40)$$

This effective diffusion coefficient is in Laplace-Fourier space and one could attempt to tackle the problem of image correlation by transforming images to the Laplace-Fourier space. Unfortunately, the product of two temporal functions leads to convolutions after Laplace transform, which prevents us from doing this with an expression similar to equation 2.30. Therefore, Laplace inversion of expression 2.39 is required. The Laplace inverse transform of the expression 2.39 gives the k-space total particle number density expression. We start by writing it in a simplified format:

$$N_{k,s} = \frac{s + x}{s^2 + ys + z} \quad (2.41)$$

after the simplification of equation 2.38 and grouping of all terms in the numerator and the denominator together we obtain expressions for x,y and z:

$$x = k_a(\eta_s + K) + \eta_s D^+ k^2 \text{ and } y = D^+ k^2 + k_a(\eta_s + K) \text{ and } z = k_a K D^+ k^2 \quad (2.42)$$

In order to apply the inverse Laplace transform to the expression 2.41 it is useful to write it as:

$$N_{k,s} = \frac{A}{s + B} + \frac{C}{s + D} \quad (2.43)$$

which gives a trivial expression after Laplace inversion:

$$N_{k,\tau} = A e^{-B\tau} + C e^{-D\tau} \quad (2.44)$$

then taking equation 2.43 and adding the fractions we get:

$$N_{k,s} = \frac{(A + C)s + (AD + BC)}{s^2 + (B + D)s + BD} \quad (2.45)$$

which when compared to equation 2.41 leads to 4 equations with 4 unknowns.

Laplace inversion leads to:

$$A = \frac{(1 - 2\eta_s)D^+k^2 - k_a(\eta_s + K) + \sqrt{(D^+)^2k^4 + 2D^+k^2k_a(\eta_s - K) + k_a^2(\eta_s + K)^2}}{2\sqrt{(D^+)^2k^4 + 2D^+k^2k_a(\eta_s - K) + k_a^2(\eta_s + K)^2}} \quad (2.46)$$

$$B = \frac{D^+k^2 + k_a(\eta_s + K) + \sqrt{(D^+)^2k^4 + 2D^+k^2k_a(\eta_s - K) + k_a^2(\eta_s + K)^2}}{2} \quad (2.47)$$

$$C = \frac{-(1 - 2\eta_s)D^+k^2 + k_a(\eta_s + K) + \sqrt{(D^+)^2k^4 + 2D^+k^2k_a(\eta_s - K) + k_a^2(\eta_s + K)^2}}{2\sqrt{(D^+)^2k^4 + 2D^+k^2k_a(\eta_s - K) + k_a^2(\eta_s + K)^2}} \quad (2.48)$$

$$D = \frac{D^+k^2 + k_a(\eta_s + K) - \sqrt{(D^+)^2k^4 + 2D^+k^2k_a(\eta_s - K) + k_a^2(\eta_s + K)^2}}{2} \quad (2.49)$$

The exponents of expression 2.44, B and D, have units of temporal frequency

$\frac{1}{\tau_k}$ , which identify the two modes by which the system decays in time. Interestingly, if one plugs B or D into equation 2.44, one finds that the exponent contains the familiar diffusion term  $D^+k^2\tau$  but also a term that is identified as the correction due to the 'reactive' part of the system,  $k_a(\eta_s + K) \pm \sqrt{(D^+)^2k^4 + 2D^+k^2k_a(\eta_s - K) + k_a^2(\eta_s + K)^2}$ . These terms contain the sum of the two reaction rates  $k_a\eta_s$  and  $k_aK$  and a correction due to the inter-conversion kinetics. The larger exponent, B, is greater than the characteristic rate in absence of microdomains,  $k^2D_{free}$ . As a result, the effective diffusion coefficient measured on large spatial scales (small k values) will be smaller than the diffusion coefficient in the absence of microdomains,  $D_{free}$ . What follows demonstrates how these

correlation functions emerge from the kICS treatment of a system where particles can chemically convert from one species to another.

## 2.4 kICS theory for a system of chemically inter-converting species

In the standard kICS treatment of two or more independently diffusing species, the correlation function is a linear combination of all independent contributions. In a system where two diffusing species can inter-convert, the cross-product terms in expression 2.52 will be non-negligible. In other words, the density of one population of particles will depend on the density of the other. An example would be a particle diffusing in a random two-phase medium, where density of the ‘free’ population depends on the density of the ‘trapped’ population.

We start the derivation by writing the intensity of images as in equation 2.15.

$$i(\vec{r}, t) = q_1 I(\vec{r}) * \rho_1(\vec{r}, t) + q_2 I(\vec{r}) * \rho_2(\vec{r}, t) \quad (2.50)$$

which on transforming to k-space and building on the same parameters gives an expression analogous to equation 2.20 :

$$\tilde{i}(\vec{k}, t) = \frac{I_0 \omega_0^2 \pi}{2} e^{-\frac{\omega_0^2 |\vec{k}|^2}{8}} \left\{ q_1 \sum_{i=1}^{N_1} \Theta_{i,1}(t) c_{i,1}(\vec{k}, t) + q_2 \sum_{j=1}^{N_2} \Theta_{j,2}(t) c_{j,2}(\vec{k}, t) \right\} \quad (2.51)$$

where  $c_{m,n}^{\sim}$  represent the  $m^{th}$  particle of the  $n^{th}$  population. Then the temporal correlation function in k-space becomes:

$$\begin{aligned} \Phi(\vec{k}; \tau, t) = & \frac{I_0 \omega_0^2 \pi}{2} e^{-\frac{\omega_0^2 |\vec{k}|^2}{8}} \langle \{ q_1 \sum_{i=1}^{N_1} \Theta_{i,1}(t) c_{i,1}^{\sim}(\vec{k}, t) + q_2 \sum_{j=1}^{N_2} \Theta_{j,2}(t) c_{j,2}^{\sim}(\vec{k}, t) \} \times \\ & \{ q_1 \sum_{i=1}^{N_1} \Theta_{i,1}(t + \tau) c_{i,1}^{\sim}(\vec{k}, t + \tau) + q_2 \sum_{j=1}^{N_2} \Theta_{j,2}(t + \tau) c_{j,2}^{\sim}(\vec{k}, t + \tau) \} \rangle \end{aligned} \quad (2.52)$$

which upon expansion leads to:

$$\begin{aligned} \Phi(\vec{k}; \tau, t) = & \frac{I_0 \omega_0^2 \pi}{2} e^{-\frac{\omega_0^2 |\vec{k}|^2}{8}} \{ q_1^2 \langle \Theta_{i,1}(t) \Theta_{i,1}(t + \tau) \rangle \langle \tilde{c}_1(\vec{k}, t) \tilde{c}_1(\vec{k}, t + \tau) \rangle \\ & + q_1 q_2 \langle \Theta_{i,1}(t) \Theta_{i,2}(t + \tau) \rangle \langle \tilde{c}_1(\vec{k}, t) \tilde{c}_2(\vec{k}, t + \tau) \rangle \\ & + q_2 q_1 \langle \Theta_{i,2}(t) \Theta_{i,1}(t + \tau) \rangle \langle \tilde{c}_2(\vec{k}, t) \tilde{c}_1(\vec{k}, t + \tau) \rangle \\ & + q_2^2 \langle \Theta_{i,2}(t) \Theta_{i,2}(t + \tau) \rangle \langle \tilde{c}_2(\vec{k}, t) \tilde{c}_2(\vec{k}, t + \tau) \rangle \} \end{aligned} \quad (2.53)$$

the first and the last terms of the above expression are simply the self-correlation contributions of each species. In the case of freely diffusing populations, these are the only two terms present as shown in equation 2.32. However, the second and third terms contain the inter-conversion factors between two populations densities. The  $\Theta(t)$  correlation terms in the above expression can be seen as the probabilities that a particle in state 1(2) at time  $t$  turns into state 2(1) at time  $t + \tau$ . The above expression can also be written as:

$$\Phi(\vec{k}; \tau, t) = \frac{I_0 \omega_0^2 \pi}{2} e^{-\frac{\omega_0^2 |\vec{k}|^2}{8}} \sum_{i,j=1}^2 \alpha_{i,j} F_{i,j}(\vec{k}, \tau) \quad (2.54)$$

where the  $\alpha$  parameters in this expression relate to  $\Theta$  temporal correlation functions and are analogous to the polarizabilities of molecules in a DLS experiment. The expression above has also an equivalent in the DLS formulation for chemical reaction [1].

Indeed, the simple chemical interconversion reaction described by  $A \xrightleftharpoons[k_b]{k_a} B$ , where  $k_a$  and  $k_b$  are the forward and the backward rate constants, can be represented by the following system of equations [1]:

$$\frac{\partial c_1}{\partial \tau} = D_1 \nabla^2 c_1 - k_a c_1 + k_b c_2 \quad (2.55)$$

and

$$\frac{\partial c_2}{\partial \tau} = D_2 \nabla^2 c_2 - k_b c_2 + k_a c_1 \quad (2.56)$$

which can be solved for the particle concentrations,  $c_1$  and  $c_2$ . In analogy to the trapping problem,  $c_1$  is comparable to the free particle concentration in medium (+),  $N_f$ , while  $c_2$  is like the concentration of bound particles  $N_b$ . The equilibrium constant  $K_{eq} \equiv \frac{k_a}{k_b} = \frac{c_2^0}{c_1^0}$  is defined in terms of equilibrium concentrations of A and B species. If we assume that the domains are large enough so that the diffusion coefficient within domains is significant and the term  $D^{-1} \nabla^2 N_b(\vec{r}, \tau)$  appears in equation 2.34, we can then see the correspondence between equations 2.33 and 2.55 and 2.34 and 2.56. Indeed, in the problem we are considering,  $K = \frac{N_f(\vec{r}^+, \tau)}{N_b(\vec{r}^-, \tau)}$  and comparing to the definition of the equilibrium constant, we deduce that the partition coefficient in trapping problem,  $K$ , is equivalent to the inverse of the equilibrium constant in the reaction system solved in [1],  $K \equiv \frac{1}{K_{eq}}$ . Moreover,

the absorption rate constant for the trapping problem,  $k_a\eta_s$  tells us the rate at which particles in medium (+) get absorbed into the domains (-). It has a similar meaning as the forward rate constant,  $k_a$ , which tells us at what rate the particles A convert to particles B. Also, the rate constant  $k_b$  for the inverse reaction matches the trapping problem product  $k_aK$  which the rate at which particles leave the bound state (microdomains). The general solution to 2.55 and 2.56 is of the form:

$$S(\vec{k}, \tau) = B_+e^{s_+\tau} + B_-e^{s_-\tau} \quad (2.57)$$

where  $S(\vec{k}, \tau)$  denotes the intermediate structure function and:

$$s_{\pm} = -\frac{1}{2}(\gamma_1 + \gamma_2) \pm \frac{1}{2}[(\gamma_1 - \gamma_2)^2 + 4k_a k_b]^{\frac{1}{2}} \quad (2.58)$$

denote the modes of relaxation of the system, while the coefficients  $B_{\pm}$  are:

$$B_{\pm} = \pm \frac{[\alpha_1^2 c_1^0 (s_{\pm} + \gamma_2) + \alpha_1 \alpha_2 (c_1^0 k_a + c_2^0 k_b) + \alpha_2^2 c_2^0 (s_{\pm} + \gamma_1)]}{(s_+ - s_-)} \quad (2.59)$$

where  $\gamma_{1,2} = D_{1,2}k^2 + k_{a,b}$ . Now, using the following correspondences between their system and our problem:  $c_1 \rightarrow N_f$ ,  $c_2 \rightarrow N_b$ ,  $k_a \rightarrow \eta_s k_a$ ,  $k_b \rightarrow k_a K$ ,  $D_1 \rightarrow D^+$ ,  $D_2 \rightarrow D^-$ ,  $c_1^0 = 1 - \eta_s$  and  $c_2^0 = \eta_s$ .

Consider the roots of the dispersion relation obtained:

$$s_{\pm} = -\frac{1}{2}(D^+k^2 + k_a(\eta_s + K)) \pm \frac{1}{2}[(D^+k^2 + k_a(\eta_s - K))^2 + 4k_a^2\eta_s K]^{\frac{1}{2}} \quad (2.60)$$

which after simplification becomes

$$s_{\pm} = -\frac{1}{2}(D^+k^2 + k_a(\eta_s + K)) \pm \frac{1}{2}[(D^+)^2k^4 + 2k_a(\eta_s - K)D^+k^2 + k_a^2(\eta_s + K)^2]^{\frac{1}{2}} \quad (2.61)$$

which are equivalent to equations 2.47 and 2.49. Similarly one can show that equations 2.59 reduce to equations 2.46 and 2.48 assuming  $\alpha_1 = \alpha_2 = 1$ . This leads us to anticipate the result if we include the diffusion coefficient within microdomains. Indeed, substitution of  $\gamma_2$  for  $D^-k^2 + k_aK$  in expressions 2.60 and 2.59 would lead to the solution which includes diffusion inside domains.

The expressions found for effective mobilities in either a heterogeneous two-phase medium or for the case of the chemical interconversion, suggest that there will be two effective mobilities emerging in such systems. If one considers the system where particles diffuse outside (inside) domains with diffusion coefficient  $D_{+(-)}$  and can partition into domains at a rate  $k_{bind}$  and out of domains at a rate  $k_{unbind}$ , then the kinetic model described above represents a good representation of this system. The rates,  $k_{unbind}$  and  $k_{bind}$ , will depend on several system parameters.

In the next chapter we will discuss how this system is simulated and explore the parameters influencing these rates. Equations 2.57 and 2.44 suggest that the kICS correlation function is composed of a sum of two Gaussians. The sum of two effective dynamic components was suggested in the spot-vary FCS adaptation in the study of isolated domains and stick-and-diffuse kinetics, but only as function of temporal lag and laser beam waist size [9]. In the present case, we should not expect the mobilities,  $s_{\pm}$ , to be simply equal to  $D_{free}\tau$  for two populations, as is the case for two freely diffusing independent species (equation 2.32). Instead we should expect to observe one faster decaying component,  $s_+$ , which will effectively represent the larger spatial scale motion that particles will undergo, as they

visit domains between two points in space separated with large distances. This component will be called 'Fast' as shown in figure 2-1. The other component,  $s_-$ , will effectively represent smaller spatial scale motions, where particles explore the region inside the domains. This component will be called 'Slow' as depicted in the figure 2-1. Both of these mobilities will be affected by all of the chemical reaction parameters,  $D_{1,2}$ ,  $k_{1,2}$ , which effectively emerge in the case of the two phase medium from the micro-structure defined by  $D_{\pm}$ ,  $k_a$ ,  $K$ ,  $\eta_s$ . The next chapter will outline the approaches used to simulate such system, compute and characterize the correlation functions by non-linear weighted fitting of a sum of Gaussians. Chapter 4 explores the characterization of heterogeneous systems through computer simulations and chapter 5 presents results from cellular imaging experiments with isolated membrane domains and heterogeneous dynamics for GPI-GFP in live COS-7 cells.

## 2.5 KICS theory for a meshwork confinement

As we have seen in chapter 1, the other type of confinement is membrane can be caused by the mesh of the membrane proximal actin cytoskeleton. In the case of meshwork like confinement, there is effectively a single probability value,  $P$ , for a particle to escape from a compartment and move to an adjacent compartment. All particles are assumed to move at same microscopic diffusion coefficient  $D$ , within a compartment of defined average mesh pore diameter,  $L$ . Depending on  $P, D$  and  $L$  values, which define the transport in system, the particles are observed to hop between compartments with a macroscopic diffusion coefficient,  $D_M$ , that is smaller

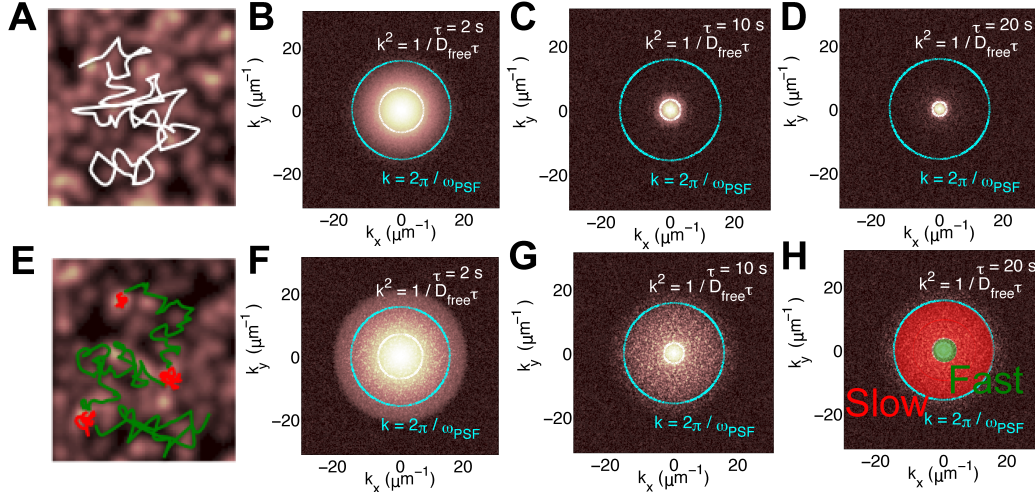


Figure 2-1: Emergence of two dynamic populations in the kICS correlation functions calculated from simulations with particles diffusing inside and outside domains on a 2D surface. Top row depicts simulated free diffusion ( $D=0.01 \frac{\mu\text{m}^2}{\text{s}}$ ,  $\omega_{PSF}=0.4 \mu\text{m}$ ,  $t_{frame}=1$  s) and bottom row depicts the simulation of diffusion on a 2D surface containing randomly distributed circular domains ( $r_{domain}=0.2 \mu\text{m}$ , domain area coverage 5 %,  $D_{in}$  and  $D_{out}$  set to 0.005 and  $0.01 \frac{\mu\text{m}^2}{\text{s}}$ , while  $P_{in}$  and  $P_{out}$  set at 0.5 and 0.1, respectively). a) and e) show schematics of sample particle trajectories superimposed on the series projection images from each simulation condition. The particle in e) visits, and is confined within small domains as is seen in red parts of the trajectory. b) and f) show the kICS correlation function for each condition at lag time  $\tau=2$  s. c) and g) show lag time  $\tau=10$  s, while d) and h) show lag time  $\tau=20$  s. The red and green areas superimposed on the correlation function in h) highlight the relevant k-vector regimes where the two dynamic populations are manifest. These are labeled Slow for particles diffusing and confined in domains (red in e and h) and Fast, for particles freely diffusing outside of domains (green in e and h).

than that of particles within a compartment. These properties differentiate the meshwork confinement from isolated domains, which is effectively a two phase system. As a result, the diffusion coefficient inside and outside domains can be different from the effective large spatial scale diffusion coefficient,  $D_{eff}$ . Also, the probabilities of particles to partition into and out of domains can vary.

Recently, several theoretical approaches were suggested to predict mesh size and microscopic diffusion coefficients on basis of either SPT or FCS experiments on meshwork like membrane confinements. In one case [10], it has been shown that for the FCS diffusion law, the time for the amplitude temporal auto-correlation function to be reduced by a factor of 2 is given by:

$$t_{\frac{1}{2}} \simeq \frac{1}{4D_M} \left( \omega^2 - \frac{L^2}{12} \right) \quad (2.62)$$

where  $D_M$  denotes the macroscopic (long range) diffusion coefficient,  $L$  is the mesh pore diameter and  $\omega$  is the  $e^{-2}$  beam waist radius. Other approaches [11, 12] quantify the SPT based data analysis. Here the authors calculated the two-time correlation of particle positions:

$$\begin{aligned} C(t) &= \langle \vec{r}(s+t)\vec{r}(s) \rangle - \langle \vec{r}(s+t) \rangle \langle \vec{r}(s) \rangle \\ &\cong \text{Const.} \exp\left(-\frac{t}{\tau}\right) \end{aligned} \quad (2.63)$$

which after expansion leads to:

$$C(t) \cong \frac{L^2}{6} \exp\left(-\frac{t}{\tau}\right) \quad (2.64)$$

with  $\tau = \frac{L^2}{12D_\mu}$  where  $D_\mu$  is the micro diffusion coefficient of the particles within the mesh pore.

These developments suggest that the correlation function should be described by a single Gaussian decay. In spot-varying FCS experiments, FCS diffusion law for meshwork gave a positive intercept which links to the diameter of the mesh pore ( $L$ ). The late temporal lags diffusion coefficient ( $D_M$ ) is an effective one that depends on the probabilities for particles to cross the meshwork barriers and on the micro diffusion coefficient ( $D_\mu$ ). With SPT one can deduce these properties from the mean square displacement (MSD) of particles [11].

In the current development, we will employ a similar approach, in which kICS correlation functions are fitted vs spatial frequency at a given temporal lag (the standard kICS approach) in order to extract the characteristic decay constant,  $D\tau$ . Plotting  $4D\tau$  vs temporal lag  $\tau$  yields the equivalent of an MSD plot 4–22 b). The plot exhibits an early and a late slope which can be fitted to give the micro and macro diffusion coefficients, respectively. The intercept on the y-axis (MSD) for the later linear regression of that curve, gives an apparent mesh size,  $L_{app}$ . The following expression links,  $D_{early}$ ,  $D_{late}$  and  $L_{app}$  to the actual mesh size:

$$L = \left(1 + \frac{D_{late}}{D_{early}}\right)L_{app} \quad (2.65)$$

The extracted  $D_{early}$  represents the micro diffusion coefficient within mesh pore,  $D_\mu$ , while the extracted late diffusion coefficient,  $D_{late}$  is linked to the macro diffusion coefficient of the particle hopping between compartments,  $D_M$ . The micro

diffusion coefficient is larger than the large scale hopping diffusion coefficient,  $D_\mu > D_M$ . Similarly, the late temporal lags diffusion coefficients reflects the opening motion of particles between mesh pores and is smaller than early temporal lag diffusion coefficient,  $D_{early} > D_{late}$ .

This is a phenomenological relation and should not be taken as an analytically derived expression. Indeed, if  $D_{late}$  equals  $D_{early}$ , then the above expression implies that the true mesh size is twice the value of the apparent. On the other hand, in the limit where  $D_{late}$  approaches  $D_{early}$ , the apparent mesh size,  $L_{app}$  would approach zero. As result, the recovered mesh size would also approach zero (i.e. there is no meshwork). The description of fitting procedures will be detailed in next chapter, while examples of simulated results for meshwork will appear in chapter 4.

## REFERENCES

- [1] Berne B.J. Pecora R. *Dynamic Light Scattering*. Dover Publications, inc., 1976.
- [2] Kolin D.L. *k-space Image Correlation Spectroscopy: theory, verification, and applications*. PhD thesis, McGill University, 2008.
- [3] Kolin D.L. Ronis D. Wiseman P.W. k-space image correlation spectroscopy: a method for accurate transport measurements independent of fluorophore photophysics. *Biophys. J.*, 91:3061–3075, 2006.
- [4] Torquato S. Kim I.C. Effective conductivity, dielectric constant, and diffusion coefficient of digitized composite media via first-passage-time equations. *Journal of Applied Physics*, 85:1560–1571, 1999.
- [5] Ernst M.H. Machta J. Dorfman J.R. Beijeren van H. Long time tails in stationary random media: I theory. *Jour. of Statistical Physics*, 34:477–495, 1984.
- [6] Bixon M. Zwanzig R. Diffusion in a medium with static traps. *J. Chem. Phys.*, 75:2354–2356, 1981.
- [7] Grassberger P. Proccaccia I. The long time properties of diffusion in a medium with static traps. *J. Chem. Phys.*, 77:6281–6284, 1982.
- [8] Ronis D. Diffusion in random two-phase media. *Phys. Rev. A*, 36:1908–1929, 1987.
- [9] Ruprecht V. Weiser S. Marguet D. Schutz G.J. Spot variation fluorescence spectroscopy allows for superresolution chronoscopy of confinements times in mebranes. *Biophys. J.*, 100:2839–2845, 2011.
- [10] Destainville N. Theory of fluorescence correlation spectroscopy at variable observation area for two-dimensional diffision on a meshgrid. *Soft Matter*, 4:1288–1301, 2008.

- [11] Destainville N. Salome L. Quantification and correction of systematic errors due to detector time-averaging in single molecule tracking experiments. *Biophys. Letters*, pages L01–L04, 2008.
- [12] Niehaus A.M. Vlachos D.G. Edwards J.S. Plechac P. Tribe R. Microscopic simulation of membrane diffusion on corrugated membrane surfaces. *Biophys. J.*, 94:1551–1564, 2008.

## CHAPTER 3

### Materials and Methods

#### 3.1 Computer simulations

##### 3.1.1 General considerations

The terms ‘domain’ and ‘raft’ are both used interchangeably in this thesis, to mean an isolated circular subregion within the heterogeneous composition relative to the bulk membrane. All simulations and data analysis were performed using Matlab (The Mathworks Inc., Natick, MA) and associated toolboxes, like Fitting and Image Processing. The analysis was performed on a laptop MacBook Pro (2.53 GHz, Dual core Intel, 4GB RAM) and on a personal desktop computer with similar specifications running on Linux Ubuntu platform. In this work, a 2D matrix representing the fluorescence microscope images are simulated containing  $N$  particles diffusing within 2D plane. The plane is composed of a uniform distribution of randomly placed circular domains, that mimic membrane heterogeneities. Images are formed by 2D convolution of 2D Gaussian filter, mimicking the PSF of a microscope, and are separated in time at a defined frame rate. It takes around 520 s to simulate 100 images of 256 by 256 pixels, including a population of 3277 particles. The time for simulation scales linearly with the number of particles and the number of images generated. It takes

around 10 s to calculate a correlation function from such an image stack, with the first 20 temporal lags. In the original implementation from the simulator from the Wiseman lab, particles were moving in a continuous 2D space, with set dynamics, and discrete pixel sampling. Since the previous simulator did not consider the possibility of a sub-pixel displacements, the particle positions were rounded to the nearest integer prior to image creation. A similar effect occurs if one considers the particles' diffusion in a multi-phase heterogeneous environment. These integer valued positions of the particles were subsequently convolved by a function 'convolve2' using a Gaussian filter, created using the function 'fspecial', to simulate particle emission profile blurred by a 2D Gaussian approximation of the PSF. Although this approach captured the main features of images collected on a fluorescence microscope, it is realistic only if the particles' displacements are integer valued, from one frame to the next. Since we are dealing with motion of particles in a heterogeneous environment, we need to allow for the flexibility of motion smaller than a pixel size during a time step. This was accomplished by a new implementation, where images are created by summing all the Gaussian functions placed at the exact coordinates of each particle at a given time. Mathematically, this gives a pixel intensity:

$$I(i, j, t) = I_0 \sum_{n=1}^N e^{-\frac{(i-x_n(t))^2}{\omega_x^2}} \cdot e^{-\frac{(j-y_n(t))^2}{\omega_y^2}} \quad (3.1)$$

where  $I_0$  is the intensity of the PSF at the origin (which can be set to 1),  $i$  and  $j$  denote integer value coordinates of the pixel, for  $N$  particles,  $x_n(t)$  and  $y_n(t)$  are the sub-pixel coordinates of particle  $n$  at time  $t$ . In this fashion, Gaussian

peaks are centred on the actual positions of particles, rather than their integer rounded values. The difference between the old and the new image simulations can be seen in figure 3–1. In the old version (Figure 3–1 a), where particles positions are rounded, the peak centre moves by a whole pixel from one frame to another. The red Gaussian spots show the previous frame and the green is the superimposed subsequent frame. Figure 3–1 b) shows that the new convolution registers properly a sub-pixel motion as witnessed by a quasi imperceptible change of PSF position from one frame to another.

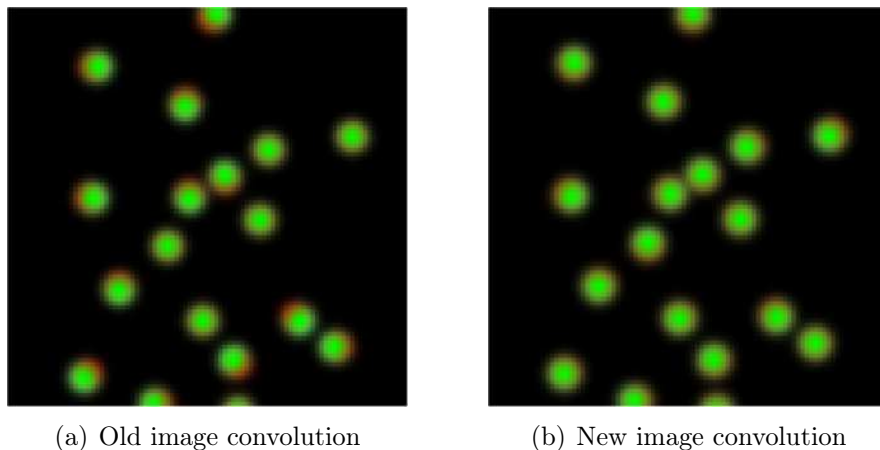


Figure 3–1: Old vs new image convolution methods. Red spots label earlier frame while green are for the superimposed subsequent frame. a) Old style image convolution. b) New simulation image creation result. The particles motion was set to be sub pixel size.

### 3.1.2 Isolated domains simulations

Simulation of isolated domains was also performed previously in the Wiseman group [1], although the new implementation has significant improvements. In the old version of the simulator, isolated domains were implemented through a ‘raftMask’, which involved creating a binary mask of the same size as the final image, which had a value of ‘1’ where the domain phase was present and zeros elsewhere. This mask was used throughout the simulation as a guide for the delimitation between raft and non-raft phases. Effectively, particles would partition into a domain phase if the probability of going in,  $P_{in}$ , was favourable. Similarly, it would leave the domain phase if the probability of exiting,  $P_{out}$ , was favourable. That implementation works if the domain radius is a few pixels in size. Then the domain will appear in the mask as a circular object, even if its boundaries are slightly pixelated. On the other hand, when the domain radius is on the order of a pixel or less, the old implementation of raftMask will force the minimum achievable radius, which in this case is a single pixel. Therefore, this mask will fail to create domains of the real sub-pixel size. The new implementation does not use a binary mask for rafts. It rather simulates a continuous case for domains, where their centers have a real value  $(x_{raft}, y_{raft})$ , which falls within the boundary of the image and they have a radius of a positive real value. Figure 3–2 demonstrates the difference between the old and the new implementations for isolated domain simulation. Figure 3–2 a) displays rafts as cross-shaped objects, because their radius ( $0.2 \mu\text{m}$ ) is close to the pixel size ( $0.1 \mu\text{m}$ ) Therefore, particles forceably explore that shape of domain. In figure 3–2 b) with the new simulation

the rafts are continuous with a radius of  $0.2 \mu\text{m}$ , so particles explore a more continuous circular raft shape.

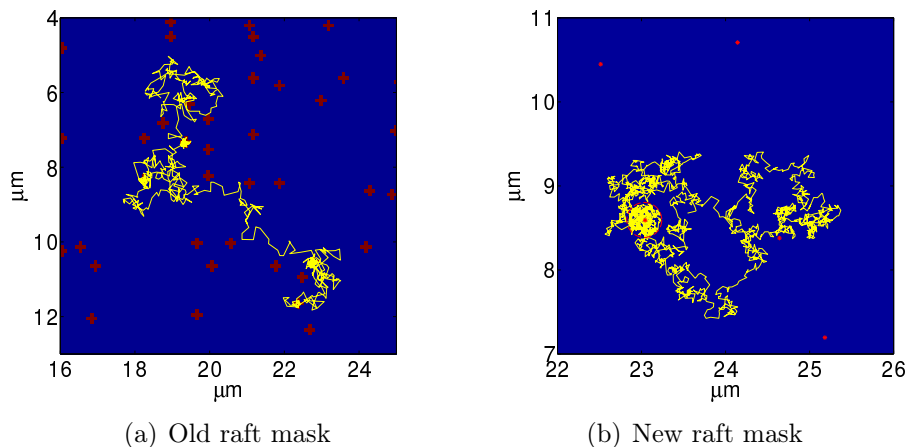


Figure 3–2: Old vs new ways of simulating rafts. In both images the yellow trace represents a particle trajectory. a) Rafts are  $0.2 \mu\text{m}$  in radius and ‘raftMask’ is composed of cross shaped domains. The pixel size is  $0.1 \mu\text{m}$ . b) Raft centres are labelled with an asterisk and their radii are  $0.2 \mu\text{m}$ . The red dashed line was added to show the boundary of one of the rafts.

The simulation of Brownian particle motion in 2D environments in the presence of circular domains proceeded as follows: Domains were stationary, of uniform finite size and randomly placed uniformly in a region defined by the boundary of an image. The centres were selected to be at least 2 times the radius apart, to avoid potential overlaps. The domain density per  $\mu\text{m}^2$  was adjusted to preserve the domain phase area coverage (fixed to 5 % unless stated otherwise) in order to account for a change of radii from one simulation to another. Initially, particles were distributed randomly uniformly within the image frame. Particles

were set to move with different diffusion coefficients inside ( $D_{in}$ ) and outside ( $D_{out}$ ) of domains. When encountering a domain boundary from the inside, a random number from 0 to 1 was generated and compared to the probability for a particle to leave the domain,  $P_{out}$ , set from 0 to 1. If the random number was greater than  $P_{out}$ , the particle would escape the domain. Otherwise, it would remain within the domain. Similarly, if encountering a domain boundary from the outside, a probability to partition into domains,  $P_{in}$ , was compared to a randomly generated number and an entry decision was made. When the particle leaves the boundary of the image, it was set to reappear on the opposite side through the implementation of a periodic boundary. This was implemented to conserve the number of particles within any simulation. Experimentally, for measurement on a cell sub regions, a periodic boundary condition does not hold, which prompted simulations of a larger area (typically 300 by 300 pixels) and then the central portion (256 by 256 pixels) was cropped and analyzed. The pixel size was set to  $0.1 \mu m$  to mimic typical pixel size of TIRF microscopy images. The diffusion coefficient within and outside of rafts typically take values of 1 and  $3 \frac{\mu m^2}{s}$  in previous simulation studies [2], although this choice of parameters was not desirable for simulation of very small rafts. Indeed, when simulating small rafts, it is not desirable for a particle to move with a step size of more than 0.2 times raft radius. This potentially creates unrealistic dynamics, where a particle encounters the boundary too frequently. Also, with a greater step size, a particle outside will less frequently encounter the small rafts. For example, for rafts of a  $0.1 \mu m$  radius, the step size would have to be  $0.02 \mu m$  or less. With  $D_{in} = 1 \frac{\mu m^2}{s}$ , this requires a frame time

on the order of 0.1 ms, which exceeds the time resolution of most commercial microscope CCD cameras. Therefore,  $D_{in}$  and  $D_{out}$  were chosen to be 0.001 and  $0.01 \frac{\mu m^2}{s}$  respectively, unless otherwise stated. The frame time was then adapted to accommodate the size of domains as follows:

$$\text{frame time} = \frac{\left(\frac{\text{raft radius}}{5}\right)^2}{4D_{in}} \quad (3.2)$$

For the raft sizes and the diffusion coefficients inside the domains considered in these simulations, frame time varied from 40 ms to few s. which matches the time frame achievable on CCD cameras used in standard TIRF microscopy. The number of simulated frames was set to 2200, and an adjustment of the frame time allowed for sampling of a reasonable number of fluctuations inside and outside the domains. The first 200 frames of the image series were not included in the calculation of the correlation function, in order to allow the particles to reach partitioning equilibrium, for the confinement scenarios considered. Images were created by a convolution of a 2D Gaussian with particles positions at each time frame, as described above. This mimics the integration of fluorescence emission by CCD-type detectors in TIRF microscopy. The PSF was approximated by a 2D Gaussian with lateral  $e-1$  radii  $\omega_x$  and  $\omega_y$  in x and y dimensions, respectively. These radii are usually approximately equal, and they represent, in the new convolution mode (see above), the radius of the PSF at  $e^{-1}$  of the peak value. The older implementation of convolution defined the ‘PSF size’ as the radius at  $e^{-2}$  of the peak value instead. Particle density was set to 5 particles per  $\mu m^2$ . Photo-physics effects (photo-bleaching and blinking) of fluorophores were not simulated

for the particles as these should not interfere with the dynamics of particles on the time scales considered. They were characterized thoroughly in [3]. The quantum yield of the particles was set to 1. There was no particle flow in any of the simulations. Background noise was implemented and varied as described below. The table 3–1 summarizes the set of parameters used in computer simulations.

Table 3–1: Adjustable parameters for isolated domains simulations

| Parameter name                            | Default values                         | Variation range                                |
|---|--|--|
| Image Series Properties                   |  |  |
| Number of pixels in x dimension           | 300 cropped to 256                     | NA   |
| Number of pixels in y dimension           | 300 cropped to 256                     | NA   |
| Number of frames                          | 2200 used last 2000                    | NA   |
| Pixel size                                | 0.1 $\mu\text{m}$                      | NA   |
| Time between frames                       | 1 s                                    | $\frac{(\text{raft radius})^2}{4D_{in}}$       |
| Imaging mechanism                         | CCD-type integration                   | NA   |
| PSF type                                  | 2D Gaussian                            | NA   |
| PSF $e^{-1}$ x, y radius                  | 0.4 $\mu\text{m}$                      | NA   |
| PSF $e^{-1}$ z radius                     | 0 (i.e. 2D simulations)                | NA   |
| Particle properties                       |  |  |
| Particle density                          | 5 per $\mu\text{m}^2$                  | NA   |
| Particle distribution (initially)         | uniformly random                       | NA   |
| Photophysics considered                   | NA                                     | NA   |
| Quantum yield                             | 1                                      | NA   |
| $D_{in}$                                  | 0.001 $\frac{\mu\text{m}^2}{\text{s}}$ | 0.001 to 0.01 $\frac{\mu\text{m}^2}{\text{s}}$ |
| $D_{out}$                                 | 0.01 $\frac{\mu\text{m}^2}{\text{s}}$  | NA   |
| Noise                                     |  |  |
| Background Noise (inverse $\frac{S}{B}$ ) | 0                                      | 0.01 to 0.2                                    |
| Domain properties                         |  |  |
| $P_{in}$                                  | 0.5                                    | 0.1 to 0.9                                     |
| $P_{out}$                                 | 0.1                                    | 0.1 to 0.9                                     |
| raft radius                               | 0.2 $\mu\text{m}$                      | 0.05 to 0.5 $\mu\text{m}$                      |
| raft area fraction (% total area )        | 5 %                                    | 0.5 to 5 %                                     |
| raft distribution                         | uniformly random                       | NA   |
| raft motion mode                          | none                                   | NA   |

### 3.1.3 Meshwork simulations

To simulate a meshwork like confinement, a network of parallel horizontal and vertical lines were simulated to create an effective mesh. The spacing between lines defined the square mesh pore diameter. Each line acted as a barrier for a particle in motion. For a time step, each particle's subsequent potential position was evaluated. If the next position implied crossing the barrier, then a random number was generated and compared to a pre-set probability of crossing the barrier to determine if the particle crosses or not. Only one particle diffusion coefficient is set for meshwork simulations for motion within compartments. Figure 3–3 shows two examples of a small (250 nm) and a large (2  $\mu\text{m}$ ) meshwork compartment size.

Many of the same simulation settings as for the domains were used for the meshwork runs. Particles were randomly seeded initially and convolution was done in the same way as for the isolated domains simulations. Since, each particle has to be checked for all boundaries making up the meshwork, the simulations were slower than for isolated domains. The direction of approach to a line for each particle needs to be checked, increasing the number of calculations. For that reason, an effective image area of 9 by 9  $\mu\text{m}$  was simulated, making up smaller images, when 0.1  $\mu\text{m}$  pixels were considered. The table 3–2 summarizes parameters varied for the meshwork simulations.

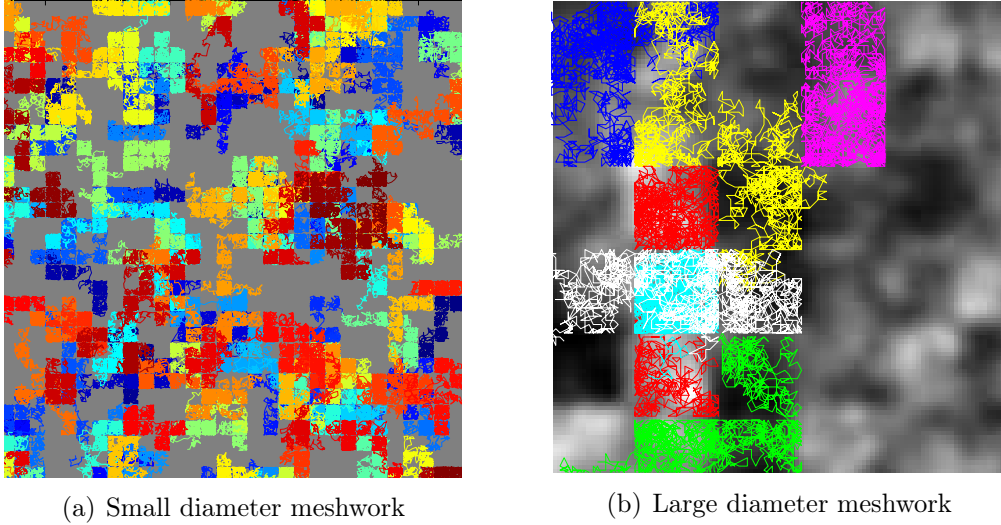


Figure 3–3: Examples of simulated meshworks. a) 200 particles trajectories (different colour for different particles) exploring a 250 nm sized mesh. There are 36 by 36 mesh lines, making up a meshwork of 9 by 9  $\mu\text{m}$ . b) Large meshwork of a 2  $\mu\text{m}$  diameter mesh, making an effective 12 by 12  $\mu\text{m}$  area. Only a few particle trajectories were superposed on top of the average image of the series produced.

### 3.1.4 Background noise implementation

Background noise was added to images in order to assess its effect on the quality of the data analysis and qualitative effect on kICS correlation function. A detailed analysis of noise effects on kICS can be found in the following manuscript [3]. Background noise comes from the sample itself, such as from cell medium or auto-fluorescence in the cell. We will simulate it as a normally distributed matrix of random values, with zero mean and pre-set standard deviation. Indeed, upon the addition of noise the image matrix with elements (pixels)  $r_{ij}$ ,

Table 3-2: Adjustable parameters for meshwork simulations

| Parameter name                            | Default values                       | Variation range                      |
|---|--------------------------------------|--------------------------------------|
| Image Series Properties                   |                                      |                                      |
| Number of pixels in x dimension           | 90                                   | NA                                   |
| Number of pixels in y dimension           | 90                                   | NA                                   |
| Number of frames                          | 1200 used last 1000                  | NA                                   |
| Pixel size                                | 0.1 $\mu\text{m}$                    | NA                                   |
| Time between frames                       | 0.01 s                               | NA                                   |
| Imaging mechanism                         | CCD-type integration                 | NA                                   |
| PSF type                                  | 2D Gaussian                          | NA                                   |
| PSF $e^{-1}$ x, y radius                  | 0.4 $\mu\text{m}$                    | NA                                   |
| PSF $e^{-1}$ z radius                     | 0 (i.e. 2D simulations)              | NA                                   |
| Particle properties                       |                                      |                                      |
| Particle density                          | 2 per compartment (initially)        | NA                                   |
| Particle distribution (initially)         | uniformly random                     | NA                                   |
| Photophysics considered                   | NA                                   | NA                                   |
| Quantum yield                             | 1                                    | NA                                   |
| D   | 0.1 $\frac{\mu\text{m}^2}{\text{s}}$ | NA                                   |
| Noise                                     |                                      |                                      |
| Background Noise (inverse $\frac{S}{B}$ ) | 0                                    | 0.01 to 0.2                          |
| Meshwork properties                       |                                      |                                      |
| P   | NA                                   | 0.001 to 0.4                         |
| mesh size                                 | NA                                   | 0.2 to 0.45 $\mu\text{m}$            |
| number of mesh                            | NA                                   | scaled to area of 81 $\mu\text{m}^2$ |
| mesh deformation mode                     | none                                 | NA                                   |

becomes a noisy signal image  $s_{ij}$ :

$$s_{ij} = r_{ij} + n_{ij} \quad (3.3)$$

where  $n_{ij}$  are the noise matrix elements. Since, the noise matrix is normally distributed around zero, then  $n_{ij}$  is set to  $\sigma u_{ij}$  where sigma is the standard deviation of the noise level and  $u_{ij}$  are the elements of the noise distribution. Hence  $\sigma$  is an

actual parameter representing the standard deviation of the background noise. The signal-to-background ratio is defined as:

$$\frac{S}{B} = \frac{\text{mean}(\text{signal})}{\sigma} \quad (3.4)$$

## 3.2 Data analysis

### 3.2.1 Data windowing

The need for image windowing prior to the kICS analysis was previously described [3]. The rationale for the windowing of images comes from the fact that the discrete Fourier transform of an image is sensitive to the sharp discontinuities at the image edges, producing non-existent high frequency components that mix with lower spatial frequencies. Mathematically, an image can be represented as a product of an infinite 2D plane with a square window function:

$$i(x, y) = i_{inf}(x, y) \cdot w(x, y) \quad (3.5)$$

when Fourier transformed, this product becomes a convolution of the two functions:

$$\tilde{i}(\vec{k}_x, \vec{k}_y) = \tilde{i}_{inf}(\vec{k}_x, \vec{k}_y) * \tilde{w}(\vec{k}_x, \vec{k}_y) \quad (3.6)$$

Therefore, high frequency components arising from the image edges discontinuities mix with the spectrum of the image at all frequencies. The standard procedure to attenuate such spectral leakage in signal processing, is through a multiplication of

the data by a window function that is equal to 1 at the centre of the signal and decays to zero toward the edges. We will use the Hann window as it attenuates optimally the spectral leakage in the low spatial frequencies, which we are mostly interested in. The 2D version of the Hann window is made using the existing Matlab function ‘hann’ for 1D signals. Indeed, by replicating a 1D window over all rows of the image and by multiplying in an element-wise fashion its  $90^0$  rotated version, we get the 2D Hann window. The image is multiplied, element-wise, with the window function before the application of the fast Fourier transform algorithm. Figure 3–4 shows an example of an image before and after windowing and the 2D Hann window function itself.

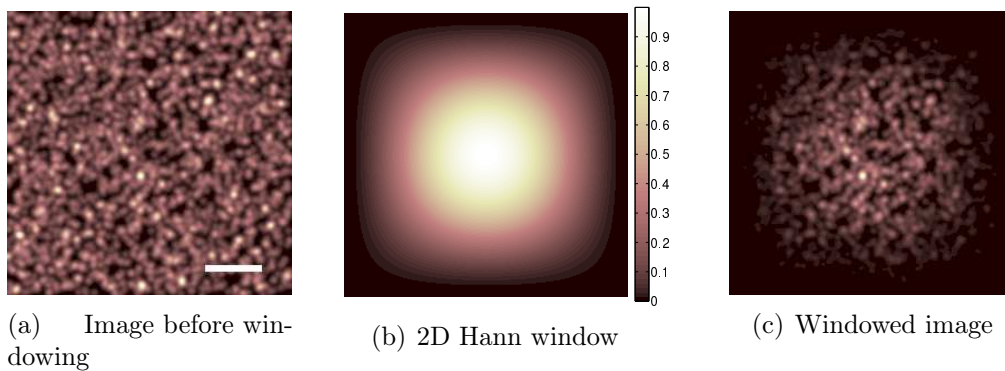


Figure 3–4: Hann windowing is applied to each image prior to the Fourier transform. a) Image prior to windowing. b) 256 by 256 Hann window. c) Image after windowing. Scalebar is  $5 \mu\text{m}$

### 3.2.2 kICS function computation, normalization and averaging

Details of kICS correlation function computations, normalization and averaging can be found in [3, 4]. The basic idea behind rapid computation of any correlation functions is the Wiener-Khinchin theorem. It states that the power spectral density,  $S_{xx}(f)$ , of a stationary random process,  $x(t)$ , is the Fourier transform of the corresponding autocorrelation function,  $r_{xx}(\tau)$ . It writes as:

$$r_{xx}(\tau) = \int_{-\infty}^{\infty} S_{xx}(f) e^{2\pi\tau f} df \quad (3.7)$$

where  $r_{xx}(\tau) = \langle x(t)x^*(t - \tau) \rangle$  is the auto-correlation of the signal  $x(t)$ . This implies that if we want to correlate two images, the fastest way to do so is by calculating the 2D fast Fourier transform of the images and then computing their cross-power spectrum, followed by computation of the inverse transform. Practically, windowed images, as described in the previous section, are fast Fourier transformed (by ‘fft2’ function in Matlab). Then pairs of transformed images,  $\tilde{i}(k_x, k_y, t)$ , separated by temporal lag  $\tau$ , are correlated and averaged producing a non-normalized temporal correlation function:

$$G(k_x, k_y, \tau) = \langle \tilde{i}(k_x, k_y, t) \tilde{i}^*(k_x, k_y, t + \tau) \rangle_{\tau} \quad (3.8)$$

This temporal correlation function forms the basis for STICS, which is then Fourier inversed and normalized by the product of the average intensity of the images in real space. In kICS, all analysis is performed in Fourier space instead, and the normalization is with the zero temporal lag ( $G(k_x, k_y, 0)$ ) of the above

expression, eliminates stationary contributions, such as the PSF. The resulting normalized correlation function is azimuthally (circularly) spatially averaged, as the system is considered isotropic. This effectively results in the minimum number of fitting parameters, as we get a 1D correlation function instead of 2D. It also reinforces the correlations present at all angles, while averaging out noisier contributions. Figure 1–18 from chapter 1, gave an overview of the operations described. We will refer to the normalized and circularly averaged correlation function as  $r(k^2, \tau)$ :

$$r(k^2, \tau) = \left\langle \frac{G(k_x, k_y, \tau)}{G(k_x, k_y, 0)} \right\rangle_t \quad (3.9)$$

### 3.2.3 Nonlinear fitting of the correlation functions

In order to extract characteristic widths and amplitudes from a correlation function, the nonlinear fitting algorithm was employed. In its original adaptation, kICS used a linear fitting of the logarithm of the correlation function [4]. This was useful only if a single dynamic species existed in the sample, since in this case the logarithm of the correlation function yielded a linear relation vs the spatial frequency squared ( $k^2$ ) for a single time lag. For multicomponent dynamical systems, the correlation function’s overall shape is fit by a sum of two or more Gaussians. The tool employed for this task was the Matlab function ‘fit’ from the Curvefit toolbox. This function is rather flexible so that the user can choose between linear and non-linear fitting schemes, methodologies, weights, bounds on parameters, and many other useful features. For our purposes, non linear least squares fitting was used. Three algorithms were tested, traditional ‘Gauss-Newton’, ‘Levenberg-Marquardt’ and the more recent and flexible ‘Trust-Region’

procedure. The best results were obtained using the Trust-Region approach, as it offered the user the possibility to define lower and upper bounds on parameters. In turn, this keeps the final solution within defined boundaries, instead of letting it diverge to some local minimum in the parameter space. The bounds were set on the basis that amplitudes of normalized correlation functions can not be less than 0 or greater than 1. Similarly, the decay rates (widths) lower bound was set to 0 and their upper bounds were set at infinity. Another advantage of the ‘fit’ function is the option ‘Robust’, which makes sure that outliers in the data set are not taken into account (or are given less weight) during the fit. In our fitting we use the least absolute residuals method for robust fitting, which ensures that the absolute difference of the residuals is minimized. Initial values for the fit relied on a logic that in the case of two dynamic components, one of them will have a larger amplitude than the other, but the sum of amplitudes is equal to one. Similarly, the widths were set initially so that one component is an order of magnitude higher than the other. The initial guess of one of the two component’s diffusion coefficient was an arbitrary task. It was estimated by forcing a linear fit through the logarithm of the correlation function, as done in kICS [4]. This yielded an average diffusion coefficient, that was used as the initial parameter in the non-linear fitting procedure.

The ultimate goal is to characterize, through fitting, the circularly averaged and normalized correlation function,  $r(k^2, \tau)$ . Figure 3–5 displays an example of  $r(k^2, \tau)$  for an isolated domains simulation where domain size was set to  $0.25 \mu\text{m}$  and mobilities were  $D_{in} = 0.001$  and  $D_{out} = 0.01 \frac{\mu\text{m}^2}{\text{s}}$ . For intermediate spatial

frequencies and intermediate times, single Gaussian fit does not characterize the whole range of  $k^2$  values. We notice that there is an initial decay at small spatial frequencies (small  $k$ ), which represents large spatial scales. This component is referred to as a ‘fast’ component, since it decays faster, reflecting faster motion at large spatial scales, which is usually due to particles’ motion outside the domains. It can be seen as a measure of the effective particle mobility through a heterogeneous medium. If there were no domains, that value would simply be the diffusion coefficient of free (Brownian) particles. Also, there is a late, larger spatial frequencies component, that reflects motion (or arrest of motion) at small spatial scales. We refer to this component as ‘slow’, since it represents effective mobility around and inside the rafts. In order to characterize these complex correlation functions, a multi-component non-linear least square fit is applied. The shape of

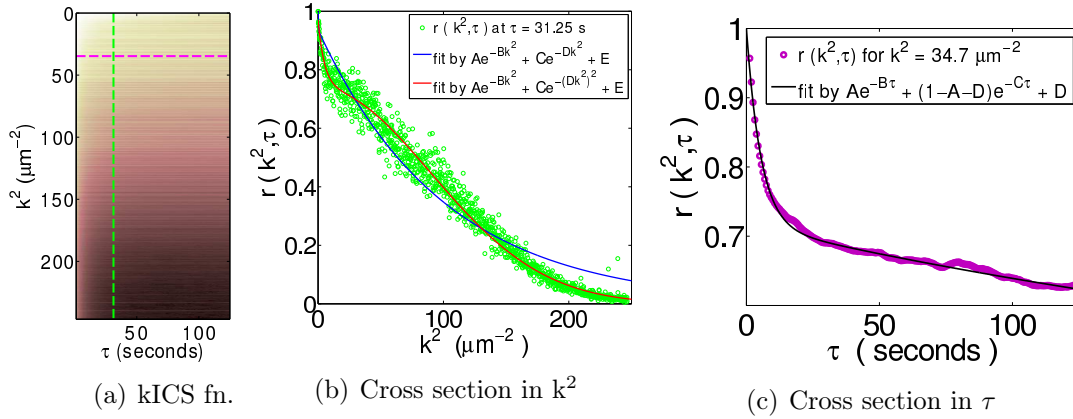


Figure 3-5: Non-linear least squares fitting k-space correlation function resulting from a heterogeneous environment. a) 2D magnitude plot of  $r(k^2, \tau)$  calculated from simulated images. b) Plot of green dashed line from a) with two possible implementations of 2 Gaussian fit. c) Plot of magenta dashed line from image on a) with its 2 Gaussian fit.

the curves at a given time (Figure 3–5 b) or a given spatial frequency (Figure 3–5 c), suggests that a sum of two Gaussians is a good approximation, as expected from the Theory, which can be used to characterize both spatial and temporal fits. The fitting equation has the form:

$$r(k^2, \tau) = Ae^{-Bk^2\tau} + Ce^{-Dk^2\tau} + E \quad (3.10)$$

where the offset parameter E, usually goes to zero in the  $k^2$  fit while it is a nonzero value in the  $\tau$  fit. We shall refer to these fits as ‘2G- $\tau$ -fit’ and ‘2G-k-fit’, respectively. It is not clear why the 2G-k-fit does not work well with a simple sum of Gaussians, but rather fits better the sum of a Gaussian and a ‘quadratic exponent’ Gaussian as shown with the red line in figure 3–5. The simplest explanation would be that the domains, have a size comparable to or smaller than the PSF set in simulations. Therefore, the zero temporal lag normalization, as described earlier, could possibly skew the shape of the second (slow) decay. Indeed, the PSF normalization factor  $e^{-\frac{k^2\omega^2}{4}}$  decays faster than the smaller raft size  $e^{-k^2a^2}$  factor, where the PSF radius,  $\omega$  is greater or equal to the raft size  $a$ . Consequently, if the highest frequencies of  $r(k^2, \tau)$  are truncated from the fit, the modified  $r(k^2, \tau)$  is better fitted by an exact sum of two Gaussians than without truncation, but that does not capture the whole range of the  $r(k^2, \tau)$  decay. The 2G- $\tau$ -fit seems more appealing for characterization of  $r(k^2, \tau)$  as it appears to be an exact sum of Gaussians. On the other hand, having a small number of temporal lags ( 200 time lags for image series of 2000 frames) makes it less appealing compared to the 2G-k-fit which is done over  $\sim 1200$   $k^2$  values.

Therefore, we will adopt the 2G-k-fit for the characterization of correlation functions for the remainder of this thesis.

Another approach for the characterization of the  $r(k^2, \tau)$  is by fitting a single Gaussian in either space or time. Figure 1–21 in chapter 1 shows an example of how forcing a single Gaussian fit in time, at a given spatial frequency, gives a first order characterization of  $r(k^2, \tau)$ . This fit formed the basis of the extraction of the FCS diffusion law in spot vary FCS experiments, even though their temporal ACF did not exhibit a single freely diffusing species decay. The fit we apply here is:

$$r(k^2, \tau)_{\tau_{max}=50 \text{ frames}} = Ae^{-B\tau} + C \quad (3.11)$$

where B is the characteristic decay at a given spatial frequency, which we define as  $B = k_{char}^2 D$ . This is used to extract mobilities at every spatial frequency. In the case of Meshwork, a single Gaussian fit vs  $k^2$  was sufficient to characterize the correlation function and produces the equivalent of an MSD plot. The fitted function was:

$$r(k^2, \tau)_{\text{mesh}} = Ae^{-Bk^2} + C \quad (3.12)$$

In this case,  $B = D\tau$  and if multiplied by 4 gives the equivalent of the MSD. Therefore, plotting each B vs  $\tau$  can be used to recover meshwork system parameters in a similar way as for MSD vs time analysis of SPT data.

The quality of fits was assessed for each scenario by  $\chi^2$  and reduced  $\chi^2$  statistics. The Matlab function ‘fit’ outputs the goodness-of-fit statistics as well as the 95 % confidence intervals for the fitted parameters. The error bars used for

each  $D\tau$  or other fitted parameters represent 95 % confidence intervals from the non-linear fit.

### 3.2.4 Extraction of domain size and particle mobilities

In order to extract characteristic system parameters such as domain and mesh size and particles mobilities, from  $D\tau$  vs  $\tau$  plots, we employ the function ‘fit’ again. This time we use it to do a weighted linear least square fit. The weights used in this fit is the inverse of the square of the error bars (defined by the 95 % confidence intervals) of each  $D\tau$  point obtained in the previously described fits. Basically, the following parameter is minimized:

$$s = \sum_{i=1}^n \frac{(D\tau_{exp}^i - D\tau_{fit}^i)^2}{\sigma_{D\tau}^2} \quad (3.13)$$

where  $\sigma_{D\tau}$  represents the 95% confidence interval on  $D\tau_{exp}^i$  recovered from the 2G-k-fit as explained above. Therefore, if the parameter  $D\tau_{exp}^i$ , extracted at a given  $\tau$ , has a high uncertainty (i.e. larger than  $\sigma_{D\tau}$ ), then the weighted least squares fit will give less weight to that value in the fit.

In order to extract the domain size, the ‘slow’ component decay constant  $D\tau_{slow}$  was plotted vs temporal lag variable  $\tau$  and the saturation point of the curve gives the value that is proportional to the radius of the domain squared. The saturation point is extracted by fitting the weighted linear regression, through the later temporal lags (typically the second half of the temporal lags). Figure 3–6 a) shows an example of a domain size extraction by weighted linear least squares fit for an isolated domains simulation with  $P_{in}/P_{out} = 5$ ,  $D_{out}/D_{in} = 10$ , 5 % raft area

fraction and  $0.2 \mu\text{m}$  radius of domains. The linear fit was done for  $\tau = 50$  to  $80$  s. The y-axis intercept was  $0.0100 \pm 0.0001$  which is within the expected  $\frac{\text{raft size}^2}{4}$ .

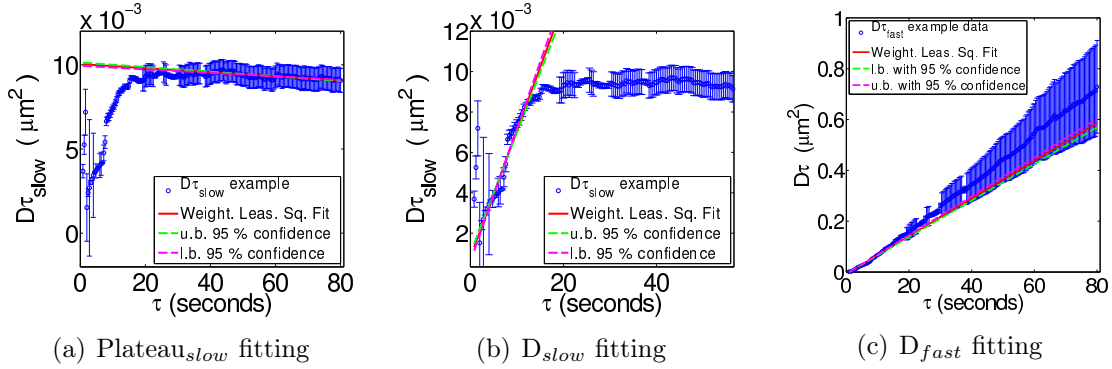


Figure 3–6: Example of data processing to extract domain size and particle mobilities. a) The blue symbols are ‘slow’ component mobilities  $D\tau$  with 95% confidence intervals. Red line shows weighted least square linear fit and dashed green and magenta lines show 95 % confidence intervals on fitted line. b) Same description as for left example, but for early slope of ‘slow’ component. c) Same descriptions but for slope of ‘fast’ component.

Similarly, the slope of the slow component is extracted by applying the weighted linear least square fit to the first 10-30 temporal lags. Figure 3–6 b) gives an example of such a fit recovering a diffusion coefficient of  $0.00063 \pm 0.00003 \mu\text{m}^2/\text{s}$ , which is slightly lower than the set diffusion coefficient inside the rafts. This difference will be discussed extensively in the following chapters. Finally, the fast component slope is recovered in a similar fashion (figure 3–6 c), reflecting the effective diffusion coefficient of particles at large spatial scales. In this example it gave a slope of  $0.0074 \pm 0.0002$  which is lower than the set diffusion coefficient

outside domains which was  $0.01 \frac{\mu\text{m}^2}{\text{s}}$ , as expected for a system with isolated domains.

The outlined weighted linear least square approach ensures that points with better confidence interval in the ‘ $D\tau$ ’ graphs have the highest impact on fitting. Also, a ‘Robust’ option of the fitting function ensures that outliers, that possibly resulted in the previous fitting step, do not contribute in the weighted least squares fit. Figure 3–7 gives a summary of the analysis and fitting steps presented above, starting from the input image time series data to the calculation and fitting of normalized correlation functions, to the retrieval of characteristic transport and confinement parameters of the two dynamic particle populations sampled in the image series.

### 3.3 Cell culture, protein labelling and enzyme treatments

All experiments were conducted with *COS-7* cells, a kidney fibroblast-like cell line derived from the *African green monkey* [5]. This cell line was used extensively in previous cellular studies of lipid rafts, especially GPI partitioning into rafts [6, 2, 7, 8, 9]. It was cultured and passaged in medium according to standard procedures prescribed for this cell line [5]. Briefly, cells were grown in glucose (0.45 % w/v), sodium-pyruvate (0.15 % w/v) and l-glutamine (4 mM) enriched Dulbecco Modified Eagle Medium (DMEM) , supplemented by 10 % fetal bovine serum (FBS) . Confluent cells were passaged (diluted) approximately every 3 days. Five days before imaging, cells were passaged into glass bottom (glass N<sup>0</sup>.1.5 of thickness 0.16-0.19 mm) MatTek (MatTek Corporation) dishes.

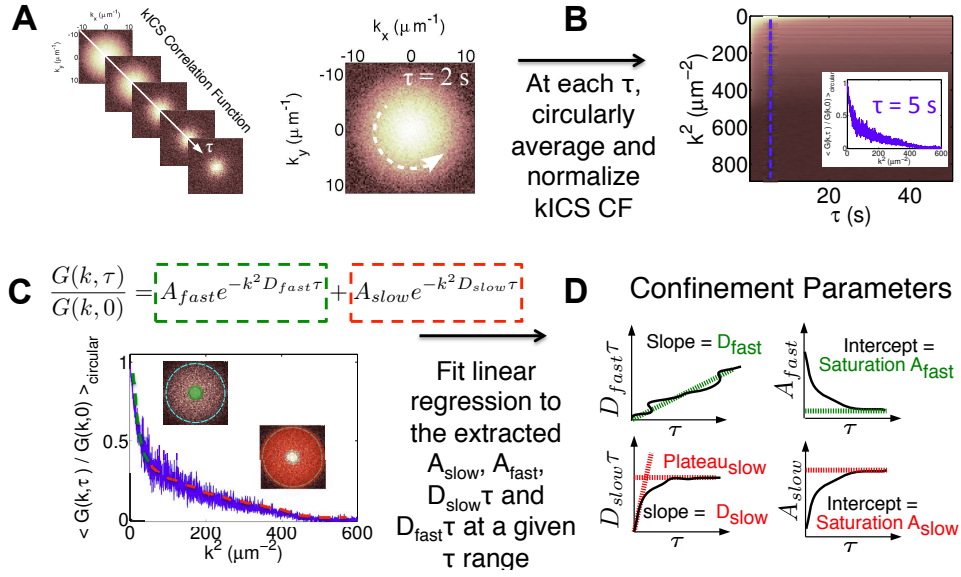


Figure 3–7: Schematic overview of the correlation function analysis, fitting and confinement parameter output calculated from image time series inputs. A) A kICS correlation function (CF) is calculated from an input image time series acquired by standard TIRF or confocal fluorescence microscopy or via computer simulation. b) The kICS CF is normalized according to eqn. 2.30. and circularly averaged for each time lag  $\tau$ . The dashed blue line and inset plot shows the CF at  $\tau=5$  s. C) Each CF obtained is fitted vs  $k^2$ , for every temporal lag  $\tau$ , with a sum of Gaussians to account for a fast (green) and slow (red) dynamical components emerging due to domain structure in a heterogeneous membrane (as derived in eqns. 2.44 and 2.57). D) The amplitudes and exponents are functions of temporal lag and are characterized by linear fitting over different temporal lag regimes, in order to extract characteristic confinement parameters.

The passaging procedure, involves washing cells twice in phosphate buffer saline (PBS) and trypsinization (0.05 % Trypsin in EDTA) for 5 min at 37°C and subsequent light centrifugation to separate them from solution. Resuspended cells were diluted 1:50 into fresh medium, and added to the fibronectin coated MatTek dish. Fibronectin, an extracellular matrix component, ensures uniform spreading of fibroblasts onto glass bottom dish. Two to three days later, cells reached 50-70

% confluence, which was optimal dish area coverage for cell transfection. This procedure consists of inserting plasmid (circular) DNA inside cells to introduce and express new genes. In order to observe GPI-GFP inside cell membrane by TIRF microscopy, the GPI-GFP gene needs to be inserted into the DNA of the cells, where it gets expressed (i.e. protein being produced). GPI-GFP plasmid DNA was kind gift of Prof. John Hanrahan (Physiology Dept. McGill University). Transfection was done using a Lipofectamine 2000 kit from Invitrogen, which consists of proprietary genetic delivery system. Briefly, an amount of plasmid DNA of GPI-GFP (approximately 1  $\mu$ g per culture dish) was mixed with Lipofectamine 2000 and incubated at room temperature for 30 min. The mixture was added to the cell culture dishes and left incubating at 37<sup>o</sup>C for 4-6 hours. DMEM was then replaced by a nutrient reduced medium (Opti-Mem I, Invitrogen), that induces cell ‘starvation’. Cell starvation is a standard procedure in cell biology, prior to biochemical assays, which enhances cellular responses to enzyme treatments and up-regulation of receptor proteins. Cells were imaged the day after transfection.

Before imaging, the medium was changed from Opti-Mem I to Hank’s Balanced Salt Solution (HBSS) supplemented by 10 mM HEPES buffer. Each MaTtek dish would have a final volume of 1 mL of HBSS/Hepes buffer. HBSS/Hepes buffer was used for all imaging, since Opti-Mem, and other cellular media contain the Phenol Red molecule which produces a fluorescence background. Moreover, reduced medium contains traces of amino-acids and nutrients, which could potentially interfere with the enzyme treatments applied to cells. HBSS contains glucose sufficient to keep cells stable throughout the imaging sessions. It contained Mg<sup>2+</sup>

ions, which are essential for activity of neutral sphingomyelinase used for domain disruption. In this study, we image cells without and post enzyme treatment by either *cholesterol oxidase* (COase: Sigma Aldrich, Cat. S8633) or *sphingomyelinase* (SMase: Sigma Aldrich, Cat. C-5421) . The first enzyme, COase, converts membrane cholesterol into cholestenone, which effectively disrupts the native membrane domains. The second enzyme, SMase, converts another raft component sphingomyelin, into ceramide, creating a similar raft disruption effect. Enzymes, were added to final concentration of 0.5 Units per mL for SMase and 1-2 Units per mL for COase. Cells were incubated with the enzymes for either 1-2 hours at 37°C or 15 min prior to imaging.

Another step before imaging was GPI-GFP labelling by anti-GFP IgG antibody conjugated with Alexa-594 fluorophores (Life Technologies, Cat. A-21312). The labelling consists in adding 2  $\mu$ L of dye (0.2 mg per mL) to 1 mL of cell solution, for about 15 min, followed by washing cells with HBSS/Hepes twice. Brief exposure of cells to the dye, ensures sufficient surface labelling of GPI-GFP by antibodies. Labelled cells were imaged immediately (control measurements) or treated with enzymes as explained above.

### **3.4 TIRF microscopy**

As outlined in chapter 1, the imaging procedures of current work was done using TIRF microscopy which takes advantage of a unique property of an induced evanescent wave within a thin sheet ( 100 nm) at the interface between two media having different refractive indices. The experimental apparatus consists of

commercial instrument (TIRF III Research platform, Carl Zeiss, Germany) on an Axio Observer Z1 microscope. The imaging was performed with 100x Alpha-Plan APO oil immersion objective lens with NA of 1.46. The microscope stage was equipped with an enclosed heating module (37°C). Prior to each imaging session, lasers were warmed up for at least an hour, to stabilize the output intensity. Beam collimation calibration was performed as described in the Zeiss user manual. Another important step prior to imaging, consists of calibrating the critical angle using a module provided by Zeiss. Indeed, this procedure ensures that laser light is incident at an optimal angle to produce best fluorescence signal. The calibration procedures were done with fluorescent beads (0.1  $\mu\text{m}$  radius) diluted in tap water, and mounted on a glass bottom MaTtek dish with a thickness appropriate for TIRF microscopy (0.16-0.19 mm). Following calibrations, a cell culture dish was mounted on the stage and coupled by immersion oil to the objective for 15-20 minutes prior to imaging, to ensure a thermal equilibrium between the cells and the microscope stage. The TIRF system employed was equipped with a CCD camera (Evolve S12 EMCCD) of 512 by 512 pixels area. With the 100x objective lens and an extra magnification lens placed in the optical path, the pixel size was 0.1  $\mu\text{m}$ . The exposure time of the image can be set as low as 1 ms, although signal is usually poor at that level. An extra 17 ms was added between each frame to account for integration and storage time of the CCD. The choice of 30 ms exposure time was made on the basis of optimal signal to noise ratio, while keeping the time per frame as short as possible. Thus the total frame time was 47 ms. Solid state lasers lines of 488 nm with 100 mW output power and 561 nm with power

output of 40 mW, were used to excite GFP and Alexa 594, respectively. GFP and Rhodamine emission filters ensured selection of green and red signal, respectively. Data was acquired using the AxioVert software customized for this microscope. Each image series consisted of an area of 256 by 256 pixels, acquired over 2000 frames. For each condition (control and enzymes) 20 image series were acquired sequentially. Data series were stored in 'zvi' files and loaded into Matlab for further analysis.

The simulation of realistic sub-pixel particle diffusion within a heterogeneous 2D environment required the careful implementation of simulator. The simulated and experimentally acquired data were processed using kICS analysis and correlation functions fit using appropriate models by the mean of non-linear least square fitting. This chapter exposed the methodologies and materials used for simulating image series and acquire the experimental data sets. It also details the analysis procedures for computation and characterization of kICS correlation functions. Next chapter explores the particles dynamics in different scenarios of heterogeneous 2D environments. It is followed by an experimental verification of the methodology using GPI-GFP anchored protein in live COS-7 cells.

## REFERENCES

- [1] Bates I.R. Hebert B. Luo Y. Liao J. Bachir A.I. Kolin D.L. Wiseman P.W. Hanrahan J.W. Membrane lateral diffusion and capture of cfr within transient confinement zones. *Biophys. J.*, 91:1046–1058, 2006.
- [2] Wawrezynieck L. Rigneault H. Marguet D. Lenne P.F. Fluorescence correlation spectroscopy diffusion laws to probe the submicron cell membrane organization. *Biophys. J.*, 89:4029–4042, 2005.
- [3] Schwartzentruher J.A. k-space image correlation spectroscopy: accuracy and precision, capabilities and limitations. Master’s thesis, McGill University, 2010.
- [4] Kolin D.L. *k-space Image Correlation Spectroscopy: theory, verification, and applications*. PhD thesis, McGill University, 2008.
- [5] Cos-7 fibroblast cell line from african green monkey kidney.
- [6] Wawrezynieck L. Conchonaud F. Wurtz O. Boned A. Guo X.-J. Rigneault H. He H-T. Marguet D. Lenne P.-F. Dynamic molecular confinement in the plasma membrane by microdomains and the cytoskeleton meshwork. *EMBO J.*, 25(3245-3256), 2006.
- [7] Manley S. Gillette J.M. Patterson G.H. Shroff H. Hess H.F. Betzig E. Lippincott-Schwartz J. High-density mapping of single-molecule trajectories with photoactivated localization microscopy. *Nature Methods*, 2008.
- [8] Sengupta P. Jovanovic-Talisman T. Skoko D. Renz M. Veath S.L. Lippincott-Schwartz J. Probing protein heterogeneity in the plasma membrane using palm and pair correlation analysis. *Nature Methods*, 8:969–975, 2011.
- [9] Serge A. Bertaux N. Rigneault H. Marguet D. Dynamic multiple-target tracing to probe spatiotemporal cartography of cell membranes. *Nature Methods*, 5:687–694, 2008.

## CHAPTER 4

### Computer simulations for characterization of kICS applied to heterogeneous 2D environments

#### 4.1 Computer simulated data for isolated domains

The following chapter presents the computer simulation results for models of isolated microdomains and meshwork type membrane confinements. The simulated isolated domains image series are presented, followed by the description of qualitative observations of the properties correlation functions calculated. The results of the characterization of the correlation functions by the nonlinear least squares fitting will be presented along with the characteristic system parameters recovered from analysis of the simulations. A discussion of the particle confinement statistics follows. We also discuss briefly the effect of the large effective confinements size observed, for the cases where small domains were simulated. The effects of background noise on images and correlation functions is discussed with their implications for the analysis. We conclude the chapter with potential new approaches for the analysis of confined membrane dynamics.

Chapter 3 of this thesis described how an image series is generated and what parameters can be varied in the simulation. An example of simulation images,

taken at time frames 1000, 1010 and 1100 of a time series, is shown in figure 4–1. The circular domain radius for this series was set to  $0.2 \mu\text{m}$ . The diffusion coefficients for particles the outside and inside the domains were set to 0.01 and  $0.001 \mu\text{m}^2/s$ , respectively. The probabilities for escaping and entering domains were set at 0.5 and 0.1, respectively. Finally, the domain density was set at 5 % of the whole image area coverage.

The bright points appearing in these images represent a local higher density, due to the larger number of particles within domains per unit area. The fainter spots outside represent unbound particles, diffusing freely with the diffusion coefficient  $D_{out}$ . Note, these domains are positionally static throughout the simulation, hence the bright points appear immobile in time. A closer inspection of the three frames, shows that some bright spots become fainter from frame 1000 to 1010, but regain their intensity at later times. This is due to particle exchange across the boundary. Particles inside the domains boundary move randomly according to  $D_{in}$ , producing fluctuations in the pixels surrounding the domain. The effects of partitioning and sub-domain diffusion give rise to the “slow” population contribution to the correlation function. The particle motion at large spatial scales, which combines both motion within and outside domains, gives rise to the “fast” population contribution in the correlation function.

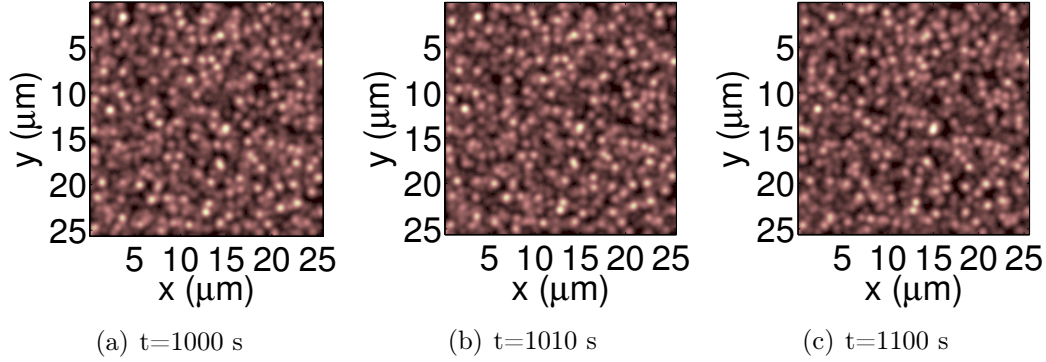


Figure 4–1: Example of computer simulated images of series for isolated domains of  $0.2 \mu\text{m}$  radius. Time points shown are 1000, 1010 and 1100 s, in a),b) and c), respectively. High intensity points denote domains, since the density is higher within.

## 4.2 kICS analysis for different confinement simulations

The following section outlines the average correlation functions for simulations where  $D_{in}$ , domain radius, domains density and  $P_{in}$  were varied. In each simulation scenario, 5 image series were simulated and their kICS correlation functions were averaged to remove the noise inherited from the discreteness of the system.

### 4.2.1 kICS analysis for simulations with a varying $D_{in}$

Figure 4–2 shows the average correlation functions for simulations in which  $D_{in}$  was varied. The range of diffusion coefficients inside domains was set from 0.001 to 0.01 while keeping  $D_{out}$  at  $0.01 \mu\text{m}^2/\text{s}$ . Qualitatively, as we decrease  $D_{in}$ , correlation functions start to show amplitude at higher spatial frequencies ( $k^2$ ). Indeed, at  $D_{in}=0.01 \mu\text{m}^2/\text{s}$  the correlation function is almost zero in the range of  $k^2$  from 100 to  $200 \mu\text{m}^{-2}$ , for  $\tau$  values above 4 s (figure 4–2 i). As we decrease  $D_{in}$  toward  $0.001 \mu\text{m}^2/\text{s}$ , that range of the correlation function increases in amplitude.

This trend results from particles spending more time confined diffusing inside domains, where the diffusion coefficient inside domains is lower. Effectively, the lower diffusion coefficient inside domains results in less frequent encounters with the domain boundary, hence a lower probability for the particle to escape.

#### **4.2.2 kICS analysis for simulations with a varying domain radius**

Variations in the domain radius result in a more drastic change in the correlation functions, as shown in figure 4–3. Increasing domain radius from 0.05 to 0.45  $\mu\text{m}$  leads to lower amplitude at higher spatial frequencies (high  $k^2$ ). The larger the spatial scale explored, the smaller the spatial frequencies that will be visible in the CF. As a consequence, the correlation function could be used to infer the effective domain size present in the system. The pixel size in all simulations was set to 0.1  $\mu\text{m}$  and the PSF  $e^{-1}$  radius to 0.4  $\mu\text{m}$ . Therefore at least one simulated scenario contains domains smaller than the pixel size while at least 6 of them have domains smaller or equal to the PSF size. The key question tested with this set of simulations is what is the minimum detectable domain size for a given set of microscopy sampling parameters.

#### **4.2.3 kICS analysis for simulations with a varying domain area occupancy**

When only the domain area occupancy increases, it is expected that we will observe an increase in the number of confined particles. Consequently, this should lead to non zero amplitudes at higher spatial frequencies in the correlation functions. Figure 4–4 shows exactly that effect. Note that for all of the correlation

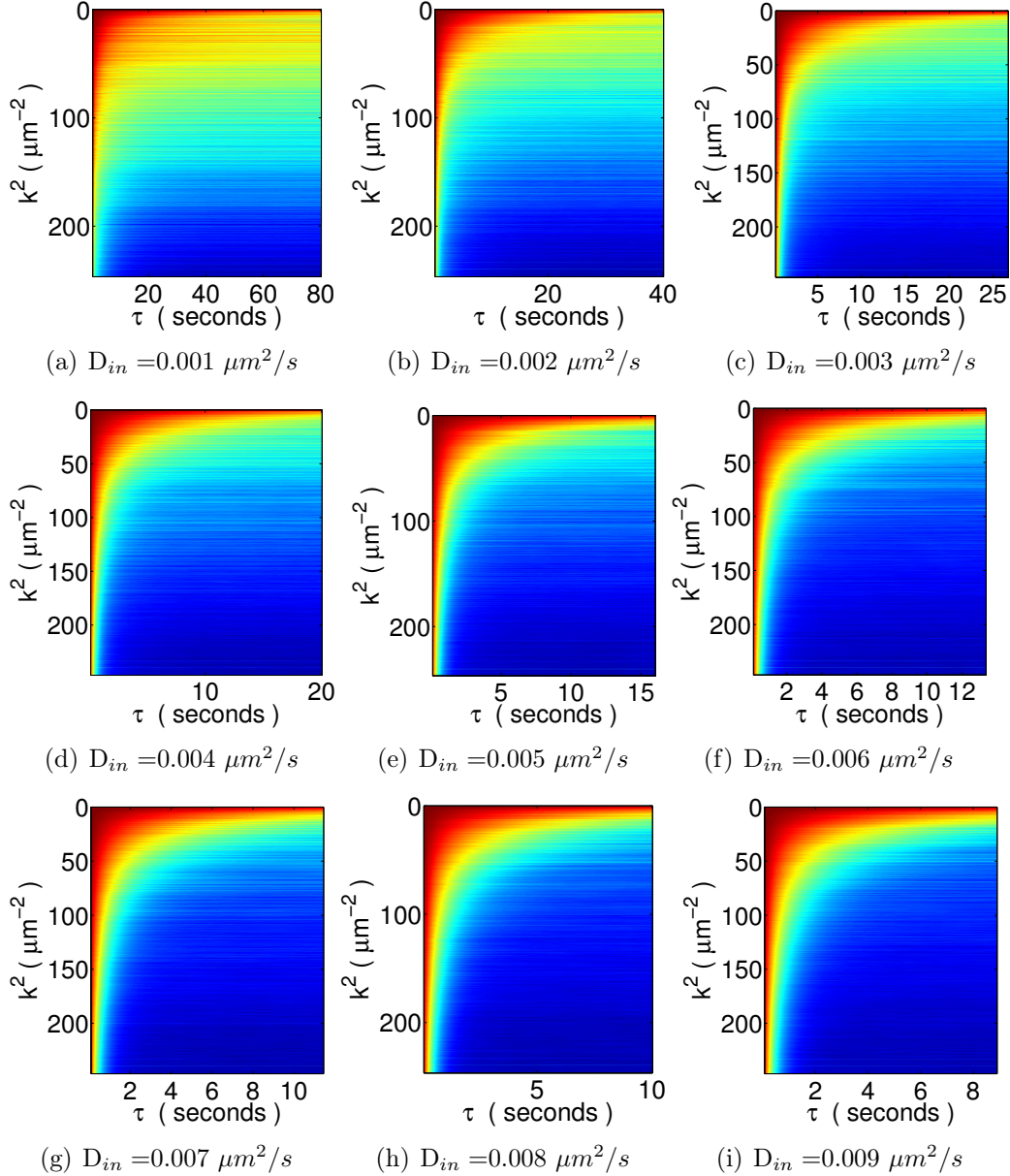


Figure 4-2: Normalized amplitude density plots of average correlation functions calculated from 10 confined domain simulations with variable  $D_{in}$ .  $D_{out}$  was set to  $0.01 \mu\text{m}^2/\text{s}$ .  $P_{in}$  and  $P_{out}$  were fixed at 0.5 and 0.1, respectively. The domain radius was  $0.2 \mu\text{m}$  while the domain area fraction was set at 5 %.  $D_{in}$  increases from a) to i). The correlation functions were normalized setting the highest equal to 1 (red) and lowest equal to 0 (blue).

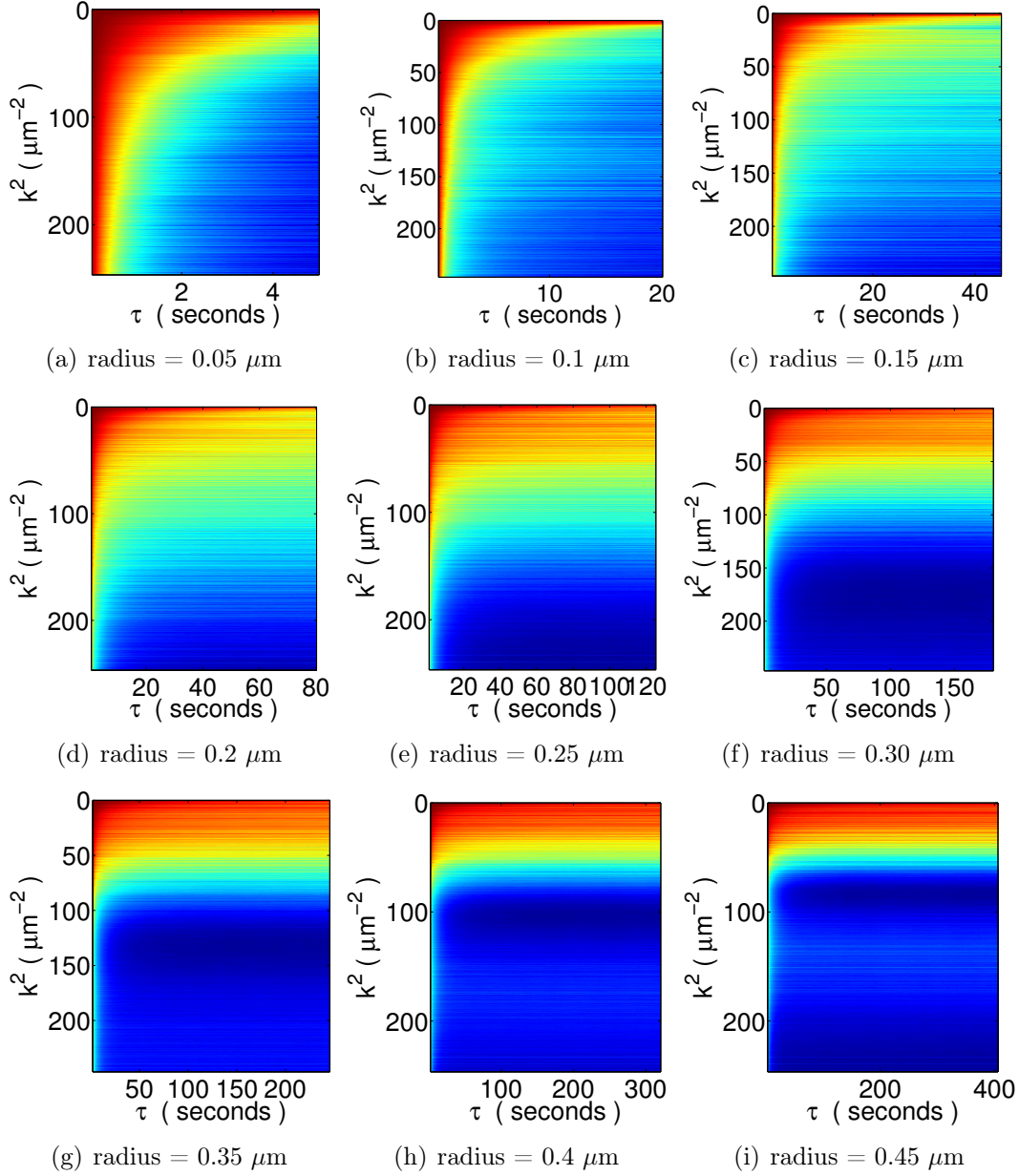


Figure 4-3: Normalized amplitude density plots of average correlation functions calculated from 10 confined domain simulations with variable domain radius. Domain radius increases from a) to i).  $D_{in}$  and  $D_{out}$  were set to 0.001 and 0.01  $\mu\text{m}^2/\text{s}$ , respectively.  $P_{in}$  and  $P_{out}$  were fixed at 0.5 and 0.1, respectively. The domain area fraction was set at 5 %. The PSF  $e^{-1}$  radius was set to 0.4  $\mu\text{m}$ . The correlation functions were normalized setting the highest equal to 1 (red) and lowest equal to 0 (blue).

functions shown so far in this chapter, there is always a fast decaying contribution at small spatial frequencies. This is due to the fast population diffusing over large spatial scales. The domain area coverage was varied from 0.5 to 5 % of the total image area. In these simulations domain radius was kept constant at  $0.2 \mu\text{m}$ , while  $D_{in}$  and  $D_{out}$  were set at 0.001 and  $0.01 \mu\text{m}^2/\text{s}$  respectively and transition probabilities  $P_{in}$  and  $P_{out}$  at 0.5 and 0.1 respectively.

#### 4.2.4 kICS analysis for simulations with varying $\frac{P_{in}}{P_{out}}$

For the variation of  $P_{in}$ , the probability for particles to exit domains,  $P_{out}$  was set to  $1-P_{in}$ . It is not until  $\frac{P_{in}}{P_{out}} \sim 0.8$  that a significant confinement effect appears, as shown in figure 4-5. At this ratio  $P_{in}=0.4$  and  $P_{out}=0.6$  which would lead to no confinement if diffusion coefficients inside and outside of domains were equal. On the other hand,  $D_{in}$  and  $D_{out}$  were set to 0.001 and  $0.01 \mu\text{m}^2/\text{s}$ , respectively, producing the emergence of the confinement effect at the  $\frac{P_{in}}{P_{out}}$  smaller than 1. Other parameters were set constant, with domain radius= $0.2 \mu\text{m}$ , domain area fraction= $5\%$ ).

The results above show that it is a combination of different parameters values that lead to the signature of confinement emerging in the correlation functions. Moreover, it is possible to produce very similar, if not the same, correlation response with two different sets of parameters. In other words, system is degenerate. This leads to several questions regarding the accuracy and precision of the kICS correlation functions as an analytical tool for characterization of dynamics in heterogeneous 2D systems. Is it possible to extract the specific

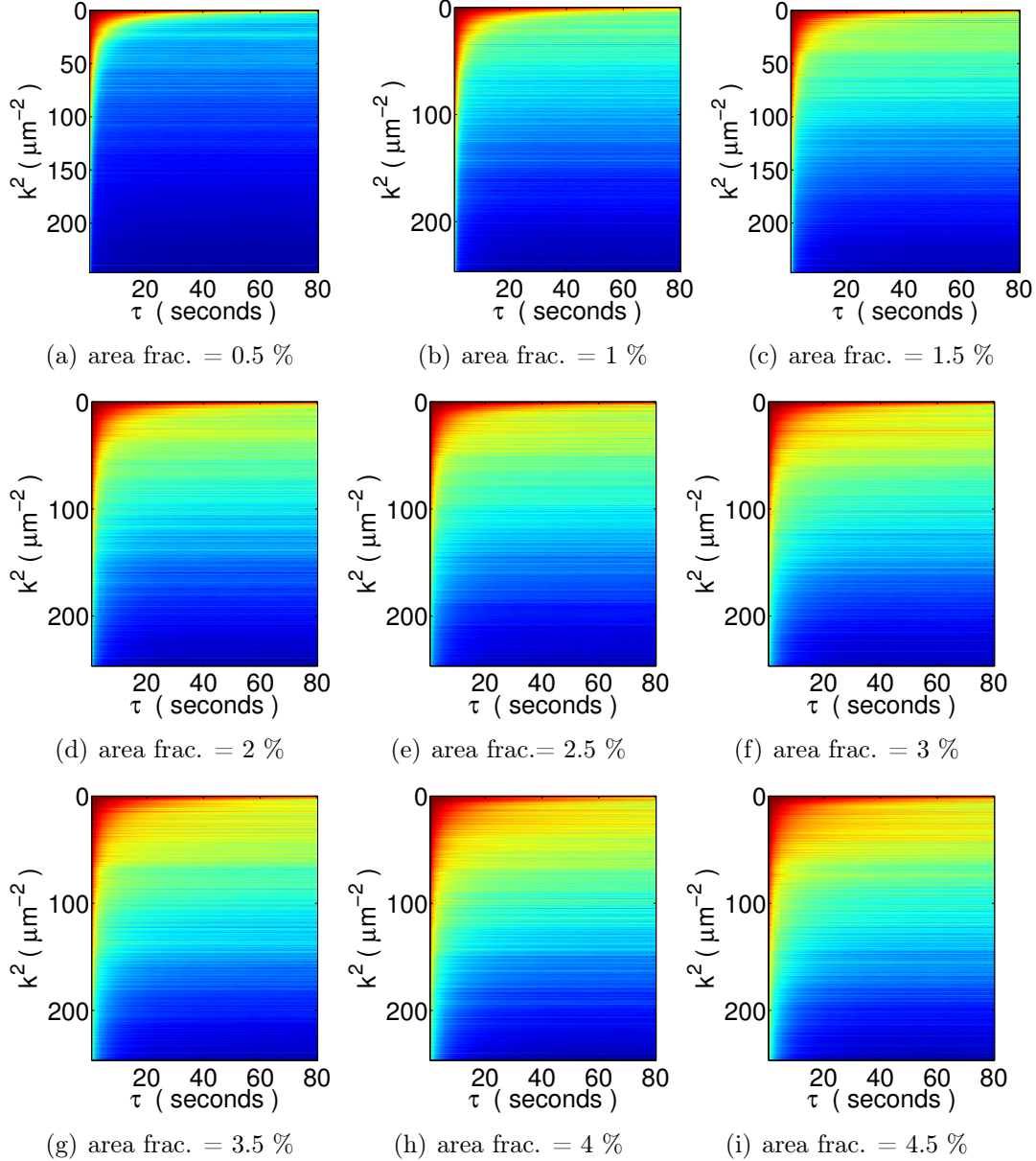


Figure 4-4: Normalized amplitude density plots of average correlation functions calculated from 10 confined domain simulations with variable domain area fraction. Domain area fraction increases from a) to i).  $D_{in}$  and  $D_{out}$  were set to 0.001 and  $0.01 \mu\text{m}^2/\text{s}$ , respectively.  $P_{in}$  and  $P_{out}$  were fixed at 0.5 and 0.1, respectively. The domain radius was set to  $0.2 \mu\text{m}$ . The correlation functions were normalized setting the highest equal to 1 (red) and lowest equal to 0 (blue).

characteristic parameters for a system with confined dynamics using image correlation analysis? Moreover, can other dynamics give rise to similar decays in the correlation function? The following section shows that the case of two freely diffusing populations, will not produce correlation function decays that can be misinterpreted as a confined scenario.

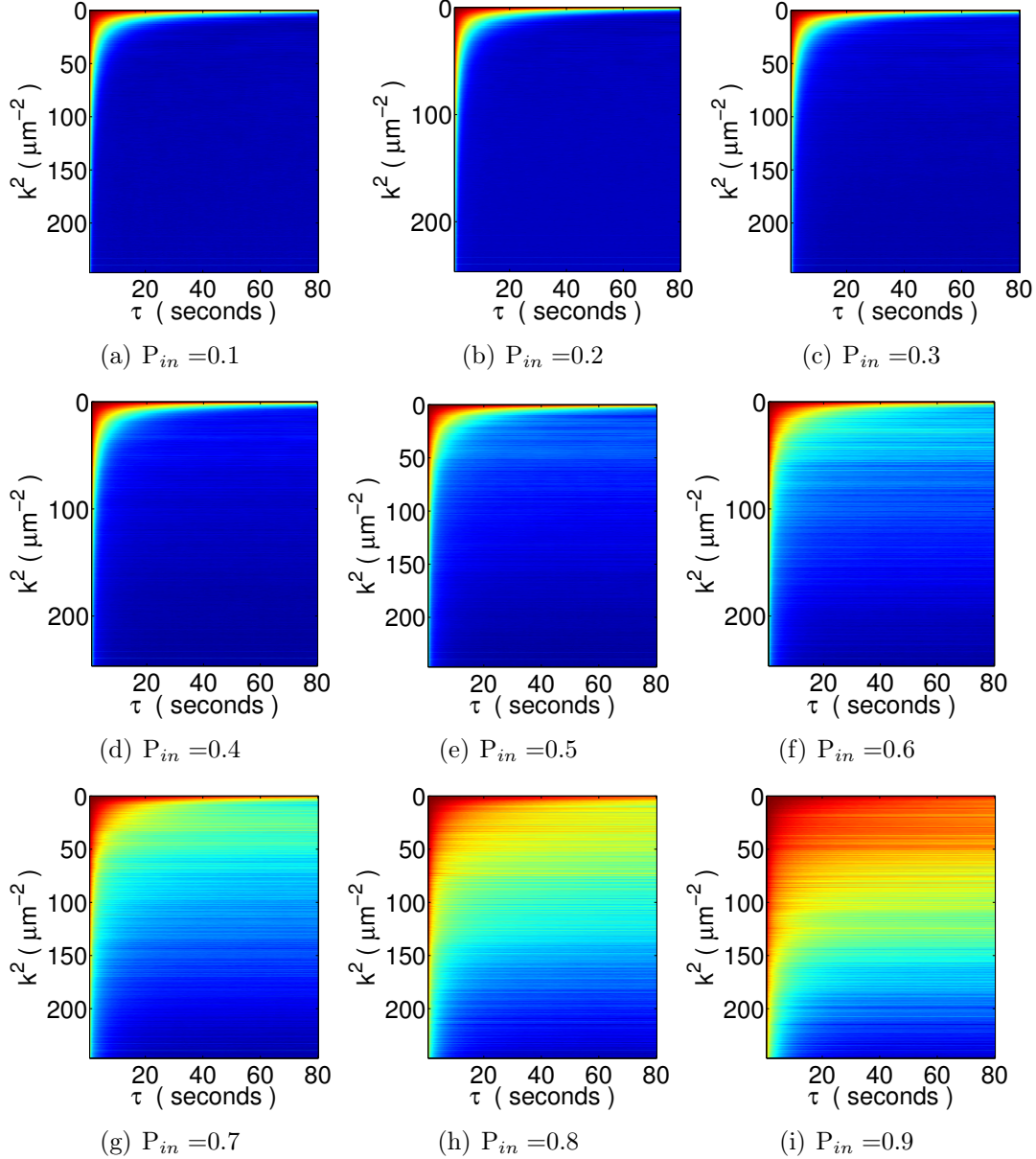


Figure 4-5: Normalized amplitude density plots of average correlation functions calculated from 10 confined domain simulations with variable  $P_{in}$  variation.  $P_{in}$  increases from a) to i).  $D_{in}$  and  $D_{out}$  were set to 0.001 and  $0.01 \mu m^2/s$ , respectively. The domain radius was set to  $0.2 \mu m$ . The domain area fraction was set at 5%.  $P_{out}$  was set to  $1 - P_{in}$ . The correlation functions were normalized setting the highest equal to 1 (red) and lowest equal to 0 (blue).

### 4.3 kICS analysis for simulations of two freely diffusing populations

Here we explore briefly, the kICS analysis for a case of two freely diffusing populations. The simulations had no domains present in the 2D system. The two diffusion coefficients set in this simulation,  $D_1=0.001$  and  $D_2=0.01 \mu m^2/s$ , were the same as  $D_{in}$  and  $D_{out}$  of the domain simulations described in the previous section. Figure 4–6 a) shows the average correlation function of 5 trials. There are no significant amplitude at large  $k^2$  values for higher temporal lags, as in the confined case. Moreover, the correlation function decays almost completely with time. The fit of the correlation function, using the sum of two Gaussians, produces two straight lines for the characteristic decay constants as plotted  $D\tau$  vs  $\tau$  (Figure 4–6 b). The fast component fit recovers the larger diffusion coefficient ( $D_1$ ) while the slow component fit recovers the smaller diffusion coefficient ( $D_2$ ). Most importantly, the slow component of the fit (red circles) does not ‘plateau’ at long temporal lags ( $\tau$ ). A plateau at long lag times is the hallmark of confinement in the system. Indeed, when the correlation function does not decay with time, it implies that some features in the image appear immobile or almost immobile. Consequently, the slow component  $D\tau$  does not grow linearly over all temporal lags for a confined case.

The ICS diffusion law (introduced in chapter 1), does bear some similarities (as shown in figure 4–6 c) with the confined case 1–21, but there is one essential difference. The slope of the slow components (green dashed line) passes through

the origin, while in the confined case, it gives a non-zero intercept at the y-axis. This will be discussed in more detail at the end of this chapter.

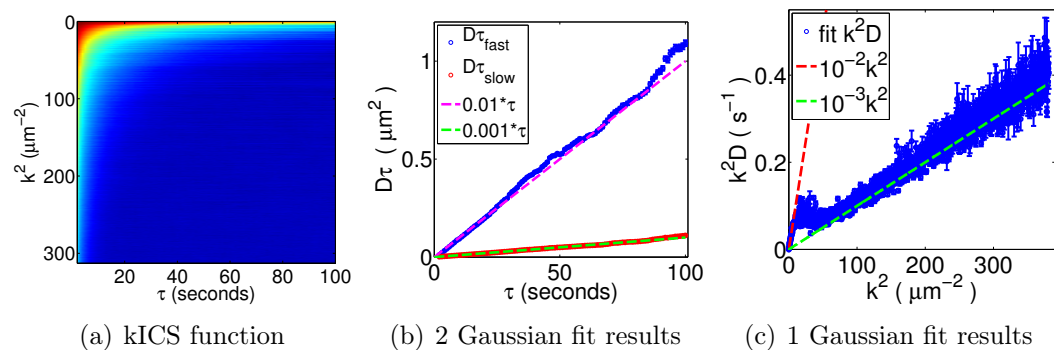


Figure 4-6: kICS analysis of simulations of two freely diffusing populations. a) Amplitude density plot for kICS CF for the case of two freely diffusing populations with coefficients  $D_1=0.01$  and  $D_2=0.001 \mu m^2/s$ . b) Results of the sum of 2 Gaussian fit of the kICS correlation function from a). Blue and red circles denote  $D\tau$  from each component of the fit, as a function of  $\tau$ , while dashed magenta and green lines show linear trends one would get if two freely diffusing species were simulated. c) ICS diffusion law extracted from the single Gaussian fit vs temporal lag of the function in a). Blue circles are fit data, while red and green dashed lines denote trends one would have for two separate cases with freely diffusing populations, with above mentioned diffusion coefficients. Error bars denote the 95 % confidence interval on fit parameters obtained from non-linear fitting at each  $k^2$ .

#### 4.4 Two Gaussian fit of the kICS correlation functions for the simulations of different confinement scenarios

This section summarizes the results of fitting the average correlation functions with a sum of two Gaussians. Fitting was done vs spatial frequencies at a given time lag, as described in chapter 3. For each  $D\tau$  vs  $\tau$  plot a limited number of error bars are superimposed to enhance the visibility of the underlying trends. The

error bars represent 95 % confidence interval on the fitted parameter at a given temporal lag.

#### 4.4.1 Two Gaussian fit of the kICS correlation functions for simulations with variable $D_{in}$

Section 4.2.1 details the parameters values used for simulations with varying  $D_{in}$ . Figure 4–2 shows average kICS CFs of each simulated scenario which are fitted in what follows with sum of Gaussians. Figure 4–7 shows  $D_{fast}\tau$  and  $D\tau_{slow}$  for each of these cases, where blue to orange circles denote trends of increasing  $D_{in}$ . A quick inspection of the fast component, does not show a particular trend as  $D_{in}$  increases. Furthermore, a decrease in  $D_{in}$  leads to a deviation of  $D_{fast}\tau$  away from the diffusion coefficient set outside of domains ( $D_{out}$  shown as a black dashed line).

For the slow contribution, it is not clear what the variation in  $D_{in}$  induced in this case (figure 4–7 b). Nevertheless, the long  $\tau$  plateau of all of these curves saturates at approximately the value of the set domain radius squared (black dashed line). The ‘4’ appearing in the y-axis label comes from the fact that for the two dimensional diffusion, the MSD of particles goes as  $4D\tau$  with time. Therefore, if one is to compare any characteristic length scale in the system, it has to be adjusted this way.

Figure 4–8 summarizes the parameters extracted from fits of the early temporal lags of the fast component, the early temporal lags of the slow component, the late temporal lags of the slow component plateau and the late temporal lags of the

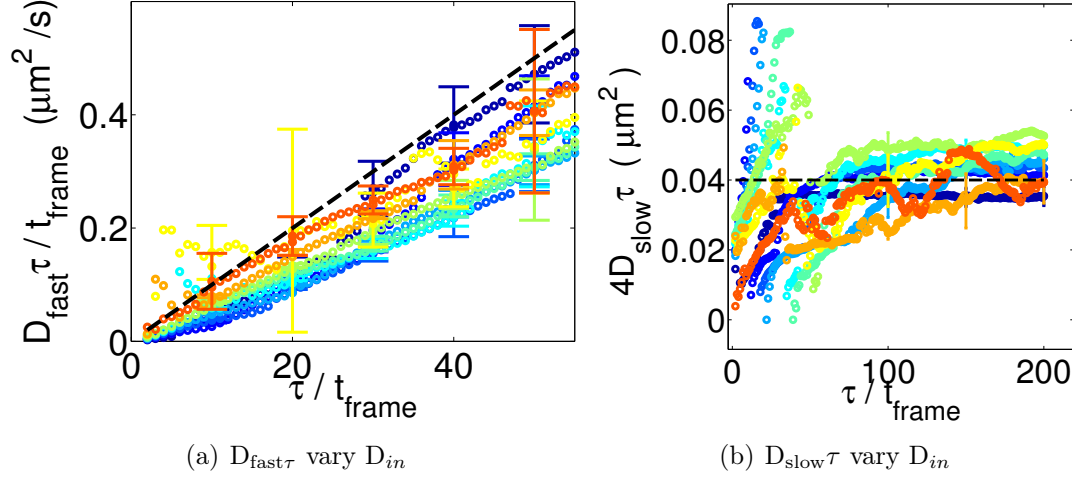


Figure 4-7: Two Gaussian fit of the kICS CF for simulations with variable  $D_{in}$ . a) Fast mobility  $D_{fast}\tau$  and b) slow mobility  $D_{slow}\tau$  as function of temporal lag. Blue to orange circles are trends for simulations with increasing  $D_{in}$ . Error bars are plotted for only some points for clarity and represent 95 % confidence intervals on plotted parameters. The frame time,  $t_{frame}$ , is variable according to equation 3.2. Black dashed lines represent  $D_{out}\tau$  and (domain radius)<sup>2</sup> used in these simulations, for a) and b) respectively.  $D_{out}$  and domain radius were set to  $0.01 \mu m^2/s$  and  $0.2 \mu m$ , respectively.

amplitudes of the correlation functions, using weighted linear least-squares fitting. Figure 4-8 a) shows that the effective  $D_{fast}$  decreases with increasing ratio  $\frac{D_{out}}{D_{in}}$ . The recovered value is always smaller than the set value of  $D_{out}$  (blue line) and so it appears to be an effective diffusion coefficient as measured at small spatial frequencies (i.e. large spatial scales). The diffusion coefficient of the slow component seems more noisy (figure 4-8 b), especially in the range where  $\frac{D_{out}}{D_{in}}$  is equal to one. It is reasonable to assume that in this particular range, particles do not remain in the domains for a long time, and thus contribute a significant number of fluctuations, that should amplify slow contribution. The slow component contribution

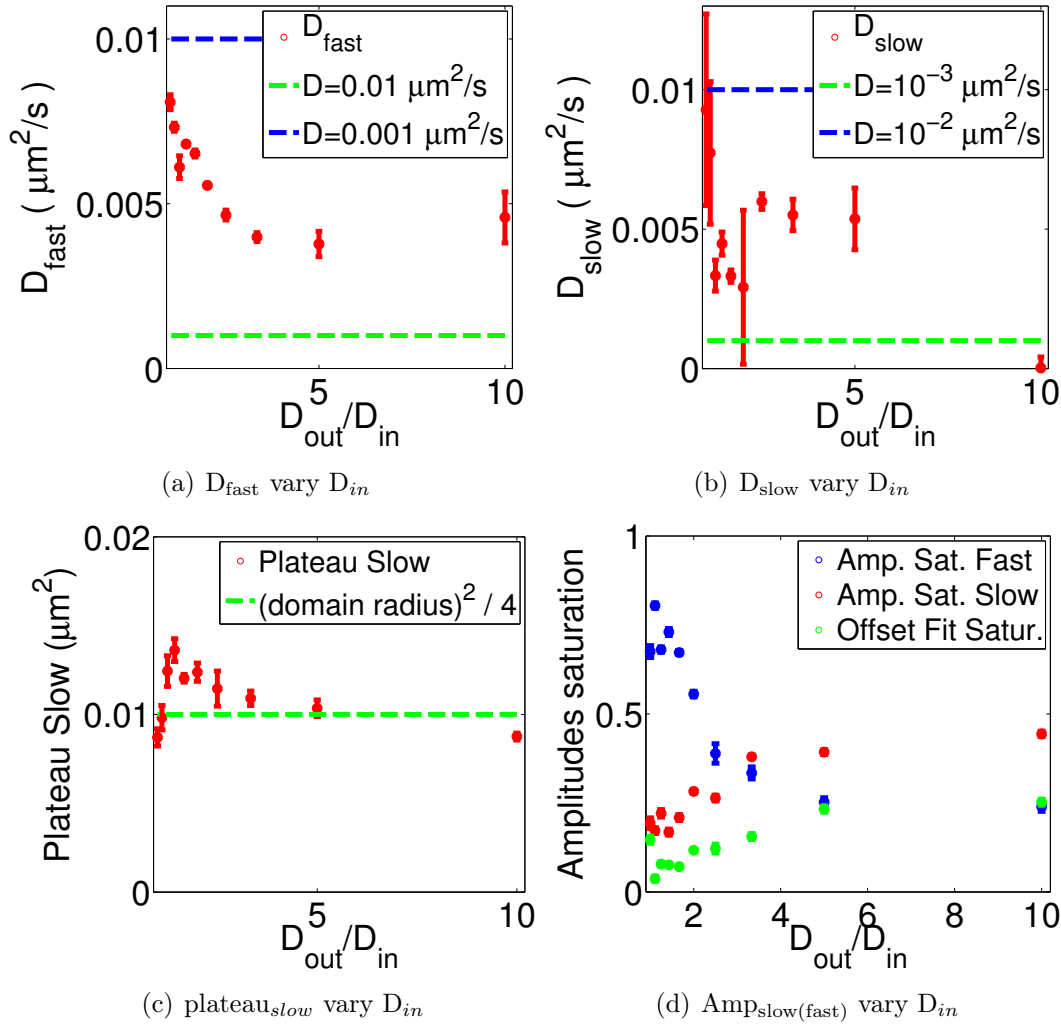


Figure 4–8: Fit parameters recovered from analysis for simulations with varying  $D_{in}$ . Error bars represent the 95 % confidence intervals on plotted parameters. Blue and green dashed lines in a) and b) are equal to  $D=D_{out}=0.01 \mu m^2/s$  and  $D=0.001 \mu m^2/s$ , respectively. Green dashed line in c) represent the domain radius ( $0.2 \mu m$ ) squared divided by 4.

plateau extracted from the long temporal lags, increases at small  $\frac{D_{out}}{D_{in}}$  values, but then drops continuously. As  $\frac{D_{out}}{D_{in}}$  ratio increases, particles become more confined which results in them tracing a smaller effective area at small spatial scales. As we decrease that ratio, particles encounter the boundaries of the domains more often which increases the probability of escape. This effect leads to the observation of an effectively greater domain area at small spatial scales, as reported by the plateau<sub>slow</sub>.

The plateaus of the CF amplitudes (chapter 3, equation 3.10) exhibit interesting trends as shown in figure 4–8 d). As one increases the ratio,  $\frac{D_{out}}{D_{in}}$ , the plateau of the amplitude of the fast component decreases while that of the slow component increases. This is simply a consequence of the increased confinement of particles with increasing diffusion coefficients ratio, which results in an increasing amplitude of slow component.

#### 4.4.2 Two Gaussian fit of the kICS correlation functions for simulations with variable domain radius

Section 4.2.2 details the parameters values used for simulations with varying domain radius. Figure 4–3 shows average kICS CFs of each simulated scenario which are fitted in what follows with sum of Gaussians. When the domain radius is increased, the fitted  $D_{fast}\tau$  and  $D_{slow}\tau$  show clear trends. For example, while the fast component y-axis intercept increases with increasing domain radius (figure 4–9 a), the slow component’s late temporal lags plateaus increase as well (figure 4–9 b).

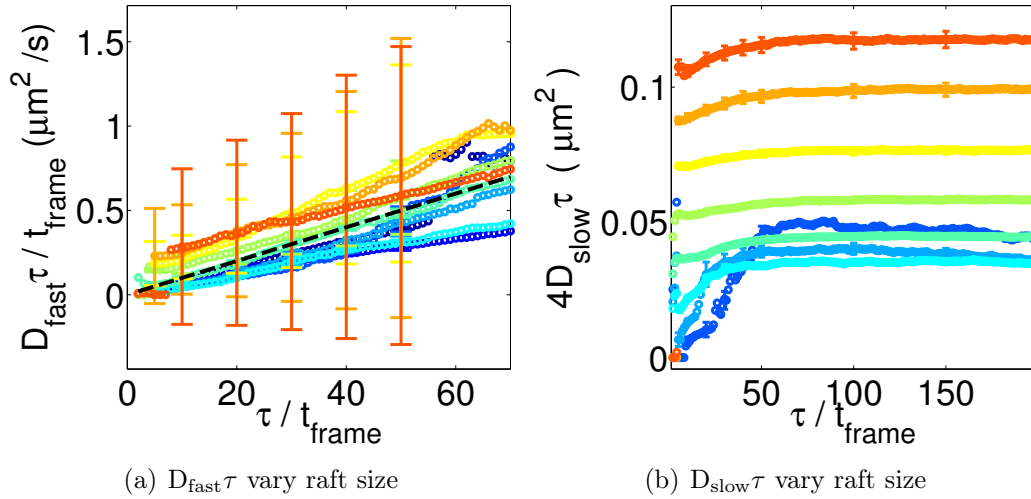


Figure 4–9: Two Gaussian fit of the kICS CF for simulations with variable domain radius. a) Fast mobility  $D_{fast}\tau$  and b) slow mobility  $D_{slow}\tau$  as function of temporal lag. Blue to orange circles are trends for simulations with increasing domain radius. Error bars are plotted for only some points for clarity and represent 95 % confidence intervals on plotted parameters. The frame time,  $t_{frame}$ , is variable according to equation 3.2. Black dashed line in a) represents  $D_{out}\tau$ , where  $D_{out}$  was set to  $0.01 \mu m^2/s$ .

Inspection of the fitted parameters (figure 4–10) suggests that the fast component slope still measures an effective diffusion coefficient, which is smaller than the set  $D_{out}$ , but greater than  $D_{in}$ . On the other hand, the early temporal lags fit of  $D_{slow}\tau$  vs  $\tau$  curve suggests that the motion is almost arrested for domains bigger than  $\sim 0.2 \mu m$  in radius (figure 4–10 b), while for smaller radius,  $D_{slow}$  recovered is lower than  $D_{in}$ . This is an important observation as the effective diffusion coefficient measured at small spatial scales is smaller than the diffusion coefficient set at those scales. The value of plateau of the slow component clearly increases linearly with domain radius squared, for domain radii equal to the  $0.2 \mu m$  or greater (figure 4–10 c). The full discussion of this phenomenon is found

later in this chapter. An interesting observation is that a theoretical domain radius of zero, the  $4\times$ plateau value should be around  $0.01 \mu\text{m}$ , which is the size of a pixel squared. This is possibly the smallest spatial scale that could, in theory, produce fluctuations that can be observed from one image to another in an image series.

#### 4.4.3 Two Gaussian fit of the kICS correlation functions for simulations with variable domain area fraction

Section 4.2.3 details the parameters values used for simulations with varying domain area fraction. Figure 4–4 shows average kICS CFs of each simulated scenario which are fitted in what follows with sum of Gaussians. When the domain area fraction is varied,  $D_{slow}\tau$  and  $D_{fast}\tau$  exhibited similar trends as for previous cases (Figure 4–11). On one hand, the diffusion of the fast component follows a decreasing trend, with increasing domain area fraction, as shown in figure 4–12 a). On the other hand, the slow component early regression slope, seems to increase with the increase in domain area fraction (figure 4–12 b). This could be due to more particles being trapped (figure 4–12 d, red symbols), hence giving rise to the emergence of the slowly diffusing population characteristics in the correlation functions. Interestingly, the domain area fraction does not seem to affect the apparent domain radius recovered (figure 4–12 c). Finally, the amplitude of the fast population decreases less abruptly suggesting that the change in domain area fraction causes only a slight change in confinement, as detected by all of the other characteristic parameters recovered.

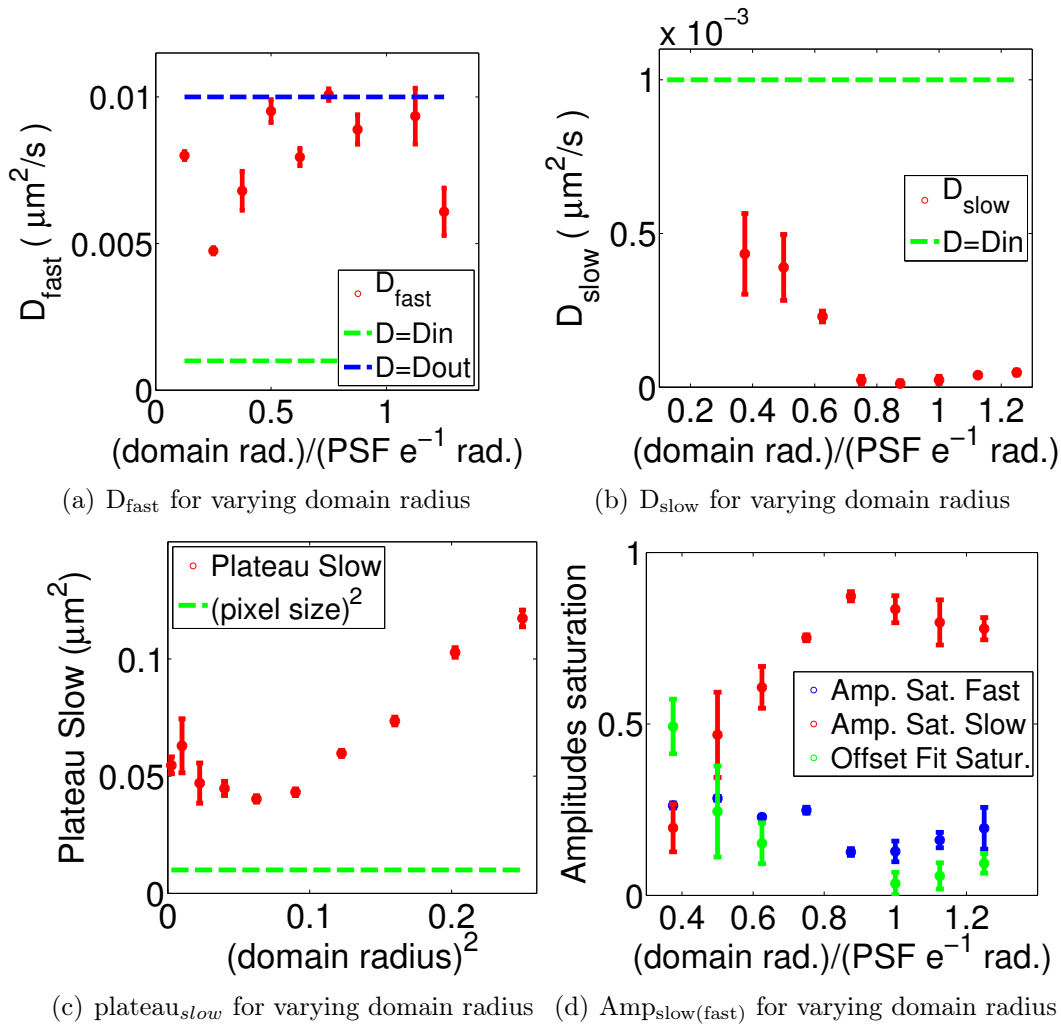


Figure 4-10: Fit parameters recovered from analysis for simulations with varying domain radius. Error bars represent the 95 % confidence intervals on plotted parameters. Blue and green dashed lines in a) and b) represent the set diffusion coefficients,  $D_{out}$  and  $D_{in}$ , respectively. The intercept of the dashed green line in c) is the pixel diameter squared.

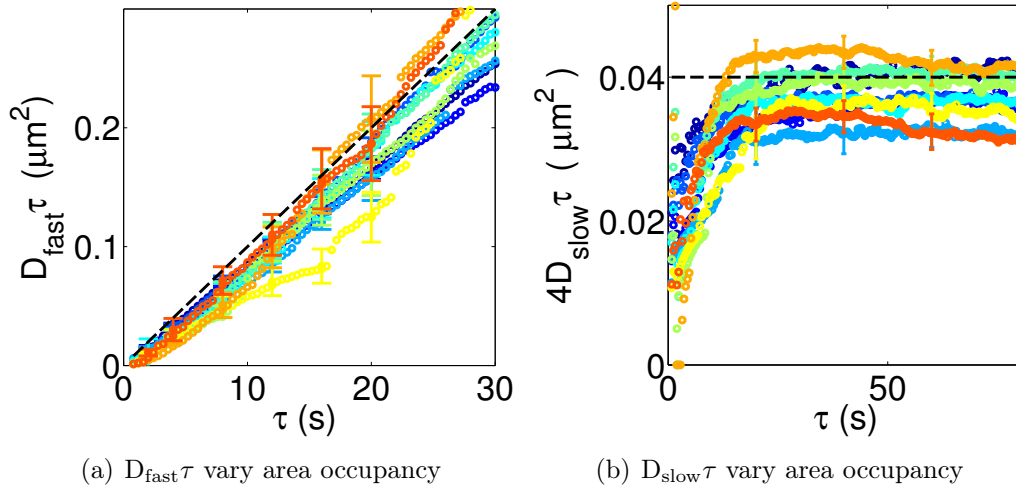


Figure 4–11: Two Gaussian fit of the kICS CF for simulations with variable domain area fraction. a) Fast mobility  $D_{fast}\tau$  and b) slow mobility  $D_{slow}\tau$  as function of temporal lag. Blue to orange circles are trends for simulations with increasing domain area fraction. Error bars are plotted for only some points for clarity and represent 95 % confidence intervals on plotted parameters. The frame time,  $t_{frame}$ , is equal to 0.4 s. Black dashed lines represent  $D_{out}\tau$  and  $(\text{domain radius})^2$ , in a) and b) respectively.

#### 4.4.4 Two Gaussian fit of the kICS correlation functions for simulations with variable $\frac{P_{in}}{P_{out}}$

Section 4.2.4 details the parameters values used for simulations with varying  $\frac{P_{in}}{P_{out}}$  ratio. Figure 4–5 shows average kICS CFs of each simulated scenario which are fitted in what follows with sum of Gaussians. The kICS analysis of simulations where  $\frac{P_{in}}{P_{out}}$  ratio was varied, shows clear trends, especially when the ratio  $\frac{P_{in}}{P_{out}}$  is greater than 1. In such cases, the fit fast diffusion,  $D_{fast}$ , deviates from the diffusion outside domains,  $D_{out}$ . In the extreme case when the ratio was 9, the particles experience complete trapping (Figure 4–13a orange symbols), which is represented by the dark orange symbols. In the case of the slow component, the

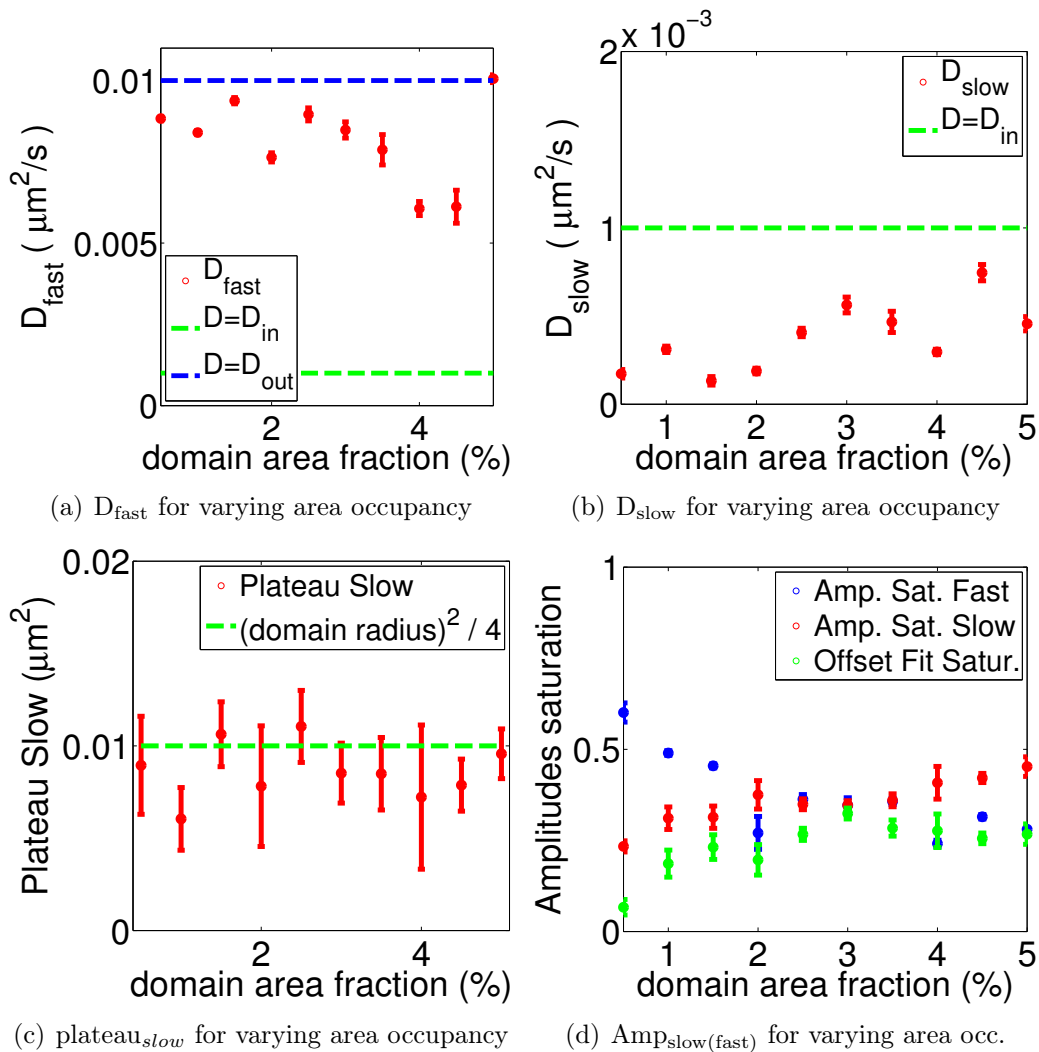


Figure 4-12: Fit parameters recovered from analysis for simulations with varying domain area occupancy. Error bars represent the 95 % confidence intervals on plotted parameters. Blue and green dashed lines in a) and b) represent the set diffusion coefficients,  $D_{out}$  and  $D_{in}$ , respectively. Green dashed line in c) represents the domain radius squared divided by 4.

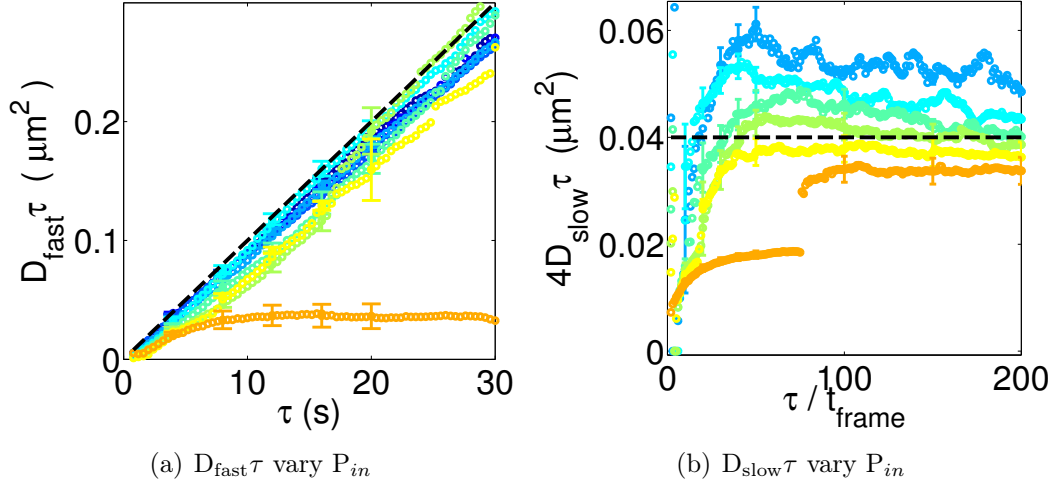


Figure 4–13: Two Gaussian fit of the kICS CF for simulations with variable  $\frac{P_{in}}{P_{out}}$ . a) Fast mobility  $D_{fast}\tau$  and b) slow mobility  $D_{slow}\tau$  as function of temporal lag. Blue to orange circles are trends for simulations with increasing  $\frac{P_{in}}{P_{out}}$ . Error bars are plotted for only some points for clarity and represent 95 % confidence intervals on plotted parameters. The frame time,  $t_{frame}$ , is equal to 0.4 s. Black dashed lines represent  $D_{out}\tau$  and  $(\text{domain radius})^2$ , in a) and b) respectively.

higher the ratio  $\frac{P_{in}}{P_{out}}$ , the closer the plateau is to the actual value of the set domain radius (figure 4–13 b).

The fitted parameters are shown in figure 4–14. The fast diffusion coefficient decreases with the increase of the  $\frac{P_{in}}{P_{out}}$  ratio, and similarly for the measured diffusion for the slow component (figure 4–14 a and b). Indeed, as we approach a ratio of 9, the fast diffusion coefficient is reduced to almost the value of the diffusion coefficient inside the domains, while the slow component approaches zero suggesting that particles are almost fully trapped. The slow component plateau decreases in value with increasing the  $\frac{P_{in}}{P_{out}}$  ratio. At intermediate ratios, the plateau value approaches that of the domain radius squared but at the highest

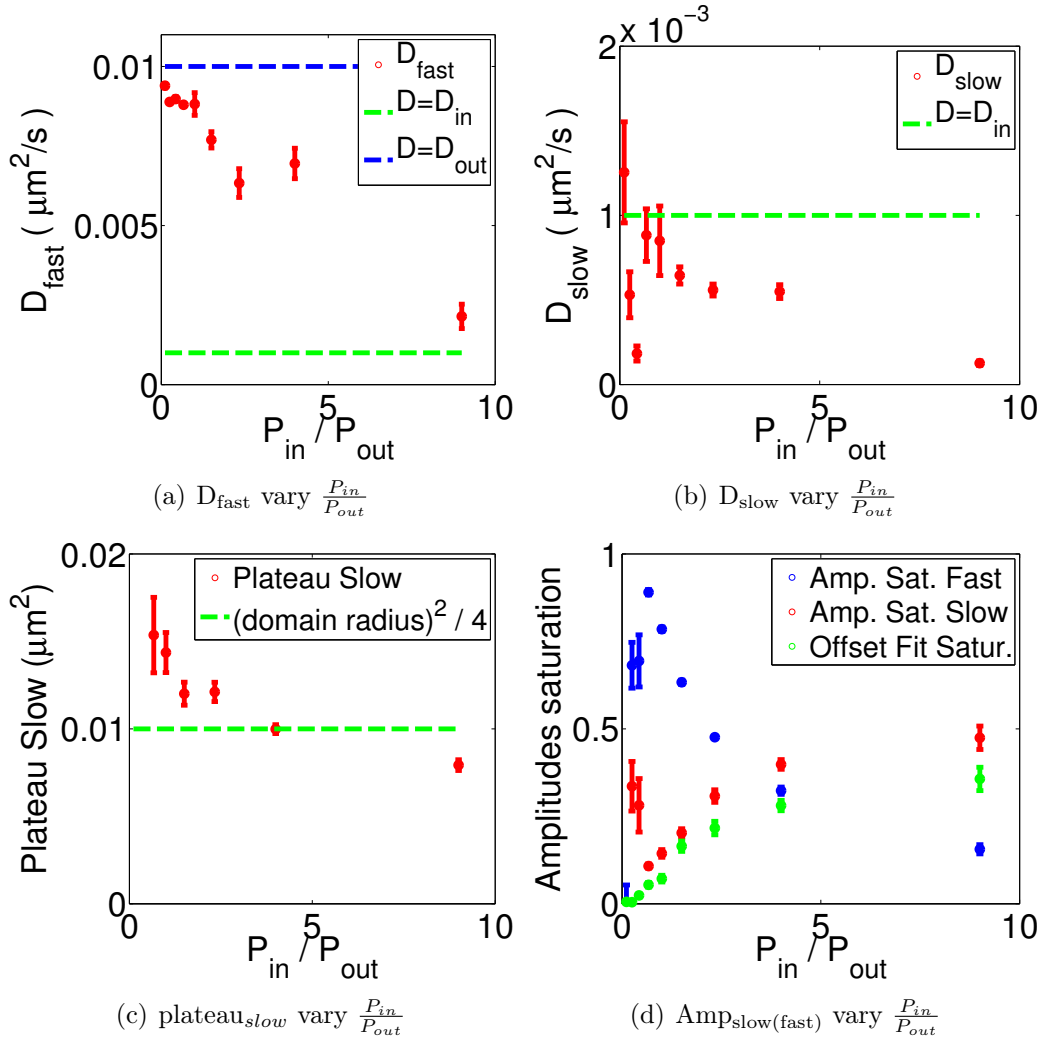


Figure 4-14: Fit parameters recovered from analysis for simulations with varying  $\frac{P_{\text{in}}}{P_{\text{out}}}$ . Error bars represent the 95 % confidence intervals on plotted parameters. Blue and green dashed lines in a) and b) represent the set diffusion coefficients,  $D_{\text{out}}$  and  $D_{\text{in}}$ , respectively. Green dashed line in c) represent the raft radius squared divided by 4.

ratio it falls slightly below this value. This effect is similar to the one observed with varying  $\frac{D_{out}}{D_{in}}$  (figure 4–8 c). Amplitudes saturations for the slow and fast components, change dramatically with increasing  $\frac{P_{in}}{P_{out}}$ . The amplitude for trapped particles increases, as expected (figure 4–14 d), while the amplitude saturation for the free particles decreases.

The results of the above section are summarized qualitatively in table 4–1. The kICS analysis by the fit of a sum of two Gaussians offers the possibility for quantifying and distinguishing between different confinement cases. The extracted mobilities,  $D_{fast}$  and  $D_{slow}$ , and their respective amplitudes, instruct us on the variability of some of the parameters controlling the underlying heterogeneous transport and exchange dynamics.

Table 4–1: Summary of results trends for the isolated domains simulations. Symbols  $\Downarrow$ ,  $\downarrow$ ,  $-$  and  $\sim$  reflect strong decrease, weak decrease, constant and undefined trends for the properties listed. The set variables  $\frac{D_{out}}{D_{in}}$ , raft size, raft density and  $\frac{P_{in}}{P_{out}}$  are all considered to increase.

| Measured \ varied          | $\frac{D_{out}}{D_{in}}$ $\uparrow$ | domain radius $\uparrow$ | domain area fraction $\uparrow$ | $\frac{P_{in}}{P_{out}}$ $\uparrow$ |
|----------------------------|-------------------------------------|--------------------------|---------------------------------|-------------------------------------|
| $D_{fast}$                 | $\Downarrow$                        | -                        | $\downarrow$                    | $\Downarrow$                        |
| $D_{slow}$                 | $\downarrow$                        | $\downarrow$             | $\uparrow$                      | $\Downarrow$                        |
| plateau slow               | $\downarrow$                        | $\uparrow$               | -                               | $\Downarrow$                        |
| amplitude <sub>fast</sub>  | $\downarrow$                        | $\Downarrow$             | $\downarrow$                    | $\Downarrow$                        |
| amplitude <sub>slow</sub>  | $\uparrow$                          | $\uparrow$               | $\uparrow$                      | $\Uparrow$                          |
| $\beta$ (partition coeff.) | $\uparrow$                          | -                        | $\uparrow$                      | $\Uparrow$                          |

## 4.5 Discussion

### 4.5.1 Characteristic times for free and trapped particles

From the particle coordinates generated in the simulations, the total time a particle spends inside and outside of a domain can be calculated. With that information, the average partition coefficient,  $\beta$ , is calculated which defines the ratio of the number of particles within domains at a given time divided by the total number of particles. Therefore, in the limit of  $\beta$  approaching zero, the occupation number of the domains becomes zero. Conversely,  $\beta$  approaching one leads to complete trapping (as in the case of the scenario of  $\frac{P_{in}}{P_{out}} = 9$ ). Figure 4-15 shows the values of  $\beta$  calculated from the simulations described in the previous sections. It appears that  $\beta$  and the amplitudes of the slow population exhibit similar trends, except for the case of the domain radius variation.

It is intuitive, in view of the data presented, that an increasing number of trapped particles would lead to a greater slow component amplitude. The parameter  $\beta$  is often used in spot-vary FCS [1, 2] data interpretation. It links the effective diffusion measured in the presence of domains to that measured in their absence:

$$D_{eff} = D_{free}(1 - \beta) \tag{4.1}$$

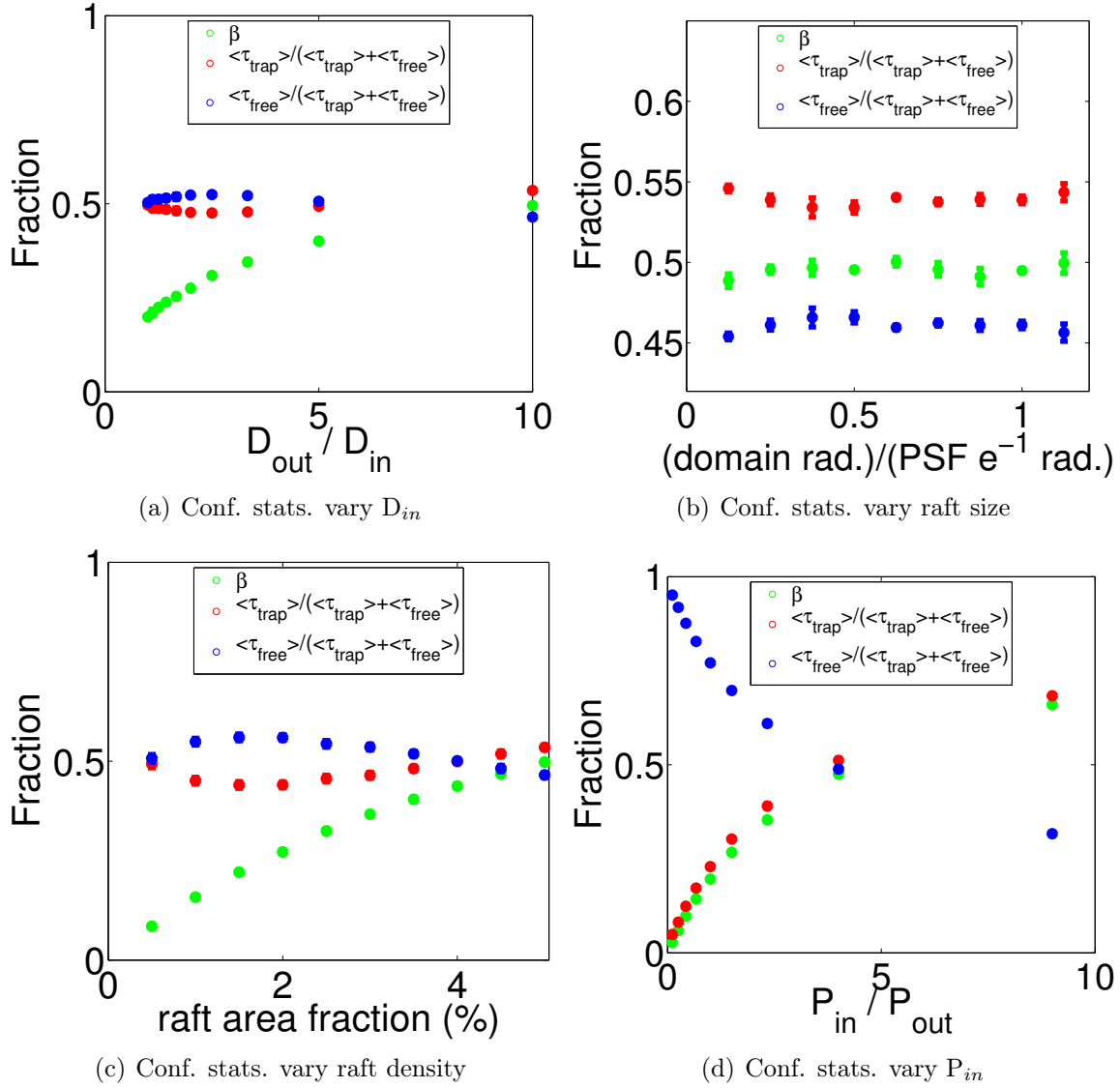


Figure 4–15: Plots of fractional confinement statistics calculated from particle positions from the computer simulations. Green symbols show the ratio of the average number of particles inside domains to the total number of particles in the system,  $\beta$ . Red symbols represent the ratio of the average time particles spend inside domains,  $\langle \tau_{trap} \rangle$  to the sum of  $\langle \tau_{trap} \rangle$  and the average time particles spend outside domains,  $\langle \tau_{free} \rangle$ . This quantity, labelled  $\beta_\tau$  should be equivalent to  $\beta$ . Blue symbols represent  $1-\beta_\tau$ .

Also, these studies define  $\beta_\tau$  in terms of the average time particles spend in the free and trapped states:

$$\beta_\tau = \frac{\tau_{trap}}{\tau_{trap} + \tau_{free}} \quad (4.2)$$

Therefore,  $\beta$  is calculated as a ratio of the number of particles within domains at equilibrium divided by the total number of particles, while  $\beta_\tau$  is recovered from the average time particles spend in the free and trapped states. Figure 4–15 shows total time normalized  $\tau_{trap}$  and  $\tau_{free}$  in red and blue symbols respectively, calculated from particle coordinates from our simulations. Equation 4.2 holds only for the variable  $P_{in}$  simulations and it is not clear at this stage why other simulated scenarios did not satisfy this equation. A later section of this chapter explores in a more systematic way the variation of  $\beta$ ,  $\tau_{trap}$  and  $\tau_{free}$  as a function of  $D_{in}$ ,  $P_{out}$ , domain radius, and domain density. It is interesting to note that the characteristic parameters,  $D_{fast}$ ,  $D_{slow}$  and  $Amp_{fast}$  follow a trend opposite to  $\beta$ . This is in agreement with the equation 4.1.

#### 4.6 Domain size: aliasing or large effective clusters?

The data presented for varying domain radius suggested that this parameter could be inferred from the plateau of the slow component  $D_{slow}\tau$  plot. Nevertheless, the data shown from expected value suggests that for domains  $\leq 0.25 \mu\text{m}$  in radius, the recovered domain radius had a systematic deviation from the expected value (see figure 4–10 c). The origin of this effect was at first considered to be due to spatial aliasing. Indeed, for the smallest spatial sampling unit of an image, a pixel, the Nyquist sampling criterion implies that any object sampled at spatial

frequencies smaller than the reciprocal of twice the pixel size, will be aliased. Therefore, a domain radius of  $0.2 \mu\text{m}$  is the minimum accurately measurable value assuming a pixel size of  $0.1 \mu\text{m}$ .

Hence, spatial aliasing could be responsible for the overestimation of the recovered radii of the small domains. Nevertheless, farther investigation suggests a different hypothesis. In the simulations reported, when the domain radius was set to smaller values, the total number of domains was increased simultaneously to maintain the pre-set domain area fraction to 5 %. Therefore, when domain radius decreased the number of domains was increased, per field of view, giving rise to possibly larger effective domains. It is important to emphasize that domains were placed such that their areas did not overlap. Therefore, when particles occupy two neighbouring domains, separated by a distance smaller than or close to the radius of the PSF, the image produced by convolution with the PSF shows the neighbouring domains as a larger connected object. Figure 4–16 shows images of the pixel averages for time series simulations DC components for the different domain radii considered in the simulations. Clearly, as radius increases, the number of domains per image decreases, leading to a well-resolved domains. Consequently, the intensity fluctuations from particle exploring domains by diffusion, will report the correct radii in cases of larger domains. On the other hand, for smaller domains the larger numbers create the appearance of larger structures due to the PSF limited resolution.

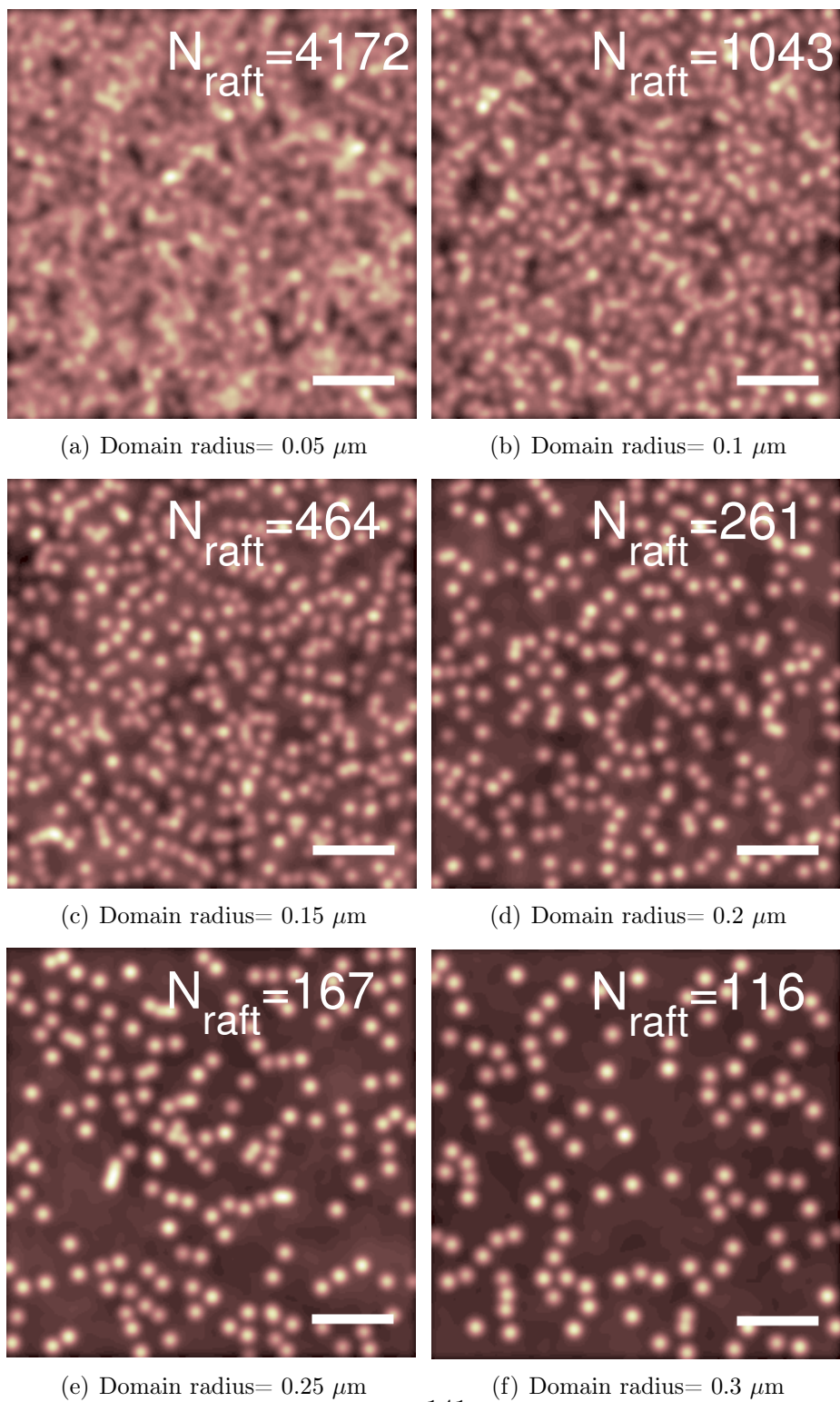


Figure 4–16: Average pixel intensity images of time series for different domain radius scenarios. In each image the total number of domains present,  $N_{\text{raft}}$ , is displayed. Scale bar is 5  $\mu\text{m}$ .

In order to further explore this idea and characterize the confinement statistics, systematic simulations were run with low numbers of rafts per field of view. The simulation parameters were varied as described in the previous sections but the number of domains was fixed 50, 100 and 200 per field of view, independent of their radius. The following section details the results, but a quick examination of figure 4–19 b, e, and h, suggests that plateau of the slow component does not follow any particular trend for small domains (less than  $0.2 \mu\text{m}$  in radius). These erratic data observed for small domains proves to be independent of their area coverage. Instead, further investigation in particles confinement statistics suggests that particles do not partition in large fraction into small domains (figure 4–18). In other words, for small domain simulations, a small fraction of particles is confined at any time during the time series. Therefore, the small subset of particles will be exploring the small domains, leading to the relatively low amplitude in correlation function and low plateau for the slow component (figure 4–19 b, e, and h).

#### 4.7 Systematic characterization of confinement statistics

This section explores by means of simulations, the relationship between the average partition coefficient,  $\beta$ , and the input parameters ( $D_{in}$ ,  $P_{out}$ , domain radius, and domain density). The probability of exiting domains was set to 0.01 or 0.1. The probability of entering domains was set to 0.5. For each  $P_{out}$  simulation scenario,  $D_{in}$  was set to 0.001, 0.005, 0.01 and  $0.02 \mu\text{m}^2/\text{s}$ .  $D_{out}$  was fixed at  $0.01 \mu\text{m}^2/\text{s}$ . The domain radius was varied in the range of 0.05 to  $0.45 \mu\text{m}$  with  $0.05 \mu\text{m}$  increments. The PSF  $e^{-1}$  radius was set to  $0.4 \mu\text{m}$ , making all except

one ( $0.45 \mu\text{m}$ ) domain radii below the optical resolution limit. In the previous simulations, when the domain radius was varied, the domain number was varied too in order to keep the total domain area coverage set to 5 %. In the simulations presented in the following section, the number of domains was fixed to 50, 100 or 200 per field of view, independent of the set domain radius. There are two main reasons for the choice of this domain density. First, as observed in the previous section, decreasing the domain radius to  $0.05 \mu\text{m}$  leads to a dramatic increase in the number of domains (4172). The high density of sub-optical resolution domains can lead to the spatial overlaps and so produce the large effective domains, as discussed in previous section. Moreover, having the smaller number of domains per field of view could simulate a more realistic scenario to test the limits of the detection of confined dynamics using kICS analysis.

In the simulations performed in this work, particles are initially randomly seeded in a 2D field of view. The system was equilibrated prior to the conversion of particle positions into an image series or other useful confinement statistics. For each simulated scenario, 12 000 time points were generated and the confinement statistics,  $\beta$ ,  $\langle\tau_{trap}\rangle$  and  $\langle\tau_{free}\rangle$  were calculated. The large number of time points was required to assess the time variation of the fraction of particles inside and outside of domains,  $\frac{N_{in}}{N_{tot}}$ . This quantity measures effectively the average partition coefficient,  $\beta$ , at each time point. For each simulation, the range of time values used for the  $\beta$  calculation was selected such that the  $\frac{N_{in}}{N_{tot}}$  is in steady state equilibrium. For all scenarios considered, the mean particle partition coefficient,  $\beta$ , fluctuated at equilibrium around a mean value, for the later time points. The

particles' positions for the last 2000 time points, situated within this equilibrium range, were selected to be used for the image series convolution as well as for the calculation of confinement statistics.

Figure 4–17 a) shows a plot of  $\frac{N_{in}}{N_{tot}}$  as a function of frame number for a simulation example with  $P_{out} = 0.01$ ,  $D_{in} = 0.001 \mu m^2/s$ ,  $D_{out} = 0.01 \mu m^2/s$ , domain radius =  $0.2 \mu m$  and 50 domains in the field of view. The characteristic  $\beta$  extracted by averaging the ratio  $\frac{N_{in}}{N_{tot}}$  over the last 2000 time points was  $0.633 \pm 0.004$ , where the error represents the standard deviation of these values. The exact times particles spend inside vs outside of domains can be calculated for these time points and distributions of times for a free and bound states are shown in figure 4–17 b). The average free and bound times,  $\tau_{free}$  and  $\tau_{trap}$ , represent averages of these distributions. Recall, that eqn 4.2 links these parameters to the partition coefficient  $\beta$ . We refer to this value as  $\beta_\tau$ .

Figure 4–18 shows the averaged simulation results for  $\langle \tau_{trap} \rangle$ ,  $\langle \tau_{free} \rangle$ ,  $\beta$  and  $\beta_\tau$ , in the case of  $P_{out} = 0.01$ . As the domain radius increases, at a given  $\frac{D_{in}}{D_{out}}$  ratio,  $\beta$  increases toward 1 (figures 4–18 b, d and f). This result is intuitive, since the time per frame ( $t_d$ ) changes with the domain radius and diffusion coefficient inside domain as  $\frac{(domain\ radius)^2/5}{4*D_{in}}$ . Consequently, an increase in domain radius increases  $t_{frame}$  for a fixed  $D_{in}$ . Therefore, for a given number of frames, particles will try to explore equivalent areas. On the other hand, for small domain radius, particles will encounter the boundary more often than for bigger ones, leading to more frequent escapes. Similarly, for a fixed domain radius, decreasing the diffusion coefficient

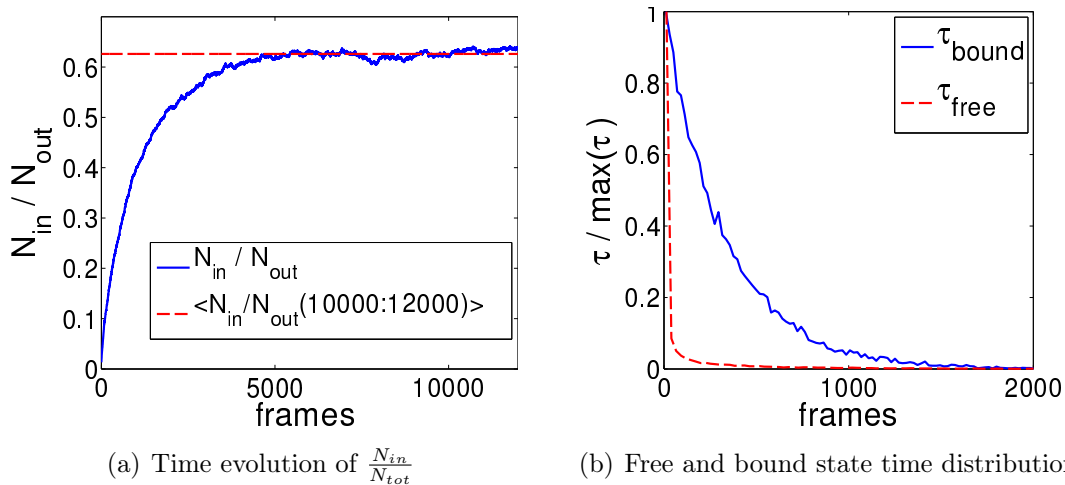


Figure 4-17: Frame series plots of  $\frac{N_{in}}{N_{out}}$  and free and bound state time distributions calculated from particle coordinates for one simulation. a) The partition fraction as a function of time frame. Red dashed line is the average of the last 2000 time points, giving  $\beta$ . b) Steady state normalized free and bound states time distributions. Blue line is the free state time distribution, while the red line is for the bound state. Each distribution was normalized by its maximum value. For both graphs, the simulation parameters were  $P_{out}=0.01$ ,  $D_{in}=0.001 \mu m^2/s$ ,  $D_{out}=0.01 \mu m^2/s$ , domain radius =  $0.2 \mu m$ , 50 domains in field of view.

increases  $\beta$ . Examination of figures 4-18 b, d and f) suggests that increasing the number of domains, from 50 to 100 per whole field of view, leads to an increase in  $\beta$ . Again, this is not surprising as increasing the number of domains leads to an increase in the total number of confined particles, for a given scenario.

Interestingly, comparing  $\beta$  and  $\beta_\tau$  in figures 4-18 b, d and f) suggests that eqn 4.2 does not hold for small domains (radius  $\leq 0.2 \mu m$ ). In parallel with this observation, the average time particles spend in the free state (figure 4-18 a, c and e) is only  $\sim 4$  times smaller for the range of small domains radii ( $0.05-0.15 \mu m$ ) and large  $D_{in}$  ( $0.01-0.02 \mu m^2/s$ ) simulated. In order to obtain the smallest  $\beta$  observed

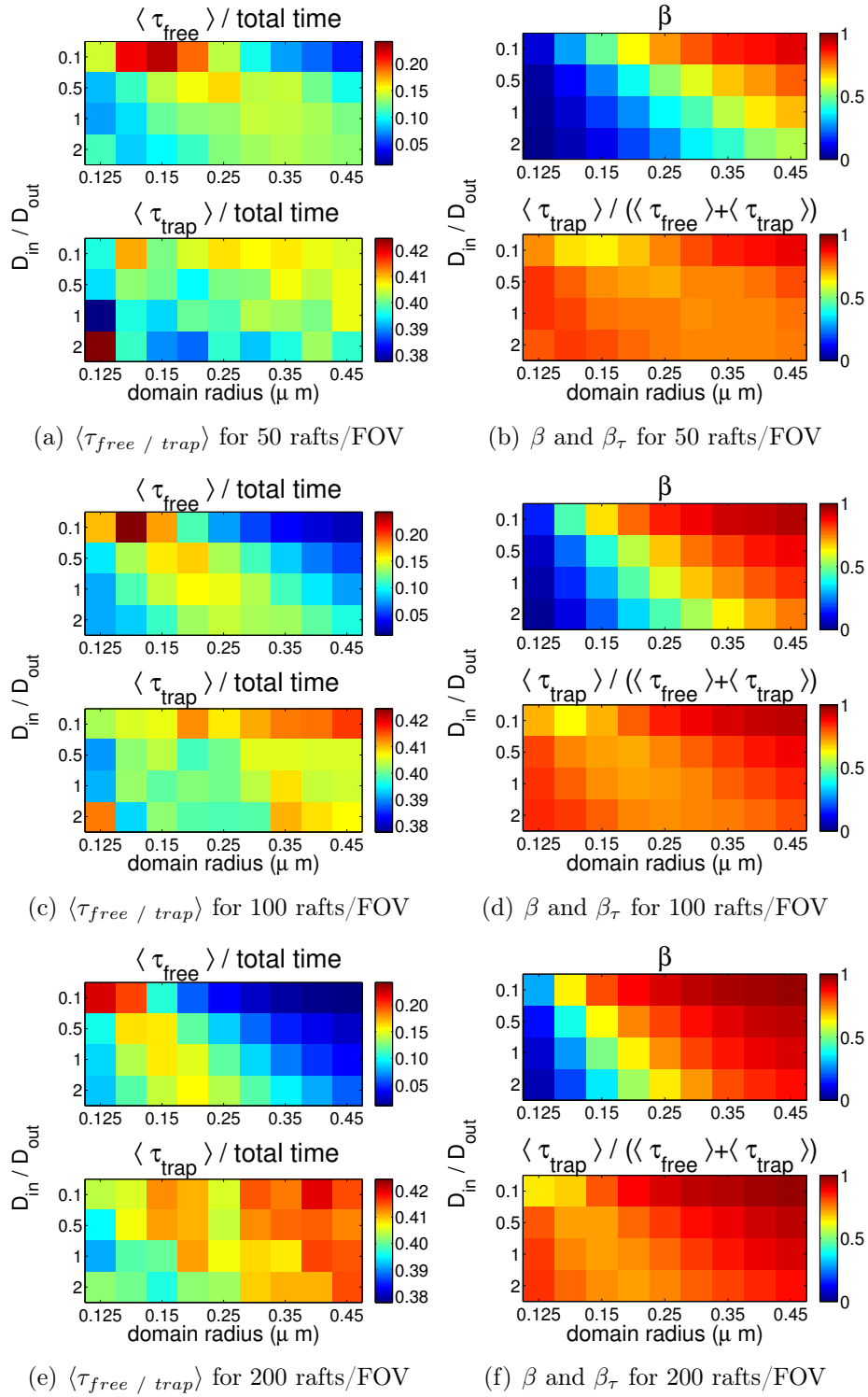


Figure 4-18: Confinement statistics for  $P_{out} = 0.01$ . a), c) and d) are  $\langle \tau_{free} \rangle$  and  $\langle \tau_{trap} \rangle$ , normalized to the total amount of frames, for 50, 100 and 200 domains per field of view (FOV), respectively.  $\frac{D_{in}}{D_{out}}$  and domain radius were varied.  $D_{out}$  was set to  $0.01 \mu m^2/s$ . b), c) and d) show calculated  $\beta$  and  $\beta_\tau$  for 3 raft densities considered.

(0.025), it would require  $\tau_{free}$  to be 39 times greater than  $\tau_{trap}$ . Similar behaviour was seen in figure 4–15 where  $\beta$  and  $\beta_\tau$  do not match, except for the case of  $\frac{P_{in}}{P_{out}}$  variation. When analyzing the overall patterns of data shown in figure 4–18, we notice that  $\beta_\tau$  depends more strongly on  $\langle\tau_{free}\rangle$  than on  $\langle\tau_{trap}\rangle$ . A similar figure for  $P_{out} = 0.1$ , can be found in the appendix at the end of this chapter. The kICS analysis and correlation functions will be similar to those presented in figures 4–10 and 4–8, as  $P_{out}$  was set to 0.1 in those simulations.

Figure 4–19 shows the results of the two Gaussian fit of the correlation functions obtained for each simulation scenario considered. These values were each obtained from a single image time series per condition, and thus exhibit large uncertainties. Indeed, that is the case for the diffusion coefficient extracted for the fast component,  $D_{fast}$  (figures 4–19 a, d and g). Fitting of  $D_{fast}\tau$  vs  $\tau$  was done for two different  $\tau$  ranges, an early ( $\tau=2$  to 10 frames) and late lags ( $\tau=30$  to 100 frames). These two different fitting regimes of  $D_{fast}\tau$  was adapted because two different apparent regimes of were apparent. In either case, the  $D_{fast}$  obtained was smaller than the  $D_{out}$  set in the simulations.

When examining the early slope of the slow component, it appears to increase with increasing  $D_{out}$  and domain radius. Figures 4–19 b), e) and h) show this within the green dashed rectangle. Outside of this rectangle, the extracted  $D_{slow}$  and  $plateau_{slow}$  are uncorrelated with the increase in the ratio  $\frac{D_{in}}{D_{out}}$  and domain radius. The increase in the number of domains from b) to h) leads to an increase in the extent of this coherence rectangle. Simultaneously, the saturation

of the slow component plateau,  $\text{plateau}_{slow}$ , increases with increasing domain radius and increasing  $\frac{D_{in}}{D_{out}}$ . This observation is in agreement with the previous simulations (figures 4–10 and 4–8 c), where increasing the domain radius and  $\frac{D_{in}}{D_{out}}$  increased the slow component plateau. The ratio  $\frac{D_{in}}{D_{out}}$  acts on the slow plateau in a fashion similar to that of the  $\frac{P_{out}}{P_{in}}$ . The smaller these ratios are, the smaller is the probability for the particles to encounter the domain boundaries which reduces the chances of escaping the domain. As a result, the effective domain area, as measured from the slow component saturation, decreases. Thus, this effective domain area measures the effective area that particles explore through diffusion and partitioning at small spatial scales.

The amplitudes of the two Gaussian fit of kICS correlation function follow the expected trends 4–19 c), f) and i). The smaller  $\frac{D_{in}}{D_{out}}$  is, the more particles are confined and so the saturation of the slow component amplitude,  $\text{Amp Satur}_{slow}$ , increases. Conversely, the fast component amplitude saturation,  $\text{Amp Satur}_{fast}$ , decreases. In parallel, an increase in the raft size leads to an increase in the slow component saturation, which was also observed in figure 4–10 d. It is not surprising that increasing the total number of domains, from 50 to 200, increases confinement as witnessed from the increase in the saturation of the slow component.

These simulation results confirm that kICS correlation function fitting with a sum of two Gaussians can differentiate between different confinement scenarios. The analysis of simulated single image series suggests that the confinement

statistics, such as  $\beta$ , correlate with the extracted fit parameters, such as  $D_{slow}$ ,  $plateau_{slow}$  and amplitude saturations. The extracted fast component diffusion coefficient,  $D_{fast}$  does not show a clear correlation and likely a greater number of simulated image series would be needed to improve the statistics.

Interestingly, the extracted phase space maps presented in figure 4–19 have very poor correlation in the region of small domain radii (0.05-0.2  $\mu\text{m}$ ). Incidentally, this was the same region for which  $\beta_\tau$  in figure 4–18 did not match  $\beta$ . It is possible that in this part of phase space, domains are too small and  $D_{in}$  is too high, which makes the average domain time occupancy very low ( $\beta \sim 0.02$ ). The low domain temporal occupancy leads to a low number of spatio-temporal intensity fluctuations, which is necessary for accurate and precise kICS analysis.

The appendix at the end of this chapter gives the average  $R^2$  extracted for the sum of two Gaussians fit applied to the kICS correlation functions of the image series generated for each simulation scenario.

#### 4.8 Effects of background noise on kICS correlation functions

In this thesis, the effects of noise on kICS correlation are not studied in detail as this has been presented previously [3]. However this section outlines the impact of background noise on the CF. Figure 4–20 shows simulated images with added background noise with signal-to-noise ratio ranging from 100 down to 5. The experimental data presented in the next chapter have fairly good signal-to-noise ratio, due to the presence of several Alexa dyes per GPI-GFP molecule observed.

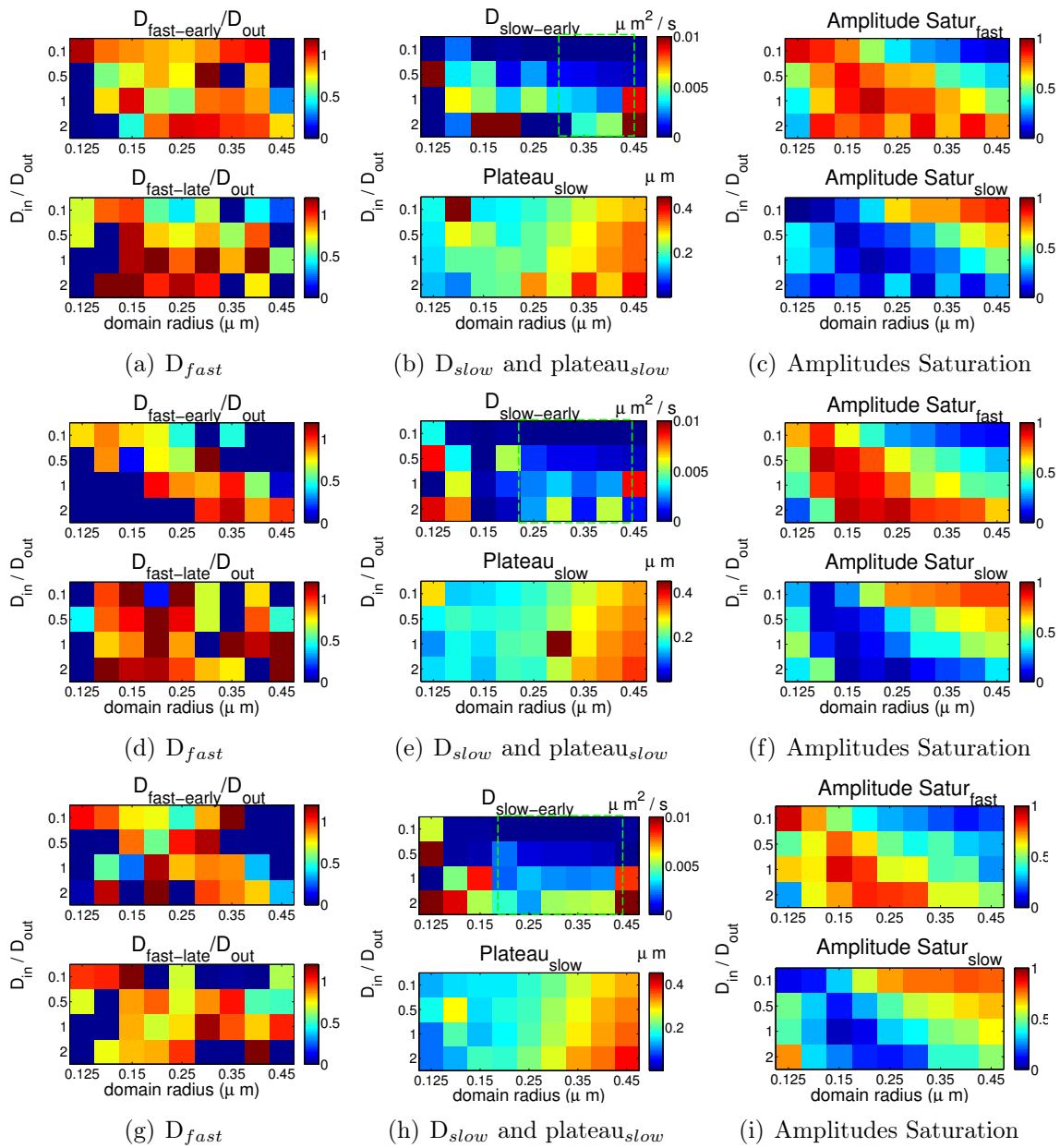


Figure 4–19: kICS analysis fitted parameters for single image series simulations with  $P_{out}=0.01$ . a), d) and g) are fast component diffusion coefficients,  $D_{fast}$ , obtained from fitting early and late temporal lags. Top to bottom rows display scenarios where the number of domains per field of view (FOV) was 50, 100 and 200, respectively.  $D_{out}$  was set to  $0.01 \mu\text{m}^2/\text{s}$ . b) , e) and h) show the early slope  $D_{slow}$  and plateau saturation of the slow component. c), f) and i) denote the saturations of amplitudes for the fast and slow components.

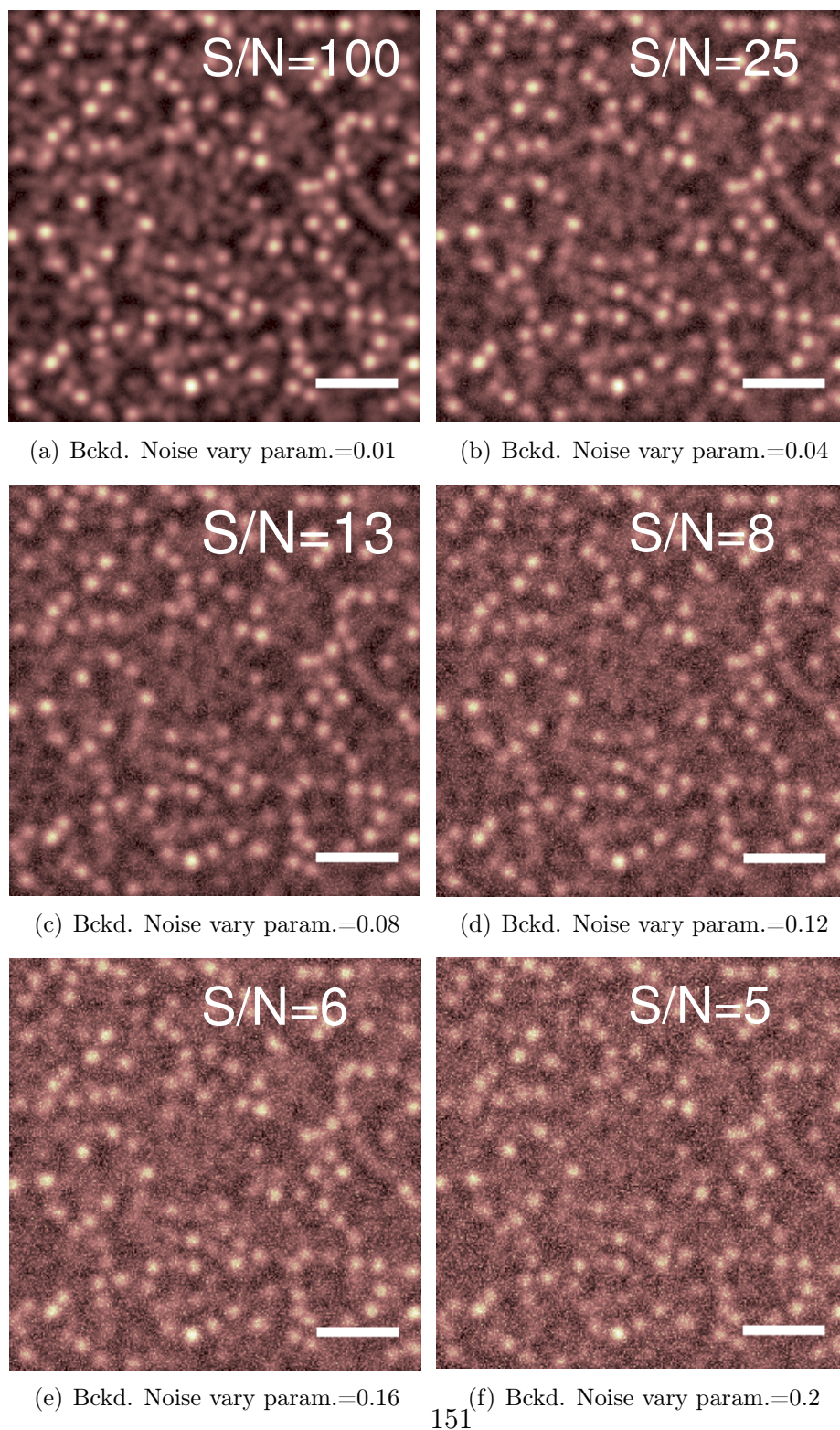


Figure 4-20: Background noise variation effect on simulated images for domain radius of  $0.2 \mu\text{m}$ . Each sub-caption identifies the value of noise parameter used in the simulation. Scale bar is  $5 \mu\text{m}$ .

The correlation functions for each  $\frac{S}{N}$  ratio simulation are shown in figure 4–21. As the background noise increases, the correlation function gets truncated at a certain cutoff value  $k_{cut}^2$ . However it can still be fit below this cutoff and parameters can be extracted. Nevertheless, for very small domains, the cutoff due to noise could remove some of the essential features of the correlation curve, needed for the fitting of the two Gaussians. It is very important that the correlation data are examined prior to fitting and further quantification. An abnormally sharp cutoff of the correlation function at all temporal lags would suggest the presence of important background noise. Since  $k_{cut}^2$  truncates the CF at all temporal lags equally, it is important to distinguish it from the features of some simulated CF observed earlier (see for example figure 4–3 g, h and i). Those CFs do not have a cutoff at all temporal lags like those CFs from background noise corrupted image series 4–21. Therefore, the rule of thumb before one proceeds with the confinement analysis of the CF calculated from image data series, is the examination of CF for a potential background noise induced cutoff. If CF is cut abruptly at all temporal lags, then the fitting range for CF should be below the value of  $k_{cut}^2$ , in order to avoid the bias in the extracted parameters.

The presence of various sources of noise in an image series will introduce an error in the estimation of the plateau saturation and other extracted parameters. Similar effects are known to occur in SPT or other single molecule techniques. Indeed, in the case of a poor signal-to-noise ratio, the extracted particle positions will be inaccurate. Consequently, the MSD curve will systematically be shifted depending on the variance of the noise present in the image series [4]. The shifted

MSD could lead to an overestimate of the domain size. Furthermore, the Gaussian background noise was shown to affect the extraction of the diffusion coefficients from the early temporal lags of the MSD curves in the SPT data [5]. Nevertheless, when all image series are acquired under the same conditions of the illumination, exposure time and EMCCD gain, a similar systematic error in the extracted parameters will be present in the analysis. Therefore, the background noise effect on CF, regardless of its amplitude, will shift the effective domain value by an equal amount for all the image series acquired under similar imaging conditions.

#### **4.9 Results for kICS analysis of simulations of meshwork confinement domains**

In this section we examine results for kICS analysis of simulations of the meshwork type of confinement. The scenarios of varying barrier crossing probability and varying mesh pore diameter ( $L$ ) are explored. A phenomenological model was developed, as outlined at the end of the Theory chapter (chapter 3), in order to characterize the calculated correlation functions. Figure 4–22 a) shows an example of a kICS correlation function calculated from a meshwork confinement simulation. A cursory assessment of this correlation function suggests that it does not exhibit a decay with two distinct regimes as in the case of isolated domains confinement. Therefore, it can be effectively fit by a single Gaussian decay as a function of spatial frequencies at a given  $\tau$ . As the temporal lag increases (blue to red lines), the correlation function collapses. The change in the decay constant,  $D\tau$ , can be plotted as  $4D\tau$  vs  $\tau$ , which effectively is equivalent to an ensemble averaged MSD vs time plot. Figure 4–22 b) shows this relation as a function of

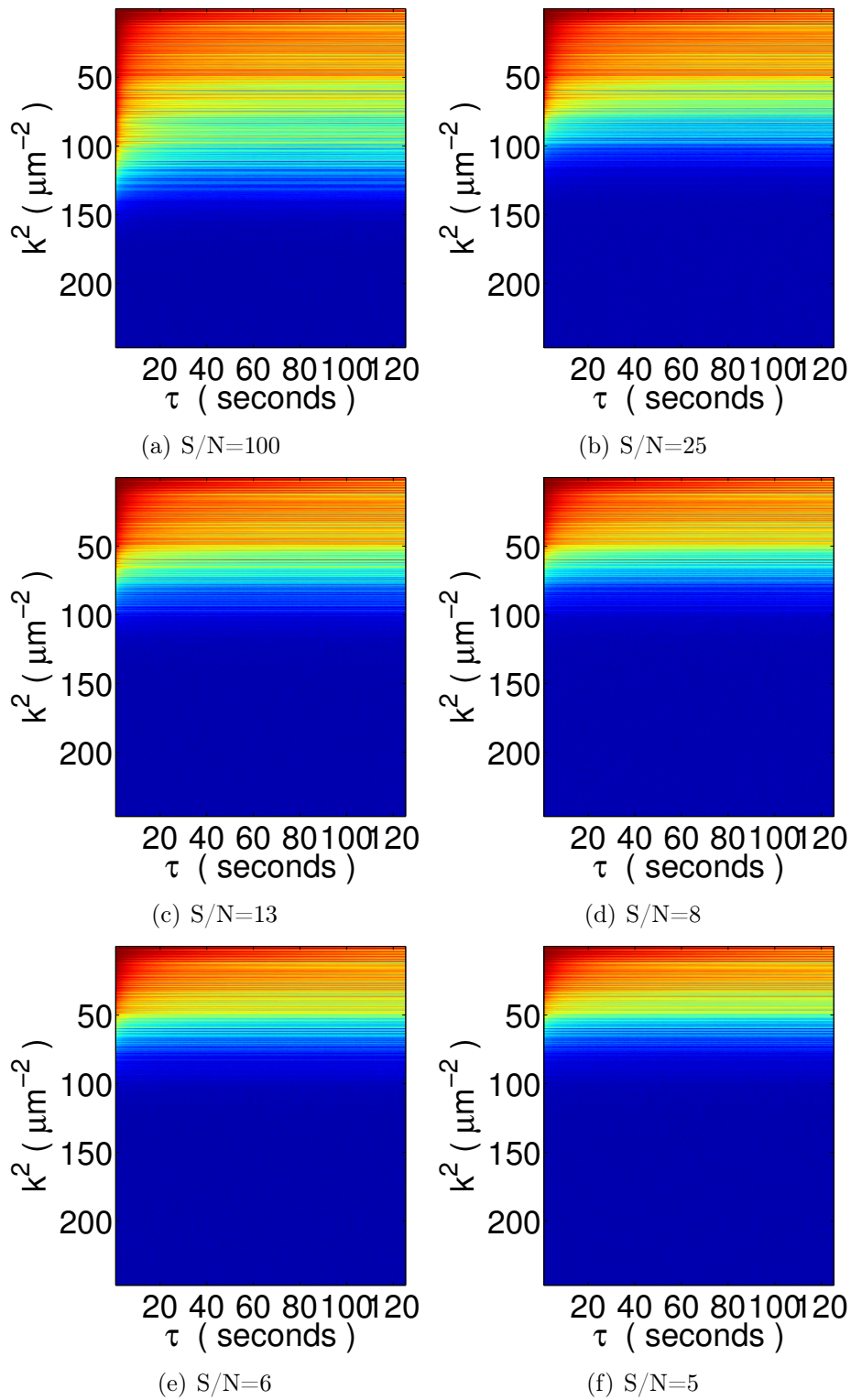


Figure 4-21: Background noise variation effect on correlation functions for data with domain radius of  $0.2 \mu\text{m}$ . Each sub-caption identify the value of signal-to-noise ratio. All correlation functions were zero temporal lag normalized to have maximum value of 1 (red) and minimum of 0 (blue).

particle crossing probability. As  $P$  decreases (going red to blue in figure 4–22 b) the  $4D\tau$  vs  $\tau$  curves deviate from  $4D_\mu\tau$ , where  $D_\mu$  labels the microscopic diffusion coefficient within mesh pore.

In meshwork confinements, the particles explore each mesh pore with a microscopic diffusion coefficient and hop from one compartment to an adjacent with a macroscopic diffusion coefficient  $D_M$ , that depends on  $P$ . In figure 4–22 b), each of the cases exhibit an early ( $\tau$  0 to 0.2 s) regime, that is labelled ‘early’. Similarly, the later temporal lags are characterized by another linear regime, which is labelled ‘late’. It is the early component that characterizes the motion of particle within a mesh pore ( $D_\mu$ ), while the late one determine the hopping dynamics on larger spatial scales. Another important parameter from the late regime fit is the intercept on the  $4D\tau$  axis. This parameter is related to the mesh size, as was shown in theory chapter 3. In order to characterize the efficiency of a given meshwork in trapping particles we define:

$$S_{conf} = A + B \frac{2\delta r}{L} \frac{1 - P}{P} \quad (4.3)$$

where  $\delta r$  denotes the diffusion step size within a mesh compartment, and  $L$  denotes the mesh pore diameter. This parameter, is comparable to the parameter  $\beta$  of the isolated domains confinement and increases with increasing confinement.

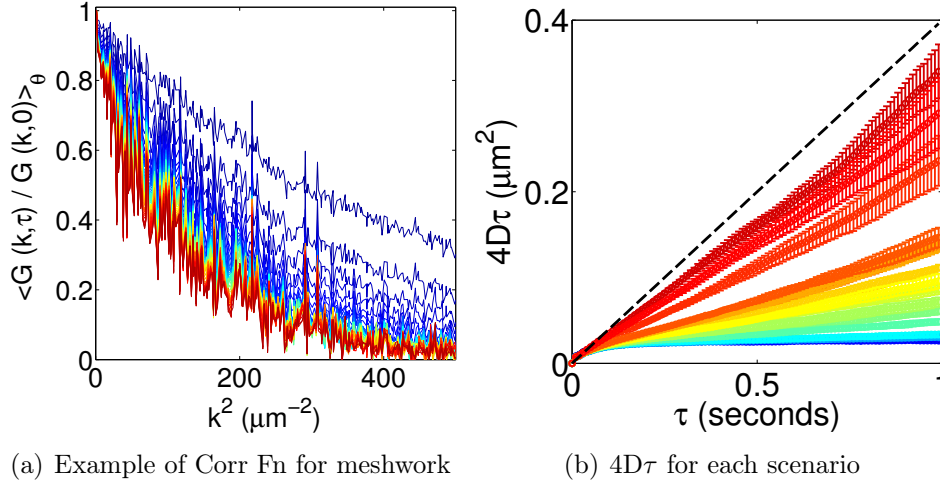


Figure 4–22: a) Example of circularly averaged and normalized kICS functions calculated for a meshwork simulation with  $P=0.1$ ,  $D_\mu=0.1\mu\text{m}^2/s$  and  $L=0.25\mu\text{m}$ . Blue to red traces label increasing temporal lag,  $\tau$ . b)  $4D\tau$  extracted for different meshwork scenario. Red to blue data points indicate the decrease in probability (0.4 to 0.001) for particles to cross the meshwork barriers, while pore mesh diameter was kept constant at  $0.25\mu\text{m}$ . The dashed black line shows  $4D\tau$  with set microscopic  $D_\mu=0.1\mu\text{m}^2/s$ .

#### 4.9.1 Results for kICS analysis of meshwork simulations to establish the ICS diffusion law

Characterization of kICS CF by single Gaussian fit for simulations with a varying crossing probability ( $P=0.001$  to  $0.4$ ,  $L=250\text{nm}$  and  $D_\mu=0.1\mu\text{m}^2/s$ ) led to  $4D\tau$  vs  $\tau$  as displayed in figure 4–22 b). Linear regression of early and late regimes of  $4D\tau$  vs  $\tau$  provide the characteristic diffusion coefficients,  $D_{early}$  and  $D_{late}$ , which can be used to infer the microscopic diffusion coefficient and meshwork confinement strength. Figure 4–23 shows that the measured diffusion coefficient for the late regime decays strongly with increasing confinement strength (figure 4–23 a), while the measured early regime diffusion coefficient was calculated to be

slightly less than the set value of  $D_\mu$ . Plotting the ratio of early and late slopes vs confinement strength, results in a linear relationship, with a y-axis intercept of 1 (figure 4–23 b). Therefore, at a confinement strength of zero, the two diffusion coefficients are equal to one. It is important to note that in the case of square mesh of a diameter  $L$ , two characteristic length scales emerge in the analysis. The first is equal to the half mesh radius  $L/2$  and the second is the distance from the center of the mesh to its corner, equal to  $L/\sqrt{2}$ . We will label these as a lower and an upper bound length scales of the meshwork.

Plots of the square root of the y-axis intercept from the fit at a later  $\tau$  regime vs confinement strength suggests that for low  $S_{conf}$  values, the recovered mesh size is inaccurate (figure 4–23). Therefore, the extracted mesh size needs to be corrected by the following expression that links  $D_{early}$ ,  $D_{late}$  and  $L_{app}$  to the actual mesh size:

$$L = \left(1 + \frac{D_{late}}{D_{early}}\right)L_{app} \quad (4.4)$$

As specified in the theory chapter, this is a phenomenological equation that is not derived from any specific model. Nevertheless, it is an empirical correction method for values of the mesh size recovered which is particularly useful in the case of intermediate to high  $S_{conf}$ . For very low confinement strength ( $S_{conf} \leq 10$ ) simulations the difference between the two regimes (early and late) is not large enough to be accurately treated using this approach.

Finally, simulations with variable mesh diameter were performed with diameters ranging from  $L=200$  to  $425$  nm, while keeping  $P=0.01$  and  $D_\mu=0.1\mu m^2/s$ .

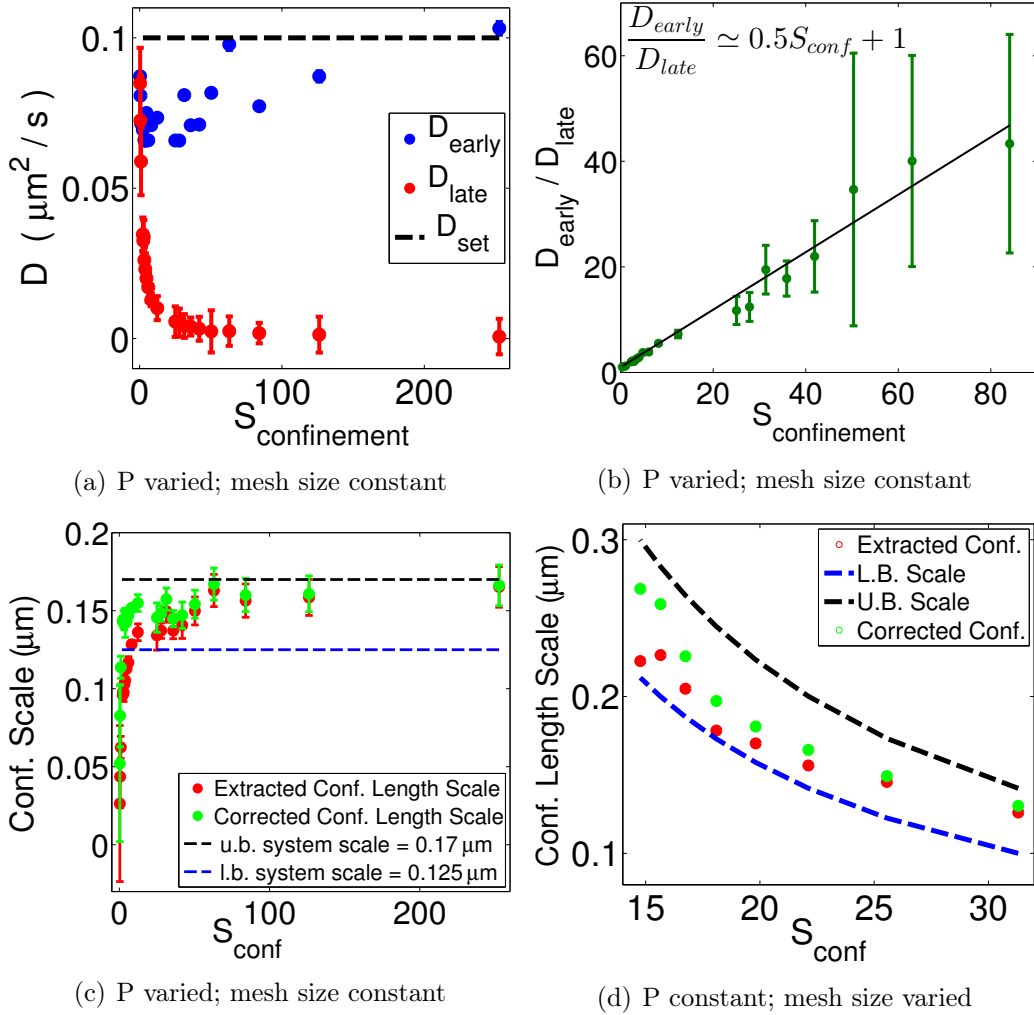


Figure 4-23: kICS analysis of simulations with either varied  $P$  or the mesh pore size of a meshwork. a) Early (blue) and late (red) diffusion coefficients for varying  $P$  ( $P=0.001$  to  $0.4$ ,  $L=250$  nm and  $D_\mu=0.1 \mu m^2/s$ ), as function of confinement strength. The dashed line shows the set microscopic diffusion coefficient. b) A plot of  $\frac{D_{early}}{D_{late}}$  versus confinement strength with linear regression (black line) outlining the emergent relation between these parameters. c) Measured and corrected confinement length scales for variable  $P$  simulations. d) Measured and corrected confinement length scales for varying mesh pore diameter ( $L=200$  to  $425$  nm,  $P=0.01$  and  $D_\mu=0.1 \mu m^2/s$ ) simulations. In c) and d) the black and blue dashed lines label the upper and lower bounds for the characteristic mesh scale, respectively.

Figure 4–23 d) shows the fit values of mesh sizes before and after correction by equation 4.4. Note that they fall within an acceptable upper and lower bound limits for the mesh sizes considered. Also, all of these mesh pore diameters were of a size smaller than twice the  $e^{-1}$  radius of PSF (set to  $0.28 \mu\text{m}$ ). This suggests that kICS CF of image time series in presence of sub-diffraction sized meshwork can be fit by a single Gaussian function in order to extract the characteristic microscopic diffusion coefficient and a good estimate of the mesh pore diameter.

#### 4.10 ICS diffusion law for Isolated domains

As seen in the introductory chapter, fitting a single Gaussian function in time to the CF measured for isolated domains, can partially characterize the characteristic mobilities and spatial scales of the system (figure 1–21). On the other hand, the analysis of a system with two freely diffusing species by the same approach led to a graph of  $k^2D$  vs  $k^2$  that exhibited similar characteristics to the isolated domains case (figure 4–6 c). Nevertheless, a close inspection of ICS diffusion laws in figure 4–24 suggests that the late regime of this plot will have a nonzero intercept on the  $k^2$  axis. On the other hand, the free diffusion populations example gave an intercept very close to zero.

The determination of slopes of  $k^2D$  vs  $k^2$  for the low and high  $k^2$  regimes, as well as the y-axis intercept from the higher  $k^2$  regime, shows some promising features to this approach for the characterization of the image correlation functions. Figure 4–25 shows these features for the case of varying domain radius simulations described in section 4.2.2. As a comparison, the parameters obtained for the fit

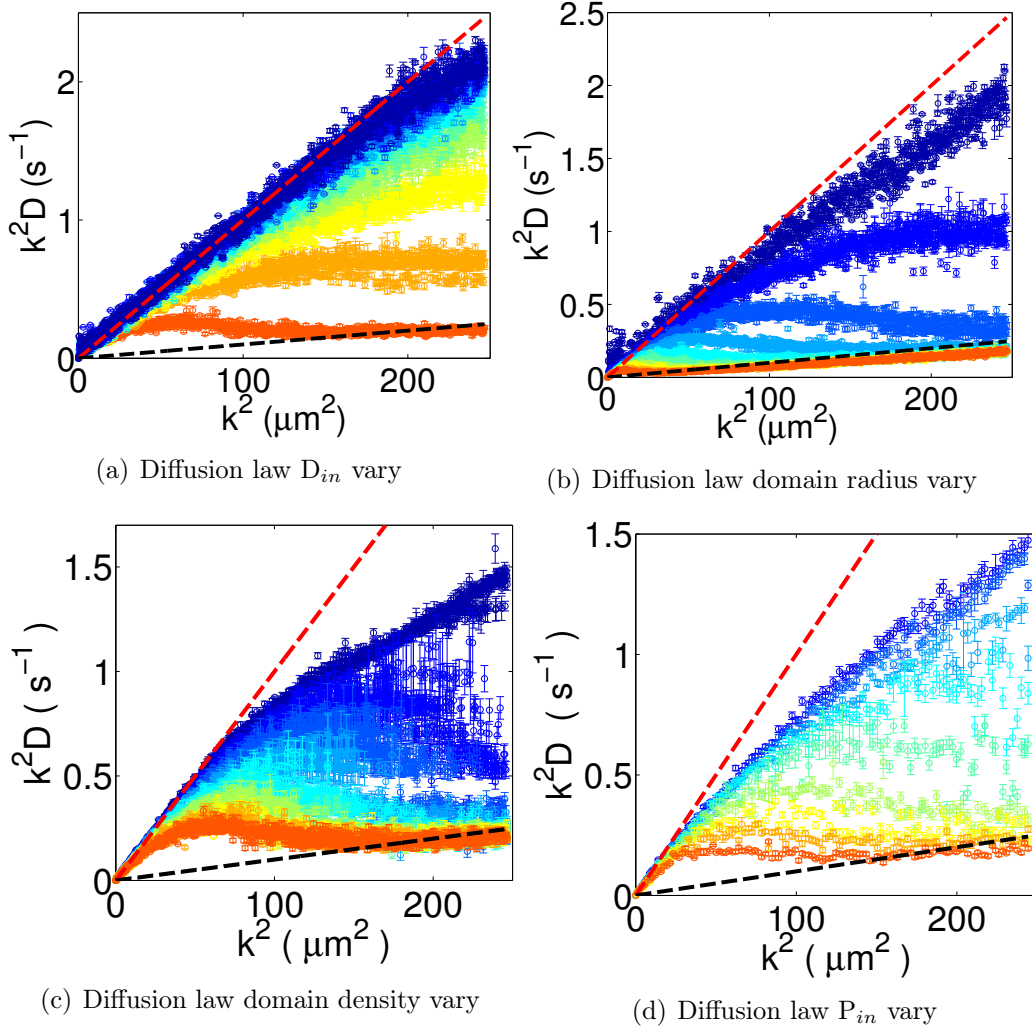


Figure 4-24: ICS diffusion law from single temporal Gaussian fit to the correlation functions. Red and black dashed lines outline  $Dk^2$  for  $D = 0.01$  and  $0.001 \mu m^2/s$ , respectively. Unless specified otherwise, simulations parameters for isolated domains were set to  $D_{in} = 0.001 \mu m^2/s$ ,  $D_{out} = 0.01 \mu m^2/s$ , domain radius =  $0.1 \mu m$ , domain area fraction =  $5\%$ ,  $P_{in} = 0.5$  and  $P_{out} = 0.1$ . The blue to red symbols show ICS diffusion laws for: a) a decreasing  $D_{in}$  ( $D_{in}$  from  $0.01$  to  $0.001 \mu m^2/s$ ), b) an increasing domain radius ( $0.05$  to  $0.45 \mu m$  at  $0.05 \mu m$  increment), c) an increasing domain area coverage ( $0.5$  to  $5\%$  at  $0.5\%$  increment) d) an increasing  $P_{in}$  ( $0.1$  to  $0.9$  at  $0.1$  increment with  $P_{out} = 1 - P_{in}$ ).

of the correlation function for two freely diffusing populations is superimposed on each graph. The diffusion coefficient,  $D_{early}$ , is calculated as a slope from the fit of first linear trend, over small values of  $k^2$  of the ICS diffusion law plots. The second linear trend, at higher  $k^2$  values is denoted  $D_{late}$ . The small  $k^2$  used for fitting is defined by the range of  $k^2$  for which  $k^2D$  increases linearly, usually up to the peak value. The large  $k^2$  range that is linearly fitted comes after the peak value of  $k^2D$ . For different domain radius scenarios (section 4.2.2),  $D_{early}$  does not follow any particular trend, although the values are below the set  $D_{out}$  ( $0.01 \mu m^2/s$ ). The diffusion coefficient recovered from later  $k^2$ ,  $D_{late}$ , increases slightly with increasing domain radius, although its value is below the set  $D_{in}$  ( $0.001 \mu m^2/s$ ). In comparison,  $D_{late}$  for the simulations of two freely diffusing populations is very close to the set value of the smallest diffusion coefficient ( 4–25 b). The y-axis intercept obtained from the late regime fit, has a nonzero value that increases with decreasing domain radii ( 4–25 c). Same figure shows as a reference (blue symbols), the value of y-intercept for the fit of the high  $k^2$  range, extracted from the ICS diffusion law of the case of two freely diffusing species (figure 4–6 c). The value of the peak position, on the other hand exhibited a significant trend. When a Gaussian is fitted in the neighbourhood of the peak, its centroid position can be determined. Plotting peak position and superposing this on the same graph, values of  $\frac{\pi^2}{(2 \times domain \ radius)^2}$  shows almost a perfect match between these two quantities. It is possible therefore, to obtain information on domain radius, even if the plot vs  $\tau$  is considered instead of vs  $k^2$ . For very small domains, noise and spatio-temporal sampling limits, can limit detection, since the peak would appear at higher  $k^2$

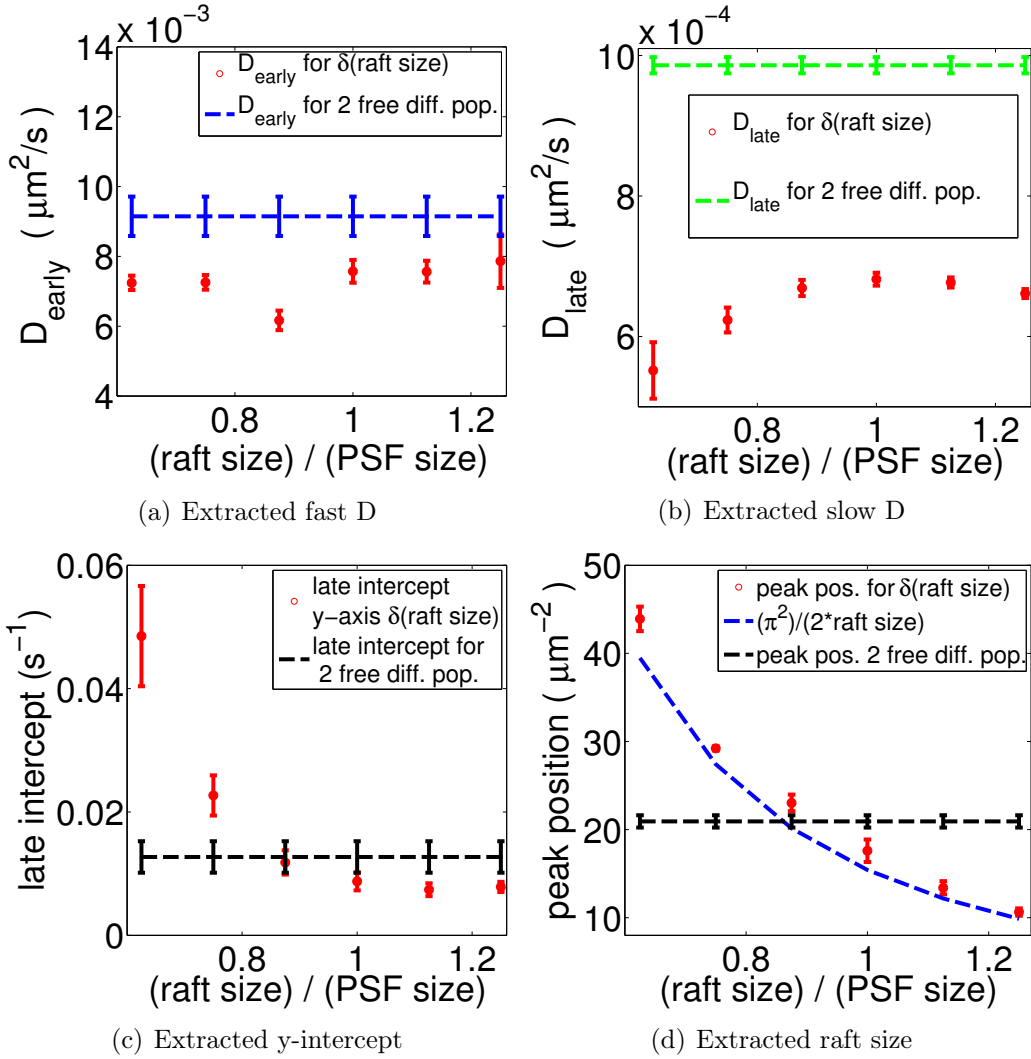


Figure 4-25: Data extracted from ICS diffusion law for the simulated data with isolated domains with the variation of domain radius (labelled raft size). X-axis for each plot was normalized by the PSF  $e^{-1}$  radius which was set to  $0.4 \mu\text{m}$ . For isolated domains simulations  $D_{in}=0.001 \mu\text{m}^2/\text{s}$ ,  $D_{out}=0.01 \mu\text{m}^2/\text{s}$ , and  $P_{in}$  and  $P_{out}$  at 0.5 and 0.1 respectively. In the case of two freely diffusing species, the diffusion coefficients ( $D_1$  and  $D_2$ ) were set to 0.01 and  $0.001 \mu\text{m}^2/\text{s}$ . ICS diffusion law extracted parameters a) to d) for isolated domains simulations with varying domain radius were compared to the parameters extracted from simulations of two freely diffusing populations.

As was shown in the last chapter, domains create apparent slow and fast mobilities, that depend on the set system properties ( $D_{in}$ ,  $D_{out}$ ,  $P_{in}$ ,  $P_{out}$ , domain radius, domain area fraction). Proper analysis of the characteristic decays of image spatio-temporal correlation can infer the characteristic effective domain sizes and effective diffusion coefficients. The amplitudes of the two characteristic modes of motion are linked to the average number of confined and trapped particles at equilibrium. Care should be taken prior to the application of this methodology in cases with poor signal-to-noise ratio. It is always important to first examine the raw data images and calculated correlation functions, before proceeding with further steps of characterization, such as fitting. The meshwork confinement is characterized by a single Gaussian decay in spatial frequencies and so can be used to extract the mesh pore sizes, in cases of moderate to high barrier crossing probabilities. The next chapter demonstrates the applicability of these methods to study isolated domains in cells, by kICS analysis of fluorescence microscopy image series of a well-characterized domain partitioned GPI anchored protein.

## Appendix Chapter 5

This appendix contains two figures from the confinement statistics characterization. The first figure 4–26 shows the confinement statistics for  $P_{out} = 0.1$ .

The second figure 4–27, shows the average  $R^2$  obtained from the sum of two Gaussians fit of kICS correlation functions, in case of each scenario considered. For each correlation function fitted, an  $R^2$  value was obtained for each temporal lag. The average is computed for all temporal lags and called  $\langle R^2 \rangle$ . A standard deviation is also computed for  $R^2$ , called  $\sigma(R^2)$ . In case of a good fit, for a given simulation scenario,  $\langle R^2 \rangle$  is close to 1 while  $\sigma(R^2)$  tends to zero. What is observed is that fit is not great for the correlation functions of small radius domains (0.05-0.15  $\mu\text{m}$ ). This region of phase space produced uncorrelated confinement properties.

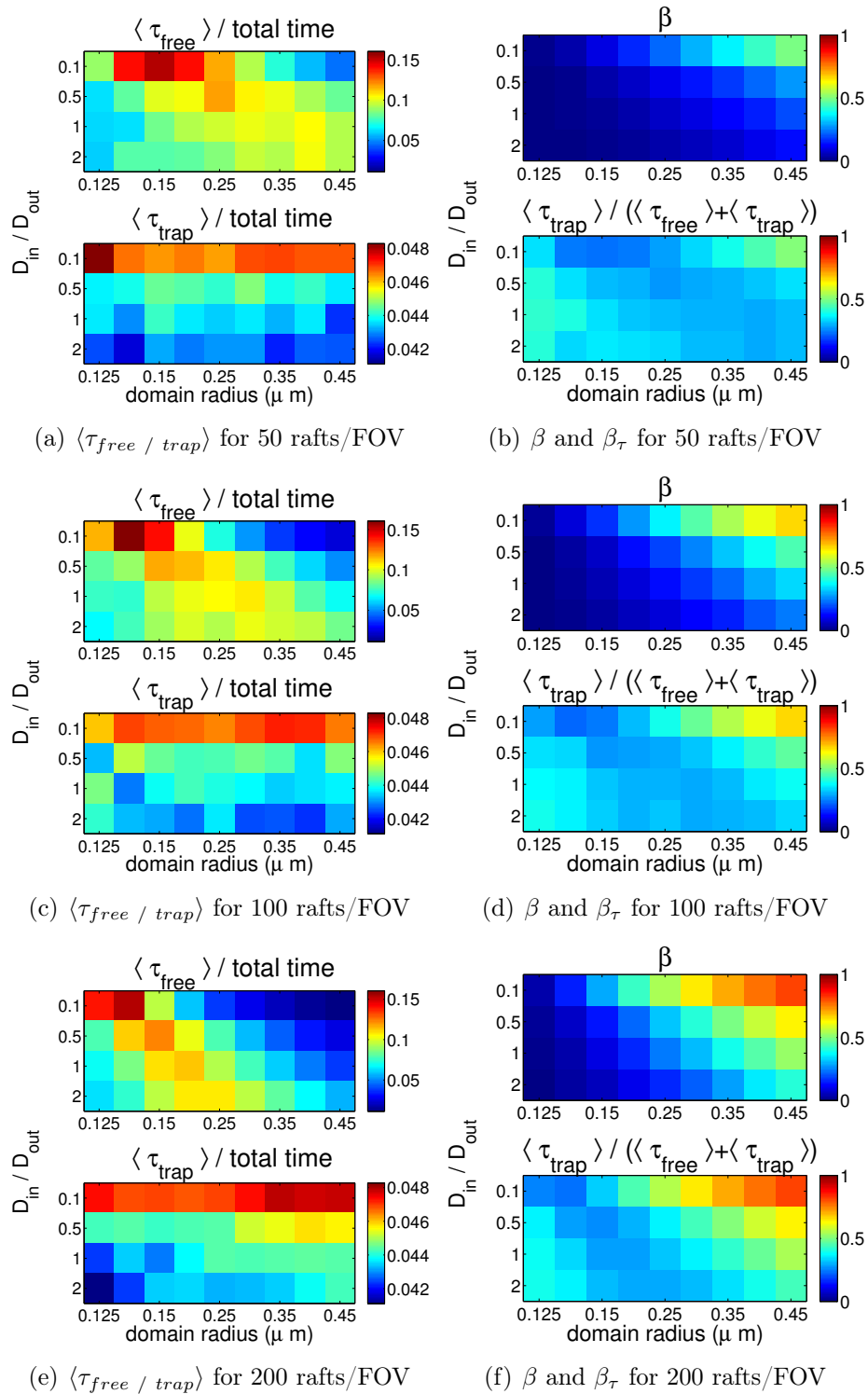


Figure 4-26: Confinement statistics calculated for simulations with  $P_{out}=0.1$ . a), c) and d) are  $\langle \tau_{free} \rangle$  and  $\langle \tau_{trap} \rangle$ , normalized to the total amount of frames, for 50, 100 and 200 domains per FOV, respectively.  $\frac{D_{in}}{D_{out}}$  and domain radius were varied.  $D_{out}$  was set to  $0.01 \mu m^2/s$ . b), c) and d) show calculated  $\beta$  and  $\beta_\tau$  for 3 raft densities considered.

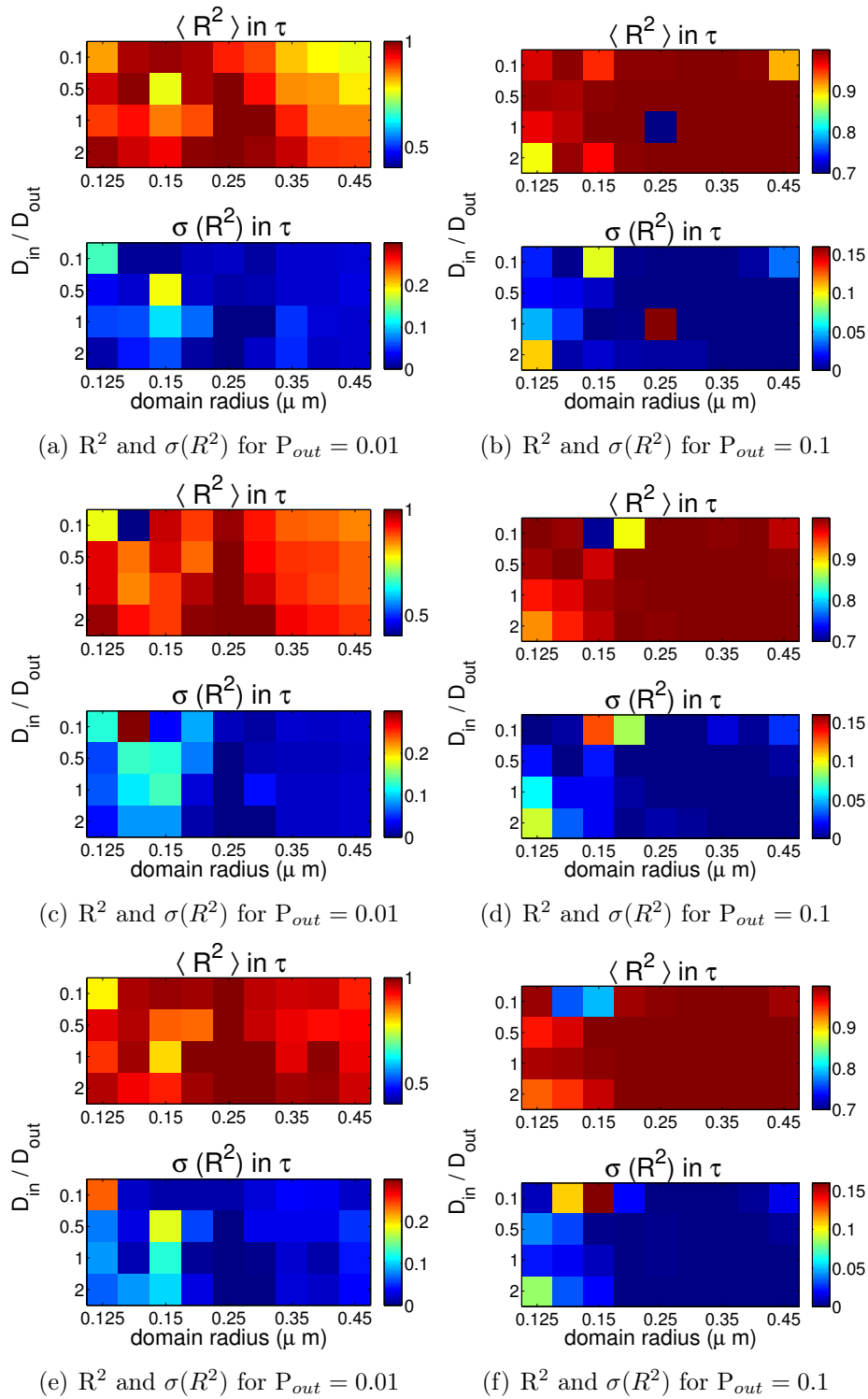


Figure 4-27:  $R^2$  and  $\sigma(R^2)$  for two Gaussians fit of kICS data of a single image series simulation for two  $P_{out}$  scenarios considered. a), c) and d) show  $R^2$  and  $\sigma(R^2)$  for case of  $P_{out}=0.01$ , while  $P_{out}=0.1$  for b), d) and f). Top to bottom row display scenarios with 50, 100 and 200 domains per field of view (FOV), respectively.

## REFERENCES

- [1] Wawrezynieck L. Rigneault H. Marguet D. Lenne P.F. Fluorescence correlation spectroscopy diffusion laws to probe the submicron cell membrane organization. *Biophys. J.*, 89:4029–4042, 2005.
- [2] Ruprecht V. Weiser S. Marguet D. Schutz G.J. Spot variation fluorescence spectroscopy allows for superresolution chronoscopy of confinements times in mebranes. *Biophys. J.*, 100:2839–2845, 2011.
- [3] Schwartzentruber J.A. k-space image correlation spectroscopy: accuracy and precision, capabilities and limitations. Master’s thesis, McGill University, 2010.
- [4] Dietrich C. Yang B. Fujiwara T. Kusumi A. Jacobson K. Relationship of lipid rafts to transient confinement zones detected by single particle tracking. *Biophys. J.*, 82:274–284, 2002.
- [5] Martin D.S. Forstner M.B. Kas JA. Apparent subdiffusion inherent to single particle tracking. *Biophys.J.*, 83(4):2109–2117, 2002.

## CHAPTER 5

### Experimental characterization of GPI-GFP dynamics in live COS-7 cells

This chapter presents the results of kICS investigation of a GPI-anchored protein expressed in living COS-7 cells. As described in the introductory chapter of this thesis, GPI-anchored proteins partition into plasma membrane domains, made primarily from cholesterol and sphingomyelin, of living cells. Addition of domain disrupting enzymes changes the domain constituents, cholesterol and sphingomyelin, which impacts the dynamics of GPI-GFP. In this chapter, we will describe the results of the kICS analysis of image time series collected using TIRF microscopy of the cell basal membranes. The diffusion coefficients and correlation amplitudes of the dynamic populations of GPI-GFP were measured for the case of unperturbed and enzyme disrupted domain scenarios and summarized here.

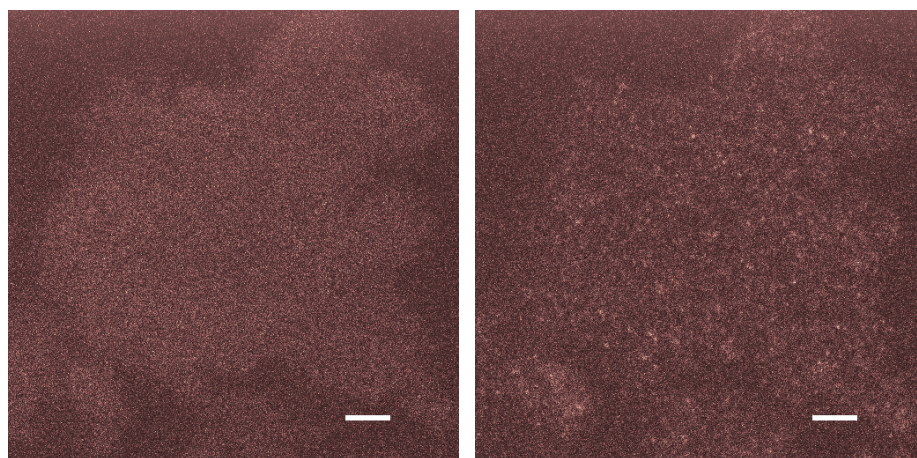
The details of cell culture, labelling, enzyme treatments and microscopy can be found in the chapter 3 (Materials and Methods).

#### 5.1 Alexa dye labelled GPI-GFP on COS-7 plasma membranes

As outlined in earlier chapters, GPI-GFP proteins are expressed in COS-7 cells and inserted into its plasma membrane. Each GPI-GFP molecule is labelled with an anti-GFP antibody, which is labelled with approximately 4-8 Alexa-594 fluorophores. Originally, the experimental data acquired by TIRF microscopy

was that of GFP signal from GPI-GFP in the cell membrane. Unfortunately, over-expression of this protein in COS-7 cells leads to spatially uniform intensity (see figure 5–1 a). Consequently, GPI-GFP signal-to-background ratio was not high enough to produce sufficient spatio-temporal fluctuations. This is an essential requirement for the application of kICS or other image correlation spectroscopy techniques. Molecular biology offers different strategies that can be employed to control protein expression from plasmid DNA in living cells. Nevertheless, these strategies involve extra time consuming steps such as copying and then cloning GPI-GFP gene into a tight control expression plasmid. Luckily, another option presented itself to increase GPI-GFP signal-to-background ratio. The idea of labelling GPI-GFP with an antibody originated accidentally during one of the imaging sessions. Addition of few micro-molars of anti-GFP-Alexa594 into the imaging cell culture dish for 10-15 min, labelled enough of GPI-GFPs to make them appear brighter against the diffuse background fluorescence of plasma membrane (see figure 5–1 b). A larger number of fluorophores (Alexa dyes) per GPI molecule makes it more visible against the noisy background.

For imaging cells, a sufficiently large flat basal membrane area of a selected cell (see figure 5–2 a) is imaged, and a central, 256 by 256 pixels region of interest (ROI) is selected for analysis (figure 5–2 b through d). Acquiring the images from the flat portion of basal cellular membrane ensures that the assumption of two dimensional motion is satisfied. Moreover, the assumption of spatial uniformity is satisfied by selecting cells with uniform expression and a spatial distribution of GPI-GFP. Selecting the region of interest away from the cell centre ensured that



(a) Image of GPI-GFP in COS-7      (b) Image of GPI-GFP-IgG-Alexa594

Figure 5–1: Comparison of old and new labelling approaches for GPI-GFP. a) GPI-GFP prior to Anti-GFP-Alexa-594 labelling. b) Image of the same cell after exposure to the Anti-GFP-Alexa-594. Image in a) was imaged using green excitation laser, while image in b) was excited with red laser. For more specification of imaging condition, please refer to the chapter 3. Scale bar 5  $\mu\text{m}$ .

TIRF visible background from the Golgi apparatus and/or endoplasmic reticulum (ER), are not included in the analysis (such as bright structures visible in lower and upper right corners of figure 5–2 a) . Indeed, GPI-GFP gets produced in the ER and transfers to the Golgi apparatus before being shuttled to the plasma membrane. A large fraction of the total population of GPI-GFP is localized to the membranes of these organelles, which could lead to misleading results if the fluorescence signal from this subpopulation of GPI-GFP is included within the ROI. The image size window was chosen on the basis that the flattest and most uniform part of the cellular membrane that could be fitted within a 256 by 256 pixel region. In the zoom view of the frames shown (figure 5–2 b through d), the white arrows label the brighter spots that appear immobile over time, but show

fluorescence intensity fluctuations over time. These immobile spots are similar to the isolated domains being populated by GPI-GFP partitioning in and out, at defined rates. The fainter features, hidden by the background noise, represent free diffusing GPI-GFP outside of membrane domains. For each cell imaged, a time series was collected of 256 by 256 pixels area and 2000 image frames. These were Hann windowed and the kICS correlation functions were calculated and fit as described in chapter 3.

## 5.2 Correlation functions for GPI-GFP under different enzyme treatments

In order to probe different scenarios of confinements of GPI-GFP in the basal membrane of adherent COS-7 cells, samples were exposed to one of the two domain disrupting enzymes, COase and SMase. These enzymes convert the two major components of membrane domains, cholesterol and sphingomyelin, into new molecules, resulting in an effective domain disruption. These enzymes were added to the cellular samples for either long (COase<sub>long</sub> and SMase<sub>long</sub>) or short (COase<sub>short</sub> and SMase<sub>short</sub>) periods of time, prior to imaging. COase and SMase proved to be most potent within the first hour of treatment. After long periods, these enzymes seem to lose their potency, while the kICS analysis suggests that the enzymatic reaction products can change the membrane microstructure and lipid organization. COase is known to convert cholesterol into cholestenone and phosphocholine, while SMase converts sphingomyelin to ceramide and hydrogen peroxide . The cholestenone is known to be a potential domain inhibitor due to its different polar head group [1]. Hydrogen peroxide was reported to induce the

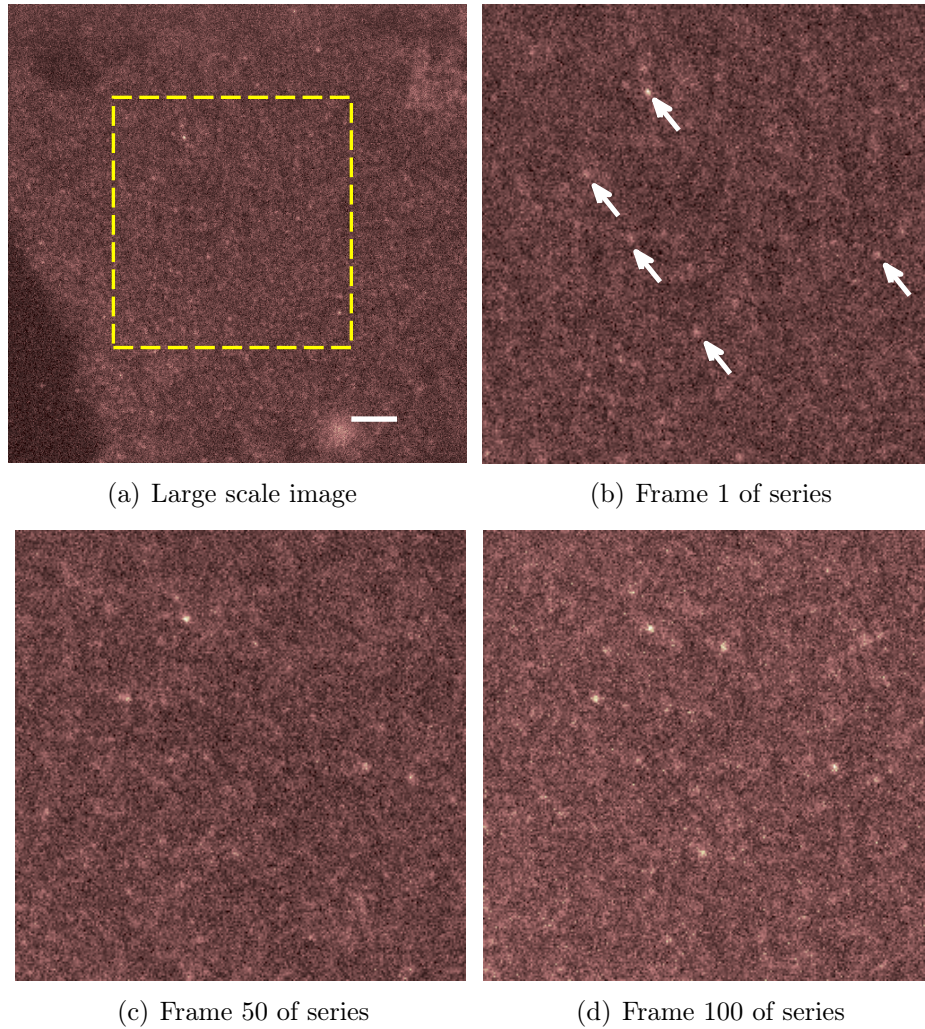


Figure 5-2: Example of GPI-GFP-IgG-Alexa594 images. Top Left: large view (512 by 512 pixels) of COS-7 expressing GPI-GFP labelled by Anti-GFP-Alexa-594. Central 256 by 256 region delimited by the yellow square in a) is selected for imaging. Frames increase in time from b) to d). Frame time is 47 ms. Scale bar is 5  $\mu\text{m}$ .

conversion of the sphingomyelin to ceramide, by acidification of membrane bound sphingomyelinase [2]. Accumulated ceramide over time can form larger membrane domains, and lead to membrane receptors clustering [3]. Ceramide domains are known to be precursors of the cell apoptosis (programmed cell death) [2]. Therefore, the two enzymes employed in these experimental assays can have either the raft disrupting and the raft inducing effects, through the various enzymatic reaction products generated. Figure 5–3 shows examples of kICS correlation functions for 5 different conditions. The top row shows the average of correlation functions calculated from ROI time-series from 20 different cells, while the bottom row displays the correlation functions for typical single cell time series, for each experimental condition.

When a temporal average image of the time series (called the DC image), is subtracted from the time series, the remaining signal contains only fast fluctuations of mobile particles. The immobile component was effectively removed by DC image subtraction. As a consequence, the kICS correlation function will contain only the remaining fast component contribution. This remaining component is not exactly equal to the fast component obtained from the two Gaussians fit of the raw correlation functions. Indeed, DC subtraction removes mostly the immobile component of the time series, but some of the mobile component from the images is also affected by the subtraction. Therefore, care should be taken in the interpretation of the DC image-removed correlation functions. Nevertheless, correlation

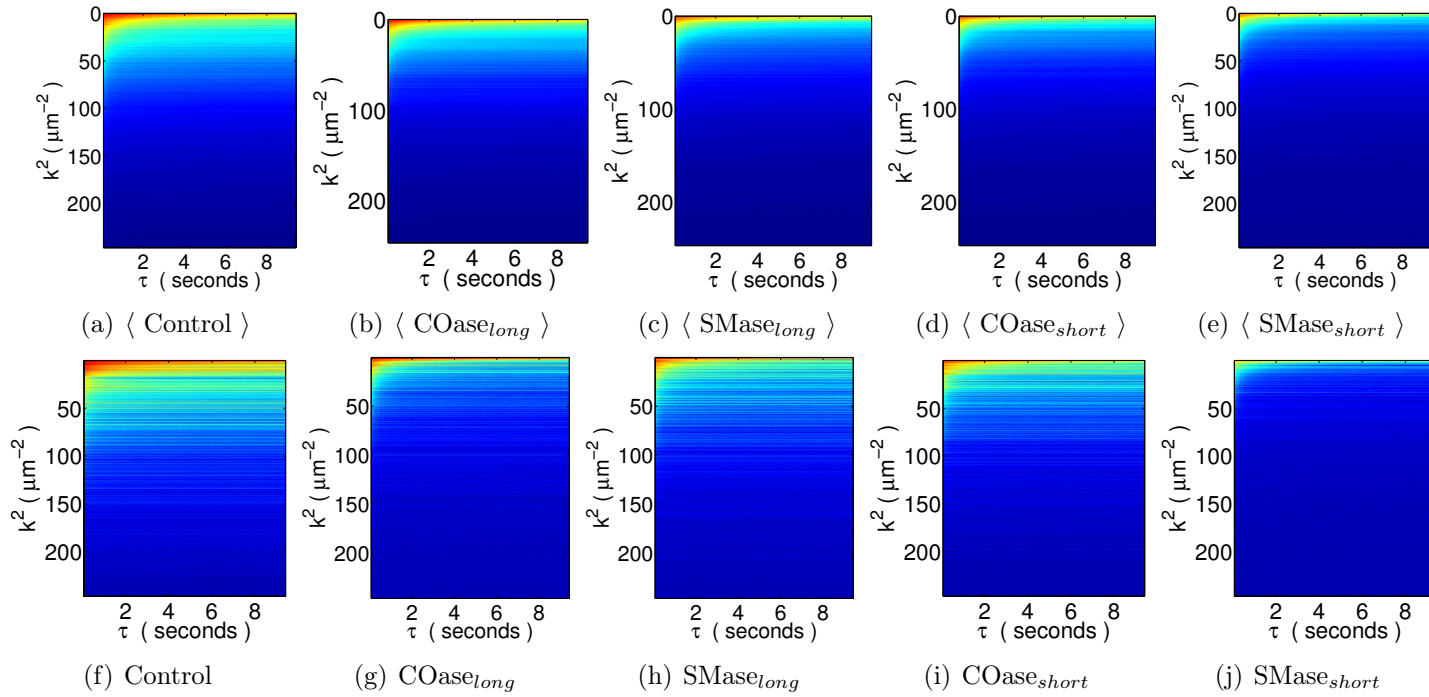


Figure 5–3: Examples of an average (top row) and a typical (bottom row) correlation functions for GPI-GFP-Alexa-594 data for 5 enzymatic conditions considered. KICS correlation functions were normalized by zero temporal lag, making the maximum value equal to 1 (red) and lowest equal to 0 (blue).

functions after DC image subtraction (Figure 5–4) can be fit with a single Gaussian, and the parameters extracted can be compared to the fast component of the two Gaussians fit.

When fitting the correlation function with the sum of two Gaussian functions, the parameters of the fit are 2 amplitudes and 2 exponents (one for the fast and one for the slow components). Since this non-linear fitting is done at each temporal lag, each fit parameter is a function of the temporal lag ( $\tau$ ). Figure 5–5 presents the average amplitudes and exponents of GPI-GFP dynamics in COS-7 cells as a function of  $\tau$  under the different treatments. These fit parameters were obtained each time series correlation function and their averages and standard deviations, from 20 cells of each enzymatic treatment, are shown as a function of temporal lag. One would expect that the domain disrupting enzymes could change the viscosity of the domains, as cholesterol is converted to the cholestenone and the phosphocholine, while the sphingomyelin is converted to the ceramide and the hydrogen peroxide. As a result, we expect to see more particles becoming mobile and an increase of the slope of the fast component,  $D_{fast}\tau$ . This effect is evident in figure 5–5 a, where the slope of the fast component,  $D_{fast}$  is greater for all of the enzyme conditions (any colour symbols) than for the case of the control sample (black symbols). Simultaneously, the slow component saturates at a lower level for control samples (black symbols figure 5–5 b) than any of the enzyme treatment conditions.

These two qualitative observations suggest two things. First, these results suggest that COase and SMase disrupt membrane domains by changing their

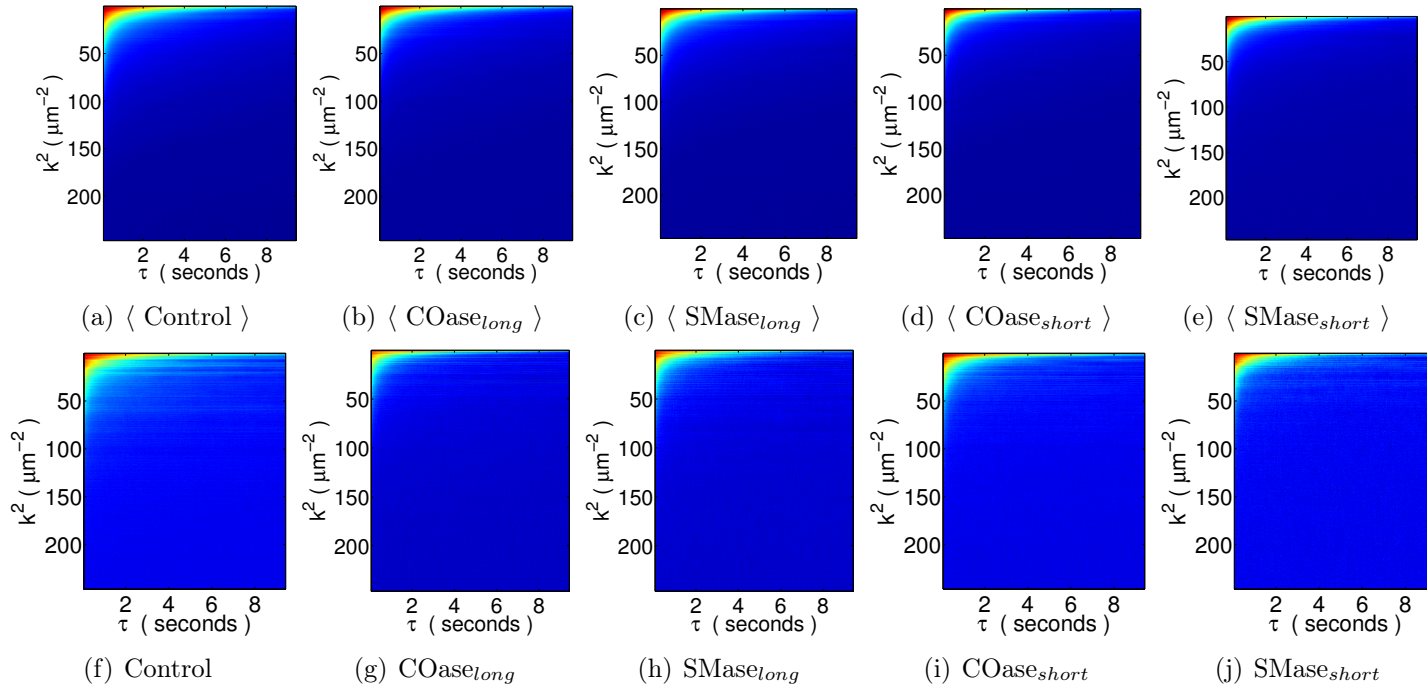


Figure 5–4: Examples of an average (top row) and a typical (bottom row) correlation functions for GPI-GFP-Alexa-594 data for 5 enzymatic conditions considered, after the DC image removal. kICS correlation functions were normalized by zero temporal lag, making the maximum value equal to 1 (red) and lowest equal to 0 (blue).

constituents, which results in higher mobility of GPI-GFP, as witnessed by higher slope in the fast component. Secondly, the increase of the plateau of the slow component, after enzyme treatment, suggests that the effective area explored by the confined particles is larger than those under the control condition. The amplitudes extracted from the non-linear fit of the sum of Gaussians, corroborate these qualitative observations. The amplitude of the fast component saturates at higher values, at later  $\tau$  range, for the enzyme treated samples than in the case of control sample (figure 5-5 c). On the other hand, the amplitude of the slow component saturates at lower values for the enzyme treated samples than the case of control (figure 5-5 d). As shown in the Theory chapter 2, the normalized correlation function amplitude is proportional to the total number of particles of given species. This suggests that after enzyme treatments, there are more particles contributing to the fast component and less to the slow.

In the following two sections we will explore quantitatively the two strategies of characterization of correlation functions fitting. Following the nonlinear fitting of the correlation function for a given scenario to the sum of two Gaussians, one needs to process the trends of  $D_{fast}\tau$ ,  $D_{slow}\tau$ ,  $Amplitude_{slow}$  and  $Amplitude_{fast}$  as a function of  $\tau$ . As detailed in the Materials and Method chapter 3, we use the least squares linear fit to extract the characteristic parameters. The first approach involved averaging all of the trends for a given scenario, as shown in figure 5-5, and linearly fitting these averages. The second approach involved a linear fit of the trends extracted for each individual time series, for a given scenario, and plotting

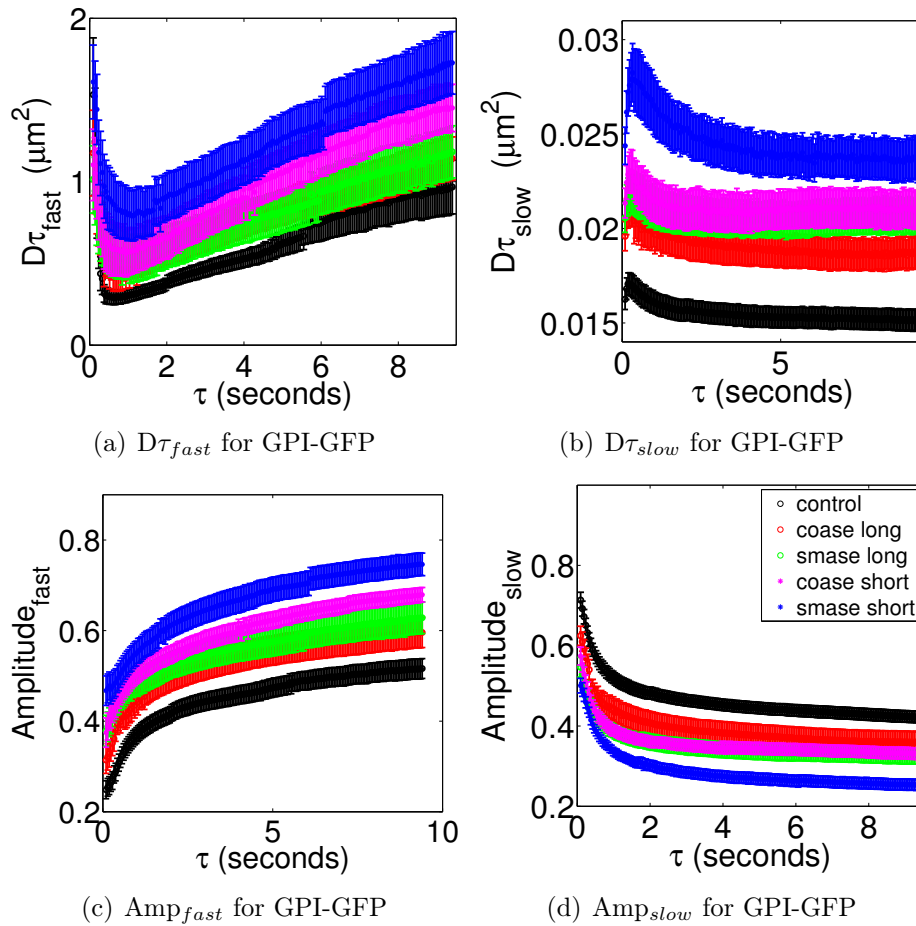


Figure 5–5: Fitted parameters as a function of time lag for the two characteristic fast and slow components of GPI-GFP data. Each trend is an average and standard deviation for 20 cells for a given enzymatic treatment. Symbols colors in a)-c) are same as in the legend of d).

the distributions of the characteristic parameters. Comparisons between the results of these two approaches are discussed later.

### 5.2.1 Characterization of the average trends from multiple cells

In this section we present the results of the linear fit of the average of trends across cells obtained for a given scenario as shown in figure 5-5. This approach seemed appropriate with the assumption that GPI-GFP from all cells have similar dynamics, under a given enzymatic condition. This procedure ensured that trends such as  $D_{fast}\tau$  vs  $\tau$  are smoother resulting in better linear fits. The standard deviations obtained from considering the ensemble of trends from all cells, are used to weight different  $\tau$  points while linearly fitting the average trends. The results from this analysis are summarized in figure 5-6. The error bars represent the 95 % confidence intervals of the fit. From this analysis it is clear that the diffusion coefficient of the fast component of GPI-GFP increases from 0.085 to  $0.115 \pm 0.002 \mu m^2/s$  as a consequence of the enzymatic disruption of the domains. The long exposure of these enzymes (labelled C2 and C3 in the figure 5-6 a) does not seem to significantly affect the diffusion coefficient of the fast component. On the other hand, short term exposure to enzymes (labelled C4 and C5) seems to have a significant effect on the diffusion coefficient of the fast component. It is possible that short term enzymatic conditions (C4 and C5) disrupt domains by conversion of cholesterol and sphingomyelin, effectively freeing more of the GPI-GFP molecules. Nevertheless, the long term exposure to these enzymes can change the effective viscosity of the cell membrane, by redistribution of cholesterol or

ceramide at intermediate spatial scales, which could translate into slower dynamics overall on the large spatial scale ( $D_{fast}$ ). It is known that ceramide forms gel-like macroscopic domains, that could, after longer times, cause the immobilization of GPI-GFP molecules [3]. One should not exclude the possibility of cellular membrane recycling of different components, such as cholesterol and sphingomyelin over longer time periods. Indeed, freshly inserted cholesterol and sphingomyelin could induce re-segregation of GPI-GFP into the composite domains. These enzymes did not seem to significantly affect the diffusion coefficient on the small spatial scales,  $D_{slow}$ , as shown in figure 5–6 b. For all conditions measured  $D_{slow}$  was in the range of  $0.007 \pm 0.007$  to  $0.02 \pm 0.02 \mu m^2/s$ . It is plausible that small spatial scale viscosity does not change significantly. The combination of observations suggests that the domains get disrupted by the enzymes, changing the structure of the membrane at intermediate spatial scales, by redistribution of the byproducts: cholestenone and ceramide.

The plateau saturation of the slow component (figure 5–6 d) does increase from 0.250 to  $0.310 \pm 0.002 \mu m$  with the enzymatic treatment. This parameter was attributed to the effective domain radius in the discussion of chapter 4. As was demonstrated, this parameter does not depend only on the actual size of the domain but also on the probabilities of the particles partitioning in and out of the domains. If the enzyme treatments have affected the domains, it is reasonable to assume that probabilities of GPI-GFP partitioning into and out of domains would be affected. As a result, GPI-GFP molecules could escape the modified domains more frequently and explore a slightly larger area in the domain surroundings

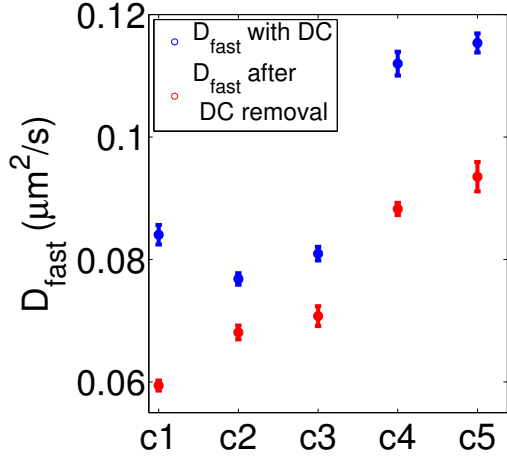
before being trapped again. This gives rise to the idea that an effective domain size is measured by slow (small spatial scale) component saturation. As discussed in chapter 4 the intercept of the linear fit of the fast component,  $\text{Intercept}_{fast}$ , only changes significantly from zero only if the domain size is actually being varied. In the previous simulation studies, variation of the raft densities, diffusion coefficients or partitioning probabilities, did not result in a change of the  $\text{Intercept}_{fast}$ . From the data presented in figure 5–6 c, in combination with results from figure 5–6 d, one can conclude that the actual domain size does increase with the enzyme treatment. It is possible that the exchange rates of particles across the domain boundaries increased as well, which would complement the previous explanation for the increase in the effective domain size, as well as  $D_{fast}$  and  $D_{slow}$ .

Finally, the saturation of the amplitude of the fast component increased from 0.48 to  $0.68 \pm 0.01$  (95 % confidence) following the enzyme treatments, while the slow component decreased from 0.48 to  $0.28 \pm 0.01$  (95 % confidence) as shown in figure 5–6 e. All these observations lead to the conclusion that both COase and SMase affect the spatio-temporal distribution of GPI-GFP fast and slow populations in living COS-7 cells. The long enzyme treatment might have induced new domains from the byproducts or from the freshly inserted cholesterol and sphingomyelin, as a consequence of cellular membrane trafficking and recycling. Nevertheless, the short term exposures to these enzymes, show significant change in the large scale dynamics,  $D_{fast}$  of GPI-GFP and the effective spatial extent they explore on the small spatial scales,  $\text{Plat}_{slow}$ . Furthermore, these observations

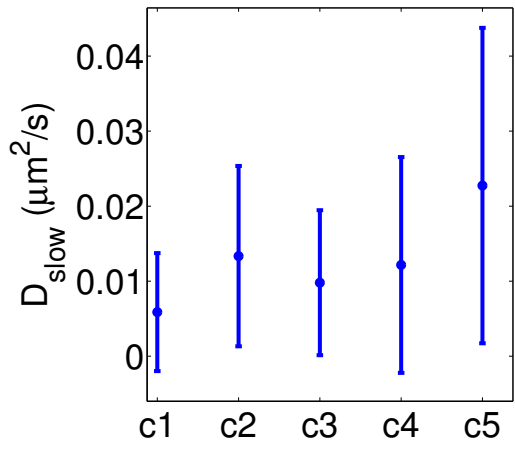
are reinforced by the trends of the amplitudes of the slow and the fast dynamical components which saturate at longer temporal lags  $\tau$ .

### 5.2.2 Characterization of the individual cell trends

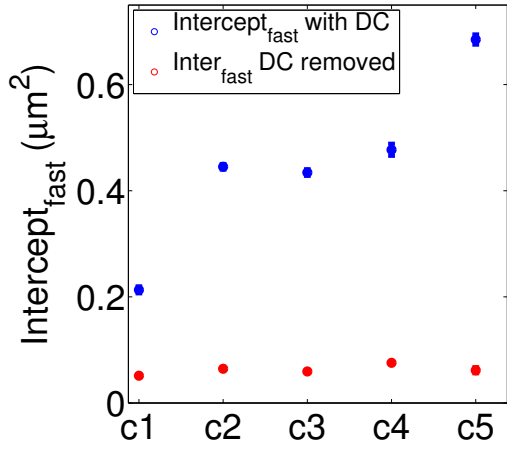
When fitting  $D\tau$ 's derived from single cell time series, the parameters recovered will vary significantly from one cell to another, even under the same treatment condition. Therefore, a relatively large number of cell time series need to be processed to build statistically significant population histograms that can be used to differentiate between conditions. For each of the treatments considered, 20 cells were imaged and the image series analyzed. The problem of the linear fit of  $D\tau$  vs  $\tau$  for a single cell data is due to the presence of sudden inflections and changes in trends at some values of  $\tau$ . Consequently, the linear fit does not capture the variations in  $D\tau$  that occur over a large range of  $\tau$  values and the linear regression will give very significant variations in  $D$  from one cell to another. The same is true for other parameters extracted from the linear trends. The averaging of  $D\tau$  for a given condition, as done in the previous section, helps smooth out the outliers' contributions and creates a trend that is more readily fitted with linear least squares. It is analogous to the averaging of MSD from different particle trajectories in order to produce a statistically significant trend. Nevertheless, we performed the analysis of the same data presented in the earlier section, by linear fitting single cell trends over restricted linear ranges of  $\tau$  values. Usually, the first 50 to 100  $\tau$  lags are less noisy as more pairs of images are used in the calculation of kICS CF



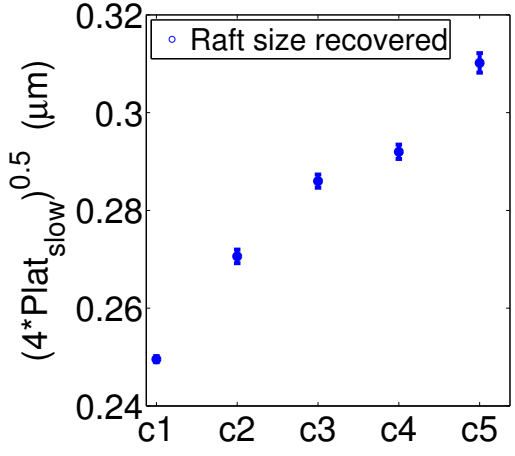
(a)  $D_{fast}$  for GPI-GFP



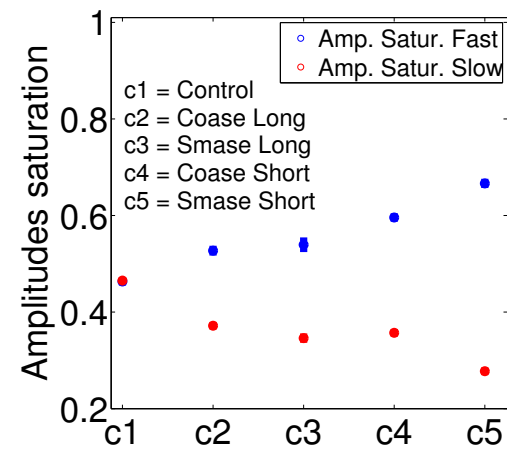
(b)  $D_{slow}$  for GPI-GFP



(c) Intercept<sub>fast</sub> for GPI-GFP



(d) Intercept<sub>slow</sub> for GPI-GFP



(e) Amplitudes of fast and slow

Figure 5–6: Results of the linear regression over the ensemble average (from 20 different cells) of the four parameters ( $D_{fast}\tau$ ,  $D_{slow}\tau$ , amplitude saturation<sub>fast</sub>, amplitude saturation<sub>slow</sub>) vs  $\tau$  trends as presented in figure 5–5. C1-C5 label enzymatic conditions as shown in legend e). Error bars show 95 % confidence intervals obtained from fits.

at small temporal lags. Figure 5–7 summarizes the results of this analysis and is presented using the boxplot graphs.

When examining and comparing boxplots, one needs to consider 5 parameters of a boxplot (take any example from figure 5–7 a): lowest observation, lower quartile (Q1), median value (Q2), upper quartile (Q3) and highest observation. The lowest and highest values show the full extent of the distributions of parameters and are depicted by the black dashed lines and whiskers. Since the data presented in figure 5–7 exhibit some outliers, they will be represented by the red plus markers. The box represent 50 % of the data in a given distribution and is called the interquartile range (IQR). The lower limit of IQR is Q1 and the upper bound is Q3. They represent 25 and 75 % of the data distribution. The upper observation is 1.5 times the IQR above the Q3, while the lower observation is the same distance below Q1. The red line represents the median, while the narrowing of the box around it is called a 'notch'. Notches offer a good guide for the significance in the differences between the medians. If confidence intervals do not overlap significantly then two medians can be considered as statistically different.

Figure 5–7 a) shows that the IQR for all the enzymatic reactions conditions (C2-C5) are shifted upward compared to the control samples (C1). In parallel, the medians for all enzymatic conditions are shifted upward compared to the control as well. The median significance intervals are quite overlapping for control and long SMase (C3) condition. Nevertheless, the clear trend of the increase of median  $D_{fast}$  with the potency of the enzymatic reactions. Interestingly, the

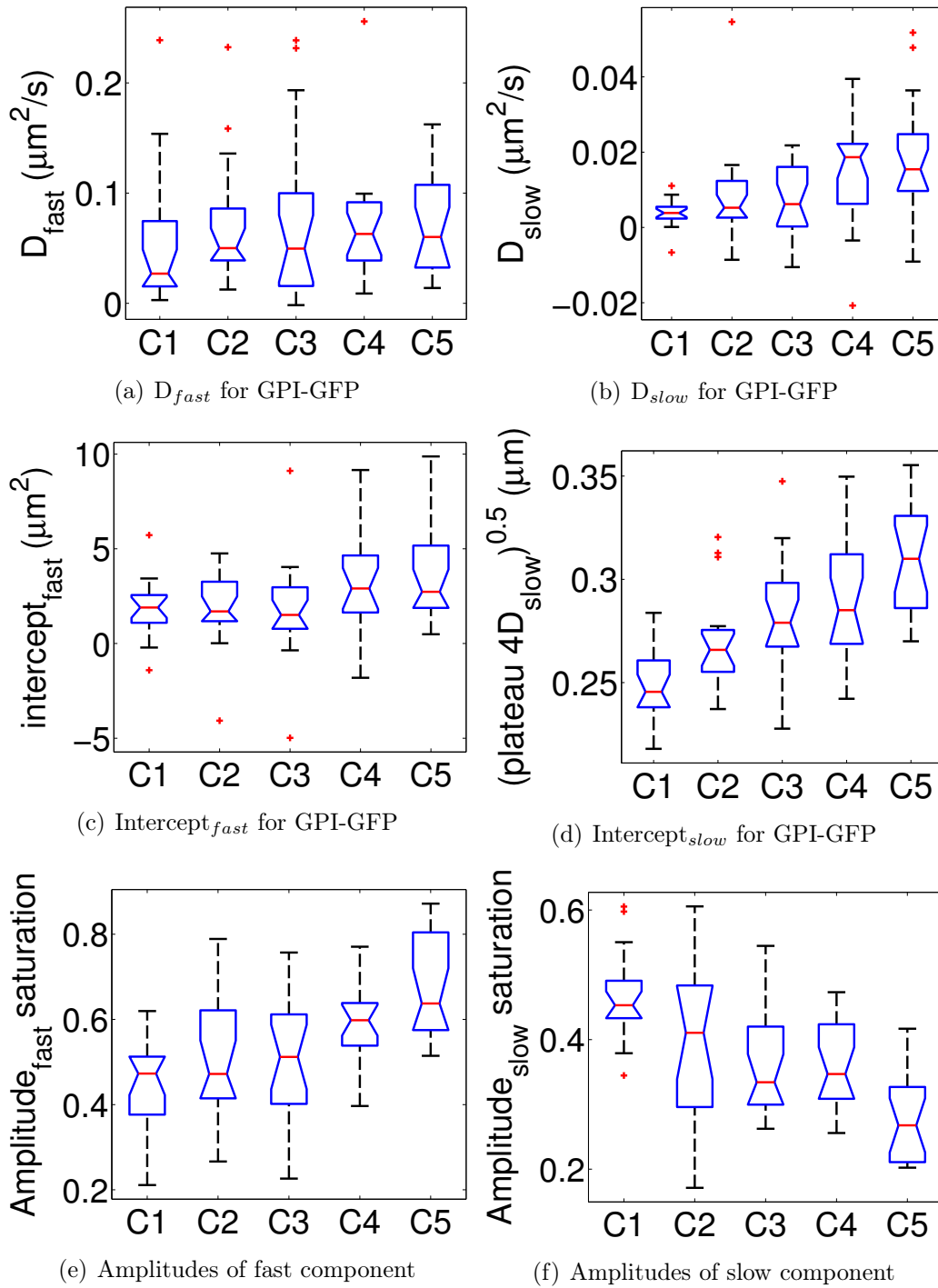


Figure 5-7: Boxplots for characteristic parameters extracted from the linear regressions calculated from CF fit parameters for a single cell image time series. C1-C5 label enzymatic conditions as shown in figure 5-6 e).

slow component slope,  $D_{slow}$  exhibits a significant increase in the median value, especially for the short enzymatic exposure conditions, C4 and C5 (figure 5–7 b). Another interesting observation is that all enzymatic conditions (C2-C5) have a larger spread of values and IQR than the control condition. It is possible that after drug treatments, especially for the short exposures, GPI-GFP explore small spatial scales at slightly larger rates than in the control case. Inspection of figure 5–7 c) suggests that the median of the intercept $_{fast}$  does not change significantly for the long enzyme exposure scenarios (C2 and C3). On the other hand, the short enzymatic exposures (C4 and C5) lead to a significant increase in the median values as well as the full distribution of values, compared to the control case (C1). When discussing the change in the plateau saturation value of the slow component,  $D_{slow}\tau$ , it is evident from figure 5–7 d), that the median increases significantly for conditions C1 to C5. The saturation of amplitudes exhibit the same strong trend as the plateau saturations, as shown in figures 5–7 e) and f).

From all of the data presented in figure 5–7, one can conclude that the ensembles of parameters, extracted from 20 cells per condition, agree with the parameters extracted from the fitting of average trends, as outlined in previous section. The enzymatic reactions increase the diffusion coefficient at large spatial scales as witnessed by the trends of  $D_{fast}$ . The increase in the slow or small spatial scale component plateau saturation, in combination with the increase of the intercept $_{fast}$ , suggest that the domain effective size grows with time of the enzymatic reaction. This effective size is a combination of the exchange of particles between the small and large spatial scales that we extract from the two Gaussian

fit of the kICS correlation function. This exchange between scales depends on the diffusion coefficient of the actual particles at each scale and the rate at which they enter and leave the effective domain area. The enzymatic reaction effectively breaks the smaller and more confining domains and resulting in a leakier and larger effective domains. Particles that were highly trapped under the control condition, explore more readily the intermediate and large spatial scales. This idea is also confirmed by the increase in the saturation of the fast component amplitude, and the decrease in the slow component amplitude saturation.

### 5.3 Discussion of experimental results

In the present study we report that two effective dynamic populations of GPI-GFP, fast and slow, diffuse at 0.06-0.11 and 0.007 to 0.02  $\mu m^2/s$ , respectively. A similar range of diffusion coefficients for GPI-GFP in COS-7 cells was observed experiments using the UPaint method [4]. The observed distribution of GPI-GFP diffusion coefficients was found to be bimodal, with the peaks of the distribution centred around 0.005 and 0.1  $\mu m^2/s$ . The assessment of the GPI-GFP trajectories suggests that confinement zones can be up to  $\sim 500 \mu m$  in diameter. The basis of the UPaint technique relies on sparse labeling of GPI-GFP with anti-GFP antibodies labelled with multiple AT647N dyes. Another study employs an anti-GFP conjugated with a quantum dot (QD) for the sparse labelling of GPI-GFP [5]. The observed distribution of GPI-GFP diffusion coefficients had peaks at  $\sim 0.25$  and 1  $\mu m^2/s$ . The larger diffusion coefficient could be attributed to the faster monomeric GPI-GFP. Indeed, similar values for the diffusion coefficient

of GPI-GFP were observed by the spot-vary FCS method [6]. Nevertheless, this technique involves an assumption of single dynamic species in their fitting procedure of the FCS' ACF. Therefore, the single species model was used in the fit of the temporal auto-correlation function, leading to the effective diffusion coefficient of  $\sim 1 \mu m^2/s$  [7]. The same study suggests that GPI-GFP resides within microdomains about 10 and 30 % of the total time, while the average time spent within domains is estimated to be between 34 and 95 ms. The same group applied a two populations fit to the ACF and proposed two diffusion coefficients of  $\sim 45$  and  $0.6 \mu m^2/s$  [8]. In a previous report, they estimated the upper bound to the GPI-GFP microdomain diameter to be  $\sim 120 \mu m$ . In agreement with this result is a recent study [9] of GPI-GFP dynamics by using the FCS-STED (stimulated emission depletion), which is an extension of spot-vary FCS with PSF radius reduced below the diffraction limit, which allows for probing of the small spatial scales. STED-FCS measured GPI-GFP domains to be on the order of 100 nm. Another conclusion from their study was that the COase treatment did not influence the GPI-GFP dynamics. In another study, a single particle tracking experiment was applied to follow the movements of Thy-1, a GPI-anchored protein [10]. The results suggest that Thy-1 visits  $\sim 230$  nm diameter domains with diffusion coefficients outside the domains in the ranges of  $2-8 \mu m^2/s$ , while inside the domains ranges  $1-5 \mu m^2/s$ . This high spatio-temporal measurement of Thy-1 suggest that this protein spends 15 % of the total trajectory time inside domains with the average  $\tau_{trap} \sim 5$  s. They report that cyclodextrin removal of cholesterol decreases the domain size to  $\sim 150$  nm diameter and the protein

raft occupancy drops to 2 % while  $\tau_{trap}$  remains unaffected. It is interesting to note that the spot vary FCS and SPT studies agree only on the estimate of the fraction of time GPI-GFP spends within microdomains. In another report, the translational motion of GPI-linked I-Ek class II MHC membrane proteins in the plasma membrane of CHO cells studied by SPT measured a diffusion coefficient of  $\sim 0.22 \mu m^2/s$ , but failed to detect any confinement of these proteins [11]. A recent study by high spatio-temporal SPT of GPI-anchored proteins, demonstrate the existence of transient homo-dimers of GPI [12]. These nano-structures were observed at low GPI-anchored protein expression levels. Nevertheless, the authors suggest that higher surface density of this protein might lead to higher order oligomers. Other conclusions were drawn about the aggregation state of GPI-GFP as measured by FRET anisotropy [13]. In this study, it was demonstrated that  $\sim 30$  % of GPI-anchored proteins exist in small,  $\sim 3$  nm, aggregates composed of up to 4 GPI molecules, while the rest of the GPI were in a monomeric state. Interestingly, the polyclonal antibody cross-linking of GPI-anchored proteins of one species was shown to lead to higher order oligomers, which was confirmed by the same author in a previous study [14]. In agreement with these results are data from a PALM study where 2-3 proteins per cluster were detected [15]. On the other hand, PALM most frequently detected clusters of PAGFP-GPI with  $\sim 80$  nm diameters while larger,  $\sim 320$  nm diameter clusters were observed as well.

In light of the literature findings on the dynamics, confinement and aggregation state of GPI-anchored proteins, we shall summarize the data observed in our current work. The range of diffusion coefficients observed for the large and small

spatial scales,  $D_{fast}$  and  $D_{slow}$ , suggest that we are observing a similar dynamic species of GPI-anchored proteins as the study done by the UPaint experiment [4]. A similar diffusion coefficient was observed when GPI was labelled with anti-GFP-QD [5]. Both of these studies share an important feature with the current study, namely the labelling of GPI-GFP with an antibody. It is possible that anti-GFP-Alexa594 used in the current work, clusters 2-4 GPI-GFP together, so these small clusters form larger domains through sphingolipids and cholesterol interactions. The hypothesis here implies that large domains observed are a result of the liquid ordered packing of sphingolipids, cholesterol and small aggregates of cross-linked GPI. This suggests that monomeric or dimeric GPI-GFP can still partition into and out of these large domains. Consequently, an enzymatic treatment changing sphingomyelin and cholesterol into new products, will disrupt the ordered phase resulting in faster exchange of particles. We observe the change in the apparent GPI-GFP domain size as the plateau of the small spatial scales component increases from 0.25 to 0.31  $\mu\text{m}$ . It was demonstrated in chapter 4 that several parameters can affect this value. The increase in domain size and the decrease in the domain binding rate will lead to the increase of  $\text{plateau}_{slow}$ . The increase in the diffusion coefficients, following the enzymatic reactions, as well as the increase in the saturation of the fast component amplitude, suggests that the domains become leaky. The plausible change in the microstructure due to the enzymatic reaction could be that small aggregates of GPI-GFP that are no longer closely packed with sphingolipids or cholesterol. Instead, the newly produced cholestenone or ceramide,

depending on the enzymatic reaction, break the ordered and tightly packed micro-domain into a more loose domain. The monomers or small aggregates of GPI-GFP, can thus explore a larger effective area that is measured with the plateau of the slow component of the kICS analysis.

It is important to state that the value of the apparent domain size extracted from the plateau saturation level of the slow component should not be taken as an absolute value of the domain size. It was shown in the previous chapter, through simulations analysis, that this value does not depend only on the actual size of domains present. Moreover, the presence of noise in an image series will introduce an error in the estimate of this plateau level. Analogous to this is the detection of particles positions in SPT. If the image series' signal-to-noise ratio is small, the accuracy of the fit particle positions will decrease. Consequently, the MSD curve shifts upwards by a positive value which depends on the variance of the noise present in the image series [10]. As a result, the shifted MSD curve will produce an overestimate of the domain size. Furthermore, the noise can produce an apparent sub-diffusion for the early temporal lags of MSD curves in the SPT data [16]. Nevertheless, the domain sizes reported in the present study are due to several system parameters and as such do not represent actual absolute values of domain sizes. Therefore, the image noise effect, whatever its amplitude, will shift the effective domain value by an equal amount for all the image series analyzed. Indeed, both of the control and enzymatic treatment image series were collected under similar conditions of the illumination, time exposure and EMCCD gain.

Hence, the variance of the counting noise is not expected to vary significantly from one series to another.

## REFERENCES

- [1] Perimutter J.D. Sachs J.N. Inhibiting lateral domain formation in lipid bilayers: Simulations of alternative steroid headgroup chemistries. *J. Am. Chem. Soc.*, 131:16362–3, 2009.
- [2] Golkorn T. Balaban N. Shannon M. Chea V. Matsukuma K. Gilchrist D. Wang H. Chan C. H<sub>2</sub>O<sub>2</sub> acts on cellular membranes to generate ceramide signaling and initiate apoptosis in tracheobronchial epithelial cells. *J. Cell Sci.*, 111:3209–3220, 1998.
- [3] Bollinger C.R. Teichgraber V. Gulbins E. Ceramide-enriched membrane domains. *Biochim. Biophys. Acta*, 1746:284–294, 2005.
- [4] Giannone G. Hosy E. Levet F. Constals A. Schulze K. Sobolevsky A.I. Rosconi M.P. Gouaux E. Tampe R. Choquet D. Cognet L. Dynamic super-resolution imaging of endogenous proteins on living cells at ultra-high density. *Biophys. J.*, 99:1303–1310, 2010.
- [5] Thoumine O. Saint-Michel E. Dequidt C. Falk J. Rudge R. Galli T. Faivre-Sarrailh C. Choquet D. Weak effect of membrane diffusion on the rate of receptor accumulation at adhesive contacts. *Biophys. Letters*, pages L40–L42, 2005.
- [6] Wawrezinieck L. Rigneault H. Marguet D. Lenne P.F. Fluorescence correlation spectroscopy diffusion laws to probe the submicron cell membrane organization. *Biophys. J.*, 89:4029–4042, 2005.
- [7] Wawrezinieck L. Conchonaud F. Wurtz O. Boned A. Guo X.-J. Rigneault H. He H-T. Marguet D. Lenne P.-F. Dynamic molecular confinement in the plasma membrane by microdomains and the cytoskeleton meshwork. *EMBO J.*, 25(3245-3256), 2006.
- [8] Wawrezinieck L. Lenne P.-F. Marguet D. Rigneault H. Fluorescence correlation spectroscopy to determine diffusion laws: application to live cell membranes. *Proceedings of the SPIE*, 5462:92–102, 2004.

- [9] Eggeling C. Mueller V. Honigsmann A. Andrade D.M. Bernardino de la Serna J. Hell S.W. New insight into lipid-protein membrane organization and its functionality with super-resolution sted microscopy. *Biophys. J.*, 104(Issue 2, Supplement 1):5a, 2013. Presented at 57th Annual Biophysical Meeting.
- [10] Dietrich C. Yang B. Fujiwara T. Kusumi A. Jacobson K. Relationship of lipid rafts to transient confinement zones detected by single particle tracking. *Biophys. J.*, 82:274–284, 2002.
- [11] Vrljic M. Nishimura S.Y. Brasselet S. Moerner W.E. McConnell H.M. Translational diffusion of individual class ii mhc membrane proteins in cells. *Biophys. J.*, 83:2681–2692, 2002.
- [12] Suzuki K.G.N. Kasai R.S. Hirosawa K.M. Nemoto Y.L. Ishibashi M. Miwa Y. Fujiwara T.K. Kusumi A. Transient gpi-anchored protein homodimers are units for raft organization and function. *Nature Chem. Bio.*, 8:774–782, 2012.
- [13] Sharma P. Nanoscale organization of multiple gpi-anchored proteins in living cell membranes. *Cell*, 116:577–589, 2004.
- [14] Mayor S. Rothberg K.G. Maxfield F.R. Sequestration of gpi-anchored poritein in caveolae triggered by cross-linking. *Science*, 264(5167):1948–51, 1994.
- [15] Sengupta P. Jovanovic-Talisman T. Skoko D. Renz M. Veath S.L. Lippincott-Schwartz J. Probing protein heterogeneity in the plasma membrane using palm and pair correlation analysis. *Nature Methods*, 8:969–975, 2011.
- [16] Martin D.S. Forstner M.B. Kas JA. Apparent subdiffusion inherent to single particle tracking. *Biophys.J.*, 83(4):2109–2117, 2002.

## **CHAPTER 6**

### **Conclusions and future perspectives**

We conclude with a summary of the new ideas and developments presented in this thesis. The problem of implementing image correlation analysis to measure dynamics within a heterogeneous membrane environment is restated and the methodology developed is summarized. The major conclusions are stated and linked. The thesis ends with suggestions of possible future perspectives and work to further extend these methods with consideration of the fundamental assumptions that were made.

#### **6.1 Conclusions**

##### **6.1.1 Adaptation of kICS to confinement analysis**

The advent of microscopy in the 17<sup>th</sup> century enabled the first observation and qualitative description of cells by Robert Hook [1]. It was not until 1925 that a series of experiments suggested the existence of the bilayer lipid membrane [2, 3]. The following decades led to a series of controversies about the role of the proteins in the cellular membrane, until finally new experimental findings in early 1970's [4] prompted the postulation of the fluid mosaic model [5]. Consequently, our view and understanding of the structure of the cellular membrane has not stopped evolving. The application of biophysical experimental techniques, such as optical

tweezers, FRET, SPT and adaptations of FCS, led to the observation of membrane heterogeneities and domain structure and a refinement of the fluid mosaic model.

Image correlation spectroscopy (ICS) and various adaptations were previously used to measure protein dynamics in cellular membranes, as well as their aggregation and oligomerization states. k-space ICS (kICS) was developed to measure protein dynamics, independent of the probe photo-physics [6, 7]. In this thesis, a new adaptation of kICS was proposed for the measurement of protein confinement and dynamics in a heterogeneous membrane. When kICS is applied to an image time series of a system with isolated membrane domains, the correlation function decays effectively as a sum of two Gaussians, in time lag ( $\tau$ ) and spatial frequency ( $k^2$ ). These two decays were linked to two effective dynamic populations that emerge from the particle diffusion within the two phase heterogeneous 2D environment as previously modelled [8]. Similarly, two effective modes of system relaxation were derived for the case of chemical reaction in the context of dynamic light scattering [9]. In both models, a particle can exist in one of two available states, free or confined. It is reasonable to assume that the emerging conversion rates that link those two states, will be a function of particle diffusion coefficients, probabilities of entering and escaping domains, domain sizes and densities.

A series of simulations were performed, where these parameters were varied according to values suggested by previous experimental studies, and kICS confinement analysis was applied in order to extract the characteristic confinement parameters. The analysis consists of calculation of the kICS correlation function from the image time series, which is then fit by a sum of Gaussians. The resulting

characteristic decays of the correlation function,  $D_{fast}\tau$  and  $D_{slow}\tau$ , as well as their amplitudes, Amplitude saturation<sub>fast</sub> and Amplitude saturation<sub>slow</sub>, are a function of time lag,  $\tau$ . These trends are fit linearly at different  $\tau$  ranges to extract the confinement parameters such as diffusion coefficients explored by particles at large and small spatial scales,  $D_{fast}$  and  $D_{slow}$ , the maximum squared displacement of particles at small spatial scales, Plateau<sub>slow</sub>, and amplitudes saturation at higher temporal lags, Amplitude Saturation<sub>slow</sub> and Saturation<sub>fast</sub>. When confinement increases, the number of particles partitioning into domains increases, which results in a decrease in Amplitude Saturation<sub>fast</sub> and an increase in Amplitude Saturation<sub>slow</sub>. Similarly, one would expect the diffusion coefficient at small scales,  $D_{slow}$ , to decrease as particles explore smaller distances at small spatial scales. This is accompanied by a decrease in the Plateau<sub>slow</sub>. Moreover, a larger fraction of particles will explore smaller overall distances at large spatial scales, as they get trapped for longer periods of time within domains, leading to a lower effective diffusion coefficient at large spatial scales,  $D_{fast}$ .

When examining the trends of confinement parameters as the ratio  $\frac{D_{out}}{D_{in}}$  is increased, it was observed that  $D_{fast}$  decreases until saturation, which occurred at a ratio  $\sim 5$ . Similarly,  $D_{slow}$  decreased with increasing  $\frac{D_{out}}{D_{in}}$ , which suggests that more particles got confined and have smaller diffusion coefficients on small spatial scales. In agreement with this observation was the increase in Amplitude Saturation<sub>slow</sub> and decrease in Amplitude Saturation<sub>fast</sub>. Interestingly, the value of the slow component saturation value, Plateau<sub>slow</sub>, was increasing up to the  $\frac{D_{out}}{D_{in}} \sim 1$ , followed by a decrease for higher ratios. This would imply that for ratio  $\frac{D_{out}}{D_{in}}$

smaller than 1, particles inside domains diffuse at higher rates than outside. This results in more frequent encounters of particles with the internal boundaries of domains, and hence a higher chance of particles escaping the domains. As a result, particles would explore the area around domains more readily giving rise to the larger measured effective domain area, or larger  $\text{Plateau}_{slow}$ , than the simulation set  $(\text{domain radius})^2$ . On the other hand, when  $1 \leq \frac{D_{out}}{D_{in}}$ , the lower diffusion coefficient inside domains increases particles partitioning into the domains, which leads to the effective area explored by particles,  $\text{Plateau}_{slow}$ , approaching the set simulation value for the  $(\text{domain radius})^2$ .

The increase in domain radius should increase the effective area particles can explore at small spatial scales, and this was observed through the linear increase in  $\text{Plateau}_{slow}$  with increase in  $(\text{domain radius})^2$ . Similarly, the effective diffusion coefficient particles explore at small scales, will decrease as particles remain more confined within larger domains, as observed with the decrease in  $D_{slow}$ . This trend is accompanied by an increase in  $\text{Amplitude Saturation}_{slow}$  with increasing domain radius. While there was no a clear trend in the change of  $D_{fast}$  with domain radius.

When it comes to the variation of the domain area fraction, all confinement parameters correlated with the change except the  $\text{Plateau}_{slow}$ . This observation was reasonable considering that changing the number of domains in the field of view, should not affect the partitioning and motion of particles at small spatial scales. Instead, it is the large spatial scale properties that will be more significantly affected. Indeed,  $D_{fast}$  drops with the increase in domain area fraction,

which can be explained by particles being trapped by more domains as they diffuse on large spatial scales.  $D_{slow}$  approaches the set  $D_{in}$  as domain area fraction is increased, which could be explained by more particles being trapped with increasing number of domains, and hence the diffusion coefficient at small scales more closely matches the set  $D_{in}$ . The Amplitude Saturation<sub>slow</sub> slowly increased as the domain area fraction increased, indicating that confinement partitioning increases with increasing domain area fraction.

Increasing  $\frac{P_{in}}{P_{out}}$  led to a decrease in  $D_{fast}$  and  $D_{slow}$  suggesting that the higher the probability for particles to enter domains, the lower the effective measured diffusion coefficients on all spatial scales. Again, this is a consequence of particle partitioning more readily into domains with increasing  $\frac{P_{in}}{P_{out}}$ , which leads to particles travelling shorter distances on large spatial scales (smaller  $D_{fast}$ ) and results in particles exploring smaller effective distances on small spatial scales (smaller  $D_{slow}$ ). As a result, Plateau<sub>slow</sub> approaches the true value of (domain radius)<sup>2</sup> as we increase  $\frac{P_{in}}{P_{out}}$ . The Amplitude Saturation<sub>slow</sub> increases with  $\frac{P_{in}}{P_{out}}$  while Saturation<sub>fast</sub> follows the opposite trend.

The information extracted from the computer simulations as detailed above, helped in understanding and interpretation of the experimental results for dynamics and confinement of GPI-GFP. The goal of the experiments was to measure the confinement parameters by adapted kICS analysis on TIRF acquired image time series of GPI-GFP-Alexa-594 in COS-7, with or without treatment with the domain disrupting enzymes, COase and SMase. The longer time exposure to either of these enzymes did not produce very significant changes in GPI-GFP-Alexa594

dynamics and confinement. On the other hand, shorter term exposure to enzymes ( $\sim 15$  min) prior to imaging was more effective in disrupting the sphingomyelin and cholesterol domains. The diffusion coefficient at large spatial scales,  $D_{fast}$  doubled in value over the range of enzymatic reactions, going from 0.085 (control) to 0.115 (short SMase)  $\pm 0.002 \mu m^2/s$ . Similarly,  $D_{slow}$  was measured to be in the range of 0.007 (control)  $\pm 0.007$  to 0.02 (short SMase)  $\pm 0.02 \mu m^2/s$ . The effective area explored at small spatial scales,  $\text{Plateau}_{slow}$  can be traced with a circle of effective radius of 0.250 (control) to 0.310 (short SMase)  $\pm 0.002 \mu m$ . The trend in these three measured confinement parameters, suggests that that ratio of  $\frac{P_{in}}{P_{out}}$  is decreasing as we go from control to the shorter enzymatic exposure. The conversion of cholesterol and sphingomyelin into cholestenone and ceramide introduces more permeable domains in the system. Therefore, GPI-GFP will more readily escape these domains exploring larger distances on both small and large spatial scales.  $\text{Amplitude Saturation}_{slow}$  decreased from 0.48 to  $0.28 \pm 0.01$ , while  $\text{Amplitude Saturation}_{fast}$  increased from 0.48 to 0.68, indicating again that more GPI-GFP particles explore larger spatial scales post enzymatic treatments.

As described in the simulations results above, the parameters that can affect  $\text{Plateau}_{slow}$  are domain radii and ratios  $\frac{D_{out}}{D_{in}}$  and  $\frac{P_{in}}{P_{out}}$ . The domains area fraction should not affect  $\text{Plateau}_{slow}$  and since we do observe a change in its experimental value, we can conclude that enzymatic reactions do not simply increase the domains surface coverage. Also, the Amplitude Saturations change by a factor of two from control to enzymatic treatment conditions. In the simulations with varying  $\frac{D_{out}}{D_{in}}$ , these amplitude saturations only happened for the range in  $\frac{D_{out}}{D_{in}}$

from 0 to 5. For that same range,  $\text{Plateau}_{\text{slow}}$  increased up to  $\frac{D_{\text{out}}}{D_{\text{in}}} \sim 1$  followed by a decrease at higher ratios. Together these suggest that a change in  $\frac{D_{\text{out}}}{D_{\text{in}}}$  is not responsible for change in confinement parameters post enzymatic treatment of GPI-GFP-Alexa-594 in COS-7, while a  $\frac{P_{\text{in}}}{P_{\text{out}}}$  variation could be occurring.

In summary, our experimental data suggest that GPI-GFP-Alexa-594 explore the effective area at small spatial scales of  $\sim 0.250 \mu\text{m}$  in radius that increases to  $\sim 0.310 \mu\text{m}$  post enzymatic treatments. In parallel, the effective diffusion coefficients at large and small spatial scales increase with enzymatic reactions, suggesting that  $\frac{P_{\text{in}}}{P_{\text{out}}}$  decreases making the effective domains more permeable. Previous reports by FRET anisotropy [10] suggest that GPI-GFP exist in small ( $\sim 3 \text{ nm}$ ) aggregates and a PALM study [11] pointed to protein clusters of 2-3 GPI, although higher order structures were detected as well. In accordance with this, recent high temporal resolution SPT [12] demonstrated that GPI form transient homo-dimers which form the basis for higher order oligomers under high physiological expression condition. Our results are in better agreement with the findings of UPaint [13], which reports a bimodal distribution of diffusion coefficient for GPI-GFP, centered around  $0.005$  and  $0.1 \mu\text{m}^2/\text{s}$ . Similarly, UPaint applied to the measurement of GPI-GFP dynamics in COS-7 cells reports the confinement zones that can be up to  $\sim 500 \mu\text{m}$  in diameter. Our experimental system is very similar to the one reported in [13] where GPI-GFP are sparsely labelled with anti-GFP antibodies labelled with multiple AT647N dyes. It is plausible that in both our kICS and UPaint studies, a fraction of GPI-GFP form dimers or small oligomers as a consequence of anti-GFP cross-linking. Consequently, it is possible

that these oligomers get stabilized into larger domains by sphingomyelin and cholesterol packing into ordered structures. Nevertheless, the enzymatic disruption of domains would create more permeable domains that these oligomers as well as GPI monomers can partition into and escape more readily. On the other hand, spot-vary FCS [14] applied to GPI-GFP, without anti-GFP labelling, reported higher order structures with upper bound of the domain diameter to be  $\sim 120 \mu\text{m}$ . Another high spatial resolution variation of spot vary FCS, called STED-FCS [15], measured a domain radius of  $\sim 100 \text{ nm}$  for GPI-GFP. Similarly, PALM [11] on fixed COS-7 cells expressing PAGFP-GPI detected a non-negligible occurrence of  $\sim 320 \text{ nm}$  diameter clusters. It is entirely plausible that we are exploring different spatial and temporal scales for GPI proteins. FRET can assess very small structures at very high spatial resolution while high temporal resolution SPT can assess very fast dynamics of GPI, that PALM, spot-vary FCS or kICS can not, due to low spatio-temporal resolution. Nevertheless, we can assess slower dynamics, on longer temporal scales and large spatial scales, that are not readily accessed with some of the high resolution techniques. Therefore, a combination of techniques is necessary to assess all spatial and temporal scales explored by GPI in live cells.

In addition to exploring the influence of isolated circular micro-domains on the kICS measured dynamics of particles in 2D, we simulated a meshwork modelling the actin cytoskeleton and its effects on particle dynamics and confinement. Our results suggest that in the presence of a meshwork the kICS CFs decay as a single Gaussian in temporal lag,  $\tau$ , and spatial frequency  $k^2$ . The non-linear fitting by a single Gaussian decay vs  $k^2$ , at given  $\tau$  produces  $4D\tau$  which is an equivalent

of the MSD. For weak confinement, when the probability (P) to cross the mesh boundary is high,  $4D\tau$  increases linearly while for higher confinement, it has an inflection at later  $\tau$ . Linearly fitting the early and late linear  $\tau$  regimes provide 3 parameters,  $D_{early}$ ,  $D_{late}$  and  $L_{app}$ , which when combined give estimates of diffusion coefficients within mesh pore,  $D_\mu$ , the hopping diffusion coefficient,  $D_M$ , and mesh pore diameter,  $L$ . The measured diffusion coefficients,  $D_{early}$  and  $D_{late}$ , combine to define the meshwork confinement strength,  $S_{conf}$ . Higher  $S_{conf}$  implies the smaller  $D_{late}$ , hence higher confinement of the mesh and smaller P. This parameter has similar significance to the partitioning coefficient,  $\beta$ , in the isolated domains simulations statistics. The increasing  $\beta$  lead to a smaller measured effective diffusion coefficient,  $D_{eff}$ , at larger spatial scales, compared to the diffusion coefficient set for diffusion outside domains,  $D_{out}$ . It is important to note that the calculated characteristic mesh pore diameter,  $L$ , can be extracted even if the set value was below the optical resolution of PSF  $e^{-1}$  diameter.

We have demonstrated that background Gaussian noise will influence higher  $k^2$  values of kICS CF, by introducing a cutoff value  $k_{cut}^2$ , above which the CF is not to be considered for fitting and confinement analysis. The  $k_{cut}^2$  varies with signal to noise ratio and an assessment of CF prior to fitting is required in order to avoid bias in extracted confinement parameters. Moreover, other sources of noise in the time image series, will introduce a systematic error in the estimation of confinement parameters, in a similar way that was reported for MSD errors from SPT conducted on noisy images [16, 17]. Nevertheless, when all image series are acquired under the same conditions of the illumination, exposure time and

EMCCD gain, a similar systematic error in the extracted parameters will occur in the analysis of all time series. Therefore, comparison of confinement parameters prior to and post enzymatic treatments are valid, in a relative sense, considering that the signal to noise ratio was same in all time series.

Our simulations suggest that the smallest domains resolvable by kICS confinement analysis are on the order of twice the smallest spatial sampling unit of an image, a pixel, which in simulation and experimental data was equal to  $0.1 \mu\text{m}$ . On the other hand, careful examination of particle statistics in chapter 4 showed that for small domains the partitioning fraction,  $\beta$  was relatively small. This suggests that particles did not visit enough small domains over the length of time series simulated, which in turn would result in a low amplitude for the confined (slow) component in the correlation functions, making the small domains invisible or undetectable by kICS confinement analysis. It would take a larger number of small domains and higher confinement (higher  $\beta$ ) to see the emergence of small domains characteristics in kICS CFs. Also, resolving the smallest particles' step sizes, due to small domains, would require higher signal to noise ratios, especially if they are smaller or equal to the pixel size. This is also the basis of sub-pixel localization of single particles in SPT, by fitting of 2D Gaussian to the particle's intensity emission diffraction profile in the image. Therefore, higher signal to noise and higher particle confinement would be necessary ingredients for the detection of small, sub-pixel, domains using kICS confinement analysis.

### 6.1.2 Perspectives and possible future directions

The main focus of this thesis was to extend the potential of kICS and other image correlation based techniques to characterize the heterogeneous membrane environments through image correlation of standard confocal or TIRF microscopy image time series. In particular, the confinement analysis extension to kICS was a natural next step to the previously established kICS analysis of dynamics in a homogeneous 2D environment [6, 7]. Future work could include some of the following improvements:

- **Transient domains and a dynamic meshwork** The isolated domains simulated in chapter 4 according to the methods in chapter 3 were monodisperse, stationary and uniformly randomly distributed in 2D. A possible extension to the current work could be adding the polydispersity to the domain radii and characterizing the change in the kICS CF. Also, domains could be made mobile, either by translating their centroid positions according to active transport or diffusion. Furthermore, the literature on membrane domains describes them as transient, which could be yet another possibility in the domains simulations. Nevertheless, making the domain appearing transiently at random positions in 2D would add yet another time constant, and should shift the partitioning coefficient,  $\beta$ , to lower values for any given condition. When it comes to meshwork simulations, we used a network of parallel horizontal and vertical lines to model a meshwork with square mesh pore of defined radius. It was set to be stationary in time. A more realistic picture would include non-parallel lines and polydisperse mesh pores. Also,

depending on the time frame considered, one could include the possibility in meshwork dynamic reorganization by translation of mesh boundary lines in time. This should cause more than one inflection point in  $4D\tau$  vs  $\tau$  curve and result in a temporal variation in diffusion coefficient as described and verified experimentally by spot-vary FCS study of artificial meshworks [18].

- **Vary step size and waiting time distributions** In the simulations performed in this thesis, the particle step size was drawn from a normal distribution of random numbers with standard deviation defined in each dimension as  $\sqrt{2Dt}$ . This of course simulates the Brownian step sizes in each dimension particle explores, while domain boundaries and probabilities of crossing were used to simulate the effect of confinement on the effective step size distribution of particles. An alternative approach to simulation of confined dynamics is to pick particles step sizes at random from a non-Gaussian distribution of waiting times. For example a power law distribution would lead to an anomalous random walk. On the other hand, if a simulated random walker jumps at each time step  $t$  in some random direction to a distance  $r$ , which is taken from a power law distribution, then the probability density would be Lévy rather than Gaussian. In these simulations, it would be interesting to observe the change in the characteristic features of the kICS CFs and see how they depend on the characteristic exponents of step size and waiting time distributions used to simulate particle trajectories.
- **More realistic models** In the theory chapter (2) we examined the solutions for density-density correlations in the cases of static traps and chemical

reactions. The model for diffusion in a two phase medium, consisting of static traps, assumes that particles become immobile when trapped while they diffuse with a finite diffusion coefficient when outside of traps. As a result, the author of study [8] assumes that the diffusion coefficient is space independent. Usually, the diffusion equation is written as:

$$\frac{\partial c(\vec{r}, t)}{\partial t} = \nabla \cdot (D(c, \vec{r}) \nabla c(\vec{r}, t)) \quad (6.1)$$

which usually reduces to:

$$\frac{\partial c(\vec{r}, t)}{\partial t} = D \nabla^2 c(\vec{r}, t) \quad (6.2)$$

when the diffusion coefficient is considered independent of diffusing species concentration ( $c$ ) and space ( $\vec{r}$ ). On the other hand, if diffusion coefficient varies in space, as in case of simulations of isolated domains considered in this thesis, then the diffusion equation should read:

$$\frac{\partial c(\vec{r}, t)}{\partial t} = \nabla c(\vec{r}, t) \cdot \nabla D(c, \vec{r}) + D(c, \vec{r}) \nabla^2 c(\vec{r}, t) \quad (6.3)$$

Therefore, the coupled diffusion equations for concentration of free and bound particles should have an extra term  $\nabla c(\vec{r}, t) \cdot \nabla D(c, \vec{r})$  that takes into account the spatial heterogeneity in diffusion coefficient values. It is reasonable to assume that this contribution to the particles motion can be seen as a change in particle concentrations due to the spatial gradient in diffusion coefficients at the boundary of each domain. Of course, this assumes that  $D(c, \vec{r})$  is function of positions of domains in 2D, but also offers the

possibility for a particle concentration dependent  $D$ . Indeed, free volume effects can become important at high concentrations of particles, leading to the concentration dependent  $D$ , which should not be neglected.

Furthermore, a parallel between solutions for the static traps model [8] and chemical reaction [9] was an appealing one for the theory development in this thesis, although an essential difference was omitted in the discussion.

In the case of chemical reaction, species  $A$  diffuses *freely* with diffusion coefficient  $D_a$  and when it is converted to state  $B$ , it diffuses *freely* with diffusion coefficient  $D_b$ . Therefore, in the chemical reaction model, particles never encounter a physical boundary, such as for the isolated domain or meshwork. Consequently, it is important to distinguish basic physical differences between the two models compared in the theory chapter, even though both solutions suggest that density-density correlation functions can be expressed as a sum of two dynamic contributions.

Finally, there is a major distinction between the two models of heterogeneous 2D membrane explored by simulations in this thesis. When particles are exploring a meshwork, at any given time frame, particles are either within a given mesh pore or are crossing from one mesh to the adjacent. Therefore, the kICS CF will distinguish between those motions at different temporal scales, as shown in  $4D\tau$  vs  $\tau$  plot, since hopping occurs more slowly than diffusion within each pore. On the other hand, when particles explore a 2D medium seeded randomly with isolated circular domains, particles can explore several different types of dynamics on the same time scale. Some

particles will be exploring the space within domains at diffusion coefficient,  $D_{in}$  while others will be diffusing between domains with set  $D_{out}$ . Moreover, a fraction of particles will be crossing boundaries of domains. As a result, the kICS CF will have two effective decays, that represent the large and small spatial scales particles explore at each temporal lags.

- **Cellular cytoskeletal meshwork confinement and in vitro model confined systems** In this thesis, the experimental verification of the developed technique was carried out by measuring dynamics and confinement of GPI-anchored membrane proteins on live COS-7 cells. This was an obvious choice for the proof of principle experiment, since GPI-anchored protein dynamics were thoroughly explored in the past using many microscopy techniques [16, 12, 19, 11, 10, 20, 21, 15].

However, in the current work, the effects of confinement due to a meshwork grid on kICS CF, was explored only through simulations and theoretical treatments, modelling the proximal cortical actin network. An experiment that could test the kICS extension would be a valuable as it would complete the story of confinement analysis using k-space image correlation spectroscopy. A possible candidate experiment to test this would involve measurements of a membrane embedded protein, such as transferrin receptor, that is known to interact or be confined by the underlying actin meshwork [21, 22]. Another possibility would be to measure the transport dynamics of fluorescent beads embedded in agarose or other artificial gels,

with varying the confinement strength or pore mesh size achieved by tailoring the gel preparation. Indeed, bead diffusion in agarose gel has been investigated previously by FCS [23]. It will be important to tailor the gel concentration as well as to choose the beads of appropriate sizes and surface chemistry, in order to be able to capture the desired confined dynamics with kICS.

Furthermore, an artificial membrane in the form of giant unilamellar vesicles [24] or a supported lipid bilayer [25] could be prepared with defined composition and incorporating a fluorescently labeled membrane protein. The variation of lipid/cholesterol/sphingomyelin concentrations will ultimately define the size and lifetime of ordered and disordered phases in such model membrane systems.

Finally, an artificial mesoporous system can be prepared with compartments of spatial dimensions ranging from a few nanometers to several micrometers. The micro-structure for such a system was already investigated by single particle tracking of embedded fluorescent dye at low concentrations [26]. The confinement analysis extension of kICS, developed in this thesis is currently being applied to map the micro-structure of such samples with embedded fluorescent dye concentrations higher than what SPT can typically handle. This application will be the subject of an upcoming publication.

All of the above topics should be explored in greater detail in a future work.

## REFERENCES

- [1] Hooke R. *Micrographia: or, Some physiological descriptions of minute bodies made by magnifying glasses*. London: J. Martyn and J. Allestry, 1665.
- [2] Fricke H. The electrical capacity of suspensions with special reference to blood. *J. of Gen. Phys.*, pages 137–152, 1925.
- [3] Gorter E. Grendel F. On biomolecular layers of lipids on the chromocytes of the blood. *J.Exp.Med.*, 41:439–443, 1925.
- [4] Frye L.D. Edidin M. The rapid intermixing of cell surface antigens after formation of mouse-human heterokaryons. *J.Cell Sci.*, 7:319–35, 1970.
- [5] Singer S.J. Nicholson G.L. The fluid mosaic model of the structure of the cell membrane. *Science*, 175:720–730, 1972.
- [6] Kolin D.L. *k-space Image Correlation Spectroscopy: theory, verification, and applications*. PhD thesis, McGill University, 2008.
- [7] Kolin D.L. Ronis D. Wiseman P.W. k-space image correlation spectroscopy: a method for accurate transport measurements independent of fluorophore photophysics. *Biophys. J.*, 91:3061–3075, 2006.
- [8] Ronis D. Diffusion in random two-phase media. *Phys. Rev. A*, 36:1908–1929, 1987.
- [9] Berne B.J. Pecora R. *Dynamic Light Scattering*. Dover Publications, inc., 1976.
- [10] Sharma P. Nanoscale organization of multiple gpi-anchored proteins in living cell membranes. *Cell*, 116:577–589, 2004.
- [11] Sengupta P. Jovanovic-Talisman T. Skoko D. Renz M. Veath S.L. Lippincott-Schwartz J. Probing protein heterogeneity in the plasma membrane using palm and pair correlation analysis. *Nature Methods*, 8:969–975, 2011.

- [12] Suzuki K.G.N. Kasai R.S. Hirosawa K.M. Nemoto Y.L. Ishibashi M. Miwa Y. Fujiwara T.K. Kusumi A. Transient gpi-anchored protein homodimers are units for raft organization and function. *Nature Chem. Bio.*, 8:774–782, 2012.
- [13] Giannone G. Hosy E. Levet F. Constals A. Schulze K. Sobolevsky A.I. Rosconi M.P. Gouaux E. Tampe R. Choquet D. Cognet L. Dynamic super-resolution imaging of endogenous proteins on living cells at ultra-high density. *Biophys. J.*, 99:1303–1310, 2010.
- [14] Wawrezynieck L. Lenne P.-F. Marguet D. Rigneault H. Fluorescence correlation spectroscopy to determine diffusion laws: application to live cell membranes. *Proceedings of the SPIE*, 5462:92–102, 2004.
- [15] Eggeling C. Mueller V. Honigmann A. Andrade D.M. Bernardino de la Serna J. Hell S.W. New insight into lipid-protein membrane organization and its functionality with super-resolution sted microscopy. *Biophys. J.*, 104(Issue 2, Supplement 1):5a, 2013. Presented at 57th Annual Biophysical Meeting.
- [16] Dietrich C. Yang B. Fujiwara T. Kusumi A. Jacobson K. Relationship of lipid rafts to transient confinement zones detected by single particle tracking. *Biophys. J.*, 82:274–284, 2002.
- [17] Martin D.S. Forstner M.B. Kas JA. Apparent subdiffusion inherent to single particle tracking. *Biophys. J.*, 83(4):2109–2117, 2002.
- [18] Masuda A. Ushida K. Okamoto T. New fluorescence correlation spectroscopy enabling direct observation of spatio-temporal dependence of diffusion constants as an evidence of anomalous transport in extracellular matrices. *Biophys. J.*, 88:3584–3591, 2005.
- [19] Thoumine O. Saint-Michel E. Dequidt C. Falk J. Rudge R. Galli T. Faivre-Sarrailh C. Choquet D. Weak effect of membrane diffusion on the rate of receptor accumulation at adhesive contacts. *Biophys. Letters*, pages L40–L42, 2005.
- [20] Mayor S. Rothberg K.G. Maxfield F.R. Sequestration of gpi-anchored poritein in caveolae triggered by cross-linking. *Science*, 264(5167):1948–51, 1994.
- [21] Wawrezynieck L. Conchonaud F. Wurtz O. Boned A. Guo X.-J. Rigneault H. He H-T. Marguet D. Lenne P.-F. Dynamic molecular confinement in the

- plasma membrane by microdomains and the cytoskeleton meshwork. *EMBO J.*, 25(3245-3256), 2006.
- [22] Wawrezynieck L. Rigneault H. Marguet D. Lenne P.F. Fluorescence correlation spectroscopy diffusion laws to probe the submicron cell membrane organization. *Biophys. J.*, 89:4029–4042, 2005.
- [23] Fatin-Rouge N. Starchev K. Buffle J. Size effects on diffusion processes within agarose gels. *Biophys. J.*, 86, 2004.
- [24] Bacia K. Scherfeld D. Kahya N. Schwille P. Fluorescence correlation spectroscopy relates rafts in model and native membranes. *Biophys. J.*, 87(2), 2004.
- [25] Oreopoulos J. Epand R.F. Epand R.M. Yip C.M. Peptide-induced domain formation in supported lipid bilayers: Direct evidence by combined atomic force and polarized total internal reflection fluorescence microscopy. *Biophys. J.*, 98, 2010.
- [26] Kirstein J. Platschek B. Jung C. Brown R. Bein T. Brauchle C. Exploration of nanostructured channel systems with single-molecule probes. *Nature Methods*, 6, 2007.

## Biohazardous Materials Certificate

## Copyright Permission Form

## KEY TO ABBREVIATIONS

|  |     |
|--|-----|
| ACF:Auto-Correlation Function                    | 28  |
| APD:Avalanche Photo-Diode                        | 28  |
| CCD: Charge Coupled Device                       | 23  |
| Coase:Cholesterol Oxidase                        | 106 |
| DLS:Dynamic Light Scattering                     | 57  |
| DMEM:Dulbecco Modified Eagle Medium              | 104 |
| DRM:Detergent Resistant Membrane                 | 4   |
| E.Coli:Escherichia Coli                          | 110 |
| EGFP:Enhanced Green Fluorescent Protein          | 12  |
| EGFR:epidermal growth factor receptor            | 44  |
| FBS:Fetal Bovine Serum                           | 104 |
| FCS:Fluorescence Correlation Spectroscopy        | 5   |
| FRAP: Fluorescence Recovery After Photobleaching | 4   |
| GFP:Green Fluorescent Protein                    | 11  |
| GPI:glycosylphosphatidyl inositol                | 4   |
| HBSS:Hank's Balanced Salt Solution               | 105 |
| ICCS:Image Cross-Correlation Spectroscopy        | 37  |
| ICS:Image Correlation Spectroscopy               | 7   |
| IgG:Immunoglobulin G                             | 14  |

|  |     |
|--|-----|
| ISF:Intermediate Scattering Function                         | 58  |
| kICS:k-space Image Correlation Spectroscopy                  | 38  |
| MSD:Mean Squared Displacement                                | 26  |
| PAINT:Point Accumulation for Imaging in Nanoscale Topography | 25  |
| PALM:Photo-Acivation Light Microscopy                        | 24  |
| PMT:Photo-Multiplier Tube                                    | 28  |
| PSF:Point Spread Function                                    | 20  |
| QD:Quantum Dot   | 13  |
| SISF:Self-Intermediate Scattering Function                   | 59  |
| Smase:Sphingomyelinase                                       | 106 |
| SNR:Signal to Noise Ratio                                    | 23  |
| spIDA:Spatial Intensity Distribution Analysis                | 37  |
| SPT:Single Particle Tracking                                 | 5   |
| STICS:Spatio-Temporal Image Correlation Spectroscopy         | 38  |
| TICS: Temporal Image Correlation Spectroscopy                | 37  |
| TIRF:Total Internal Reflection                               | 8   |